CIVIL ENGINEERING JOURNAL

číslo 4/2023

Obsah:

CIVIL ENGINEERING JOURNAL

Article no. 33

THE CIVIL ENGINEERING JOURNAL 4-2023

LIQUID-SOLID COUPLING RESPONSE OF SURROUNDING ROCK MASS OF LARGE-DIAMETER RIVER-CROSSING SHIELD TUNNEL

Shanglong Zhang[1], Xuansheng Cheng[2], Xiaoshuang Li[2], and Lei Qi[2]

1. *Hexi University, School of Civil Engineering, Department of Civil Engineering, Zhangye 734000, China; zsl889712@126.com*
2. *Lanzhou University of Technology, School of Civil Engineering, Department of Civil Engineering, Lanzhou, 730050, China*

ABSTRACT

The purpose is to investigate the response of the surrounding rock mass's seepage field, displacement field, and stress field during dynamic tunneling in soft soil. Relied on a large-diameter river-crossing shield tunnel project, considering driving force, shield tail grouting pressure, and the friction resistance between the shield shell and the soil, a three-dimensional fine tunnel model taking into account the liquid-solid coupling effect (LSCE) in the soil during dynamic tunneling was established by employing the finite difference method. The response characteristics of pore water pressure(PWP), displacement and stress in the surrounding rock mass were obtained. The results show that due to the liquid-solid coupling(LSC) in the surrounding rock mass, the PWP in the range of 0.5 times the hole diameter around the tunnel reduces and increases, respectively, during shield tunneling and shield tail grouting. The PWP of the soil close to the vault falls as the shield tunneling recedes, whereas the PWP close to the tunnel arch bottom rises. The impact range of shield tail grouting on the vertical settlement of the overlying soil is about 0.5 times the hole diameter. The shield tail grouting can significantly lessen the vertical settlement of the overlying soil and moderate the vertical uplift of the bottom soil. During shield tunneling the vertical stress distribution of the soil above the vault of the working position and around the excavation surface is funnel-shaped, and the vertical stress around the excavated tunnel decreases.

KEYWORDS

River-crossing tunnel, Dynamic tunneling, Liquid-solid coupling, Seepage field, Displacement field, Vertical stress

INTRODUCTION

With the advancement of urbanization, the problem of traffic congestion on the ground is becoming more and more prominent. Therefore, the development of underground traffic has become an important way to alleviate traffic congestion in large and medium-sized cities [1,2]. A great many river-crossing shield tunnels have been constructed or under construction along the river and coastal areas around the world, such as Seikan Tunnel (Japan), The Channel Tunnel (Britain and France), Jiaozhou Bay Undersea Tunnel (China), Cross Harbour Tunnel (Hong Kong), and Oujiang North Tunnel (China). Many challenges face the construction of a river-crossing shield tunnel under complex environmental conditions such as saturated soft soil, high water pressure and safety problems [3-5]. The shield tunneling will inevitably disturb the surrounding rock mass, and then the LSCE becomes obvious between soil particles and pore water. The PWP, displacement and stress of saturated soil are dynamically changed. Time-varying water-soil pressure severely affects the sealing of segments and the grouting quality behind the segments. In severe cases, it will threaten

the safe construction of shield tunnel, and the impact is particularly serious for large-diameter shield tunnel. Therefore, it is of great significance to explore the liquid-solid coupling response of saturated soft clay during dynamic tunneling of large-diameter river-crossing shield tunnels.

For the liquid-solid coupling response in the soil around the tunnel during the shield tunneling, researchers have conducted a lot of researches by employing theoretical analysis, numerical analysis and test methods, and fruitful results have been achieved. In terms of theoretical research, Zareifard and Fahimifar [6] analyzed the stability of underwater tunnel while taking the seepage force into account, and established the analytical solution of stress field and displacement field of surrounding rock mass of underwater tunnel. Wang et al. [7] considered the spatial variability of geotechnical parameters and applied random field theory to the reliability index analysis of ground settlement induced by the shield tunneling. According to the elastic-plastic theory, Pinto et al. [8] deduced the analytical solution of ground subsidence caused by shallow tunnel excavation in soft soil strata. Using the complex variable function theory, the distribution laws of the displacement, stress and PWP were obtained under the special conditions around the tunnel [9-12]. Taking the tunnel project in karst area of Dalian Metro Line 5 as the background, Zhang et al. [13] derived the linear relationship between $S_{max,0}/S_{max,z}$ and $(1-H_z/h)$ and its influence parameters based on the principle of similar soil loss. Using the multiple linear regression method, the prediction formula of the maximum ground subsidence caused by shield excavation under the condition of karst cave was established. Using extreme gradient boosting, artificial neural network, support vector machine, and multivariate adaptive regression spline, Zhang et al. [5] proposed a ground subsidence prediction model for EPB tunnel in Singapore. Ocak and Seker [14] employed artificial neural network, support vector machine and Gaussian processes to predict the ground settlement of Istanbul Metro tunnel excavated by earth pressure balance shield. However, in most theoretical methods the strata were regarded as homogeneous when studying the displacement field and PWP field during shield tunneling, and the influence of the actual multiple strata was not considered. Most methods are only applicable to specific conditions, and could not be widely used in the practical project due to the complexities of the ground conditions. In addition, numerical analysis is a favorite method for studying ground deformation caused by shield tunneling. Liu et al. [15] established a three-dimensional finite difference numerical model employing FLAC 3D, considering the factors such as trapezoidal support force, shield cone, trapezoidal grouting pressure, grouting body solidification, timely placement of lining, the soil settlement caused by shield tunnel excavation in silty sand stratum was studied. Using the discrete element method, Hu et al. [16] studied the surface and underground deformation characteristics of sandy soil under various burial depths and screw conveyor speeds. Based on the shield tunnel project in water-rich soft stratum, Li et al. [17] established a three-dimensional refined model considering fluid-solid coupling during shield tunneling, the effects of excavation face support pressure, friction between shield and soil, and synchronous grouting amount on ground settlement and structural deformation were mainly studied. To analyze the distribution of the stress field, displacement field, and PWP field in the soil during shield tunneling, numerical models with liquid-solid coupling were developed in the relevant literature [18-20]. Cheng et al. explored fluid-solid interaction response of subsea tunnel taking high water pressure [21] and under earthquake [22] into account. Yao et al. [23] studied the ground collapses in sand cobble strata caused by shield tunnel construction of Lanzhou Metro Line 1, divided the ground collapses into three types, A, B and C, and put forward corresponding control measures. Yuan et al. [24] used field monitoring to investigate the disturbance mechanism and the influence law on the surrounding rock soil in each stage of shield tunneling of a super-large diameter slurry shield tunnel. Using model test and finite element simulation, Shahin et al. [25] investigated the impact of ground overload and construction sequence on ground subsidence brought on by tunnel construction. Relied on Luoyang urban rail transit engineering, Wang et al. [26] conducted field tests in sandy cobble stratum, and studied the excavation disturbance and influence range of soil in each stage of earth pressure balance shield tunneling. Using numerical simulation, the disturbance characteristics of deformation, seepage and stress state of sandy cobble stratum during shield tunneling were obtained. Xie et al. [27] used the finite difference method to optimize the construction parameters of an EPB shield

tunnel, and validated the applicability of the numerical model of a large-diameter tunnel through field monitoring. However, in most numerical methods, the influence of liquid-solid coupling on seepage field and displacement field during dynamic shield tunneling was not considered, and most studies mainly focused on sandy soil strata, there were relatively few studies concentrating on dynamic tunneling in the silty soft soil strata with overlying water.

Relied on the large-diameter river-crossing shield tunnel project of S2 line of Wenzhou city railway, considering relevant parameters of shield tunneling, a fine numerical model considering the LSCE in the soil around the tunnel during dynamic excavating of a large-diameter river-crossing shield tunnel was established by employing finite difference method. The response characteristics of PWP, displacement and stress in the soil were obtained, and the influence of shield tail grouting on settlement characteristics and mechanical properties of strata during shield excavation was also analyzed. The findings of this research have significant theoretical implications for the construction of large-diameter river-crossing shield tunnels.

BASIC PRINCIPLE OF LIQUID-SOLID COUPLING

Seepage field equation of saturated soft soil

It is supposed that the flow of pore water in soil obeys Darcy's law. The compression of porous media follows the principle of Terzaghi effective stress. The seepage in soil is saturated flow. According to the porous media seepage theory, only considering the vertical compression, the three-dimensional seepage continuity equation of porous media single-phase fluid is as follows [28].

$$\frac{\partial}{\partial \mathrm{x}}\left(\frac{\rho K}{\mu}\frac{\partial p}{\partial x}\right)+\frac{\partial}{\partial \mathrm{y}}\left(\frac{\rho K}{\mu}\frac{\partial p}{\partial y}\right)+\frac{\partial}{\partial \mathrm{z}}\left(\frac{\rho K}{\mu}\frac{\partial p}{\partial z}\right)+\rho(\alpha+n\beta)\frac{\partial p}{\partial t}=0 \quad (1)$$

Where ρ is the fluid density, K is the permeability of porous media (m^2), μ is fluid viscosity (Pa·s), p is pore pressure (kPa), n is the porosity of porous media, t is time (s), a is compressibility coefficient of porous media $\alpha=-\frac{1}{V_b}\cdot\frac{dV_b}{dp}$, (1/kPa), β is coefficient of fluid compressibility $\beta=\frac{1}{\rho}\cdot\frac{d\rho}{dp}$, (1/kPa).

In the actual seepage, the source term w is considered to be added at the left of the above equation to obtain the basic seepage differential equation of single-phase fluid in compressible media.

$$\frac{\partial}{\partial \mathrm{x}}\left(\frac{\rho K}{\mu}\frac{\partial p}{\partial x}\right)+\frac{\partial}{\partial \mathrm{y}}\left(\frac{\rho K}{\mu}\frac{\partial p}{\partial y}\right)+\frac{\partial}{\partial \mathrm{z}}\left(\frac{\rho K}{\mu}\frac{\partial p}{\partial z}\right)+w+\rho(\alpha+n\beta)\frac{\partial p}{\partial t}=0 \quad (2)$$

The seepage field equation can be solved according to the constant pressure boundary condition or the constant flow boundary condition.

Displacement field equation of saturated soft soil

For small deformation, the fluid particle balance equation without considering the temperature effect is

$$-q_{i,\,j}+q_v=\frac{1}{M}\frac{\partial p}{\partial t}+\alpha\frac{\partial \varepsilon}{\partial t} \quad (3)$$

Where $q_{i,j}$ represents flow velocity of fluid, q_v represents fluid source intensity (1/s), M is biot modulus (N/m^2), a is biot coefficient, and ε is volume strain.

The variation of fluid pore pressure is caused by changes in the volume strain of the rock-soil mass. Meanwhile, changes in fluid pore pressure results in the variation of volume strain. The incremental form of the porous media constitutive equation can be expressed as

$$\Delta\tilde{\sigma}_{ij}+\alpha\Delta p\delta_{ij}=\hat{H}_{ij}(\sigma_{ij},\Delta\varepsilon_{ij}) \quad (4)$$

Where $\Delta\sigma_{ij}$ represents stress increment; H_{ij} represents a given function; ε_{ij} represents the total strain.

The compatibility equation can be used to characterize the relationship between strain rate and velocity gradient.

$$\dot{\varepsilon}_{ij}=\frac{1}{2}[\frac{\partial \dot{u}_i}{\partial x_j}+\frac{\partial \dot{u}_j}{\partial x_i}] \quad (5)$$

Where $\dot{u}$ represents velocity at some point in the medium.

The displacement field can be solved by knowing the surface displacement of rock and soil skeleton $u_{ij}=u_{ij}(x, y, z)$.

ENGINEERING CASE

Calculation parameters

Taking the river-crossing shield tunnel project of S2 line of Wenzhou city railway as the background, the project adopted the pressure balance shield machine with a diameter of 14900mm, which started from the Jiangnan working well and then advanced to the north, crossed the waters of Oujiang North Estuary, and reached the Jiangbei receiving well. The working diagram of mud balanced shield is shown in Figure 1. The tunnel lining ring has an outer diameter of 14500mm, an inner diameter of 13300mm, a ring width of 2000mm, and a segment thickness of 600mm.. The schematic diagram of shield tunneling across river is shown in Figure 2.

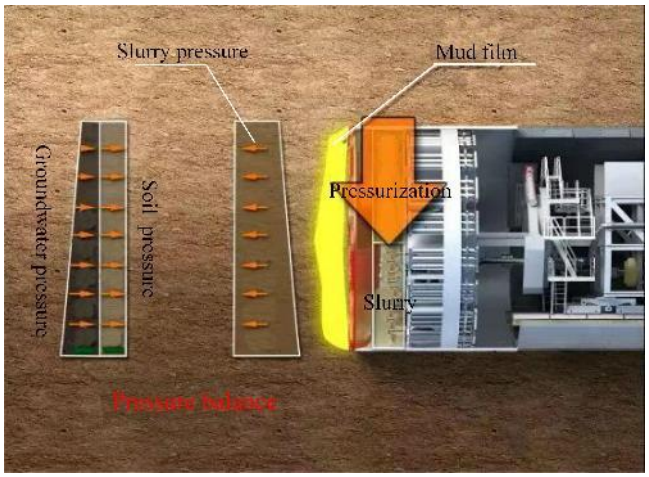

Fig. 1 –The working diagram of mud balanced shield.

Fig. 2 – Schematic diagram of shield tunneling across river

Table 1 displays the stratigraphic distribution and the parameters of a typical stratigraphic section. Affected by sea tide, the depth of the overlying water on the riverbed of Oujiang River is 8-16 m.

Tab. 1 - Lithologic parameters

Stratum	Moisture ratio under natural status /%	ρ/（kN/m³）	Es/MPa	φ/°	c/kPa	μ
Silt(1)	61.84	16.5	1.97	2.93	6.05	0.3
Silt(2)	56.34	16.8	2.09	3.11	6.38	0.3
Silt clay	50.05	17.3	2.5	3.89	6.24	0.32
Clay	40.46	18.4	3.6	4.12	6.76	0.35

The physical characteristics of the shield shell, lining, and grouting body are presented in Table 2. The lining structure's rigidity has been reduced to 85% of its original stiffness due to the impact of the staggered arrangement of segments and the segment joints.

Tab. 2 - Physical and mechanical parameters

	ρ/（kg/m³）	μ	E/MPa
Shield machine shell	7850	0.3	200000
Lining	2500	0.2	30600
Grouting body	2200	0.25	400

Computational model and boundary conditions

Employing the finite difference software FLAC3D, the calculation model of shield dynamic tunneling across river in multi-layer is established taking the liquid-solid coupling effect into account. Because of the structure's symmetry, half of the model is established for analysis. The model size is 65.45m×100m×78.2m based on the actual project size and taking the influence of the boundary effect into account, as shown in Figure 3. The water level above the riverbed is 12 m. The length of the shield machine is selected as 6 m. According to the technical data of the project, the weight of the shield machine is 1655 t. The lining segment has a width of 2 m, a thickness of 0.6 m, and the thickness of the grouting layer behind the lining ring is 0.2m. The surrounding rock mass and grouting layer adopt an 8-node solid element, and the lining and shield shell adopt shell element. The following are the boundary conditions: The upper surface of the model is subjected to 120 MPa pore water pressure and 120 MPa vertical force. The horizontal displacements on the model's four sides are constrained, as is the vertical displacement at the bottom. The model's four sides and the bottom have impermeable boundaries.

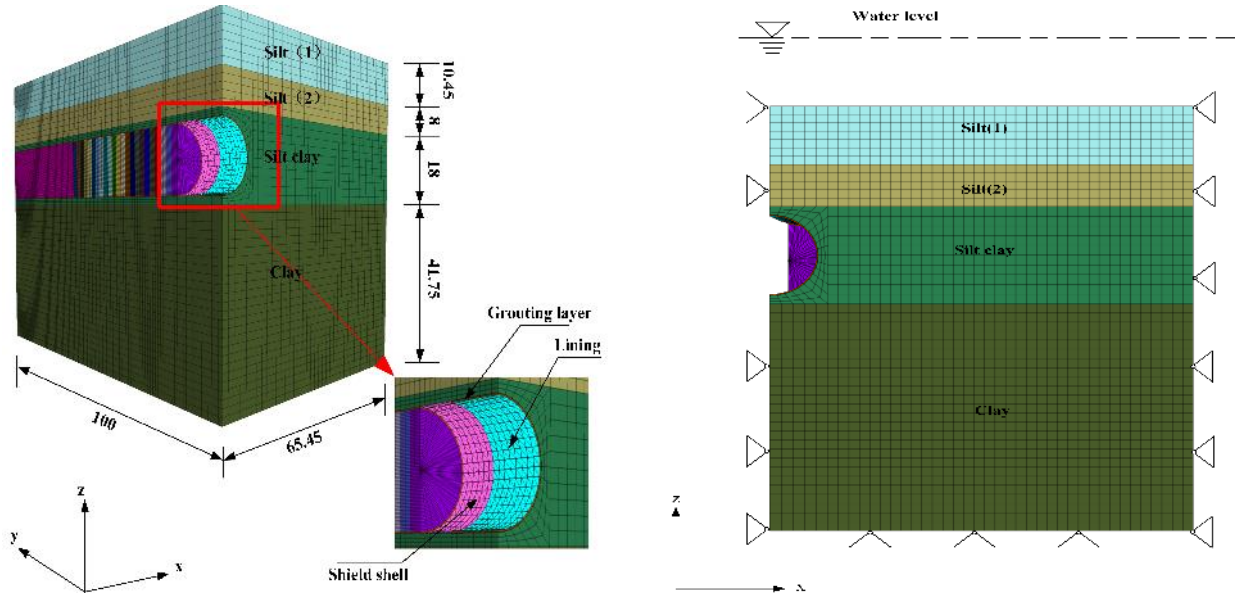

(a) Integral model of shield tunnel (b) Boundary constraints of shield tunnel

Fig. 3 – Schematic diagram of river-crossing tunnel model

Numerical procedure

For the soil, the Mohr-Coulomb (M-C) criterion is chosen, and the elastic model is applied to the lining segment and the shield shell. The total overburden pressure is chosen in the calculation.

To mimic the consolidation settlement of underwater strata prior to tunnel excavation, the ground stress balancing is performed, and at this point, the PWP in the soil is treated as hydrostatic pressure.

In the numerical simulation of shield tunneling across river, the shield machine advances 2 meters for each excavation ring. According to the monitoring data of the practical project, the tunneling speed of the river-crossing shield tunnel is low, which is 6-8m/d. In addition, the supporting pressure on the excavation face is constant, which is simulated as the surface load distributed along the depth trapezoid, so the tunneling speed is considered to be constant. Therefore, the influence of tunneling speed on the surrounding rock soil is not considered in this paper. The supporting pressure acting at the tunnel surface center is obtained by Equation (6), and the gradient pressure is acted on the tunnel surface. The tail grouting pressure is set as 0.5273MPa according to the water-soil pressure around the hole. Considering the condensation and hardening of shield tail grouting is completed within 8~11 hours, and the excavation of one ring is completed within about 6 hours, it is assumed that the shield machine excavates two rings during this period. To simplify the calculation, the grouting pressure of the former ring on the surrounding rock soil and lining segment is considered as 0.2637MPa when the shield tail grouting of back ring is carried out [29]. The friction resistance between the shield shell and the soil is calculated by Equation (7), which is 159132N/m^2. By using a method in which fluid calculations and solid mechanics calculations are performed simultaneously, the liquid-solid coupling effect is obtained during shield tunneling across river.

$$\sigma_x=\sigma_y=[k_0\rho_d+(k_0(n-1)+1)\rho_w]gh \quad (6)$$

Where, k_0 is the lateral pressure coefficient, and n is the porosity. Based on the results of engineering geological investigation, k_0 is 0.674, and n is 0.51.

$$F_1=\frac{1}{4}\times(p_0+p_{01}+p_1+p_2)\cdot u \quad (7)$$

$$p_{01}=p_0+W/(D\cdot L) \quad (8)$$

$$p_1=p_0\cdot k_0 \quad (9)$$

$$p_2=(p_{01}+\gamma'\cdot D)\cdot k_0 \quad (10)$$

where, p_0 is the soil's vertical force at the top of the shield machine, p_{01} is the soil's vertical force at the bottom of the shield machine, p_1 is the lateral force at the top of the tunnel, p_2 is the lateral force at the bottom of the tunnel, D is the shield machine's outer diameter, L is its length, u is the friction coefficient between the soil and the steel body, and u is 0.3.

To avoid the effect of boundary conditions on the seepage, displacement and stress in the soil around underwater tunnel, the 29m section of the 15th ring in the middle of the tunnel was taken as the analysis section, and the measuring points were arranged on this section. It is assumed that the shield machine has completed the excavation of the first three rings at the beginning, and the soil is in a stable state.

LIQUID-SOLID COUPLING RESPONSE OF SURROUNDING ROCK SOIL

Pore water pressure analysis

Figures 4 and 5 show the variation laws of PWP at measuring points with shield tunneling from the fourth ring to the 24th ring. Measuring points are arranged at different radius (7.45m, 8.45m, 9.45m, 10.45m, 11.45m, 12.45m, 13.45m, 14.45m, 15.45m) along 45° direction between arch waist and vault of the tunnel in 29m section of the 15th ring in Figure 4. In Figure 5, measuring points are arranged at different heights (7.45m, 8.45m, 9.45m, 10.45m, 11.45m, 12.45m, 13.45m, 14.45m, 15.45m) above the tunnel vault in 29m section of the 15th ring. It can be seen from the figures that during the shield tunneling from the 14th to the 17th ring, owing to the continuous disturbance to the soil of the analysis section, the stress of the surrounding soil releases, the PWP of the measuring points around the tunnel in a certain range of the analysis section is reduced because of the decrease

of porosity and permeability. And the PWP of the measuring points in this range dropped most during the excavation of the 17th ring. As the shield machine excavates to the 18th ring, at this time the shield tail grouting of the 15th ring is carried out. Due to the reinforcement effect of grouting pressure and grouting amount on the soil, the PWP at the measuring points of the analysis section rises sharply. During the excavation of the 19th ring, the grouting in the 15th ring has not been completely solidified and hardened, and there is still a certain grouting pressure on the soil. The PWP at the measuring points in the surrounding rock soil decreases to a certain extent, but it is generally higher than that of the 17th ring tunneling. After that, the PWP of the measuring points gradually become stable. From Figures 4 and 5, it can be concluded that the impact range of the PWP in surrounding rock soil around the tunnel during the underwater shield tunneling is about 0.5R (R is the outer diameter of the shield tunnel).

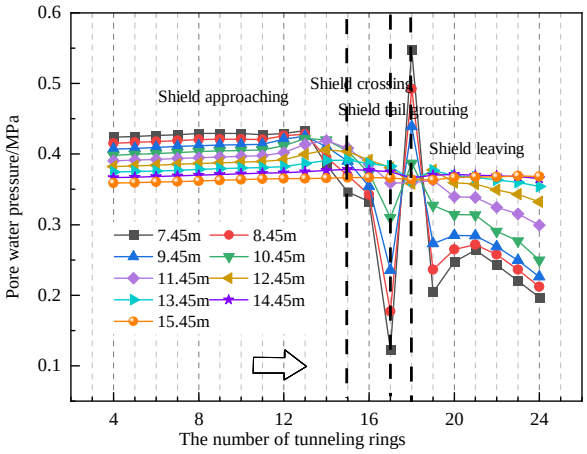

Fig. 4 – Pore water pressure of measuring points along 45°direction

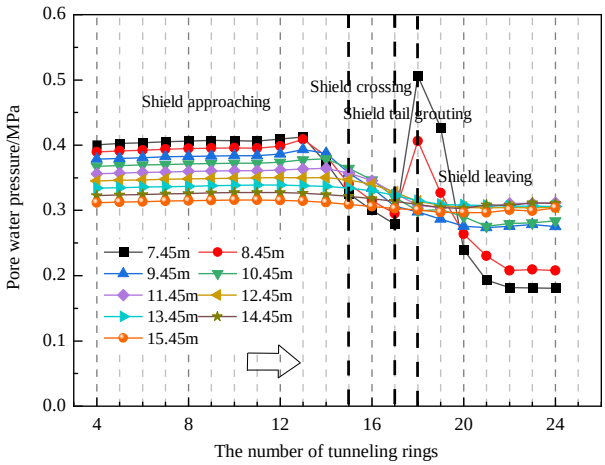

Fig. 5 – Pore water pressure of vertical measuring points above tunnel vault

Figures 6(a) and 6(b) show the PWP distribution of the longitudinal section containing the tunnel axis and the monitoring cross section when the shield machine excavates to the 16th and the 18th ring, respectively. It can be obtained from Figure 6(a) that when the shield tunneling reaches the 16th ring, because of the disturbance to the soil in a certain range around the tunnel, the effective stress of the soil in this range is released. And there is a significant liquid-solid coupling in the soil, which lowers the PWP in this range. It can be obtained from Figure 6(b) that when the shield tunneling reaches the 18th ring, the shield tail grouting of the 15th ring is carried out. The effective stress of soil particles increases in a certain range around the tunnel, the soil particles undergo compression deformation, and the liquid-solid coupling raises the PWP.

The distribution of PWP on the longitudinal section containing the tunnel axis is roughly similar when the shield reaches the 16th and the 18th ring. In the completed construction section (1-12 rings in Figure 6(a), 1-14 rings in Figure 6(b)), the PWP in the soil near the vault decreases and increases near the tunnel arch bottom. The reason is that with the solidification and hardening of the grouting body, the soil above the vault sinks under the vertical water-soil pressure, and the effective stress of soil particles increases. The soil under the tunnel arch bottom uplifts, and the effective stress decreases. Under the assumption that the total stress of the soil remains constant, the PWP in the soil above the vault decreases, while the PWP in the soil near the tunnel arch bottom increases. So, tunnel anti-floating measures such as secondary grouting should be taken during construction. Furthermore, the PWP distribution around the excavation surface is funnel-shaped. To summarize, it is suggested that the PWP in the surrounding rock mass be regarded as dynamic water pressure caused by the liquid-solid coupling in the underwater shield tunnel construction.

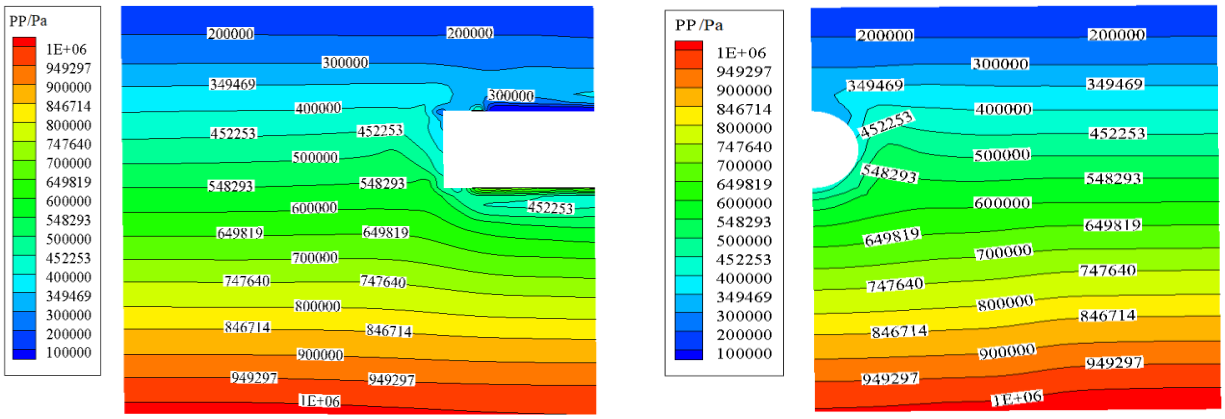

(a) PWP when shield crossing

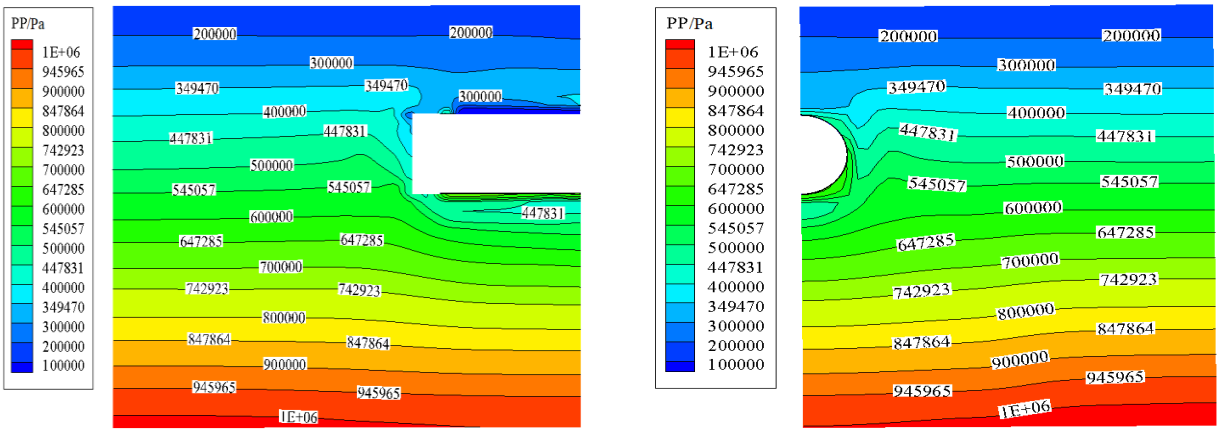

(b) PWP when shield tail grouting

Fig. 6 – PWP of monitoring section

Displacement field analysis

Vertical displacement during shield tunneling

Figure 7 presents the variation laws of vertical displacement at measuring points with shield tunneling from the fourth ring to the 24th ring. Measuring points are arranged at different heights (7.45m, 8.45m, 9.45m, 10.45m, 11.45m, 12.45m, 13.45m, 14.45m, 15.45m) above the tunnel vault in 29m section of the 15th ring. The vertical subsidence of the monitoring point decreases as the distance between the monitoring point and the tunnel axis increases above the tunnel vault. When the shield machine excavates to the 8th ring, the small vertical settlement of the monitoring point above the vault of the 15th ring analysis section begins to produce. After that, with the shield machine excavating forward the disturbance to the monitoring section increases, and the vertical settlement of the monitoring point continues to increase. It shows that the influence range of the underwater shield tunneling on the vertical displacement of the front surrounding rock soil is about 1R. From the 14th ring to the 17th ring, with the continuous shield tunneling, the vertical displacement of the monitoring points continues to increase due to the release of soil stress caused by the disturbance to the soil of the analysis section. When the shield tunnel is excavated to the 18th ring and the 19th ring the vertical displacement growth of the monitoring points tends to be gentle due to the reinforcement effect of the grouting pressure and grouting amount behind the 15th ring segment. The maximum vertical settlement of the vault measuring point (0,29,7.45) is 14.88mm. According to the excavation of the 20th and subsequent rings, the influence range of the synchronous grouting of the shield tail on the vertical settlement of the surrounding rock soil above the vault is approximately 0.5R

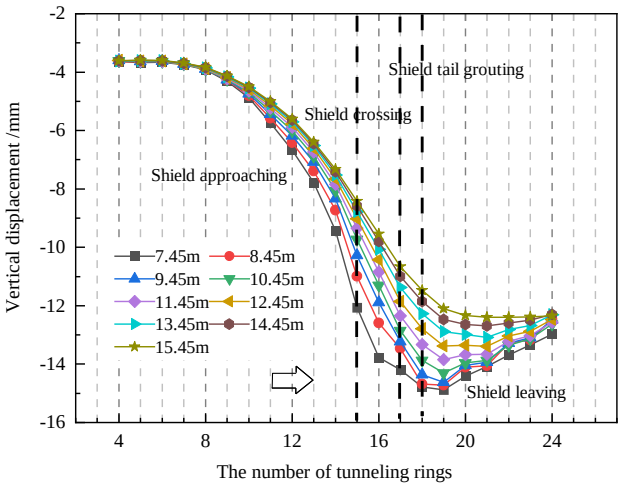

Fig. 7 – Vertical displacement of measuring points above tunnel vault

Figure 8 presents the vertical displacement distribution of the longitudinal section containing the tunnel axis and the monitoring cross section when the shield machine excavates to the 18th ring. It can be concluded that the LSCE in the soil is obvious during the underwater tunnel excavation, and the distribution of vertical displacement in surrounding rock mass is complex, especially around the tunnel. With the shield machine moving forward, the arch bottom of the tunnel uplifts and the vault sinks. Due to the grouting amount and grouting pressure behind the 15th ring lining segment, the vertical displacement of the soil above the 15th ring segment is significantly reduced. The local surrounding rock soil at the tunnel's bottom in front of the excavation face has a slight upward uplift, indicating that the slurry pressure on the excavation surface should be controlled to avoid excavation surface instability during the shield tunnel construction.

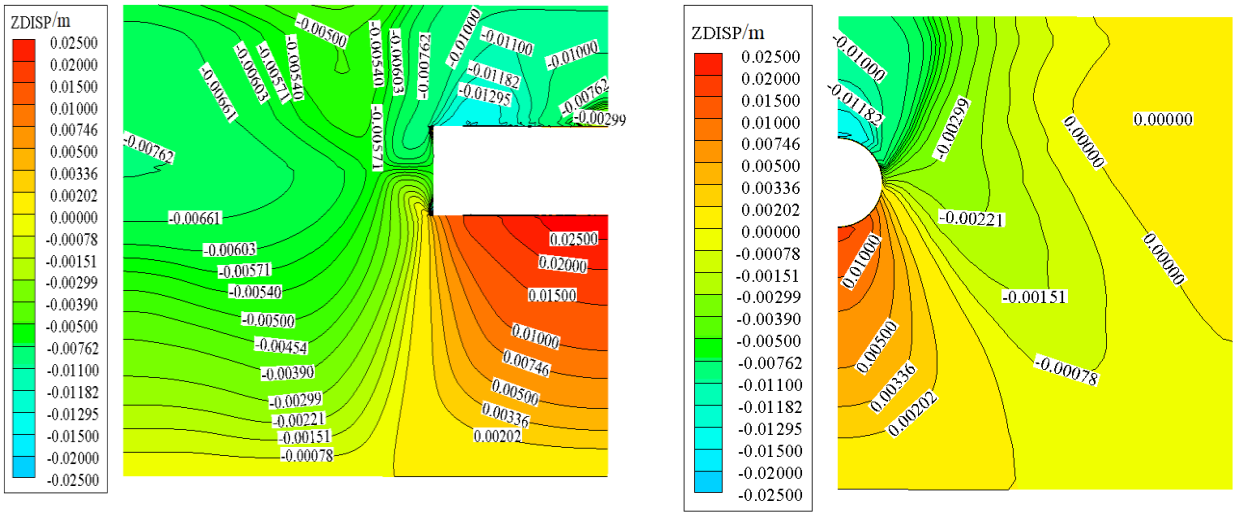

Fig. 8 – Vertical displacement when shield tail grouting

Strata settlement

Figure 9 presents the vertical settlement of different strata above the vault of the tunnel in the 29 m monitoring section of the 15th ring when tunneling in the 19th ring. It can be obtained that the maximum ground subsidence occurs at the upper part of the shield tunnel axis, and with the increase of stratum depth, the vertical settlement above the axis of the tunnel is larger. The shape of the settlement curve of each stratum is similar, and all conform to the Gaussian normal distribution of Peck curve. The deeper the depth of the stratum, the narrower the settlement trough width, indicating

that the disturbance range of the soil is smaller. This is consistent with the conclusions of existing studies, and also proves the correctness and reliability of the numerical analysis method in this paper.

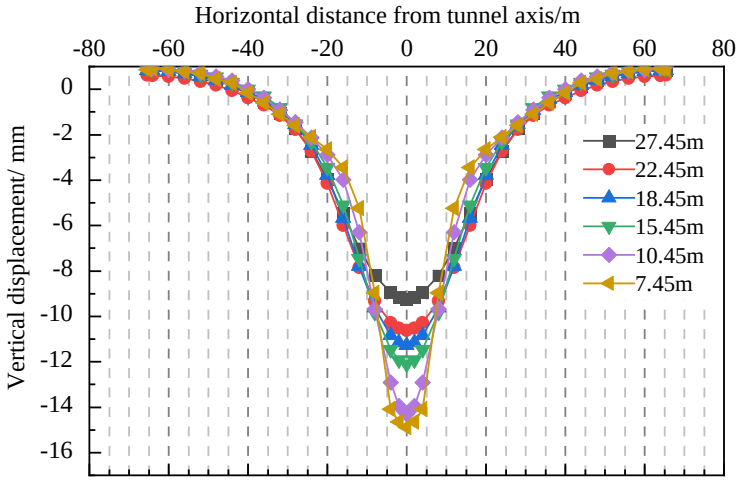

Fig. 9 – Vertical settlement of different strata

Vertical settlement of tunnel vault and arch bottom

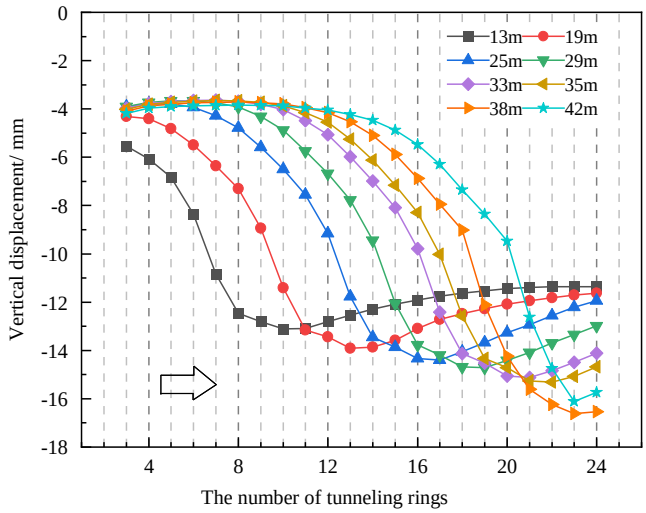

Fig. 10 – Vertical displacement of measuring points at tunnel vault

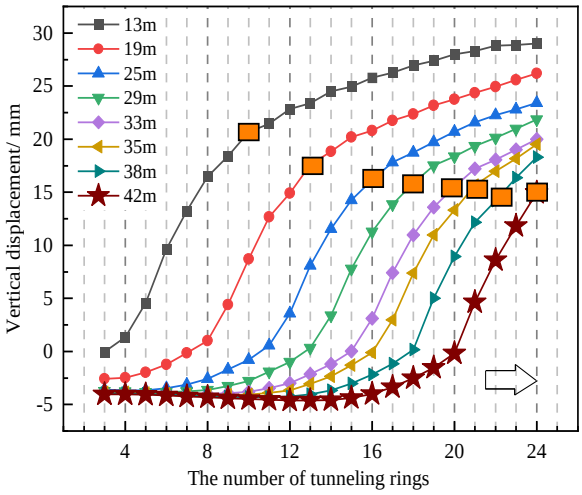

Fig. 11 – Vertical displacement of measuring points at arch bottom of tunnel

Figures 10 and 11 show the relation curves between the vertical displacements of the measuring points and the number of tunneling ring along the tunnel excavation direction. The measuring points are located at the top and bottom of the tunnel at 13m, 19m, 25m, 29m, 33m, 35m, 38m, and 42m, respectively. It can be obtained from the figure that the support of each lining segment and the grouting significantly reduce the vertical settlement rate of the vault and the vertical uplift rate of the arch bottom, which indicates that the shield tail synchronous grouting can effectively reinforce the surrounding rock soil. The displacement of the tunnel vault and arch bottom is typically stable while the shield machine advances. The final settlement of the tunnel vault is about 11.35 mm, and the uplift of the arch bottom's uplift is about 28.97 mm.

Vertical stress analysis

Figure 12 shows the distribution of vertical stress on the longitudinal section along the tunnel axis and the monitoring cross section at the 29m section of the 15th ring in different stages of underwater shield tunneling. In different rings tunneling, the vertical stress distribution of the longitudinal section is basically similar. Due to the disturbance and stress release of the surrounding rock mass, the shield machine's continued forward motion significantly reduces the vertical stress of the soil surrounding the excavated tunnel. With the continuous advance of shield tunneling, the vertical stress around the tunnel tends to be stable, which is generally smaller than the initial stratum stress. It is advantageous for the safe operation of the shield tunnel in the later period. The vertical stress of the soil above the vault at the working position of the shield machine and at the excavation face presents a funnel-shaped distribution. For the vertical stress distribution of the monitoring cross section in different tunneling stages, in Figure 12(a), the shield tunneling has not reached the monitoring section, due to the disturbance to the front soil, the vertical stress of the front soil is released and reduces. In Figure 12(b), the shield machine crosses the monitoring section as the shield tunneling reaches the 16th ring. The soil around the monitoring section is disturbed, and the vertical force of the soil around the tunnel further reduces compared with the 13th ring. In Figure 12(c), the shield tunneling reaches the 18th ring, and the tail grouting is carried out behind the 15th ring segment. The vertical stress of the soil on the upper part of the arch waist around the tunnel of the monitoring section continues to decrease, and the stress reduction range is greater than that of the 16th ring. The vertical stress of the soil at the lower part of the arch waist increases compared with that of the 16th ring, which indicates that the shield tail grouting can effectively resist floating. When the shield machine excavates to the 21st ring, far from the monitoring section, as shown in Figure 12(d), the vertical stress of the monitoring section gradually becomes stable.

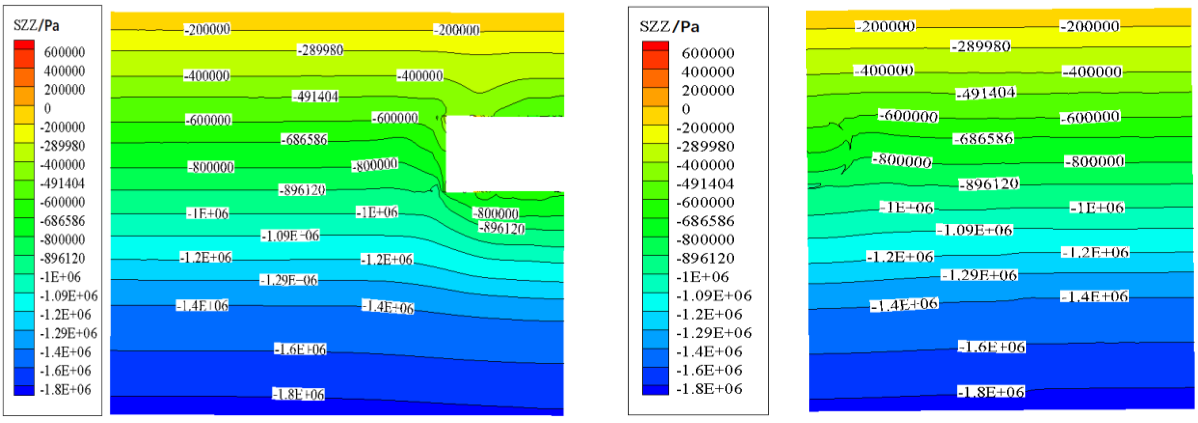

(a) The 13th ring

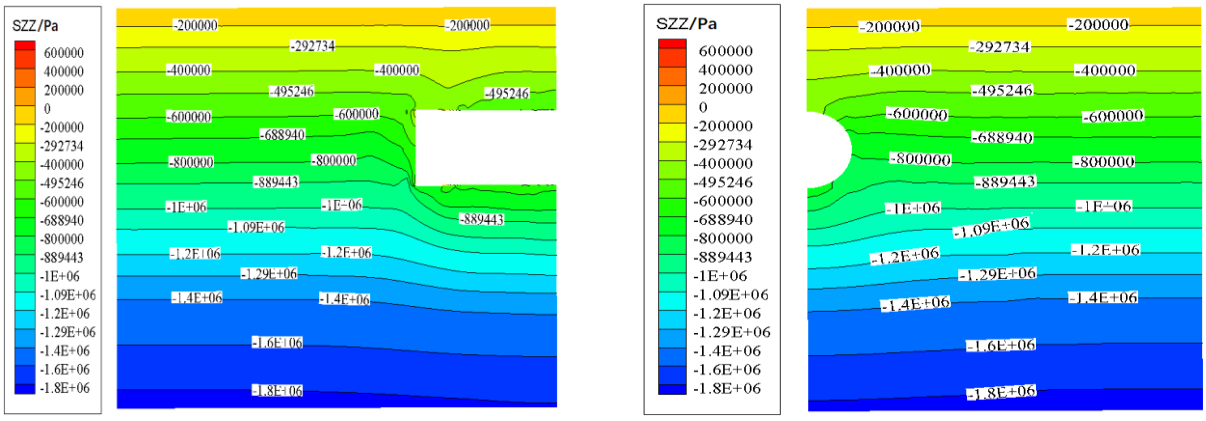

(c) The 16th ring

Fig. 12 – Vertical stress of monitoring section

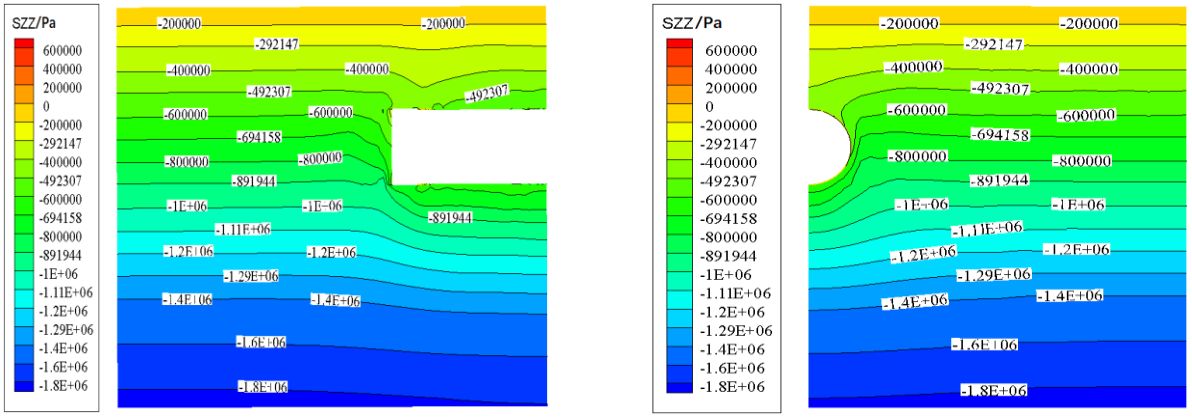

(d) The 18th ring

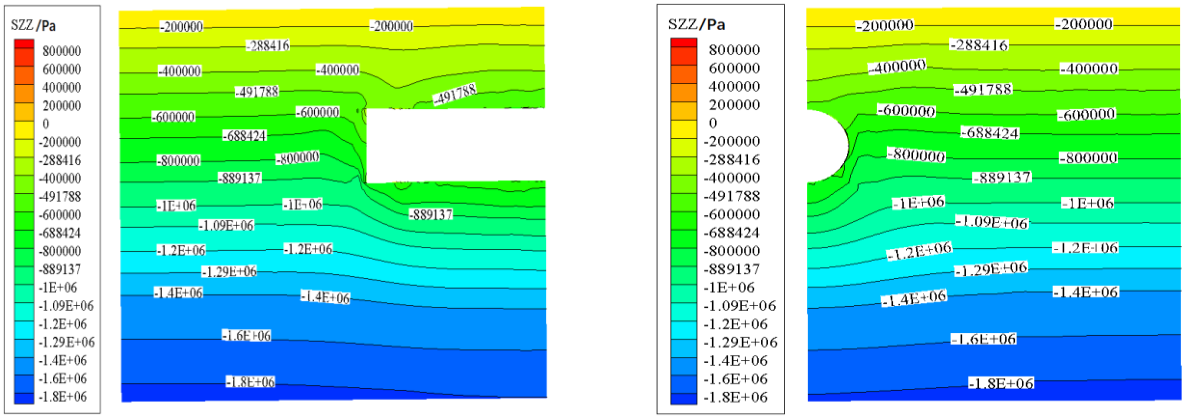

(e) The 21st ring

Fig. 12 – Vertical stress of monitoring section

CONCLUSIONS

(1) During the underwater shield tunneling and the shield tail grouting, the PWP in the range of 0.5R around the tunnel reduces and increases respectively due to the liquid-solid coupling. When the shield moves away, the PWP of the soil near the tunnel vault decreases, and grows near the arch bottom of the tunnel, the tunnel anti-floating measures such as secondary grouting should be taken. The PWP in the surrounding rock soil should be regarded as hydrodynamic pressure in the construction of an underwater large-diameter shield tunnel.

(2) The influence range of underwater shield excavating on the vertical displacement of the front soil is about 1R. Due to stress release, the vertical settlement of the surrounding soil above the vault increases as the shield approaches the monitoring section. The reinforcement effect of shield tail grouting behind the lining segment can effectively reduce vault soil vertical subsidence and slow down arch bottom soil uplift. The influence range of shield tail grouting on the vertical subsidence of the soil above the vault is about 0.5R.

(3) The deeper the burial depth of the stratum, the narrower the ground subsidence trough and the smaller the ground disturbance range. The local soil at the bottom of the tunnel in front of the excavation surface uplifts, indicating that the slurry pressure on the excavation surface should be controlled to avoid the instability of the excavation surface during the tunneling.

(4) The vertical stress of the soil surrounding the tunnel reduces during the excavation of the shield, and the vertical stress of the soil above the vault of the working position of the shield machine and around the excavation face is funnel-shaped distribution due to the influence of liquid-solid coupling. After the vertical stress around the excavated tunnel tends to be stable, the vertical stress

is generally lower than the initial formation stress, which is advantageous for the safe operation of the shield tunnel in the later stage.

ACKNOWLEDGMENTS

This research is supported in part by the National Natural Science Foundation of China (Grant No. 52178389), the Science and Technology Planning Project of Zhejiang Traffic Quality Supervision Industry (Grant No. ZJ201906).

REFERENCES

[1] Zhang Z.G., Huang M.S., Pan Y.T., et al., 2021. Analytical prediction of time-dependent behavior for tunneling-induced ground movements and stresses subjected to surcharge loading based on rheological mechanics. Computers and Geotechnics, Vol.129: 103858. https://doi.org/10.1016/j.compgeo.2020.103858

[2] Liang Y., Chen X.Y., Yang J.S., et al., 2020. Analysis of ground collapse caused by shield tunnelling and the evaluation of the reinforcement effect on a sand stratum. Engineering Failure Analysis, Vol. 115: 1-15. https://doi.org/10.1016/j.engfailanal.2020.104616

[3] Zhang S.L., Cheng X.S., Qi L., et al., 2022. Face stability analysis of large diameter shield tunnel in soft clay considering high water pressure seepage. Ocean Engineering, Vol.253: 111283. https://doi.org/10.1016/j.oceaneng.2022.111283

[4] Pan Q.J., Dias D., 2018. Three dimensional face stability of a tunnel in weak rock masses subjected to seepage forces. Tunnelling and Underground Space Technology, Vol.71, 555-566. https://doi.org/10.1016/j.tust.2017.11.003

[5] Zhang J. S., Xu M. Y., Cui M. H., et al., 2022. Prediction of ground subsidence caused by shield tunnel construction under hidden karst cave. Geotechnical and Geological Engineering, Vol.40: 3839-3850. https://doi.org/10.1007/s10706-022-02136-3

[6] Zareifard M.R., Fahimifar A., 2016. A simplified solution for stresses around lined pressure tunnels considering non-radial symmetrical seepage flow. KSCE Journal of Civil Engineering, Vol.20: 2640-2654. https://doi.org/10.1007/s12205-016-0105-5

[7] Wang C.H., Zhu H.H., Xu Z.C., et al., 2018. Ground surface settlement of shield tunnels considering spatial variability of multiple geotechnical parameters. Chinese Journal of Geotechnical Engineering, Vol.40:270-277. https://doi.org/10.11779/CJGE201802007

[8] Pinto F., Zymnis D.M., Whittle A.J., 2014. Ground movements due to shallow tunnels in soft ground. II: Analytical interpretation and prediction. Journal of Geotechnical and Geoenvironmental Engineering, Vol. 140, 80-90. https://doi.org/10.1061/(ASCE)GT.1943-5606.0000947

[9] Wang L.Z., Lv X.J., 2007. A complex variable solution for different kinds of oval deformation around circular tunnel in an elastic half plane. Chinese Journal of Geotechnical Engineering, Vol.29:319-327. https://doi.org/10.1016 / S1874-8651(08)60042-3

[10] Huangfu M., Wang M.S., Tan Z.S., et al., 2010. Analytical solutions for steady seepage into an underwater circular tunnel. Tunnelling and Underground Space Technology, Vol.25:391-396. https://doi.org/10.1016/j.tust.2010.02.002

[11] Song H.R., Zhang D.L., Fang Q., 2015. Analytic solution on the stress of surrounding rocks for shallow subsea tunnel. China Civil Engineering Journal, Vol.48: 283-288 https://doi.org/CNKI:SUN:TMGC.0.2015-S1-048

[12] Wu Z.S., Liu X.R., Liang B., et al., 2014. Study of seepage property and calculated watershed around underwater tunnels. Chinese Journal of Rock Mechanics and Engineering, Vol.33:2402-2408. https://doi.org/10.13722/ j.cnki.jrme.2014.12.005

[13] Zhang W. G., Li H. R., Wu C. Z., et al., 2019. Soft computing approach for prediction of surface settlement induced by earth pressure balance shield tunneling. Underground Space, 1-29. https://doi.org/10.1016/j.undsp.2019.12.003

[14] Ocak I., Seker S.E., 2013. Calculation of surface settlements caused by EPBM tunneling using artificial neural network, SVM, and Gaussian processes. Environmental Earth Sciences, Vol. 70: 1263-1276. https://doi.org/ 10.1007/s12665-012-2214-x

[15] Liu C.L., Yang S.Y., Liu W.J., et al., 2022. Three-dimensional numerical simulation of soil deformation during shield tunnel construction. Mathematical Problems in Engineering, Vol. 2022: 1-11. https://doi.org/10.1155/2022/5029165

[16] Hu X.Y., He C., Lai X.H., et al., 2020. A DEM-based study of the disturbance in dry sandy ground caused by EPB shield tunneling. Tunnelling and Underground Space Technology, Vol.101: 1-16. https://doi.org/10.1016/j.tust.2020.103410

[17] Li X.Y., Zhang D.L., Hou Y.J., 2022. Analysis of shield tunnel ground deformation characteristics and affecting factors in water-rich soft stratum: A case study on the section tunnel of Tianjin Metro Line 6. Applied Sciences. Vol. 12: 1-22. https://doi.org/10.3390/app12126208

[18] Jin X.G., Li X.H., Zhang Y.Q., 2010. Seepage-stress coupling analysis of rive-crossing tunnel excavating. Hydrogeology & Engineering Geology, Vol.37: 62-67.https://doi.org/10.3969/j.issn.1000-3665.2010.01.013

[19] Ji Y.J., Liu J.J., Cheng L.S., 2011. Numerical simulation of tunnel excavation considering fluid solid coupling. Rock and Soil Mechanics, Vol.32: 1229-1233. https://doi.org/10.4028/www.scientific.net/AMR.211-212.106

[20] Wang C., 2018. Disturbance analysis of shallow buried and small interval shield tunnel excavation based on fluid-solid coupling. Subgrade Engineering, Vol.4:40-44.

[21] Cheng X.S., Zhang S.L., Qi L., et al., 2021. Fluid-solid coupling response of shield tunnel lining structure under high water pressure. Marine Georesources & Geotechnology, 1-11. https://doi.org/10.1080/1064119X.2021.1971805.

[22] Cheng X.S., Xu W.W., Yue C.Q., et al., 2014. Seismic response of fluid-structure interaction of undersea tunnel during bidirectional earthquake. Ocean Engineering, Vol.75:64-70. https://doi.org/10.1016/j.oceaneng. 2013.11.017

[23] Yao Q.Y., Di H.G., Ji C., et al., 2020. Ground collapse caused by shield tunneling in sandy cobble stratum and its control measures. Bulletin of Engineering Geology and the Environment. Vol. 79: 1-16. https://doi.org/10.1007/s10064-020-01878-9

[24] Yuan D.J., Yin F., Wang H.W., et al., 2009. Study of soil disturbance caused by super-large diameter slurry shield tunnelling. Chinese Journal of Rock Mechanics and Engineering, Vol.28:2074-2080. https://doi.org/10.3321/j.issn:1000-6915.2009.10.015

[25] Shahin H.M., Nakai T., Hinokio M., et al., 2004. Influence of surface loads and construction sequence on ground response due to tunnelling. Soils and Foundations, Vol.44: 71-84. https://doi.org/10.3208/sandf.44.2_71

[26] Wang W., Liu J.J., Zhang X.M., et al., 2022. Researches on the excavation disturbance of shield tunnel in sandy cobble ground. Geofluids, Vol. 2022: 1-15. https://doi.org/10.1155/2022/2373133

[27] Xie X.Y., Yang Y.B., Ji M., 2016. Analysis of ground surface settlement induced by the construction of a large-diameter shield-driven tunnel in Shanghai. Tunnelling and Underground Space Technology, Vol.51: 120-132. https://doi.org/10.1016/j.tust.2015.10.008

[28] Yuan L.J., Li Z.Q., Wu S.Z., et al., 2001. Mechanics of engineering seepage and its application. China Building Materials Industry Press, Beijing, China.

[29] Yu L.B., 2018. Study on the seepage field variation and soil deformation caused by synchronous grouting of large diameter shield machine during the construction of a tunnel. Master's thesis, South China University of Technology, Guangzhou, China.

CIVIL ENGINEERING JOURNAL

Article no. 34

THE CIVIL ENGINEERING JOURNAL 4-2023

RESEARCH ON THE PROTECTIVE EFFECT OF TWIN-GROYNE ARRANGEMENT ON RIVERBANK

Xi Mao[1], Xiaofan Liu[2], Chengle Xie[1], Zhongquan Xu[1], Jiawen Huang[1], Henggan Li[1], Nengzhong Lei[1], Shuiqian Wang[3], Lele Wang[4], Songliang Chen[1] and Hongyu Qiu[3]

1. *School of Civil Engineering and Architecture, Wuyi University, 358 Baihua Road, Wuyishan, Fujian, China; maowhiteknight@163.com*
2. *Yalong River Hydropower Development Company Limited, 288 Shuanglin Road, Chengdu, Sichuan, China*
3. *Water Conservancy Management Center of Fujian Province, 34 Wushan Road, Fuzhou, Fujian, China*
4. *Fujian Key Laboratory of Hydrodynamics and Hydraulic Engineering, 158 Dongda Road, Fuzhou, Fujian, China*

ABSTRACT

A curved channel with intersecting streams can be easily scoured by incoming flow, and the concave bank is badly damaged. The twin-groyne is a unit of the spur dike group, which can effectively adjust the flow structure and achieve the purpose of bank protection. This study simulates the intersection of river channels through experiments, and compares the influence of twin-groyne on the flow structure and protection of the curve. This research showed that the twin-groyne could effectively adjust and optimize the flow velocity distribution, change the shape of the free water surface of the bend, prevent erosion, and promote silting on the concave bank, and it could provide a scouring and silting effect on the convex bank. When the spacing of twin-groyne was increased to more than four times the body length of the single-groyne (spur dike), the protective effect on the concave bank was weakened, and the scouring and silting effect of the convex bank was reduced. Excessive spacing of the twin-groyne could cause local erosion damage to the concave bank. When the distance exceeded the theoretical optimum, it was equivalent to the effect of single-groyne. With the increase in the submergence degree of groynes, the velocity of the concave bank decreased first and then increased, while the velocity of convex bank decreased continuously. The protective effect of a non-submerged twin-groyne with a dam spacing of four times the body length of the single-groyne was better than that of other conditions, and it is recommended to be used in practice.

KEYWORDS

Erosion prevention, Hydraulics, Scour, Spur dike, Twin-groyne

INTRODUCTION

For a curved channel that intersects with branches, the flow patterns and hydraulic conditions are more complex than those of a straight channel or a channel with a single bend. Under the same flow rate, concave bank erosion and damage are severe. Convex bank siltation and the narrowness of the channel further aggravate the damage of the concave bank.

Riverbed evolution is the result of the interaction between water flow and riverbed. A certain riverbed morphology and composition determines the flow condition suitable for it, and a certain flow condition makes the riverbed morphology and riverbed composition produce a certain riverbed evolution suitable for it. The river conditions in nature are complex and diverse, and the complexity of flow patterns and hydraulic conditions of different types of rivers is often quite different. For example, curved rivers are more complex than straight rivers, and curved rivers with confluence of

tributaries are more complex than single bends. Generally, under the same conditions, the erosion damage of concave banks in curved river channels will be more serious, and the siltation of the convex bank narrows the river channel, which will further aggravate the damage of the concave bank, resulting in the acceleration of the evolution rate of the river channel in the unfavorable direction. As a common hydraulic structure of waterway regulation, spur dikes are widely used in river control engineering [1]. In a revetment project, the main function of spur dikes is to change the form of the original riverbed cross-section and adjust the surrounding flow structure to protect the riverbank from being scoured directly by incoming flow, resulting in brush damage [2]. For different types of rivers, different spur dikes arrangements are needed to achieve good protection effects. Generally speaking, the joint action of simultaneous spur dikes is usually used in engineering practice. The number and spacing of spur dikes will directly affect the engineering effect and cost, so it is of great significance to study the flow of spur dikes.

A twin-groyne is a combination of two independent spur dikes. The reasonable arrangement of a twin-groyne directly influences the effect of a waterway regulation project [3][4]. The spacing between two spur dikes and the submergence degree of groyne are two important parameters to describe the function of the twin-groyne. The spur dikes cannot cooperate with each other when the spacing is too large, and the purpose of river regulation cannot be achieved. Meanwhile, if the spacing is too small and the number of spur dikes increases, the quantity and cost of materials used in engineering will increase accordingly. The submergence degree of groyne is the ratio of the water depth to the height of the spur dikes. With the change of the submergence degree of groyne, the overflow of the dam top and the lifting action of the dam head will also change; so, the protective effect on the riverbank will also change accordingly [5]. Pandey et al. focused on experimentally assessing the temporal variation of the scour depth around a vertical wall spur dike and identifying the parameters that most influenced the spur dike performance for a channel bed surface composed of sand-gravel mixtures [6].

At present, there are many research results on the shape and pick angle of spur dikes. Vaghefi et al. studied the water flow near the T-type spur dike by numerical simulation, and analyzed the supporting structures upstream of several T-type spur dikes with different wing lengths [7]. Vaghefi et al. showed the flow patterns of 90° oblique t-shaped vertical breakwaters in repulsive, attractive and vertical positions. The numerical results show that with the increase of the angle of the straight dike, the size of the vortex downstream of the straight dike decreases [8]. Bahrami-Yarahmadi et al. studied the scour patterns formed around triangular spur dikes under different hydraulic conditions, and compared these patterns with the scour patterns of ordinary types of spur dikes (rectangular spur dikes) [9]. Haider et al. studied the turbulence and flow characteristics around the straight dike in the open channel. The results show that the permeable straight dike with pore angle is an ideal choice to protect the tip of the straight dike, the river bank and the aquatic habitat in extreme floods. It also reduces reattachment length and roughness coefficient [10].

Gu et al. quantitatively studied the influence of the spacing threshold of non-submerged double spur dikes on the spacing threshold of non-submerged double spur dikes arranged orthogonally on the same side in a straight rectangular river by combining numerical research and experimental measurement [11]. Jiao et al. studied the influence of different spur dike lengths and riverbank elevation differences on hydraulic power through physical model experiments [12]. They found that the difference of riverbank elevation is the decisive factor of lateral water and sediment transport.

Shampa et al. found that the high-permeability spur dike group could reduce the longitudinal velocity and turbulence intensity along the channel and increase the transverse flow [13]. A staggered arrangement of the pile grid in the spur dike group could reduce the shear stress of the riverbed while improving the flow pattern in the turbulent area. Sharma et al. performed a study on the flow characteristics behind the spur dike of a curved river [14]. Kiani et al. evaluated the effect of the relative distance between two spur dikes in the bend on the scour using a laboratory Plexiglas flume with a rectangular section and a 180° bend [15]. They found that there was a direct relationship between the maximum relative depth of the scour and the relative length of the spur dikes, the relative distance between the spur dikes, and the Froude number. By increasing the relative

distance, relative length, and Froude number, the maximum relative depth of the scour at the noses of the spur dikes increased.

Duan used a microacoustic Doppler velocimeter to study the three-dimensional turbulent flow field around a spur dike in a planar fixed-bed open channel in the laboratory and found that the maximum bed shear stresses estimated using Reynolds stresses were about three times as large as the mean bed-shear stress of the incoming flow[16]. The studies discussed above mainly examined the influence of the flow field, velocity, and flow behind dams with different spur dike structures in straight and curved river courses. However, there are few related studies on the use of twin-groyne in a curved channel with intersecting streams.

The protective effect of a groyne group can be correlated with a reduction in the magnitude of depth-averaged velocity along the channel bank. Through physical model tests and theoretical analysis, this research examined impermeable solid twin-groynes (double spur dikes). By changing the spacing and submergence degree of the spur dikes, the velocities, water surface line distributions, and water flow patterns near the bend were compared, and the effect of the twin-groyne layout on the protection of a curved channel connected to branches under the same flow rate was explored. The research results have a certain reference value for the selection, optimal arrangement, and rational use of the twin-groynes in waterway regulation and revetment engineering.

METHODS

Experimental model

The main structure of the model was a 45° curved flume attached to a straight section of branches. The water cross-sections of the main trough and branch trough were rectangular, and the trough depth h was taken as the reference length. The width of the main trough d was 1.5h, the width of the branch trough was 0.75h, and the radius of the outer curve R was 10h. To ensure the stability of the flow conditions and the authenticity of the experimental simulations, the inlet and outlet of the bend were provided with a straight grooved transition section, and the head and tail of the flume were respectively provided with a steady flow grid and a water retaining weir to adjust the water level. The length of the spur dike was D = 0.25d, and the spur dikes were arranged on the concave bank of the bend perpendicular to the bank. The experiment used clean water, which was supplied by a pump. The water head was stabilized by a concrete reservoir, and the flow was regulated by a water-retaining gate. The flow depth H was defined as the reference depth in the middle of the inlet of the flume. The U was the mean longitudinal velocity in the inflow straight channel reach without spur dikes. Among them, one side of the experimental model had a branch, and the branch switch controled whether the water flow in the branch can enter the main channel. The “with branch” indicates that the branch switch is in an open state, and the water flow in the branch can flow into the main channel; the “no branch” means that the branch switch is in a closed state, and the water flow in the branch cannot flow into the main channel, as shown in Figure1 (a).

Experimental design

Details of the experimental model are shown in Figure 1 (a)-(e). Under all the working conditions shown in Table 1, the position of spur dike 1 remained unchanged at 1/4 of the river bend. Spur dikes 2’, 2’’, and 2’’’ had spacings of 4D, 6D, and 8D, respectively, between two spur dikes, as shown in Figure 1 (d). The locations of the spur dikes, the locations where the velocity and water level were measured, and the grid of measuring points distributed on the bend section are shown in Figure 1 (a)-(e). Flow measuring sections were set along the outer arc, which contained measurement points with spacings of 0.2d. Similar sections were established around the groyne dam. A total of 26 measurement sections were established. Each flow measuring section had eight measurement points, which were labelled as lines 1-8, with distances from the concave bank of 0.1d, 0.2d, 0.3d, 0.4d, 0.5d, 0.6d, 0.8d, and 0.9d, respectively.

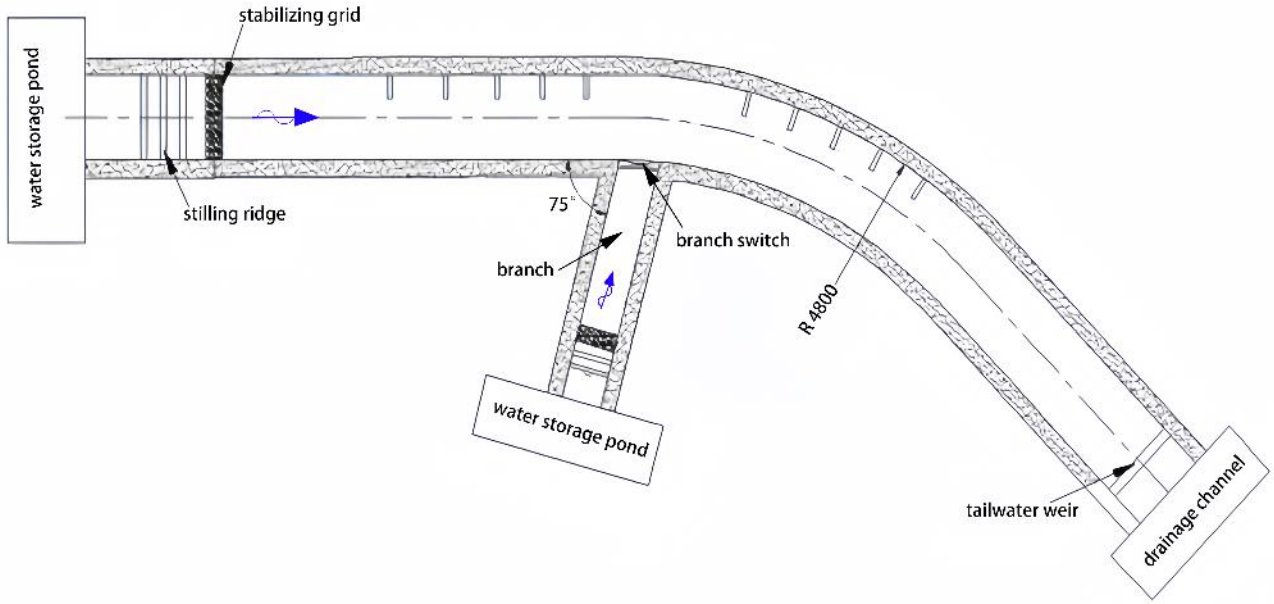

(a) planview of experimental model

(b) overall layout

(c) detailed view to the model section with groynes

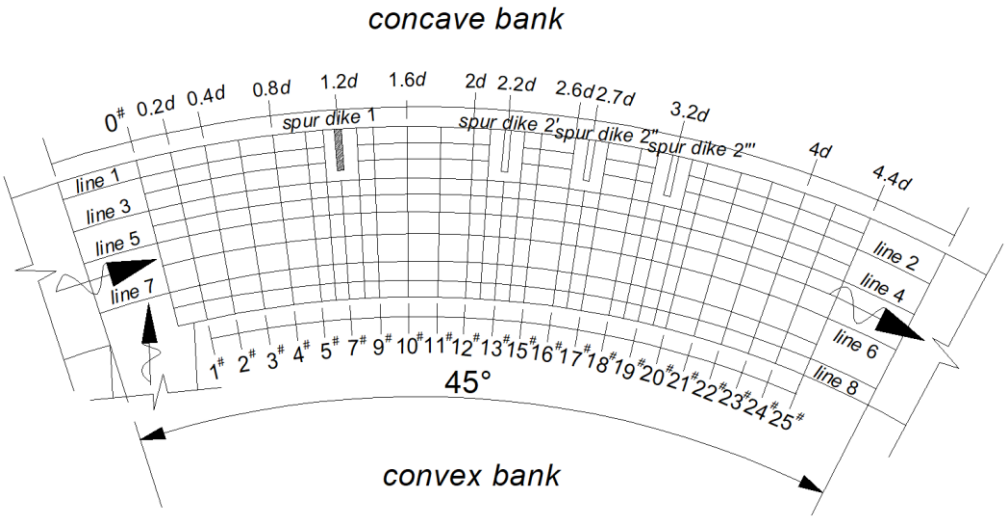

(d) experimental measurement line distribution diagram

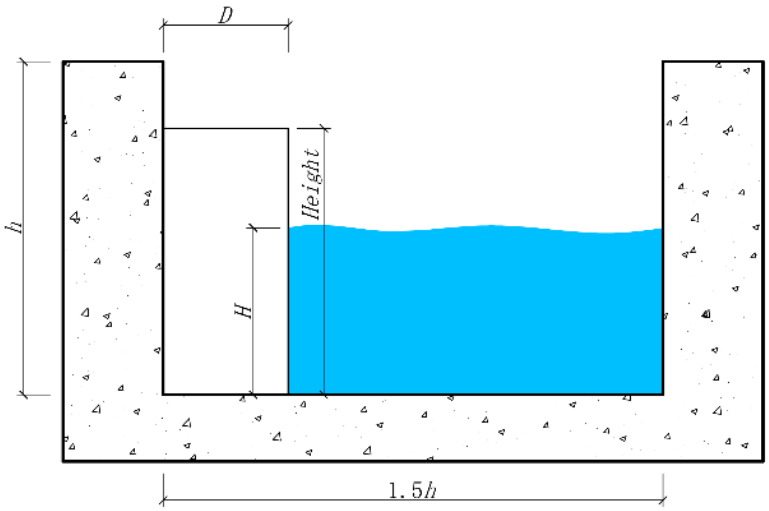

(e) diagrammatic cross-section

Fig. 1 - Experimental model

Experimental conditions

The empirically determined spacing of impervious non-submerged twin-groynes is usually 2–4 times the dam length, and the optimal theoretical value of the dam spacing is 9*D*[17]. Based on the empirical values and the optimal theoretical value of the dam spacing, the dam spacing and degree of submergence were varied for comparison experiments. These experiments involved a total of six working conditions, and the characteristics of each experimental condition are shown in Table 1.

The submergence degree of groynes (σ) as follows:

$$\sigma = H / Height$$

It should be noted that in formula and Table 1, the *Height* represented the height of the spur dikes, as shown in Figure 1 (e). Among them, submergence degree of groynes (σ) greater than 100% indicated that the flow depth exceeded the height of the spur dikes.

Tab. 1 - Working conditions

Condition	Height	Submergence degree of groynes(σ)	Spacing between two spur dikes
1	-	-	-
2	0.5*h*	100%	4*D*
3	0.4*h*	125%	4*D*
4	0.8*h*	62.5%	4*D*
5	0.8*h*	62.5%	6*D*
6	0.8*h*	62.5%	8*D*

RESULTS AND DISCUSSION

Analysis of influence of arrangement of twin-groyne on river surface line

Figure 2 shows the distribution of the longitudinal water surface lines in the curved channel with the twin-groyne and connected branches under the same flow. The velocity measurement method here adopts the three-point method in hydraulics: the velocity measurement points were set at 0.2, 0.6, 0.8 relative water depths below the water surface, and the average or weighted average

of the velocity of the three measuring points is the vertical average velocity. The channel flow was affected by the twin-groyne, and the water surface line changed significantly. The water level near the central axis was relatively high, and the highest water level appeared between the spur dikes. The top-thrusting action of the branches caused the water surface line to be inclined to the central axis and the concave bank side. The concave bank of section 0# had the highest water level of the whole measured bend, while the convex bank had the lowest water level, which was mainly caused by the arrangement of the twin-groyne on the concave bank, and the twin-groyne blocked and deflected the water flow. From the characteristics of the water flow itself, the first spur dike blocked the water, causing the upstream water level to rise. The water level along the dam head was higher than the back water level, and the water level near the central axis of the bend and along the convex bank increased significantly. The water level near the head of the spur dike was again elevated due to the high flow velocity in the narrow area of the downstream beam. The water level near the central axis of the bend and along the convex bank increased again. A certain distance after the second dam, the water level slowly decreased and gradually became stable.

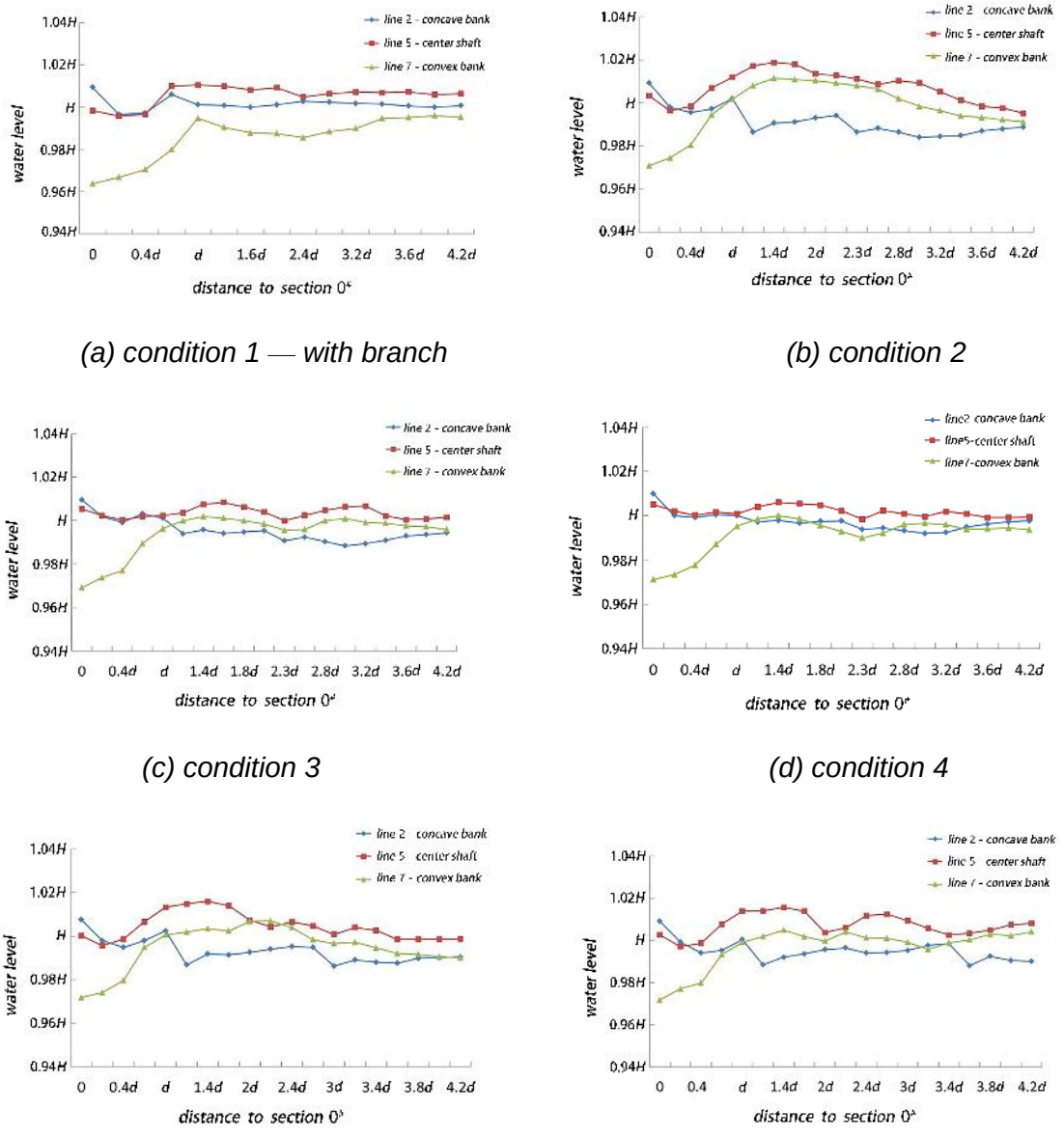

(a) condition 1 — with branch

(b) condition 2

(c) condition 3

(d) condition 4

(e) condition 5

(f) condition 6

Fig. 2 – Longitudinal water surface line distribution diagram under each working condition

Analysis of influence of arrangement of twin-groyne on velocity of river concave bank and convex bank

The velocity measurement method here adopts the three-point method in hydraulics: the velocity measurement points are set at 0.2, 0.6, 0.8 relative water depths below the water surface, and the average or weighted average of the velocity of the three measuring points is the vertical average velocity. Figure 3 shows the longitudinal velocity distribution of the concave bank (line 2) and convex bank (line 7) under each working condition. It can be observed that the velocity along the concave bank was greater than that along the convex bank after adding a branch for the same flow. Under condition 1, the maximum scouring velocity of the concave bank was 0.2 m/s. After the twin-groyne was installed, the velocity of the concave bank decreased significantly, while the velocity of the opposite bank increased significantly, with a maximum value of 0.28 m/s. The maximum velocity of the concave bank and the minimum velocity of the convex bank were located upstream of the twin-groyne, and the minimum velocity of the concave bank and the maximum velocity of the convex bank occurred between the two spur dikes. Due to the obstruction of the spur dikes, a relatively still area formed behind them. The flow velocity of the dam head increased due to the bunching action of the spur dike. After bypassing the spur dike, the flow deflected to the side without the spur dike and formed a shear flow with a relatively still area between the two spur dikes, resulting in a vortex between the spur dikes.

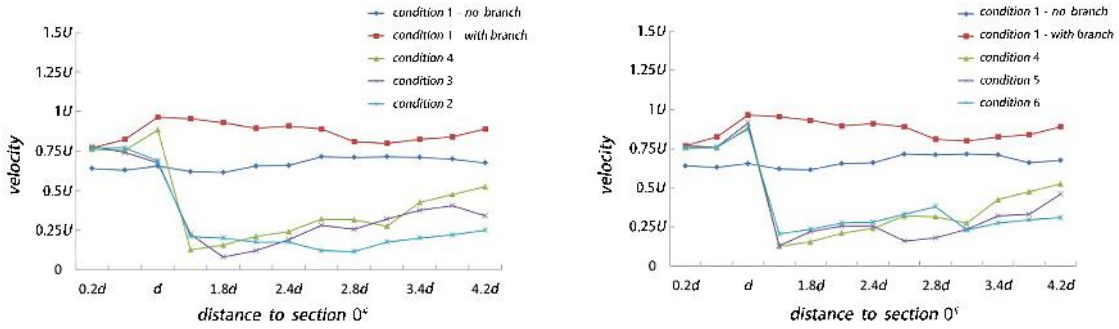

(a) concave bank

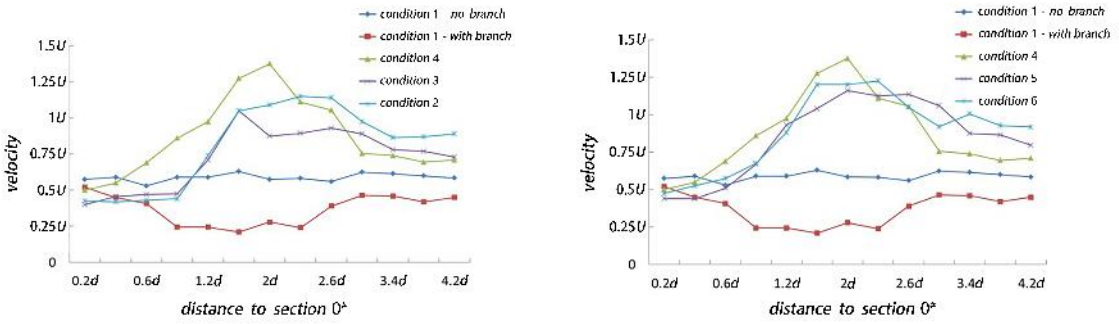

(b) convex bank

Fig. 3 – Comparisons of flow velocities in cross-sections of bending channels

Based on contrastive analysis of Figure 2 and Figure 3, the water level difference in the bend caused the exchange of flow potential energy and kinetic energy, and the water level and flow velocity changed differently along the channel under different twin-groyne arrangements. However, the variation characteristics were generally similar. The twin-groyne obstructed the flow and caused the water level behind the spur dike to decrease. The flow around the dam consumed the kinetic

energy of the flow and the velocity behind the spur dike decreased significantly. The narrow flow of the spur dike caused the water level of the central axis and convex bank of the bend to rise, and the water flow area suddenly decreased, thus increasing the flow velocity. A certain distance after spur dike 2, the flow velocity gradually became stable.

Analysis of influence of inundation degree on velocity distribution

Figure 4 shows the velocity distribution of the river channel under different submergence degrees. The distribution of the main flow area of the curve changed from the side near the concave bank to the side near the convex bank after the twin-groyne was added on the concave bank. The velocity of the concave bank decreased, some basins had negative velocities, and the maximum velocity appeared on the opposite side between the two spur dikes. With the increase in the submergence degree of groyne, the flow velocity in the main flow area that was greater than the scour velocity *v* was significantly reduced, and the scour and silting effect was weakened. The area of the negative velocity zone between the two spur dikes and downstream decreased, and the submergence degree of groyne was 125%. The negative velocity zone behind spur dike 2 basically disappeared, which was not conducive to the siltation of the dam field. For working conditions 2 and 3, the flow velocity distribution in the concave bank between the two spur dikes was unstable. The flow velocity of condition 2 on the convex bank side was larger and relatively uniform, and thus, this condition was more conducive to river protection than condition 3. Under condition 4, the maximum negative flow velocity of concave bank was 0.05 m/s, and the flow velocity in the vortex areas between and behind the two spur dikes was small and relatively uniform, which was conducive to the erosion and silting prevention of the concave bank. However, the convex bank side had a large flow rate and a better scouring and silting effect, which was more conducive to the overall river protection than the submerged condition.

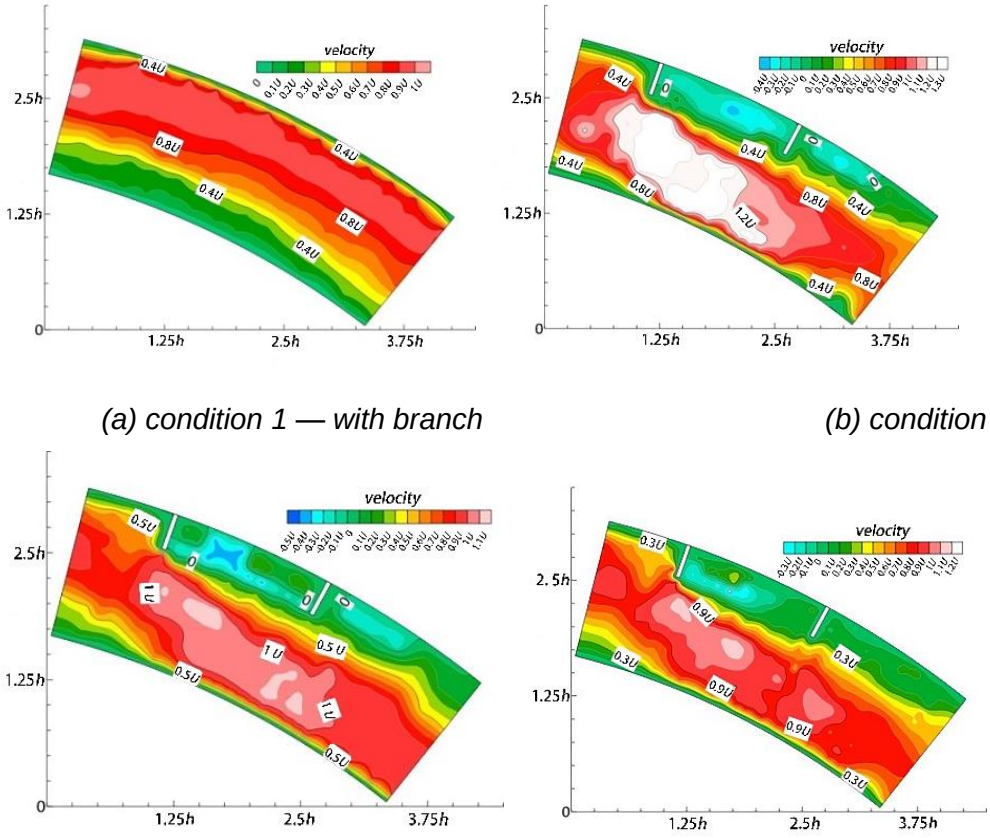

(a) condition 1 — with branch *(b) condition 4*

(c) condition 2 *(d) condition 3*

Fig. 4 – Velocity distribution of the river channel under different submergence degrees

From the perspective of the flow characteristics of the submerged twin-groyne, the water flowing past the dam body was divided into two parts: surface flow and bottom flow, and there was a water separation phenomenon at the top of the dam [2]. Under the same incoming flow, the discharge of the surface water through the dam crest increased with the increase in ΔH (ΔH = *Height* − *H*), leading to a decrease in the range of the return area between and behind the two spur dikes. Part of the bottom flow rose over the top of the dam and flowed downstream, and it tended to spread toward the head of the dam, while the other part went around the head and released. The interaction conditions between the surface flow and bottom flow led to the presence of two horizontal and vertical return zones with different rotation directions between and behind the spur dikes, and their interactions consumed a large amount of kinetic energy [6]. When ΔH was small, the bottom flow had significant action around the dam, and the water level changes and velocity distribution were similar to those of the non-submerged twin-groyne. As ΔH increased gradually, the water blocking ability of the double groyne dam bundle weakened, the surface water discharge increased, the convex bank velocity decreased continuously, and the local shore–base erosion and silting effect weakened. The flow velocity of the concave bank changed significantly, the effect of the bottom flow was gradually weakened, the surface flow gradually became dominant, and the flow velocity increased after it decreased to a certain extent, which was not conducive to the protection of the bank.

Analysis of influence of distance between two spur dikes on velocity

Figure 5 shows the velocity distributions for different dam spacings. Based on the comparison of Figure 4 and Figure 5, with the increase in the dam spacing, the velocity distribution in the main flow zone and the vortex zone changed significantly. Under condition 5, the distance between the two spur dikes was 6*D*, and the variation of the longitudinal velocity between the two spur dikes was larger than that under condition 4. The maximum negative velocity in the vortex zone reached 0.1 m/s, which was not conducive to the deposition of sediments in the concave bank. Under condition 6, when the spacing between the two spur dikes reached the theoretical optimal value of 9*D*, the vortex zone between the two spur dikes was disconnected. Currently, the two spur dikes were outside the mutual cover range, and the disconnection position in the return area could easily cause partial scouring damage, which was unfavourable for the protection of the river. For the convex bank, the increase in the dam spacing increased the range of scouring and silting, but the scouring and silting effect was lower in local areas. The flow velocity at the tail area of the convex bank under condition 6 was uneven in the transverse distribution, and the overall scouring and silting effect was weaker than that under condition 4.

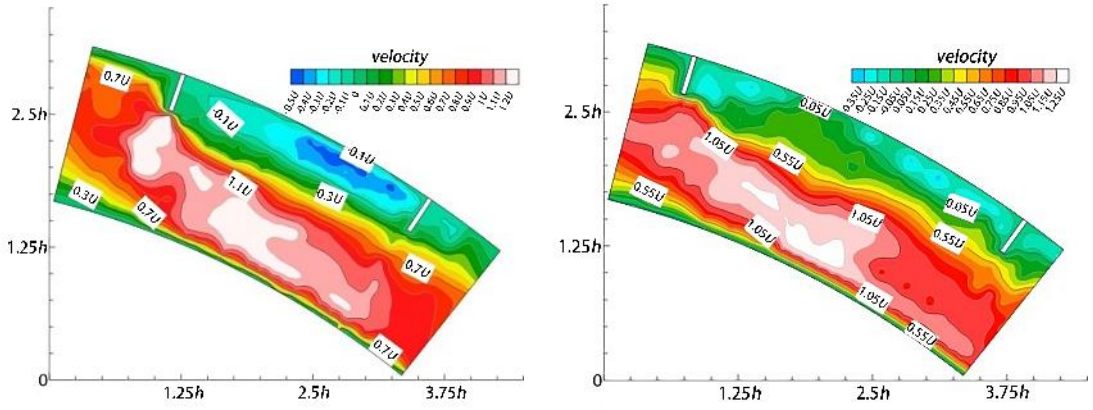

(a) condition 5 *(b) condition 6*

Fig. 5 – Velocity distribution diagram with different dam spacings

From the perspective of the flow characteristics of the non-submerged twin-groyne, the first spur dike (spur dike 1) had a strong flow deflection ability, a large flow inertia effect, slow flow velocity recovery across spur dike 1 to the downstream area, and a large scouring range of the flow. The placement of the second spur dike (spur dike 2) weakened the inertial action of the water flowing over it, and the water flow could be diverted to the main channel, which not only reduced the scouring effect on the concave bank but also promoted the scouring and silting effect on the convex bank. If the dam spacing were too large or too small, it would not be conducive to riverbank protection. If the dam spacing were too large, it would be equivalent to the two spur dikes playing separate roles. If the dam spacing were too small, the full effect of spur dike 2 would not be realized. Under each experimental condition, when the spacing of the two spur dikes was 4*D*, it had an ideal effect on the river protection.

CONCLUSIONS

Twin-groynes with different dam spacings and submergence degrees were established on the concave bank of a curved river channel with intersecting branches. Through comparative analysis of the effect of the twin-groynes on the water level, velocity change, and flow characteristics, the protective effects of different arrangements on the curved river bank were determined.

(1) The water blocking of the twin-groyne led to water free surface and velocity changes in the curved channel. A twin-groyne arranged in the curved channel could prevent erosion, promote silting on the concave bank, and provide a scouring and silting effect on the convex bank. The differences of the water level in the bend led to the exchange of potential energy and kinetic energy of the flow. When the twin-groyne layout was changed under the same inlet flow, the water level and velocity changed differently along the channel, but the overall variation characteristics were similar.

(2) The non-submerged twin-groyne had a more significant effect on the flow structure and velocity distribution of the bend. When the spacing of twin-groyne was greater than 4*D*, the velocity distribution of the concave bank was unstable, and the scouring and silting effect of the convex bank was reduced. When the distance was greater than the theoretical optimum, it was equivalent to two spur dikes playing separate roles, the concave bank of the local damage was severe, and the configuration was not conducive to river protection.

(3) The water level variations of the bend were smaller than those of the channel with a non-submerged twin-groyne. With the increase in the submergence degree of groyne, the overflow effect of the dam crest was strengthened, the water blocking and water flow deflection effects of the dam head were weakened, the velocity of the concave bank decreased first and then increased, the velocity of the convex bank decreased continuously, the velocity of the convex bank gradually approached the condition with no dam, and the overall protective effect of the river was weakened.

(4) The non-submerged twin-groyne with a spacing of 4*D* allowed the full effect of the twin-groyne on controlling water potential and deflecting water flow, and the surface flow pattern of the bend was stable, which had a better protective effect on the riverbank compared to other spacings.

ACKNOWLEDGEMENTS

This research was supported by the Department of Science and Technology of Fujian Province (grant number: 2023J011046), the Education Department of Fujian Province (grant number: JAT220379), Innovation and entrepreneurship training program for college students (grant number: S202310397060), Wuyi University (grant number: YJ202216), Sichuan University (grant number: SKHL2117), and Nanping Science and Technology Bureau Resources Chemical Industry Science and Technology Innovation Joint Funding Project (grant number: N2021Z004). The authors declared that they have no conflicts of interest to this research.

REFERENCES

[1] Tripathi, R. P. and Pandey, K. K., 2021. Experimental study of local scour around T-shaped spur dike in a meandering channel. Wat. Sci. Tech.: Wat. Sup, vol. 21(1/2): 542-552.
[2] Tripathi, R. P., and Pandey, K. K., 2022. Scour around spur dike in curved channel: a review. Acta Geophysica, vol. 70: 2469-2485.
[3] Sumi, T., Takebayashi, H., Sakuma, M., Hasegawa, M., Ito, K., Yamamoto, S., and Shibata, G., 2021. Installation and adaptive management of T-shaped and L-shaped spur dikes to control bed deformation and diversify physical environment in rivers. Hydro-Environ, vol. 37: 13-31.
[4] Zamani, M., Rabiefar, H., and Rostami, M., 2020. Experimental evaluation of spur dikes placement position effect on the hydraulic and erosion conditions of intakes. Wat. Sci. Tech.: Wat. Sup, vol. 20(3/4): 900-908.
[5] Vaghefi, M., Safarpoor, Y., and Akbari, M., 2016. Numerical investigation of flow pattern and components of three-dimensional velocity around a submerged T-shaped spur dike in a 90° bend. J. CENT. SOUTH. UNIV, vol. 23: 2984–2998.
[6] Pandey, M., Valyrakis, M., Qi, M. L., Sharma, A., and Lodhi, A. S., 2021. Experimental assessment and prediction of temporal scour depth around a spur dike. Int. J. Sediment. Res, vol. 36(1): 17-28.
[7] Vaghefi, M., Ahmadi, A., and Faraji, B., 2018. Variation of hydraulic parameters with different wing of a T-shape spur dike in bend channels. J. CENT. SOUTH. UNIV, vol. 25: 671-680.
[8] Vaghefi, M., Radan, P., and Akbari, M., 2019. Flow Pattern Around Attractive, Vertical, and Repelling T-Shaped Spur Dikes in a Mild Bend Using CFD Modeling. Int. J. Civ. Eng, vol. 17: 607-617.
[9] Bahrami-Yarahmadi, M., Pagliara, S., Yabarehpour, E., and Najafi, N., 2020. Study of Scour and Flow Patterns around Triangular-Shaped Spur Dikes. KSCE. J. Civ. Eng, vol. 24: 3279-3288.
[10] Haider, R., Qiao, D. S., Yan, J., Ning, D. Z., Pasha, G. A., and Iqbal, S., 2022. Flow Characteristics Around Permeable Spur Dike with Different Staggered Pores at Varying Angles. Arab. J. Sci. Eng, vol. 47: 5219-5236.
[11] Gu, Z. H., Cao, X. M., and Gu, Q. Y., 2020. Exploring Proper Spacing Threshold of Non-Submerged Spur Dikes with Ipsilateral Layout. Water, vol. 12(1): 172.
[12] Jiao, Z. X., Dou, X. P., Zheng, J. H., Zhang, X. Z., and Gao, X. Y., 2017. Influence of spur dike on hydrodynamic exchange between channel and shoal of generalization estuary in physical model test. China Ocean Eng, vol. 31(5): 624-630.
[13] Shampa, Hasegawa, Y., Nakagawa, H., Takebayashi, H., and Kawaike, K., 2020. Three-Dimensional Flow Characteristics in Slit-Type Permeable Spur Dike Fields: Efficacy in Riverbank Protection. wat, vol. 12(4): 964.
[14] Sharma, K., and Mohapatra, P. K., 2013. Separation zone in flow past a spur dyke on rigid bed meandering channel. Hydraul. Eng, vol. 138(10): 897-901.
[15] Kiani, A., Masjedi, A., Pourmohammadi, M. H, Heidarnejad, M., and Bordbar, A., 2017. Experiment of local scour around a series of spur dikes in river bend. Fresen. Environ. Bull, vol. 26(8): 5331-5339.
[16] Duan, J. G., 2015. Mean Flow and Turbulence around a Laboratory Spur Dike. Hydraul. Eng, vol. 135(10): 803-811.
[17] Ning, J., Li, G., and Li, S., 2019. Numerical Simulation of the Influence of Spur Dikes Spacing on Local Scour and Flow. Appl. Sci, vol. 9(11):2306.

CIVIL ENGINEERING JOURNAL

Article no. 35

THE CIVIL ENGINEERING JOURNAL 4-2023

REDUCTION OF INDOOR RADON CONCENTRATION IN A ROOM USING HEAT RECOVERY VENTILATION

Matúš Krajčík[1], Nataliia Mahas[1], František Ďurec[2]

1. *Slovak University of Technology in Bratislava, Faculty of Civil Engineering, Department of Building Construction, Radlinského 11, Bratislava 810 05, Slovakia; matus.krajcik@stuba.sk*
2. *Regional Public Health Authority in Banska Bystrica, Department of Radiation Protection, Cesta k nemocnici 1, Banská Bystrica 975 56, Slovakia; frantisek.durec@vzbb.sk*

ABSTRACT

Increased requirements for the energy efficiency of buildings often lead to an increase in the tightness of the building envelope. Tightness of the external cladding has a significant effect on the intensity of air exchange. A lower level of ventilation subsequently worsens the quality of the indoor air and also causes an increase in the indoor radon concentration. This problem can be solved by using ventilation devices with heat recovery. The paper deals with the influence of local ventilation equipment with heat recovery on indoor radon concentration. The case study compares different settings of ventilation equipment from the point of view of pressure ratios between interior and exterior. During the measurements, external weather conditions are also monitored, which may affect the results. The aim of the paper is to evaluate the rate of reduction of indoor radon concentration by using this method of ventilation and determine the correct way to set up the ventilation equipment.

KEYWORDS

Mechanical ventilation, Radon concentration, Energy saving

INTRODUCTION

In times of energy crisis and high energy prices, people are forced to take measures to reduce energy consumption in buildings. Funds to ensure these measures can currently be obtained from the Recovery and Resilience Plan approved by the European Commission. Part of these funds is intended precisely for improving the energy efficiency of family homes and the restoration of public historic and heritage-protected buildings. Investments are also intended for the renewal of the building envelope, the replacement of windows or the provision of a more efficient heat source [1]. With these solutions, it is also important to think about the need for sufficient ventilation as energy-saving measures which usually reduce heat loss through the building envelope and subsequently reduce the rate of air exchange [2], [3]. The purpose of ventilation is to remove contaminants, to create good indoor air quality and to reduce the risk of health problems by introducing and circulating fresh air throughout the building.

Among the health-threatening substances accumulating in the internal environment of buildings is radon. Radon mixes with atmospheric air in exterior. However, in closed indoor spaces it accumulates and increases in harmful concentrations [4]. Among the most important sources of radon in the interior are subsoil, groundwater and building materials. With its products, radon enters the respiratory tract by inhalation, which can subsequently cause cancer. According to the World Health Organization, it is the second most common cause of lung cancer after smoking [5].

The necessity to deal with indoor air quality while increasing the energy efficiency of buildings was confirmed in a French study [6]. It demonstrated the significant impact of renovation and modernization of buildings on the increase in indoor radon concentrations. The study from the United Kingdom [7] investigated the consequences of reducing the ventilation of buildings by increasing the air tightness of the envelope, demonstrating the possibility of increasing radon concentration by more than 56 %.

It is possible to achieve the required air exchange and reduction of energy losses through ventilation with heat recovery at the same time. The results of a simulation study from Ireland [8] highlight that radon concentrations in buildings could potentially change depending on the ventilation strategies designed during renovations. Currently, there are many central and decentralized recuperation units on the market that can be used for this purpose. The contribution is devoted to measuring the indoor radon concentration in a room that uses a local heat recovery unit for ventilation.

CASE STUDY

The measured room is located on the ground floor of the three - floor administrative building in Banská Bystrica. Based on the radon risk map, there are several places with increased radon risk in the city. What is more, based on the information from recent measurements in the building, an increased indoor radon concentration was measured. The building was built in the 70´s of the last century, but a few years ago, the building underwent a complete renovation of the outer shell. As a part of renovation, the window structures were completely replaced. The contact insulation system was applied to the façade of the building and flat roofs were in insulated.

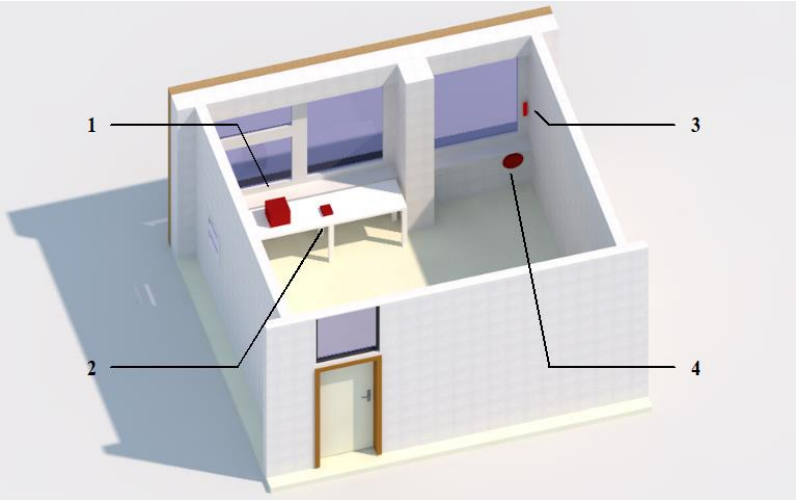

Fig. 1 – Axonometry of the monitored room with the location of the ventilation equipment and measuring devices: 1- Radon monitor AlphaGuard, 2- Testo 400, 3- TFA – Thermo-Hydro Sensor, 4- Prana 150

A local recovery unit Prana 150 is used to ventilate the measured room. It is a two-way recuperation with independent adjustment of the volume of incoming and outgoing air. This unit is intended for the ventilation of smaller spaces up to 60 m² of floor area, while it can provide air exchange with a volume of approximately 100 m³/h. The warm exhaust air removed from the interior transfers heat in the copper exchanger to the supplied air from the exterior, while there is no mixing of the removed and supplied air. The manufacturer indicates the efficiency of the device in terms of energy savings of up to 95 % [9]. The principle of installation of the recovery unit is shown in Figure 2.

Fig. 2 – Installation of the ventilation device in the prepared place.

MEASUREMENT METHODS

An AlphaGuard radon monitor was used to measure the radon concentration, which enables continuous radon measurement and measurement of selected climatic parameters such as temperature, pressure and air humidity at the same time. This device works on the principle of an ionization chamber [10]. The working space with the collecting central anode is filled with the working charge - air. The examined air passes into the ionization chamber through a filter that allows only radon 222Rn molecules, i.e. without the products of its transformation. The filter also prevents contamination by dust particles. During the transformation of radon, alpha particles are released, which ionize the gas. The resulting positive and negative ions are captured on the electrodes of the chamber. The size of the generated electric charge is proportional to the volumetric activity of radon [11].

The WeatherHub SmartHome System device for wireless observation of climatic conditions was used to record outdoor weather conditions. To verify the temperature and humidity parameters, a TFA – Thermo- Hydro Sensor recorder was used. It was placed on the outside of the window frame of the examined room. The Testo 400 universal instrument for measuring climatic variables was also placed in the examined space. The instrument includes a probe that allows parallel measurement of humidity and temperature in the room in addition to CO_2. The measuring devices used during the experiment are shown in Figure 3.

Fig. 3 – Measuring devices used during the experiment:

1- Radon monitor AlphaGuard, 2- Testo 400, 3- TFA – Thermo-Hygro Sensor

RESULTS

The entire research consisted of several measurements throughout different seasons of the year. Two long – term measurements took place in the winter period and were subsequently supplemented by shorter measurements in April and May.

The first measurement took place between 07. 12. 2021 and 20. 01. 2022 (45 days). Between 22. 12. 2022 – 10. 01. 2022 (20 days) the ventilation device with heat recovery was out of operation.

The other days, it worked in overpressure ventilation mode. The development of the radon concentration in the measured room is captured in Figure 4. Based on the measured values, it can be deduced that the radon concentration values in the interior increased significantly when the ventilation device was turned off.

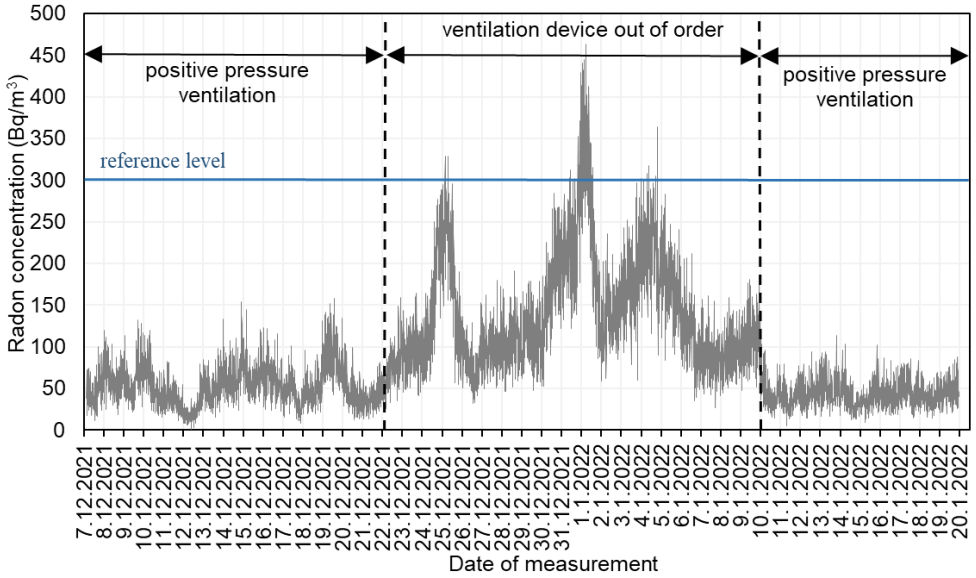

Fig. 4 – The course of the measured values of the internal radon concentration during the first part of the measurement.

In this interval, a value of 300 Bq/m³ was exceeded for six days, while the highest measured value was 463 Bq/m³. During the operation of the ventilation equipment, the highest measured value of the indoor radon concentration was 158 Bq/m³. This represents an almost threefold increase in concentration when the ventilation device is turned off.

A similar increase was also recorded for the other parameters listed in Table 1. However, the increase was not only recorded for the maximum values, but also for the others. The comparison of measured values is graphically displayed in Figure 5. Median measured concentration values increased by 178 % after ventilation was turned off. An average increase of 190 % was measured, and the third quartile of measured values increased by up to 202 %. The median was slightly lower than the mean, indicating the presence of some extreme values. When evaluating these values, radon concentration values were not taken into account on days when the ventilation operation was changed (turning off/on the ventilation system), as these values could distort the values during normal days.

Tab. 1 - Measured values of radon concentration.

Parameter	Radon concentration (Bq/m³) Ventilation device in use	Radon concentration (Bq/m³) Ventilation device out of order
1. quartile (25 %)	34	91
Median	45	125
Mean	49	142
3. quartile (75 %)	60	181
Maximum	158	463

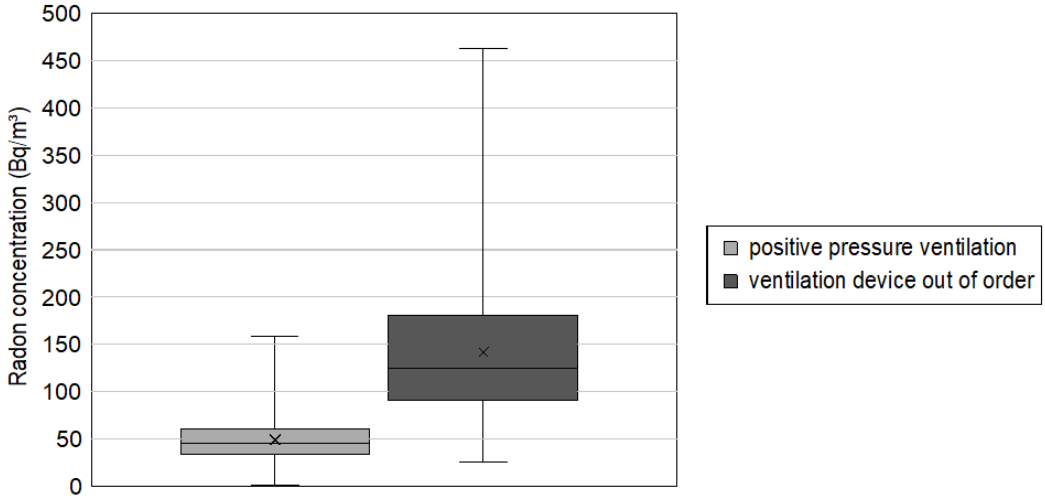

Fig. 5 – Graph of the measured values of the internal radon concentration during the first part of the measurement.

The course of the indoor radon concentration during the day when the ventilation equipment was turned off can be seen in Figure 6. During operation, the concentration value was in the range of 60-80 Bq/m³, then after the ventilation equipment was turned off, the radon concentration began to increase. Within 6 hours, it reached a value of 100 Bq/m³ and within 16 hours it reached a value of 150 Bq/m³. In Figure 7, you can see the opposite case of the course of the radon concentration when the ventilation device is switched on again. The reduction of the radon concentration to a value of 50 Bq/m³, which represents the average measured values, occurred after 14 hours of operation of the ventilation equipment.

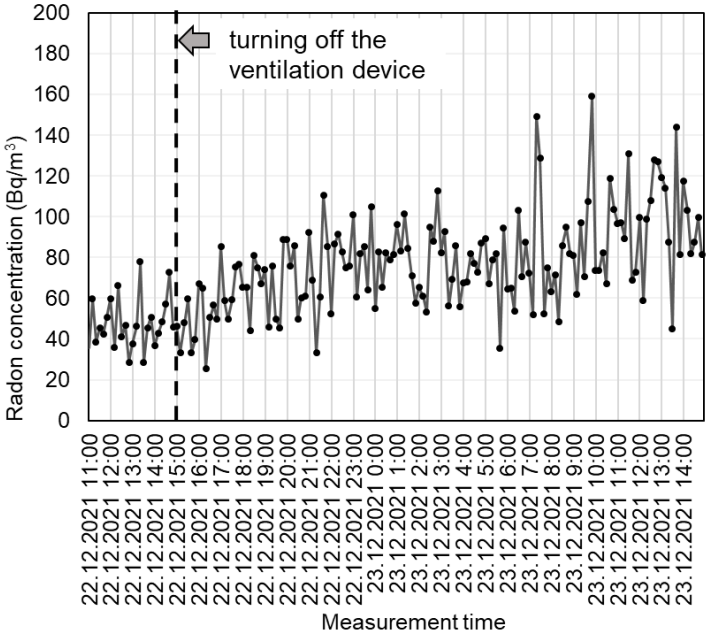

Fig. 6 – Course of radon concentration after switching off the ventilation device.

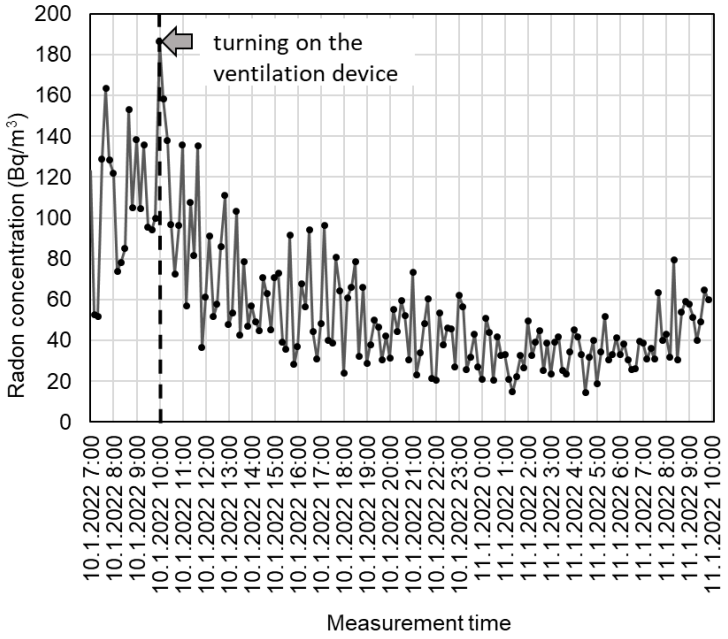

Fig. 7 – Course of radon concentration after switching on the ventilation device.

The second part of the measurements started already during the autumn period. During this time the ventilation device was set in the overpressure ventilation mode. The measurement lasted from 14. 09. 2022 – 13. 11. 2022 and then continued after a short break from 21. 12. 2022 – 12. 01. 2023. During the period from 21. 12. 2022 – 09. 01. 2023 the setting of the ventilation device was changed to equal pressure. The course of radon concentration during the entire measurement is shown in Figure 8.

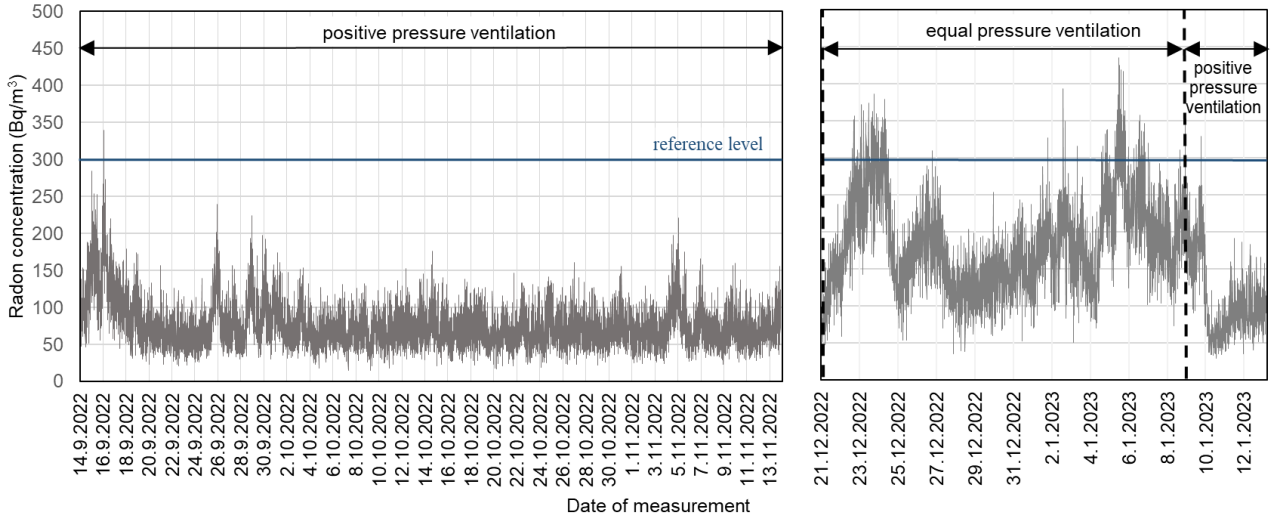

Fig. 8 – Course of the measured values of the internal radon concentration during the second part of the measurement

From the course of the radon concentration shown in Figure 8, the change of ventilation mode resulted in a significant increase in the indoor concentration. The measured values are shown in table no. 2 and their graphic comparison in Figure 9. The positive pressure ventilation was in

operation for 20 days, while the radon concentration exceeded the reference level only during 11 days. The highest measured value was 435 Bq/m3. However, the reference value was exceeded one day even with positive pressure ventilation. The median of measured concentration values increased by 151% after ventilation was turned off, while the other parameters also showed a similar increase.

Tab. 2 - Measured values of radon concentration during the second part of measurements.

Parameter	Radon concentration (Bq/m³) Positive pressure ventilation	Radon concentration (Bq/m³) Equal pressure ventilation
1. quartile (25 %)	55	136
Median	70	176
Mean	76	184
3. quartile (75 %)	91	222
Maximum	339	435

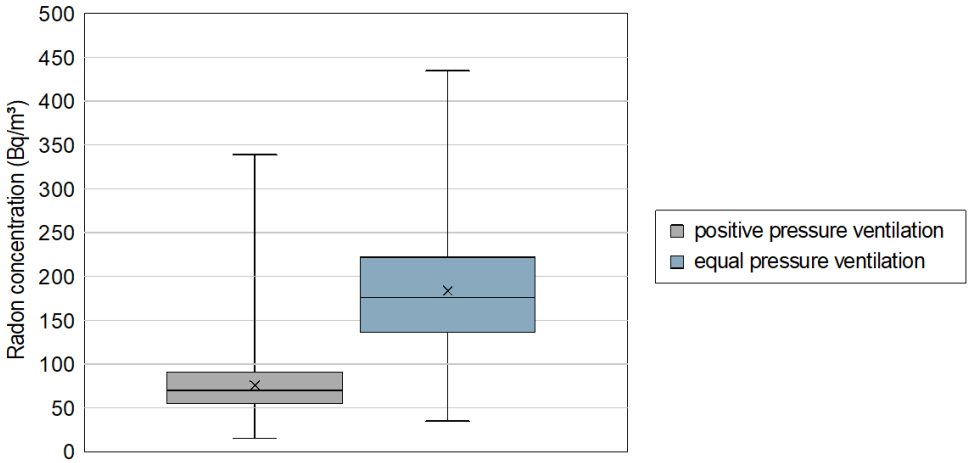

Fig. 9 – Graph of the measured values of the internal radon concentration during the second part of the measurement.

On 01. 09. 2023, the setting of the ventilation device was changed from equal pressure ventilation mode to positive pressure again. Considering the previous measurement, it was assumed, that within a few hours, there will be a significant decrease in the indoor radon concentration. Figure 10 shows the plotted course during the following hours. The radon concentration remains at the same level as during equal pressure ventilation until the morning of the next day. In this case, the drop in the radon concentration occurs only after 24 hours, while the radon concentration subsequently remains at the the level of 40 – 80 Bq/m3.

Due to the weather conditions during these days a delayed drop in concentration was noticed. Figure 11 shows the course of precipitation and outdoor air humidity. The rainy weather on the day of the change in the setting on the ventilation equipment caused that the radon in the soil air was not released to the surroundings but the flooded pores in the soil air caused a greater supply of radon from the subsoil into the building. After the end of the rain and the subsequent drop in exterior humidity, there is also a drop in the indoor radon concentration.

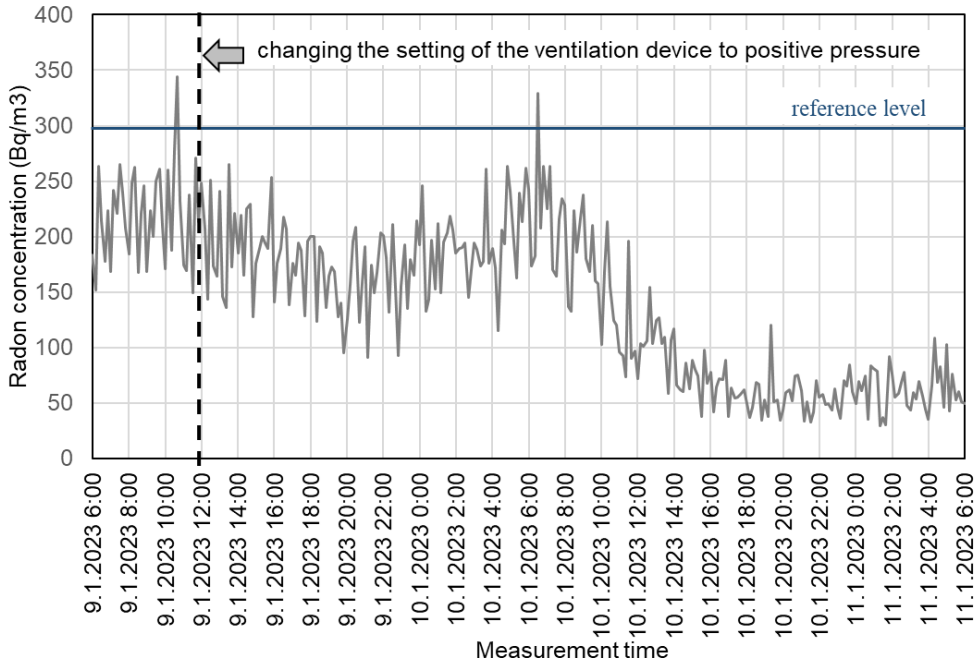

Fig. 10 – Course of radon concentration after turning on the ventilation device in overpressure mode.

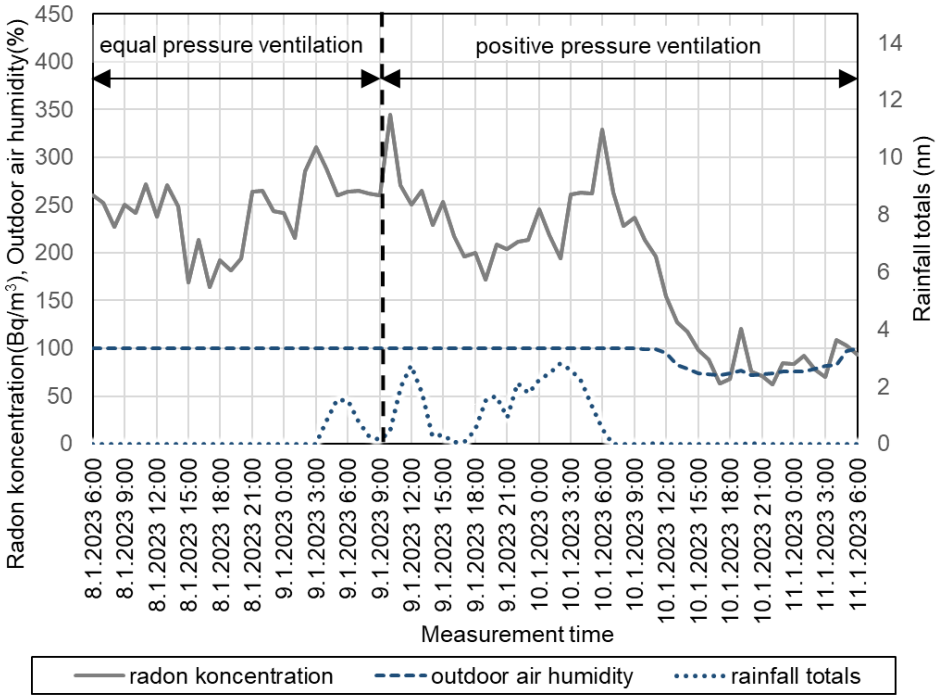

Fig. 11 – Comparison of the course of radon concentration, rain volume and exterior humidity after switching on the ventilation device in overpressure mode.

The last part of the measurements started on 17.04. 2023 and was finished on 15. 05. 2023. During these days, the setting of the ventilation device was changed at approximately weekly intervals. At the beginning, the ventilation was set as overpressure, while at the end the possibilities of setting the ventilation were investigated. During one week, the ventilation was turned off and later the measurement was made in the mode of under pressure (vacuum mode) and equal pressure ventilation. Figure 12 shows the course of concentration during these days.

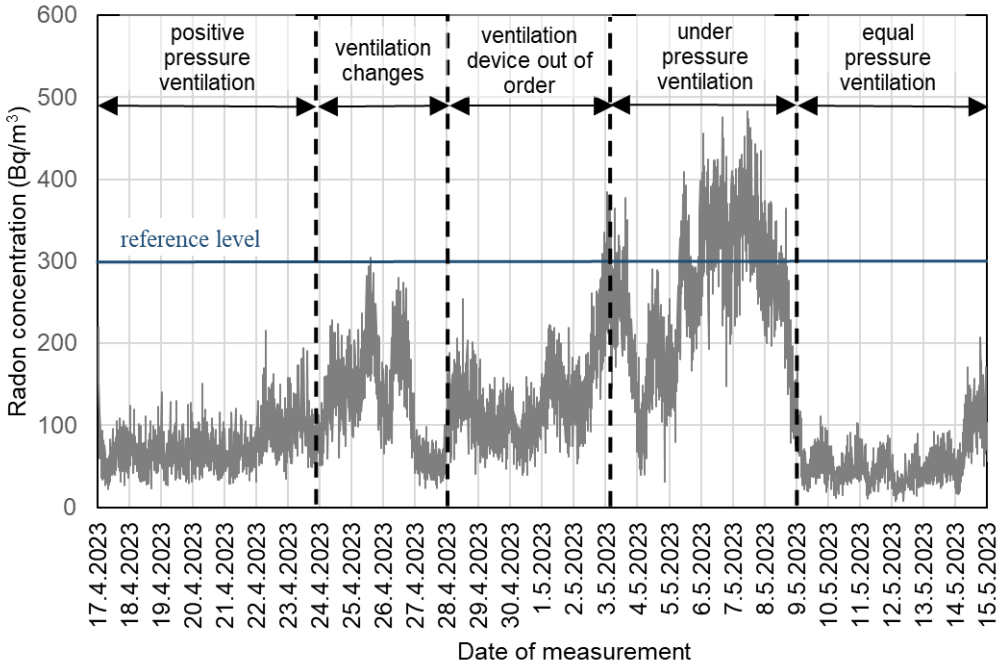

Fig. 12 – The course of the measured values of the internal radon concentration during the third part of the measurement.

In contrast to the previous measurements, in this case the radon concentration was measured also during under pressure (vacuum) ventilation. However, this type of ventilation causes an increase in the supply of radon from the soil air what was also reflected in the course of radon concentration. During this week, the highest indoor concentration value for the entire length of the measurement was measured – 482 Bq/m3. Only one day during this week radon concentration did not exceed the reference level of 300 Bq/m3. The equal pressure ventilation, which in the winter caused an increase in radon concentration, proved effectiveness in decreasing the indoor concentration and kept the values at an average of 55 Bq/m3 in this case.

Tab. 3 - Measured values of radon concentration during the third part of measurements

Parameter	Radon concentration (Bq/m³) Positive pressure ventilation	Radon concentration (Bq/m³) Ventilation device out of order	Radon concentration (Bq/m³) Under pressure ventilation	Radon concentration (Bq/m³) Equal pressure ventilation
1. quartile (25 %)	54	93	194	8
Median	69	124	266	48
Mean	74	134	259	55
3. quartile (75 %)	89	161	325	66
Maximum	220	384	482	208

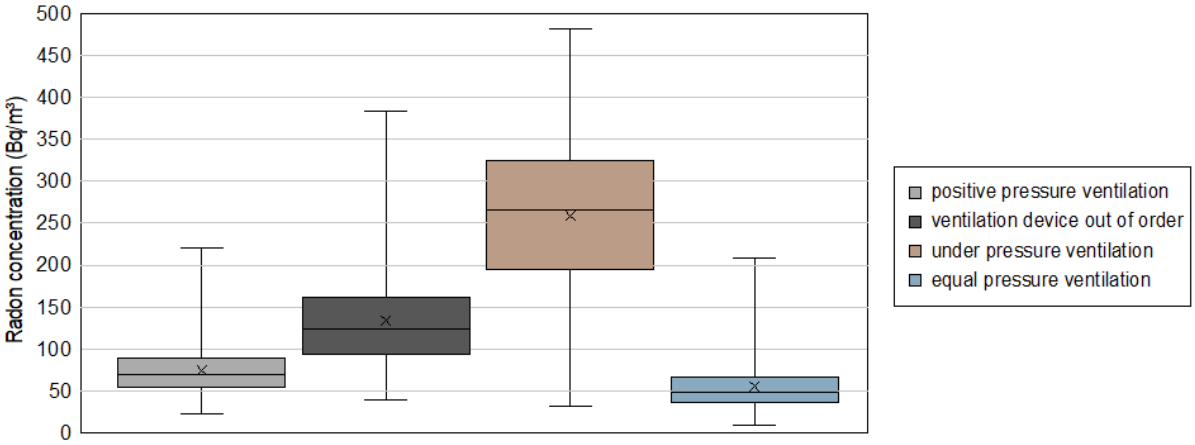

Fig. 13 – Graph of the measured values of the internal radon concentration during the third part of the measurement.

DISCUSSION

Mechanical ventilation with heat recovery helps significantly to reduce indoor radon concentrations and at the same time contributes to energy savings. However, the correct setting of the ventilation unit is important. The volume of incoming and outgoing air causes pressure differences between the interior and exterior and ultimately affects the indoor radon concentration [12], [13], [14]. If ventilation creates negative pressure in the room, indoor concentrations rise above the reference level. In the case of setting the equal pressure ventilation mode, low radon concentrations were measured in the summer. In winter, however, this type of ventilation has not proven to be effective in terms of reducing indoor radon concentration. Positive pressure ventilation is the only one that has proven itself in both summer and winter and was able to significantly reduce indoor concentrations. However, we must take into account the fact that the radon concentration values are very variable and often change significantly over the course of hours.

The way the building is used has also a significant influence on the radon concentration values. Reducing of frequency of use of the investigated space during weekends or holidays can also cause an increase in the indoor radon concentration.

Another factor that could affect the radon concentration values is the external weather conditions and the permeability of the subsoil. It follows from the measurements during rainy days that the radon concentration values increased significantly at this time.

CONCLUSION

From the measurement results and considering the facts that could influence the resulting values of radon concentration in the interior, it can be concluded that ventilation with heat recovery has proven to be a suitable anti-radon measure while simultaneously saving energy and having a positive effect on carbon dioxide and humidity values in the interior. The measurements achieved similar results as in previous studies. It is important to note that with the wrong method of ventilation, its effect on reducing the radon concentration could be reduced or even the opposite. Mechanical ventilation as an anti-radon measure is also suitable to be combined with other passive anti-radon measures (e.g. radon insulation or subsoil ventilation), since in the event of a malfunction of the ventilation equipment, the values can quickly rise above the limits set by the norm. The next experiment could follow up on the obtained results with a computer simulation of this monitored space.

ACKNOWLEDGEMENT

This article was created with the support of the RadoNorm project performed within the Euratom research and training programme 2019-2020 under the grant agreement No. 900009 and also funded by the EU NextGenerationEU through the Recovery and Resilience Plan for Slovakia under the project No. 09I03-03-V01-00036. The Euratom agency's nor the RadoNorm's nor the European Commission's support for the production of this article does not constitute an endorsement of the contents, which reflect the views only of the authors, and the Euratom, the RadoNorm Initiative and the Commission cannot be held responsible for any use, which may be made of the information contained therein.

REFERENCES

[1] Recovery plan of the Slovak Republic, 2021, Complete recovery plan, Available online in Slovak: https://www.planobnovy.sk/kompletny-plan-obnovy/ (accessed on 20 February 2023)

[2] Pompuri, L., Caputo, P., Valsangiacomo, C., 2018. Effects of buildings' refurbishment on indoor air quality. Results of a wide survey on radon concentrations before and after energy retrofit interventions, In: Sustainable Cities and Society,Volume 42, p. 100-106, ISSN 2210-6707. DOI: https://doi.org/10.1016/j.scs.2018.07.007

[3] Vasilyev A.V., Yarmoshenko I.V., Zhukovsky M.V., 2015 Low air exchange rate causes high indoor radon concentration in energy-efficient buildings. Radiat Prot Dosimetry. Ekaterinburg, p. 601-605. doi: 10.1093/rpd/ncv319

[4] Jiránek, M., Honzíková, M., 2017. Anti-radon insulation. Radon construction context I. Prague: ČVUT, p. 5-26 ISBN 978-80-01-05023-1.

[5] Hajo, Z., Shannoun, F., 2009. World Health Organization. WHO handbook on indoor radon: a public health perspective, Geneva: WHO Press, p.100, ISBN 978 92 41547673. DOI: http://dx.doi.org/10.1080/00207230903556771

[6] Collignan, B., Ponner, E., Mandin, C., 2016. Relationships between indoor radon concentrations, thermal retrofit and dwelling characteristics, In: Journal of Environmental Radioactivity, p. 124-130, ISSN 0265-931X. DOI: https://doi.org/10.1016/j.jenvrad.2016.09.013

[7] Milner, J., Shrubsole, C., Das, P., Jones, B., Ridley, I., Chalabi, Z. et al., 2014 Home energy efficiency and radon related risk of lung cancer: modelling study, London. DOI: https://dx.doi.org/10.1136/bmj.f7493

[8] McGrath, J.A., Aghamolaei, R., O'Donnell, J., Byrne, M.A., 2021. Factors influencing radon concentration during energy retrofitting in domestic buildings: A computational evaluation, Building and Environment, Dublin, Volume 194, p. s 231-245, ISSN 0360-1323, DOI: https://doi.org/10.1016/j.buildenv.2021.107712.

[9] PRANA 150 Premium, Available online in Czech: https://www.pranacz.cz/prana-150-premium/ (accessed on 20 February 2023)

[10] Bujnová, A., 2007 Comparison of the results of continuous measurements of 222Rn, Student Scientific Conference 2007. Bratislava, p. 9,

[11] ALPHAGUARD - radon monitor, Available online in English: https://www.bertin-instruments.com/product/radon-professional-monitoring/radon-alphaguard/ (accessed on 20 February 2023)

[12] Akbari, K., Öman, R., 2012. Radon Mitigation using Heat Recovery Ventilation system in a Swedish Detached House. WSEAS Transactions on Environment and Development, vol. 8, p. 73-82. E-ISSN: 2224-3496.

[13] Burghele, B.D., Botoș, M., Beldean-Galea, S., Cucoș, A., Catalina, T., Dicu, T., Dobrei, G., Florică, S., Istrate, A., Lupulescu, A., Moldovan, M., Niță, D., Papp, B., Pap, I., Szacsvai, K., Sainz, C., Tunyagi, A., Țenter, A., 2021. Comprehensive survey on radon mitigation and indoor air quality in energy efficient buildings from Romania, In: Science of The Total Environment, Volume 751, ISSN 0048-9697. DOI: https://doi.org/10.1016/j.scitotenv.2020.141858

[14] Holmgren, O., Arvela, H., 2012. Assessment of current techniques used for reduction of indoor radon concentration in existing and new houses in European countries. Helsinki, p. 56-59, ISBN 978-952-478-681-2.

CIVIL ENGINEERING JOURNAL

Article no. 36

THE CIVIL ENGINEERING JOURNAL 2-2023

SAFETY ASSESSMENT OF CONTINUOUS CONCRETE GIRDER BRIDGES SUBJECTED TO RANDOM TRAFFIC LOADS CONSIDERING COUPLED FLEXURAL-SHEAR FAILURE

*Ruifeng Nie, Jinfeng Yao and Songhui Li**

Shandong University of Science and Technology, Shandong Key Laboratory of Civil Engineering Disaster Prevention and Mitigation, Qingdao, 266590, China; qingdaonieruifeng@163.com; 15136450120@163.com; songhui.l@163.com

ABSTRACT

Bridges generally exhibit complicated mechanical behaviors under external loads, such as flexural-shear coupling, compression-bending coupling, and flexural-shear-torsion coupling. In the context of deterministic design approaches such as design codes, these complicated coupled issues are generally simplified to the safety verification of bridge components under a single mechanical state (i.e. flexural, shear, torsion). Currently, it is available to collect external loads acted on bridges and understand bridge performance under these stochastic external loads. In this manner, the reliability-based full probabilistic approach could be applied to investigate the performance of bridges over their lifetime. However, the majority of existing bridge reliability assessments involving site-specific traffic load measurements focuses on the analysis of bridge components under a single mechanical state. To address this shortcomings, a reliability-based probabilistic analytical framework is established to investigate the flexural-shear capacity of girder bridges subjected to random traffic loadings. The flexural-shear coupled failure path of bridge girders under random traffic loading is characterized for the first time, where the bivariate extreme value theory is incorporated to develop the extreme value distribution of combined flexural and shear load effects. The modified compression field theory recommended by AASHTO is employed to establish the coupled flexural-shear coupling resistances. Finally, the reliability of the flexural-shear performance of bridge girders is evaluated by solving the multivariate ultimate limit state equation. The proposed analytical framework is applied to a realistic bridge. The results show that the reliability index of the flexural-shear coupling evaluation is lower than that of the flexural or shear evaluation, which highlights the importance of the flexural-shear performance checking in the reliability assessment of bridges under random traffic loading. The proposed analytical framework could be further applied to the probabilistic assessment of bridge components subjected to combined loading mechanisms under random loadings.

KEYWORDS

Girder bridge, Safety assessment, Flexural-shear failure, Random traffic load, Multi-variate extreme value modelling

INTRODUCTION

The transport industry has achieved rapid growth over the past two decades. The bridge structure, as a lifeline node in the transport network, is of great importance. However, due to the high degree of temporal and spatial variability of traffic loads, the estimation of bridge load effects and resultant structural safety becomes a difficulty in focusing. As is well known, the actual traffic loads are not accurate to reflect the service loads which given by current design specifications [1-2]. It is, therefore, necessary to conduct traffic load modelling and bridge load effects analysis based on these measurements. This could provide more confidence in evaluating the bridge service life, and allocating limited maintenance resources.

The current studies of traffic load modelling and bridge load effect analysis mainly focus on the evaluation of simple mechanisms, such as flexural or shear, of bridge components. These studies well expound the structural responses and reliability of bridges under site-specific traffic loads. However, bridge components are often subjected to combined forces. For example, the internal force for girder is bending moment and shear force, but axial force cannot be neglected for arch. Besides, due to the spatial randomness of degradation of structural materials, the concerned bridge position that only requires simple mechanism assessment before, may need a re-evaluation but based on a combined mechanism state [3]. Therefore, it is required to establish a probabilistic evaluation method for the combined loading mechanism of bridges under random traffic loading.

At present, a wide range of studies has been dedicated to investigating the structural performance, failure mode, and ultimate design principles of bridge components under combined forces. The flexural-shear coupling of steel members has been a key concern from the past to the present. As early as 1936, Way proposed the elastic critical force equation through the deflection-shear coupling experiment for steel structure. The flexural-shear coupling equation was first proposed by Basler in 1961 on the basis of forces, where the shear force is assumed to be carried only by the web. Then the theory was improved and used by the Eurocode. On this basis, researchers have improved and updated the designed flexural-shear coupling model for steel structures [4]. Meanwhile, the flexural-shear coupling is also important for steel-concrete composite structures. For example, Liang et al. [5] pointed out that the conventional shear design theory of steel plate was conservative as the effect of the deck was not considered, and proposed an improved resistance design formula considering the flexural-shear coupled failure in continuous composite beams. The formula was derived from the nonlinear finite element analysis of the ultimate bearing capacity of continuous beams under bending moments and shears. The angular formulation of the pressure field for flexural-shear coupled effect of concrete members was first proposed by Nilsen and Lampert, which is mainly based on the plasticity theory. Then, Elfgen conducted concrete strength tests and obtained the relationship between flexural-shear interaction of concrete structures through the constitutive model of concrete. Later, due to the effect of tensile stresses in cracks in concrete structures, based on strain coordination in the truss model, Vecchio and Collins proposed the modified compression field theory (MCFT) based on experimental research, which is mainly an analytical model for predicting the load-deformation response of concrete elements under shear stress and normal stress [6-7]. This theory was incorporated into design codes in Canada and the United States and still used now [8]. In summary, the combined resistance of structures under flexural-shear has been thoroughly studied by many scholars and abundant theoretical and experimental results have been obtained. However, few attention has been paid to the combined load effect of the flexural-shear combination of the structure under external loads.

In this paper, the flexural-shear coupling performance of a slab bridge under random traffic loading is focused. The framework structure of this paper is organized as follows. Section 2 introduces the basic description of the studied slab bridge. Section 3 calculates the flexural-shear resistances of bridge slabs according to the MCFT, where several critical girder sections are analyzed. Section 4 presents the modelling of flexural-shear coupling load effects caused by random traffic loading, which is the first time that such an issue is focused. Wherein, the extreme values of flexural-shear load effects are extrapolated using peaks-over-threshold (POT) based bivariate extreme value theory. Section 5 probabilistically evaluates the failure path incorporating the flexural-shear coupling load effects and resistances. This study provides a general framework using probabilistic reliability theory to evaluate the flexure-shear performance of bridges under random traffic loads. Since bridge components are generally subjected to combined forces such as bending, shear, compression, and torsion. This study will provide an approach basis for clarifying the probabilistic reliability evaluation of bridge components under such complicated loading states.

DESCRIPTION OF THE BRIDGE

In the study, a continuous concrete slab bridge is investigated. It has four equal spans with an arrangement of 4×16m. The bridge structure was designed according to the Chinese standard drawings of JT/GQB008-96. Figure 1 shows the layout of the bridge. The bridge carried two lanes of unidirectional traffic. The grade of the constructed concrete is C25, and the bridge deck is paved with 20~110mm concrete cushion and 40mm asphalt concrete pavement. It is noted the studied beam sections shown in Figure 1(a) are sequenced number of 1 to 7 from the left to the right, where the section 4# is the cross-section of the left second-side support.

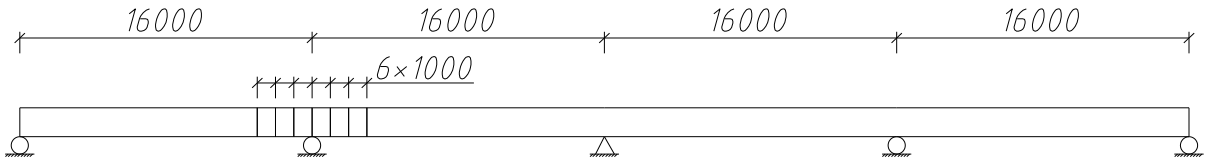

(a) Vertical diagram

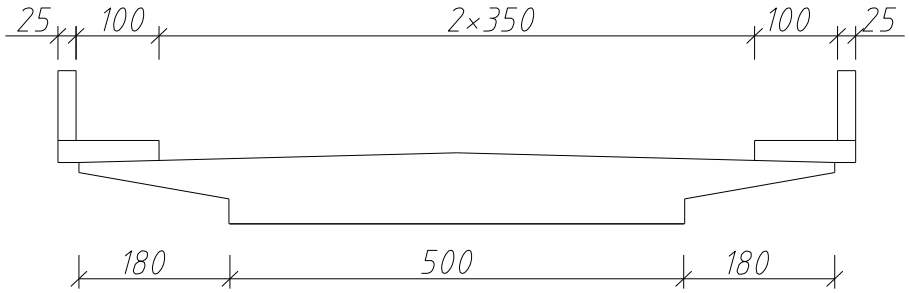

(b) Cross-section diagram

Fig. 1 –The vertical and cross-section diagrams of the studied bridge (unit: mm)

To evaluate the bridge performance under random traffic loading, 90 days of weigh-in-motion (WIM) data from another site are used for the analysis. It is found from the statistics of the WIM data that the 2-axle truck has a proportion of 65.21%, and that for 3-axle, 4-axle, 5-axle, and 6-axle trucks are 6.79%, 10.86%, 2.29%, and 15.03%, respectively. The daily truck flow of the WIM data is 4000 veh/d. To study the performance of the flexural-shear performance of the slabs, 7 sections are studied as shown in Figure 1(a). For these cross-sections, bending moment and shear force are equally significant both under dead loads and live loads.

FLEXURAL-SHEAR COUPLING CAPACITY

Modified compression field theory

The flexural capacity of the normal section of beams is generally obtained based on the limit state equation where the longitudinal bars yield. However, in the design of inclined sections, excessive longitudinal bars are used in the beam bottom to prevent the failure of the normal section. In doing so, the longitudinal rebars generally not yield even though the beam failed. This calculates larger flexural capacities of normal sections. Several investigations have shown that the performance of longitudinal reinforcement is influenced by the shear forces in inclined sections. Therefore, if the design equations for the bearing capacity of section bending and shear are considered separately, the results are too conservative and the design cost is increased. The MCFT shows that cracked concrete is considered as a new material. Residual tensile stresses between cracks should be taken into account despite the cracking of the concrete and the effect of longitudinal reinforcement on its shear should not be overlooked. In MCFT, the constitutive equation can well reflect the interaction of the bearing capacity between bending and shear, which is mainly established by the average

stress and strain. In MCFT, the shear force of the beam section is shared jointly by the shear-compression region of concrete and the stirrup intersecting with the inclined cracks. The contribution of the stirrup is based on the variable-angle frame model, while the contribution of concrete is provided by the tensile stress of the inclined cracked concrete. AASHTO (2012) [9] adopted MCFT for the design of concrete beams. In many national design codes, including the Chinese design specifications, the flexural-shear coupling effect is not taken into account for the design of concrete beams. In the following study, the flexural-shear relationship of the structure is established using the MCFT as specified in AASHTO (2012) [9].

In MCFT, for reinforced concrete beams subjected to flexural-shear coupling, the shear performance of the skewed section mainly depends on the shear-to-span ratio, the reinforcement ratio of ordinary longitudinal and hoop bars, the strength of concrete, and the aggregate biting force. Therefore, when cracks appear in the diagonal section of a concrete beam, its shear bearing capacity is mainly borne by the tensile stress of the diagonally cracked concrete in the shear-compression zone, the aggregate occlusion force in the tension zone, the shear force of the bending-up reinforcement, and the shear force provided by the configuration of the hoop reinforcement. Therefore, the shear capacity of the concrete beam is determined as the minimal value between Equations (1) and (2), as specified in AASHTO (2012) [9]:

$$V_n = 0.25 f_c b_v d_v + V_p \tag{1}$$

$$V_n = V_c + V_s + V_p = 0.083\beta\sqrt{f_c} b_v d_v + \frac{A_v f_y d_v (\cot\theta)}{s} + V_p \tag{2}$$

where V_n denotes the minimum flexural capacity value of the sloped section; V_p denotes the vertical component provided by the prestressing force; V_c denotes the component provided by the tensile stresses of the cracked concrete of the sloped section; and V_s denotes the component provided by the tensile stresses of longitudinal reinforcement in the concrete; f_c denotes the design value of compressive strength of the concrete; b_v denotes the actual width of the web; d_v denotes the actual shear height of the sloped section; θ denotes the angle of inclination of the bar stress; β denotes the tension transfer coefficient of cracked concrete in the diagonal section, where θ and β are mainly determined by the characteristics of the sloped section as well as the applied external load; s denotes the spacing of the configured hoops; A_v denotes the area of the configured hoops; and f_y denotes the yield strength of longitudinal reinforcement in the sloped section.

Affected by the flexural-shear coupling effect, reinforced concrete beam cross-section under external loading usually appears complex mechanical behavior, such as flexural-shear coupling, compression-flexural coupling, flexural-shear-torision coupling, etc., and then produce a certain amount of external bending moments; with the increase of sustained load, these external moments in the beam cross-section is gradually differentiated into tensile stresses, and the resulting tensile stresses are mainly borne by the longitudinal steel reinforcement. Therefore, the tensile strength of the longitudinal reinforcement should be considered when calculating the shear capacity of the beam section under the flexural-shear coupling, and its tensile capacity should be calculated and verified whether it meets the requirements through equation (3).

$$A_{ps} f_{ps} + A_s f_y \geq \frac{|M_n|}{d_v} + (|V_n - V_p| - 0.5 V_s)\cot\theta \tag{3}$$

where A_{ps} denotes the cross-sectional area of prestressing reinforcement; f_{ps} denotes the yield strength of prestressing reinforcement; A_s and f_y denote the cross-sectional area and yield strength of flexural reinforcement; M_n denotes the bending resistance; and V_n denotes the shear resistance.

Analyzing the coupled flexural-shear resistance based on the MCFT, the total cross-section strain generated in the concrete beam section under flexural-shear coupling is equal to the sum of the cross-section strains generated under bending moments and pure shear, and the same is true for the total reinforcement strain. In practical calculations, the strain produced by the longitudinal reinforcement is equal to twice the strain in the beam section. The strain in the longitudinal reinforcement can be obtained from equation (4).

$$\varepsilon_{x=}\frac{\frac{|M_n|}{d_v}+0.5|V_n-V_p|\cot\theta-A_{ps}f_{ps}}{2(E_sA_{s+E_p}A_{ps})} \quad (4)$$

where ε_x denotes the total strain of the flexural reinforcement on the bending side of the member; E_s and E_p denote the modulus of elasticity of the flexural and prestressing reinforcement respectively.

Based on Equations (3) and (4), the flexural capacity of normal section for beams can be obtained. It is shown that the coupling of flexural and shear behavior of concrete beams is considered by the MCFT. The coupling effect makes the beam in the risk state. When the beams under loads, the coupling effect of the flexural-shear behavior could be considered.

For the parameters of stirrups and concrete strength, the values of θ and β under different ε_x can be obtained based on AASHTO (2012)[9]. The shear capacity can be calculated by Equations (1) and (2). The flexural capacity can be calculated by Equations (3) and (4), approximately. Finally, the coupling curve of flexural-shear resistance is obtained.

Flexural-shear resistance curve

In the framework of probabilistic reliability, material property and geometric sizes are random variables. It is generally assumed that these parameters are normally distributed. The statistical distribution of these parameters can be referred to Wang et al [3], which are shown in Table 1. Based on these variables, the flexural-shear resistances under any εx can be calculated using Monte-Carlo modelling. 108 groups of variables are modelled to determine the resistance model of any given beam section, and the sole flexural resistance, shear resistance, and flexural-shear resistance are obtained. For instance, the mean value of flexural resistance of section 4# is 1.385×10^4kN·m, and the standard deviation is 1.155×10^3 kN·m. The mean shear resistance of section 4# is 7.525×10^3kN, the standard deviation is 8.361×10^2 kN. For the special concern of flexural-shear resistance, Fig. 2 gives the results. It is found from the figure that the flexural-shear coupling reduces the sole flexural (or shear) capacity. It is, therefore, very important to consider the coupling behavior of the flexural-shear resistance curve in the evaluation of beam performance.

Tab. 1 - The random variables of material property and geometric sizes [3]

Parameters	Unit	Deviation	COV	Nominal value
fcu	MPa	1.5868	0.1928	17
fy	MPa	1.0821	0.1211	235
fy	MPa	1.0849	0.0719	335
h0	mm	1.0124	0.0229	628
b	mm	1.0013	0.0081	5400
A	mm²	1.0000	0.0350	70224
As	mm²	1.0000	0.0350	20944
as	mm²	1.0000	0.0350	1621
a	mm	1.0179	0.0496	60
s	mm	1.0000	0.1000	100

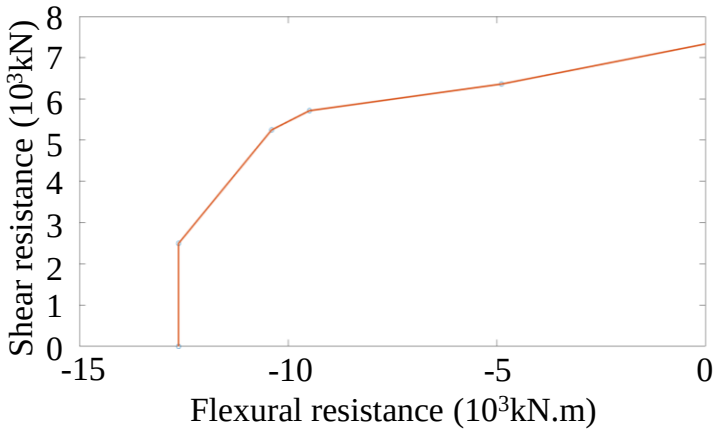

Fig. 2 – Flexural-shear resistance curve based on mean values

FLEXURAL-SHEAR COUPLING LOAD EFFECTS

Time-history of bending moments and shear forces under random traffic loads

The internal forces for beams are time-varying under random traffic loading. They are also correlated since their time-history is induced by the same traffic fleet. In conventional bridge design, only the most unfavorable bending moment or shear is concerned. However, for girder sections, they do not present the most unfavorable bending moment or shear, but the significant bending moment and shear concurrently, which are also drawn as the flexural-shear resistance curve as shown in in Figure 2. The magnitude of the correlation between bending and shear in any beam section is determined by their corresponding influence lines. To ensure the safety of given girder sections subjected to bending moment and shear force, the calculated concurrent bending moment and shear force should be within the envelope of the bend-shear resistance curve. It is generally assumed the bending moment and shear force under dead loading are constant with very small variability. Therefore, the safety assessment of flexural-shear behavior is to determine the failure path of coupling bending moment and shear force under traffic loading based on Figure 3.

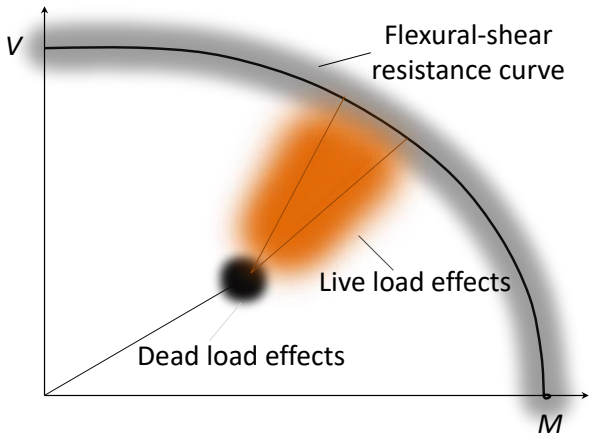

Fig. 3 –Schematic diagram of failure path determination of flexural-shear coupling

To obtain the most unfavorable load effects of the section, it is necessary to consider that the symbol of internal forces generated by dead load and live load is the same. Under this circumstance, the failure probability may be the largest. Fig. 4 shows the time-history curve of the bending moment and the shear force for section 4# under traffic loading. It can be seen clearly that the bending

moment and the shear force have a strong correlation The bending moment and the shear force are likely to reach their large values concurrently. It is also can be seen that the bending moment is positive and the shear force is negative caused by traffic loads. Therefore, the negative bending moments and positive shear forces produced by random traffic loading are extracted as the underlying data for further analysis.

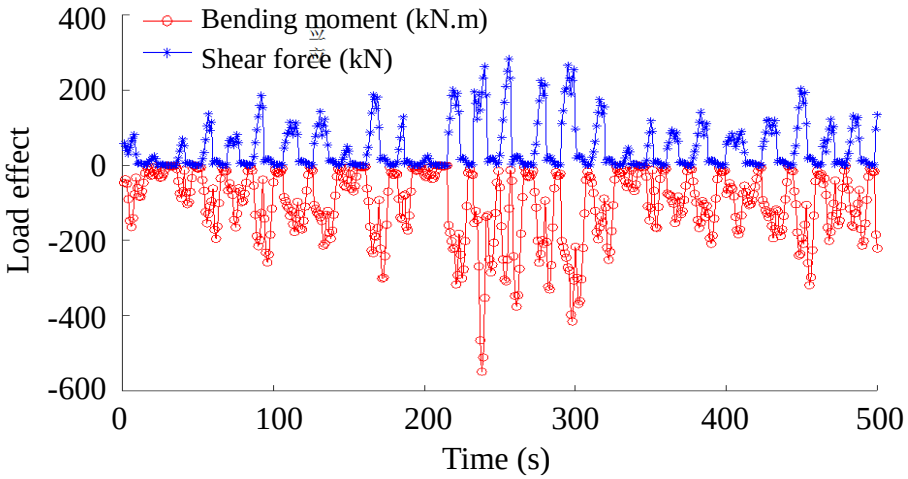

Fig. 4 –Parts of time-history of bending moment and shear force of section 4# under traffic loads

Extreme extrapolation of combined bending moments and shear forces

The safety assessment of flexural-shear coupling, as shown in Figure 3, is to determine the closest path between dead load effects and the flexural-shear resistance curve. Due to the randomness of live load effects caused by traffic loading, it is important to infer the characteristic traffic load effects of high return periods based on limited traffic measurements. Therefore, the bivariate extreme value extrapolation algorithm is required to determine the characteristic value [10].

Bivariate extreme value theory is to solve the modelling of extremely small probability events with bivariate variables reaching their maximum concurrently. Obviously, the extrapolation of extreme bending moment and shear force under random traffic flow is to establish their coupling probability model using this approach. The bivariate extreme value theory is developed from the classical extreme value theory, which can be approximated by using the block maxima based generalized extreme value distribution extrapolation, or POT based GPD (generalized Pareto distribution) extrapolation. The POT theory is more suitable for the extreme value modelling of limited underlying samples than the block maxima theory. In the paper, the bivariate POT theory is used to analyze the probabilistic extreme value model of coupling load effects of bending moment and shear under traffic loading.

According to the classical POT theory, the distribution function of the load effects X caused by traffic loading is F_x. For a sufficiently large threshold u_x, the tail of X can be approximated by GPD, given by

$$F_x(x) = 1 - \varsigma_x[1 - G_x(x)] = 1 - \varsigma_x\left(1 + \xi_x \frac{x-u_x}{\sigma_x}\right)^{-1/\xi_x}, x > u_x \quad (5)$$

where G_x is the GPD function of x; ξ_x, σ_x, and u_x are the shape parameter, scale parameter, and position parameter (threshold) of G_x respectively; $\xi_x = \Pr(x > u_x)$ is the probability of sample x exceeding u_x.

For two load effect samples, X and Y, the distribution functions are F_x and F_y respectively. It is necessary to find the case where x and y reaching their maximum concurrently. That is to analyze the tail characteristic of their joint distribution $F(x, y)$. According to Eq. (5), the marginal distributions for X and Y could be approximated by GPD when the threshold u_x and u_y are large enough. The

relevant parameters for G_x and G_y are $(\xi_x, \sigma_x, u_x, \varsigma_x)$ and $(\xi_y, \sigma_y, u_y, \varsigma_y)$ respectively. Making the following changes [11], we have

$$\bar{X} = -\left(\log\left\{1-\varsigma_x\left[1+\xi_x\frac{X-u_x}{\sigma_x}\right]^{-1/\xi_x}\right\}\right)^{-1}, X > u_x \tag{6-1}$$

$$\bar{Y} = -\left(\log\left\{1-\varsigma_y\left[1+\xi_y\frac{X-u_y}{\sigma_y}\right]^{-1/\xi_y}\right\}\right)^{-1}, Y > u_y \tag{6-2}$$

$\bar{X}$ and $\bar{Y}$ can be approximated to the standard Fréchet distribution. Provided the distribution function of $(\bar{x}, \bar{y})$are $\bar{F}(\cdot)$, $F(x, y)$ can be expressed as follows when $X > u_x$ and $Y > u_y$,

$$F(x,y) \approx G(x,y) = \bar{F}(\bar{x},\bar{y}) = \exp\{-V(\bar{x},\bar{y})\} = \exp\left\{-\left(\frac{1}{x}+\frac{1}{y}\right)A\left(\frac{x}{x+y}\right)\right\} \tag{7}$$

where $A(t) = \int_0^1 \max\big(w(1-t), t(1-w)\big)\, dH(w)$, V is the dependent function of the bivariate Fréchet marginal distribution H. $A(t)$ is the Pickands convex dependent function, satisfying $\{t, (1-t)\} < A(t) < 1$ where t is the coefficient of correlation.

Therefore, the extreme value models of coupling bending moment and shear force under traffic loading could be established using GPD and its dependent function.

Moment-shear coupling load effects

According to the bivariate POT theory, the optimal threshold based on marginal data can be used as the joint threshold of the bivariate distribution. For the studied bridge, the best thresholds of bending moment and shear effect of live load are determined by the Kolmogorov–Smirnov test and maximum likelihood approach. The GPDs for the bending moment and shear force can be obtained from the above thresholds. Figure 5 shows an example of using GPD modeling of marginal traffic load effects of section 4#. It is seen from the figure that the GPD well captures the tail tendency of the underlying data.

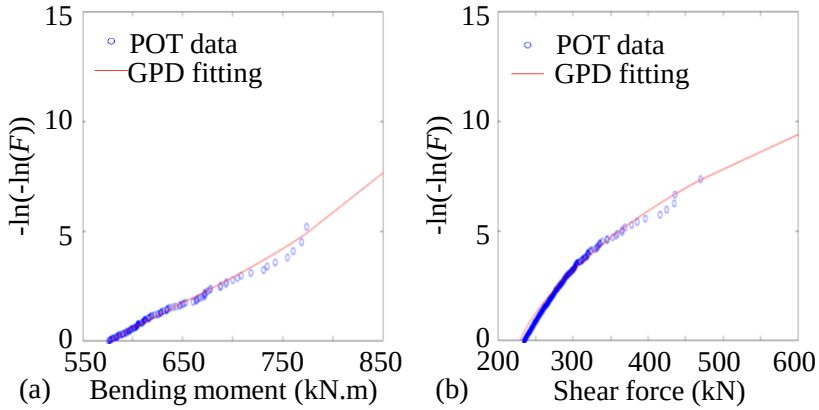

Fig. 5 –GPD modeling of marginal traffic load effects of (a) bending moment and (b) shear force: an example of section 4#

Using the bivariate thresholds, dependent functions can be used to model the tail tendency between the bending moment and shear force. Herein, many dependent functions provided in the R package are analysed [12]. It is found the bivariate logical copula was better to describe the dependency between bending moment and shear force. Fig. 6 shows an example of modelling the dependence between bending moment and shear force caused by traffic loading using the bivariate logical copula. The relative fitting parameters for section 4# are given in Table 2. The fitting results show that the bending moment has a strong tail correlation with the shear force. Based on these

analyses, the maximum distributions of bending moment and shear force under traffic loading can be modelled, which can be further used for structural safety assessment.

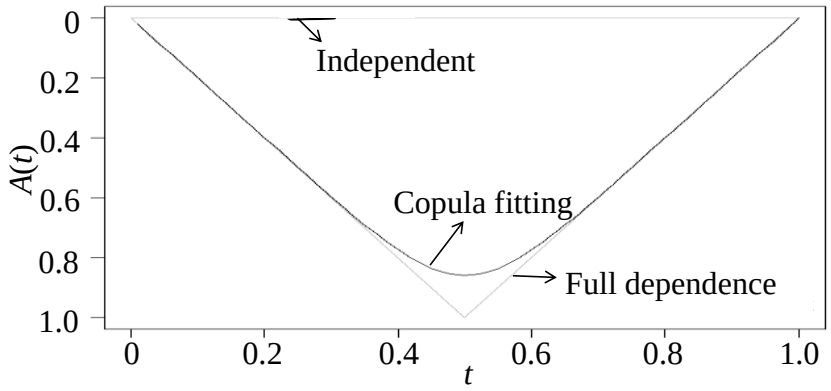

Fig. 6 –Copula fitting on tail dependence of bending moment and shear force caused by traffic loading: an example of section 4#

Tab. 2 - The fitting parameters of marginal GPDs and bivariate logical copula of section 4#

Marginal distribution						Dependence structure
Bending moment (kN•m)			Shear force (kN)			
σ	ξ	u	σ	ξ	u	t
51.6	0.099	550	19.6	0.139	220	0.19

PROBABILISTIC RELIABILITY ASSESSMENT

Limit state equation

Considering the dead load effects and traffic load effects, the limit state equation for flexural-shear assessment is given by

$$Z = R(M,V) - S_d(M,V) - S_q(M,V) \tag{8}$$

where R is the resistance; S_d is the dead load effect; S_q is the traffic load effect.

The flexural resistance is coupled with the shear resistance, as shown in Figure 2. However, the bending moment and shear force under dead loads could be regarded to be independent of each other. Figure 6 and Table 2 are also shown that the bending moment is strong coupled with the shear force under traffic loads. Therefore, the probability of failure is calculated based on $\Pr(Z < 0)$. In the paper, Monte-Carlo modelling is used to calculate the failure probability and reliability index.

Safety assessment

The reliability indexes of the concerned 7 cross-sections are calculated. Three failure modes with their corresponding reliability indexes are analyzed, which are flexural failure, shear failure, and flexural-shear failure. The results are given in Table 3.

The results show reliability indexes of flexural and shear are both greater than 5.61, indicating the failure probability is less than 10^{-8}. This is because most bridges in China have a good safety margin. However, for other engineering cases, the results might be different. However, when considering the coupling of flexural and shear both in resistances and load effects, the calculated reliability index is much lower, especially for section 4. The lowest probability reliability index for flexural-shear failure mode is 4.53, which is much lower than those calculated by flexural failure and shear failure. It illustrates the flexural-shear failure mode controls the safety of the beam section.

The conventional consideration of flexural checking or shear checking is unsafe, and it is required to consider the flexural-shear coupling both in traffic load effects and structural resistances.

Tab. 3 - Reliability indexes of concerned beam sections under different failure modes

Section	Failure mode		
	Flexural	Shear	Flexural-shear
1	>5.61	>5.61	>5.61
2	>5.61	>5.61	>5.61
3	>5.61	>5.61	4.83
4	>5.61	>5.61	4.53
5	>5.61	>5.61	5.07
6	>5.61	>5.61	5.51
7	>5.61	>5.61	>5.61

CONCLUSION

Safety assessment of bridges subjected to traffic loads is a research focus owing to the availability of site-specific traffic data. However, these studies mainly focused on the probabilistic evaluation of simple failure mechanisms of bridge components, such as flexural failure or shear failure. However, the critical components of bridges are often subjected to combined forces, such as flexural-shear, compressive-flexural, flexural-shear-torsion, etc. This paper proposed a novel framework for the probabilistic reliability evaluation of bridges subjected to combined forces. The flexural-shear performance of bridge girders is focused. Based on an exampled continuous concrete slab bridge, the flexural-shear coupling resistance and the flexural-shear coupling load effects under random traffic loading are investigated. Special attention is paid to the bivariate extreme value modelling of coupling bending moment and shear force under random traffic loading, which is to determine the most adverse failure path. Finally, the performance of bridge girders subjected to flexural failure, shear failure, and flexural-shear failure is investigated and compared. Main conclusions are as follows:

(1) According to the MCFT specified in AASHTO, the flexural resistances are coupled with the shear resistances. The existence of the bending moment (or shear force) reduces the shear (or flexural) resistance.
(2) Due to the randomness and uncertainty of traffic loads, the safety assessment of flexural-shear performance is to find the most adverse failure path based on the coupled resistance and dead load effects. It belongs to the scope of bivariate extreme value modelling.
(3) It is found from the studied case that the reliability index subjected to flexural-shear failure is much lower than that subjected to flexural failure or shear failure. It highlights the conventional safety checking of flexural or shear performance is unsafe, and it is required to consider the flexural-shear coupling effect both in traffic load effects and structural resistances for precise structural assessment, which is not covered by current design standards.

This study provides a methodology for estimating the structural safety of concrete beam bridges under random traffic loads, considering coupled flexural-shear failure. To obtain a more comprehensive understanding of the benefits of considering coupled flexural-shear failure compared to conventional flexural failure and shear failure, more example cases are required for thorough investigations.

ACKNOWLEDGEMENTS

This work was supported by Shandong Provincial Natural Science Foundation, China [grant number ZR2020ME241]; Shandong Provincial Natural Science Foundation, China [grant number ZR2021ME004]; Shandong housing and urban rural construction science and technology plan project, China [grant number 2020-K4-12].

REFERENCES

[1] Ruan, X., Zhou, J., Shi, X., Caprani, C. C., 2017. A site-specific traffic load model for long-span multi-pylon cable-stayed bridges. Structure and Infrastructure Engineering, vol. 13(4): 494-504 (In the case of journal articles)

[2] Zhou, J., Shi, X., Zhang, L., Sun, Z., 2019. Traffic control technologies without interruption for component replacement of long-span bridges using microsimulation and site-specific data. Structural Engineering and Mechanics, vol. 70(2): 169-178 (In the case of journal articles)

[3] Wang, X., Shi, X. F., Ruan, X., 2012. Beam bridges reliability assessment with a consideration of flexural-shear coupling effect, Journal of Tongji University (Natural Science), vol. 40(3): 338-343 (In the case of journal articles)

[4] White, D. W., Barker, M. G., Azizinamini, A., 2008. Shear strength and moment-shear interaction in transversely stiffened steel I-girders. Journal of structural engineering, vol. 134(9): 1437-1449 (In the case of journal articles)

[5] Liang, Q. Q., Uy, B., Bradford, M. A., Ronagh, H. R., 2004. Ultimate strength of continuous composite beams in combined bending and shear. Journal of Constructional Steel Research, vol. 60(8): 1109-1128 (In the case of journal articles)

[6] Vecchio, F. J., Collins, M. P., 1986. The modified compression-field theory for reinforced concrete elements subjected to shear. ACI Structural Journal., vol. 83(2): 219-231 (In the case of journal articles)

[7] Vecchio, F. J., Collins, M. P., 1988. Predicting the response of reinforced concrete beams subjected to shear using modified compression field theory. ACI Structural Journal, vol. 85(3): 258-268 (In the case of journal articles)

[8] Schlune, H., Plos, M., Gylltoft, K., 2012. Safety formats for non-linear analysis of concrete structures. Magazine of Concrete Research, vol. 64(7): 563-574 (In the case of journal articles)

[9] American Association of State Highway and Transportation Officials, 2012. AASHTO LRFD Bridge design specifications. Washington, DC (In the case of a specification)

[10] Zhou, J., Shi, X., Caprani, C. C., Ruan, X., 2018. Multi-lane factor for bridge traffic load from extreme events of coincident lane load effects. Structural Safety, vol. 72: 17-29 (In the case of journal articles)

[11] Rootzén, H., Segers, J., Wadsworth, J. L., 2018. Multivariate peaks over thresholds models. Extremes, vol. 21(1): 115-145 (In the case of journal articles)

[12] Gilleland, E., Katz, R. W., 2016. extRemes 2.0: An Extreme Value Analysis Package in R. Journal of Statistical Software, vol. 72(8): 1-39 (In the case of journal articles)

CIVIL ENGINEERING JOURNAL

Article no. 37

THE CIVIL ENGINEERING JOURNAL 4-2023

MECHANICAL CHARACTERISTICS OF LARGE-SECTION TUNNEL IN SOFT ROCK BASED ON VARIOUS ROCK CONDITIONS AND EXCAVATION FOOTAGES

Zengyin Xia[1], Chi Zhang[2], Pan Cao[3], Bin Li[2], Gongning Liu[3] and Huijian Zhang[3]

1. *China Railway Tunnel Group Road & Bridge Engineering Co.，Ld.，Tianjin 30030 China*
2. *China Railway Design Corporation, Tianjin 300308, China*
3. *Southwest Jiaotong University, Key Laboratory of Transportation Tunnel Engineering, Ministry of Education, Chengdu, No. 111, North Section, Second Ring Road, Jinniu District, 610031, China; 305434884@qq.com; 2995484603@qq.com; huijianz@163.com*

ABSTRACT

At present, few studies have taken both the rock conditions and the excavation footages into account to study the mechanical and deformation characteristics of the tunnel in soft rock area, and the existing results cannot be simply applied. Therefore, taking the Qianqi tunnel in V-class surrounding rock area as an example, based on the numerical calculation method, the mechanics and deformation rules about the tunnel under various rock conditions as well as excavation footages are analyzed in detail, aiming to provide some vital references for the on-site construction of the relied tunnel project. The results show that the displacements of the surrounding rock are greatly influenced by the excavation footages, namely, the arch settlements, horizontal convergences of the tunnel as well as the surface settlement increase significantly with the excavation footages. For the competent rock condition, the maximum bending moments of the preliminary lining after excavation occurs in the vault, and its increase amplitude has little correlation with the excavation footage that is more than 1.5m. For the poor surrounding rock, the maximum bending moment is transferred from the vault to the arch waist with the increase of the excavation footage, and it is basically manifested as the inner tension of the lining. The relationship between the excavation footage and maximum deformation as well as the mechanical index of the vault is also revealed, respectively. The excavation footage of the relied tunnel project is suggested as follows: 1.8m and 1.2m for the competent and poor rock conditions, respectively.

KEYWORD

Excavation footage, Soft rock, Three-bench method, Shallow-buried tunnel, mechanical property

INTRODUCTION

The stability of tunnel is always the focus of research [1, 2], especially for the tunnel in the weak surrounding rock [3, 4], and its stability is also closely related to construction method. According

to domestic and foreign engineering experience, if the full-section excavation method is not suitable for tunnels, bench method is often used [5]. As one of the main methods of mine tunnel construction, the bench method is essentially a geologically oriented excavation method [6]. With the change of surrounding rock conditions, the length of steps, the number and size of divided sections can also be changed accordingly, and the method is flexible in form, featuring fewer excavation disturbance of surrounding rock, favorable control of surrounding rock deformation and timely lining [7-10]. However, when the bench method is used in construction, there is no clear standard for the excavation footage, and the existing research results cannot be simply applied. If the excavation footage is set too small, it will prolong the excavation period as well as increase the construction cost. If the excavation footage is too large, when the rocks is poor, the stabilities of the surrounding rock at the tunnel vault as well as the excavation face will be particularly prominent, which is extremely unfavorable to the safety of the tunnel, and may even cause collapse in serious cases [11-17].

Scholars pointed out that the large deformation of tunnel excavation face could be effectively controlled by using the three-bench temporary invert method and reinforcing the upper step with the fibreglass bolts [18]. Within a certain range, the spacing of up and down steps of the tunnel, the spacing of annular and longitudinal bolts are negatively correlated with the stabilities of tunnel, and the parameters should be adjusted according to the actual situation [19]. The construction disturbance of super-large section tunnel is mainly concentrated in the excavation stage of the soil of upper step [20]. Using the bench method, the deformation properties about the tunnel during construction with freezing pipe roof was analyzed, and it was found that the demolition of temporary linings had a great effect on the displacement as well as the force of the tunnel, and the force centralization about the linings was alleviated after thawing [21]. The formation settlement properties about the tunnel in loess were analyzed, and it was found that the upper strata of the tunnel area sank as a whole after excavation, which developed rapidly and was destructive [22].

As can be seen from the previous studies, although many researches have been carried out on the construction of tunnel using the bench method, while few studies have comprehensively considered both the rock conditions and excavation footages. At the same time, due to the differences in engineering geological conditions (including the parameters of surrounding rock and lining, high in-situ stress, buried depth, etc.) of the tunnels in different studies [23, 24], the existing results cannot be simply applied to the relied project of this paper, and further studies should be carried out based on specific projects to provide more targeted construction suggestions.

Based on the two engineering examples of Qianqi Tunnel with similar excavation depth, similar strata and different water content, the deformation rules as well as the mechanics about the tunnel in various excavation footages for these two conditions are compared by numerical calculation, and the reasonable excavation footage of tunnel in V-grade soft rock is also proposed accordingly, aiming to provide relevant reference for the construction and design about similar project.

ENGINEERING BACKGROUND

Qianqi Tunnel locates in Ulanqab City, Inner Mongolia Autonomous region. It is a high-speed railway tunnel with a starting as well as ending mileage of DK32+380 ~ DK36+649. The total length and maximum buried depth about the tunnel are 4,269 m and 141 m, respectively. The total length

of the V- grade rock section about the whole tunnel is 2349 m, occupying 55.03% of the whole length. The plan view and cross-section map of tunnel is shown in Figure 1. The tunnel span and height are 14.96m and 13.14m, respectively. According to the geological data, the entrance as well as the exit section about the tunnel mainly passes through the highly weathered mudstone stratum. Mudstone is in brown grey, brown yellow, strong weathering, argillaceous structure, layered structure, joint fracture development, and the mineral composition is mainly clay minerals.

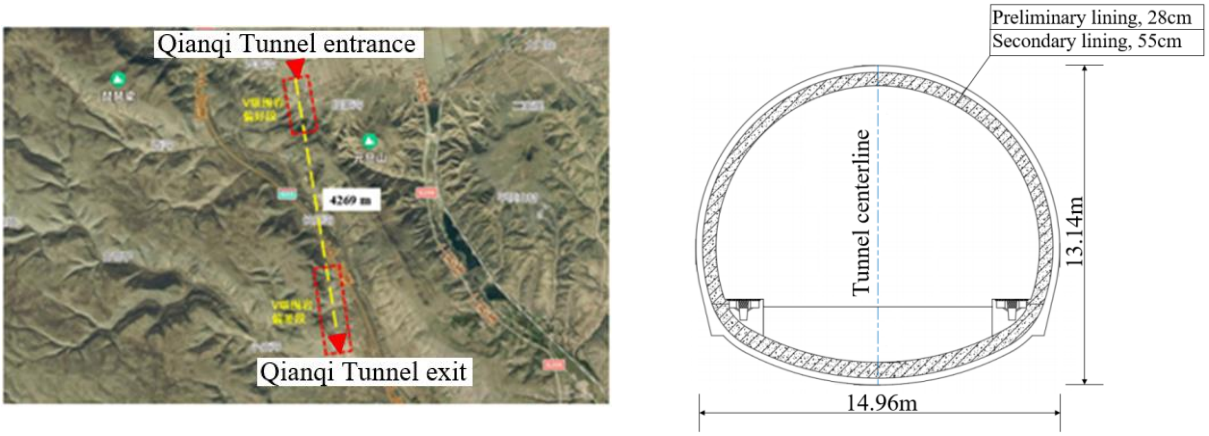

(a) Tunnel plan view *(b) Cross-section map*

Fig. 1 - Plan view and cross-section map of the Qianqi tunnel

NUMERICAL CALCULATION INSTRUCTIONS

Numerical model and calculation parameters

FLAC3D software is used to establish a numerical calculation model for the entrance (competent V-grade surrounding rock section, called condition I) and exit (poor V-grade surrounding rock section, called condition II) of Qianqi tunnel, as shown in Figure 2. As the buried depths of the entrance and exit of tunnel are similar, the buried depth is all taken as 28 m according to the site condition. To reduce the impact about boundary effect, the distance from the tunnel outline to the boundaries is generally taken more than 3 times the tunnel diameters. Therefore, the model size is: length × height × longitudinal length =150 m×110 m×30 m. Normal constraint is set to the front, back, left, right as well as bottom boundaries of the model, and the up boundary is a free surface [25, 26]. The rock and preliminary linings adopt solid element and shell element respectively, obeying Mohr-Coulomb yield criterions and elastic criterion respectively. The calculation parameter about rock as well as the lining is displayed in Table 1. Note that the calculation parameters are all taken from the on-site geological investigation and designed data.

Tab. 1 - Calculation parameter

Name	Density ρ /(kg.m^{-3})	Elastic modulus E /GPa	Poisson's ratio μ	Cohesion c /kPa	Internal friction angle φ/°
Condition I	2200	0.29	0.21	46	31
Condition II	1950	0.15	0.23	29	27
Preliminary lining	2300	34.9	0.2	-	-
Secondary lining	2500	31.5	0.2	-	-

The preliminary lining adopts C25 shotcrete, and the steel arch adopts I22a I-steel. The effect about the steel arch is transformed to the shotcrete by its elastic modulus. The calculation method [27] is as Equation (1):

$$E = E_0 + \frac{S_g E_g}{S_c} \tag{1}$$

Where: ***E*** refers to the elastic modulus about the concrete after conversion; E_0 refers to the elastic modulus about the original concrete; S_g refers to the cross-sectional area about the steel arch; E_g refers to the elastic modulus about the steel; S_c refers to the cross-sectional area about the concrete.

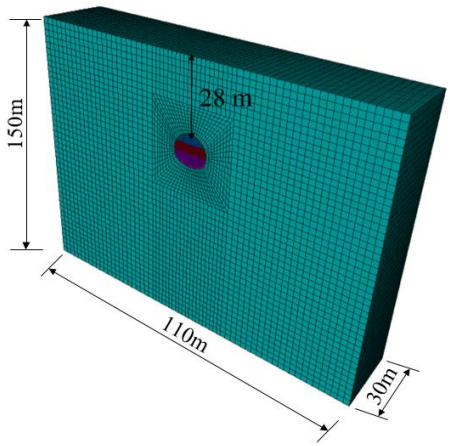

Fig. 2 - Calculation model

Calculation step

The tunnel construction method uses the three-bench excavation method, and the step length is generally 3~5 m ultra-short step. According to the on-site excavation footage (taken as 1.2m), the initial step shown in Figure 3 is excavated first, which is used as the basic model for the excavation footage studied in this paper. This paper mainly analyzes the deformation law as well as the mechanics about surrounding rock and preliminary linings under different excavation footage (1 m, 1.5 m, 2 m, 2.5 m, 3 m, 3.5 m), aiming to obtain the optimal excavation footage.

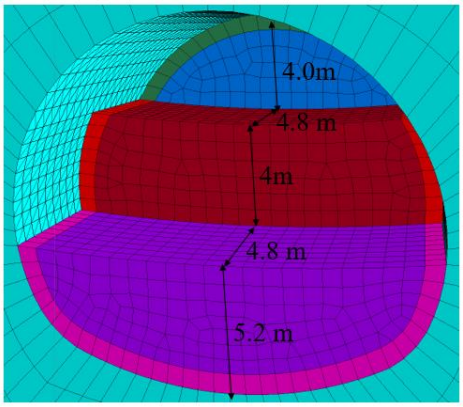

Fig. – 3 Initial step

The main calculation steps are as follows: (1) establish the calculation model; (2) ground

stress balance (only consider the self-weight stress); (3) partial excavation forms initial steps. First, the upper step is excavated at a depth of 1.2m, and the preliminary lining is applied with a lag of one footage. In the cycle of this excavation footage, the upper step is excavated to a depth of 9.6m, and then the middle step is similarly excavated cyclic to a depth of 4.8m, forming the basic model of excavation footage research in this paper; (4) excavate the tunnel according to the planned different footage.

ANALYSIS OF THE CALCULATION RESULTS

Deformation characteristics about the surrounding rock

Settlement characteristics of the vault

Under different excavation footages, the settlement and deformation about the surrounding rock at vault in front of the initial excavation face are shown in Figure 4. The zero of the horizontal coordinate corresponds to the initial excavation face of the upper step of the tunnel (called as the initial excavation face), that is, the longitudinal coordinate y= 9.6m, and the horizontal coordinate increases with the excavation direction of tunnel.

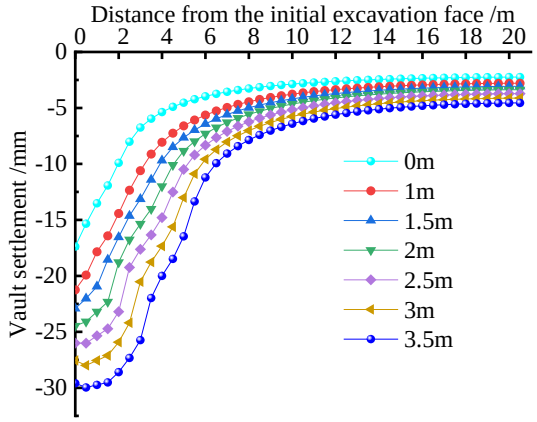

(a) Condition I

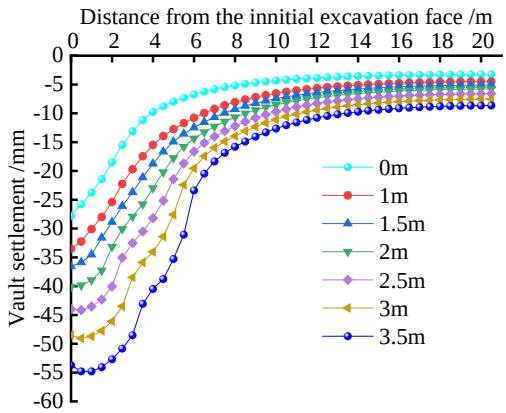

(a) Condition II

Fig. 4 - Distribution rule of the vault settlement under different excavation footages

In Figure 4, under conditions I and II, the law of the vault settlement is basically the same, all indicating that the larger the excavation footages, the larger the growth extent and influence range of settlement, and this law is nearly coincident with the previous literature [28]. Under 3.5m excavation footage, the maximum settlement is 1.95 times and 1.97 times of the initial settlement, respectively. And the larger the excavation footage, the longer the longitudinal range required for the settlement curve to decay to the stable state, that is, the larger the excavation footage, the wider the settlement influence range. Under different excavation footages, the increment of the maximum vault settlement caused by excavation of one cycle footage is relative to the initial step state. The fitting function curve and relation of the maximum increment of vault settlement with the excavation footages is shown in Figure 5. And the function is: y=-3.4478x-17.681 for condition I and y=-1.0538x^2-3.305x-29.197 for condition II.

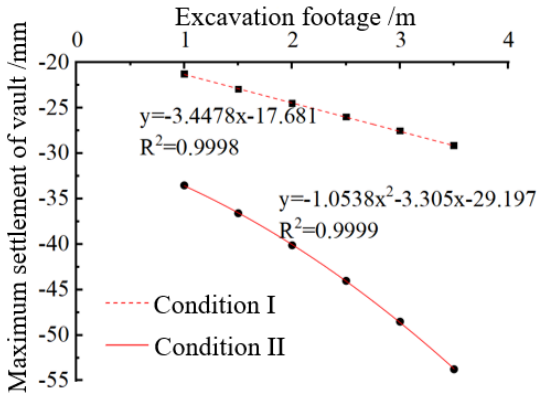

Fig. 5 - Fitting curve between the excavation footages and maximum vault settlement

To study the impact about various excavation footages on the vault settlement of the existing lining of the initial step, the monitoring points at vault in the middle of the vault of the initial step are selected as the investigation section, namely, middle step at y= 2.4m (Point A) and the upper step at y= 7.2m (Point B).

Figure 6 shows the curve of the vault settlement increment led by tunnel excavation in the middle step as well as the up step along with the excavation footages.

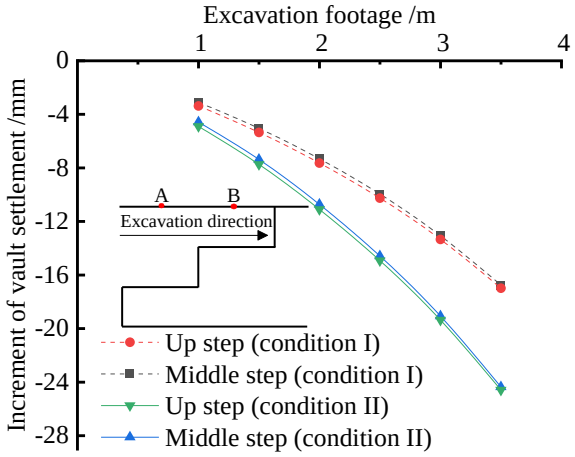

Fig. 6 - Curve diagram of the vault settlement increment and excavation footages at the monitoring points A and B

In Figure 6, under the same surrounding rock condition, the increment curves of the vault settlement of the middle step and the up step almost coincide. Therefore, it can be inferred that the initial settlement about vault above the step led by excavation is basically the same no matter how much the excavation footage is. The settlement increment about the vault of preliminary lining increases nonlinearly with the excavation footages, and the difference of the vault settlement increment in condition II is more obvious than that in condition I.

Horizontal deformation characteristic

The cloud image of horizontal displacement of rock under condition I with the excavation footage of 2 m is displayed in Figure 7. After tunnel excavation, the maximum horizontal deformation

of rock mainly occurs at the side wall of the newly-closed preliminary lining.

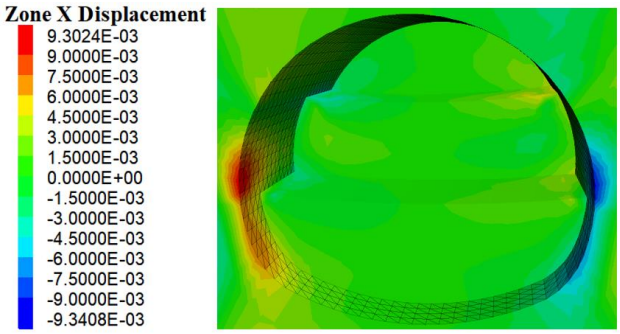

Fig. 7 - Horizontal displacement cloud nephogram of the surrounding rock in condition I /m

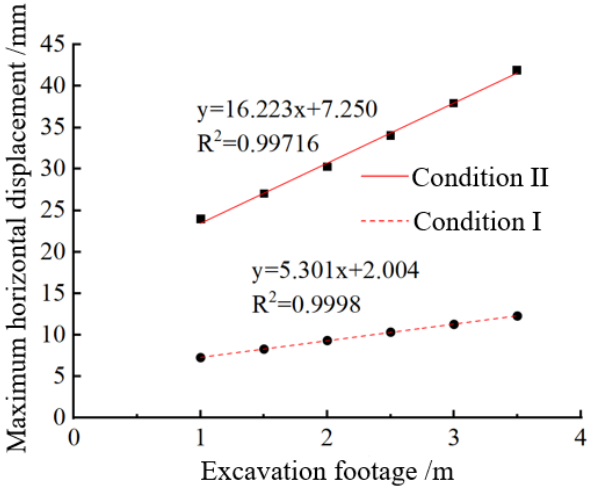

Fig. – 8 Fitting function curves of the maximum horizontal displacement and excavation footages in the excavated section

The fitting function curve of the largest horizontal displacements and excavation footages is displayed in Figure 8. There are good linear relationships between the largest horizontal displacements and excavation footages under the conditions I and II, and the specific fitting function relationship is as follows: y=5.301x+2.004 for condition I and y=-16.223x+7.250 for condition II.

The slope of the curve of condition II is much higher than that of the condition I. Therefore, the greater the excavation footages, the greater the maximum horizontal displacements about condition II. For the poor rock condition, the monitoring about the side wall of the newly-closed preliminary lining in each excavation cycle should be strengthened after construction.

Surface settlement law

The surface settlement curve of the section at longitudinal distance y= 9.6m under different excavation footages of conditions I and II is displayed in Figure 9. The influencing ranges about the settlement are nearly 60 m, and the largest settlement appears at the center line of tunnel. Under the adopted excavation footages ranging from 1 m to 3.5 m, the maximum surface settlement about the condition II is 2.02, 2.08, 2.16, 2.25, 2.35 and 2.47 times that of condition I, respectively. Similar to the spatial distribution of the vault settlement in front of the initial excavation face, that is, the larger the excavation footages, the larger the surface settlements as well as the growth rate.

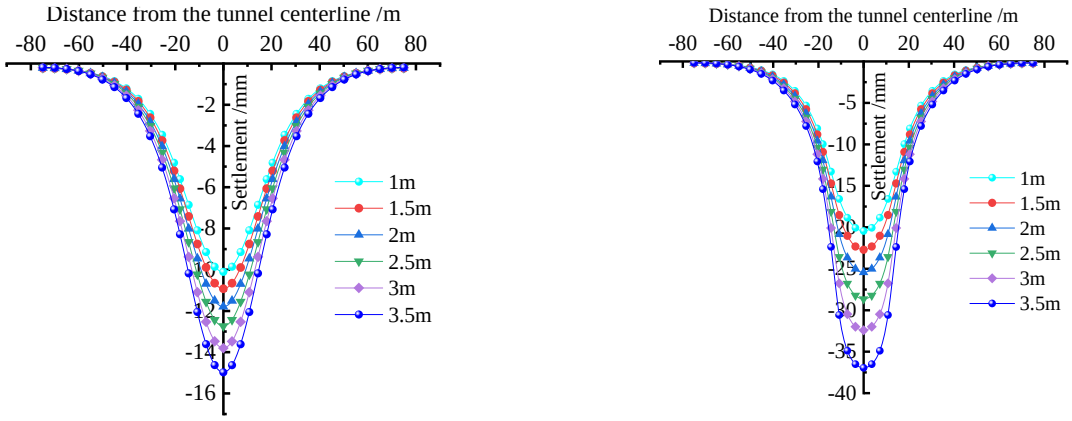

(a) Condition I (b) Condition II

Fig. 9 - Surface settlement curve under different excavation footages

Deformation characteristics of the excavation face

Figure 10 shows the on-site extrusion deformation phenomenon of the excavation face of tunnel. After exploration and analysis, the main reason is that groundwater develops in the rock in front of the excavation faces. Furthermore, highly weathered mudstone is a kind of rock that is more sensitive to water and is prone to strength softening and disintegration after encountering water, thus losing its bearing capacity.

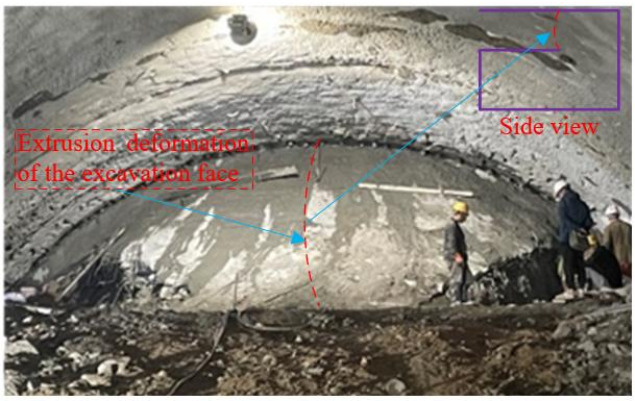

Fig. 10 - The on-site extrusion deformation phenomenon of the excavation face of tunnel

The fitting curves about the largest extrusion deformation of the up-step excavation faces and excavation footages under different rock conditions is displayed in Figure 11. Under these two surrounding rock conditions, the fitting function relationship between the maximum extrusion deformation of excavation face and excavation footages is as follows: $y=3.0857x^2-7.68x+51.309$ for condition I and $y=0.7143x^2-1.4886x+19.646$ for condition II.

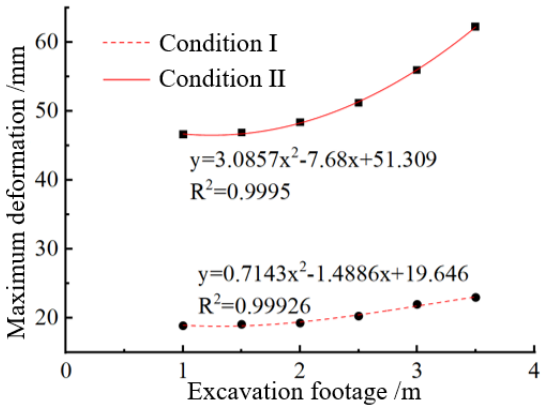

Fig. 11 - The function fitting relationship between the largest deformation about the excavation face and excavation footages

In Figure 11, under conditions I and II, the largest extrusion deformation about the excavation face and excavation footage show a significant quadratic function relationship. The maximum deformation about the excavation faces in condition II is much greater than that under condition I, so the strength of surrounding rock greatly influences the extrusion deformation characteristic of excavation face, and the maximum extrusion deformation increases nonlinearly with the excavation footages. Under condition I, the maximum extrusion deformations about the excavation faces increase little with the excavation footages. While under condition II, the maximum extrusion deformation increases slowly when the excavation footage is 1~2 m, and then the continuous increase of the footages will lead to a rapid increase of the extrusion deformation.

Mechanical characteristic analysis

Mechanical characteristic of the preliminary lining

The positions on the tunnel vault and both sides of the middle and upper steps are selected as the monitoring points, and the bending moment diagram of the preliminary lining at the longitudinal depth of 4 m under various excavation footages is also drawn, as shown in Figure 12.

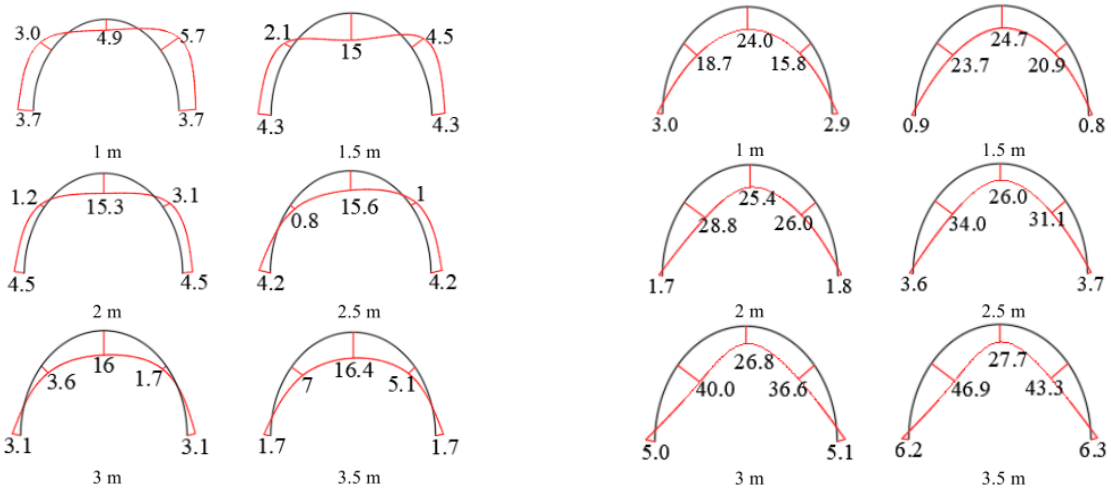

(a) Condition I (b) Condition II

Fig. 12 - Distribution of the bending moment of the preliminary lining under different excavation

footages /(KN.m)

Under condition I, the maximum bending moment generally appears at the vault of lining. The bending moment value about vault increases slowly when the excavation footage is more than 1.5m, the force state of the arch shoulder is gradually changed from the outer tensioned state to the inner tensioned state, and the inner tension range of the lining structure is gradually enlarged. Under condition II, the maximum bending moment is no longer located at the vault with the increase of excavation footages, but gradually shifts from the vault to arch shoulders. Bending moment at the arch shoulder increases more rapidly, while the bending moment at the vault increases slowly.

Mechanical characteristic of the surrounding rock

Figure 13 shows the distribution curves of the maximum principal stress (MPS) of surrounding rock at the vault as well as side wall about tunnel under different excavation footages in conditions I and II.

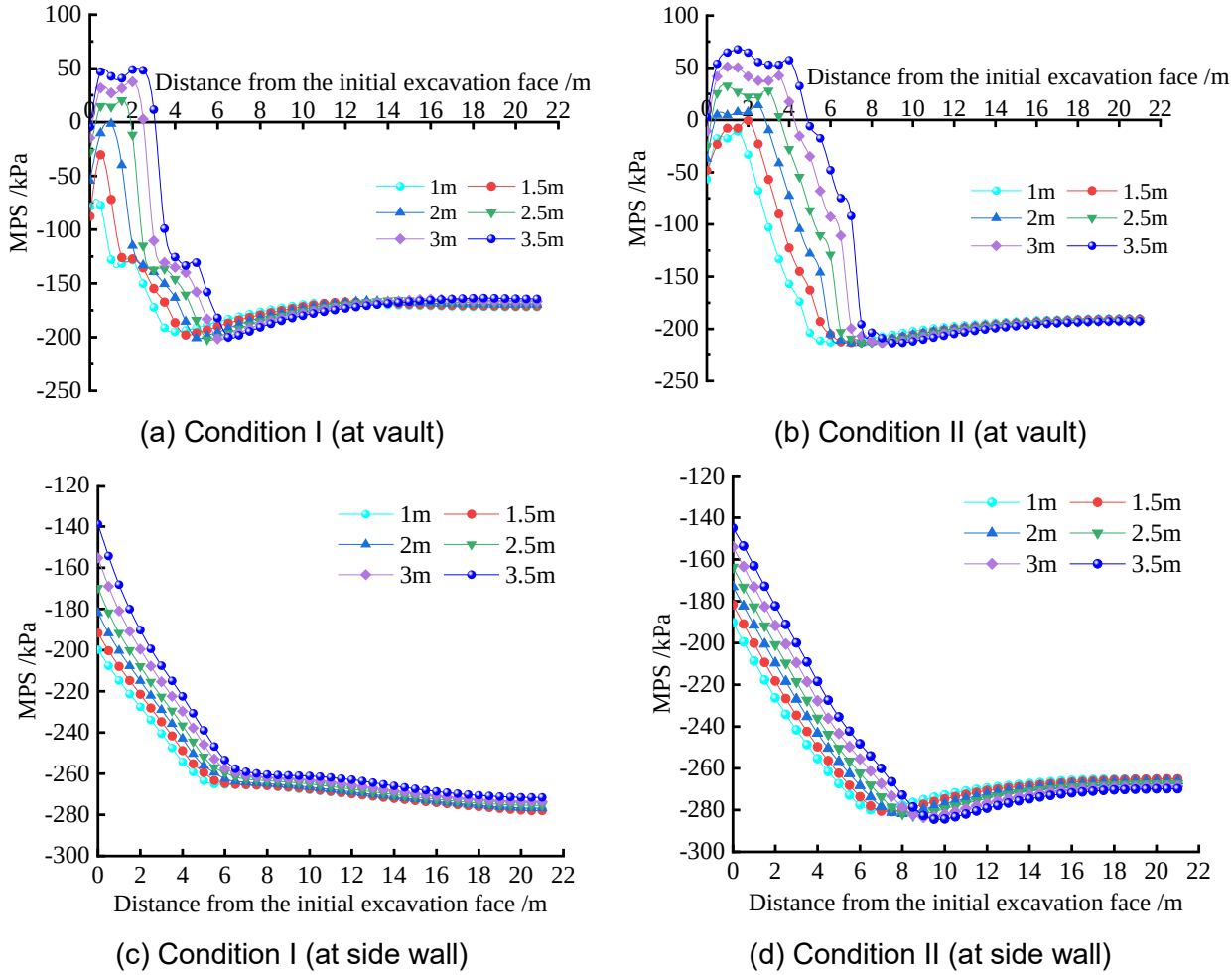

(a) Condition I (at vault)

(b) Condition II (at vault)

(c) Condition I (at side wall)

(d) Condition II (at side wall)

Fig. 13 - Mechanical characteristic curves of the surrounding rock under different excavation footages

In Figure 13, for both conditions I and II, the MPS curves show the law of first rapidly increasing, then rapidly decreasing, and finally stabilizing, and the rapid changes mainly occur near the excavation area. Under condition I, when the excavation footage is 1 m and 1.5 m, the peak MPS

of the surrounding rock is compressive stress. When the excavation footage reaches 2 m, the peak MPS of the vault of tunnel will be manifested as tensile stress, the main tensile stress and the action range of the vault gradually increases with the excavation footages. For the side wall, all of them are compressive stress, and the MPS is the minimum when the distances from the initial excavation face are zero. With the increase of distance from the initial excavation face, the MPS increases rapidly and then becomes stable. In general, under conditions I and II, it is still safer for the rock at the side wall of tunnel even if the excavation footage is larger.

According to Figure 13, the peak MPS corresponding to different excavation footages is extracted, and the fitting function curve between the peak MPS and excavation footages is drawn, as shown in Figure 14. The specific fitting relationship is as follows: $y=-3.0723x^3+23.884x^2-24.53x-7.3673$ for condition I and $y=5.0898x^3-50.345x^2+191.79x-223.41$ for condition II.

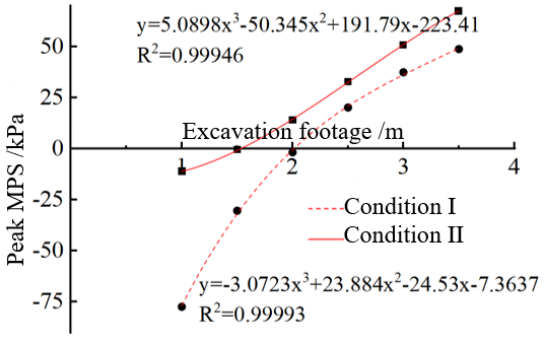

Fig. 14 - Fitting function curve of the peak MPS of the vault and excavation footages

Under condition I, for the excavation footages are more than 2 m, the tensile stress appears in the vault of surrounding rock. Under condition II, tensile stress occurs when the excavation footages are greater than 1.5m. In geotechnical engineering, it is generally believed that soil cannot withstand tensile stress, so the excavation footage under condition I should be less than 2 m, and the excavation footage under condition II should be less than 1.5 m. In order to ensure that no tensile stress occurs in the tunnel vault after excavation, the safety factor of 1.2 is adopted in this paper. Therefore, it is suggested that the excavation footage of the relied tunnel project of this paper should be 1.8m (for condition I) and 1.2m (for condition II).

CONCLUSION

(1) The deformation about V-grade surrounding rock is largely influenced by the excavation footages. The vault settlement and horizontal displacement of the tunnel as well as the surface settlement increase significantly with the excavation footages. Moreover, excavation in poor surrounding rock will not only lead to the increase of deformation, but also lead to the increase of the influence range of vault settlement.

(2) Under the competent or poor rock conditions, the maximum vault settlement in front of the initial excavation face, the maximum extrusion deformations about the excavation faces and excavation footages mainly show a positive correlation of quadratic function or linear relationship. The parameters of surrounding rock greatly influence the deformation about excavation face. For the lined steps behind the initial excavation face, the horizontal deformation of surrounding rock has

linear positive correlations with the excavation footages. Under the same surrounding rock condition, the vault settlement increment led by one excavation round is basically the same.

(3) For the competent surrounding rock, the maximum bending moments about preliminary lining at the middle step after excavation occurs in the vault, and the increase rate decreases when the excavation footage is more than 1.5m. For the poor rock condition, the maximum bending moment is transferred from the vault to the arch waist with the increase of excavation footages, and it is basically manifested as the inner tension of the lining. It is suggested that the optimal excavation footages about the relied tunnel project are 1.8m for the competent rock condition and 1.2m for the poor rock condition.

It should be noted that the comparison of the excavation methods and the influence of lining stiffness on tunnel in such soft rock are not considered in this paper, which can be further studied in the future.

COMPETING INTERESTS

The authors have no relevant financial or non-financial interests to disclose.

DATA AVAILABILITY

All data, models, and code used or used during the study appear in the submitted article.

REFERENCES

[1] Liu, J.G., Zhou, X.J., Xiao, Q.H., et al, 2017. Fault-related instability problems of tunnels - the host rock slip criterion and characteristics of the tunneling-induced shear displacements. Stavební Obzor - Civil Engineering Journal, Vol. 26, 441-458. https://doi.org/10.14311/CEJ.2017.04.0036

[2] Hou, F.J., Luo, Y.B., Jiang, Q., et al, 2020. Analysis on construction deformation and supporting structure of two-step and three section excavation method for super larger span highway tunnel. Stavební Obzor - Civil Engineering Journal, Vol.29, 110-123. https://doi.org/10.14311/CEJ.2020.01.0010

[3] Zhao, J.P., Tan, Z.S., Wang, X.Y., et al, 2022. Engineering characteristics of water-bearing weakly cemented sandstone and dewatering technology in tunnel excavation. Tunnelling and Underground Space Technology, Vol.121, 104316. https://doi.org/10.1016/j.tust.2021.104316

[4] Zhao, J.P., Tan, Z.S., Yu, R.S., et al, 2023. Mechanical responses of a shallow-buried super-large-section tunnel in weak surrounding rock: A case study in Guizhou. Tunnelling and Underground Space Technology, 131, 104850. https://doi.org/10.1016/j.tust.2022.104850

[5] Huang, J.Y., 2012. Parameters analysis and application of bench method for high-speed railway tunnels. Modern Tunnelling Technology, Vol.49, 77-82. https://doi.org/10.13807/j.cnki.mtt.2012.03.013

[6] Guan, B.S., 2016. Tunneling by mining method: lecture IX: methods for tunnel excavation and support. Tunnel Construction, Vol.36, 771-781. https://doi.org/10.3973/j.issn.1672-741X. 2016.07.001

[7] Wang, M.S., 2010. Tunnelling and underground engineering technology in China. China Communications Press, Beijing.

[8] Chen, L.B., 2008. Application of three bench method in reinforcing weak surrounding rock of railway mountain tunnel of passenger dedicated line. Journal of Railway Engineering Society, Vol. 25, 72-74.

[9] Sun, S.F., 2012. Construction technique for the Gujiping tunnel portal section in shallow-buried loess.

Modern Tunnelling Technology, Vol.49, 83-88. https://doi.org/10.13807/j.cnki.mtt.2012.04.017

[10] Liu, C., Peng, L.M., Lei, M.F., et al, 2019. Applicability & mechanical characteristics of shallow buried soft red clay tunnel under 3-step benching tunneling method with large arch feet. Journal of Railway Science and Engineering, Vol. 16, 2006-2017. https://doi.org/10.19713/j.cnki.43-1423/u.2019.08.018

[11] Zhang, X.L., 2012. Key factors affecting bench construction of a tunnel in soft rock. Modern Tunnelling Technology, Vol. 49, 60-62. https://doi.org/10.13807/j.cnki.mtt.2012.04.013

[12] Wang, Z.D., Gong, X.N., 2010. Calculation method of digging length in underpass with underground excavation under shallow cover. Rock and Soil Mechanics, Vol. 31, 2637-2642. https://doi.org/10.16285/j.rsm.2010.08.018

[13] Peng, X.J., Zhang, D.B., Yin, H.D., et al, 2022. Optimization of excavation footage of three-step method of shallow tunnels based on element safety coefficient method. Science Technology and Engineering, Vol. 22, 13973-13979.

[14] Li, H., Tian, X.X., Song, Z.P., et al, 2018. Study on calculation method of digging length for shallow tunnel based on Xie Jiajie's surrounding rock pressure formula. Journal of Xi'an University of Architecture and Technology, Vol. 50, 662-667. https://doi.org/10.15986/j.1006-7930.2018.05.007

[15] Jia, X.X., Zhao, Y.C., 2016. Analysis of mechanical behavior of tunneling in weak surrounding rock by CD method and benching method. Railway Standard Design, Vol. 60, 121-125. https://doi.org/10.13238/j.issn.1004-2954.2016.07.028

[16] An, Y.L., Ouyang, P.B., Yue, J., et al, 2019. Influence of excavation footage on shallow tunnel face stability and deformation and mechanics. Journal of Disaster Prevention and Mitigation Engineering, Vol. 39, 787-794. https://doi.org/10.13409/j.cnki.jdpme.2019.05.012

[17] Lu, X.G., Geng, J.Y., Pang, L., et al, 2022. Analysis of construction mechanical behavior and parameter optimization for subsequent tunnel tube of double-arch tunnel without middle drift. Modern Tunnelling Technology, Vol. 59, 80-90. https://doi.org/10.13807/j.cnki.mtt.2022.05.011

[18] Zhang, J.R., Wang, Z.Y., Feng, J.M., et al, 2021. Deformation control for large-section tunnel construction in fractured carbonaceous slate. Proceedings of the Institution of Civil Engineers: Geotechnical Engineering, Vol. 176, 132-145. https://doi.org/10.1680/jgeen.20.00212

[19] Zheng, C.C., He, P., Wang, G., et al, 2023. Simulation of bench stepping and optimization of bolt parameters based on multiple geological information fusion. Journal of Building Engineering, 79, 107941. https://doi.org/10.1016/j.jobe.2023.107941

[20] He, J.X., He, S.H., Liu, X.B., et al, 2023. Investigating the mechanical responses and construction optimization for shallow super-large span tunnels in weathered tuff stratum based on field monitoring and Flac3D modeling. International Journal of Civil Engineering, online. https://doi.org/10.1007/s40999-023-00891-9

[21] Zhou, Z.L., Zhao, J.P., Tan, Z.S., et al, 2021. Mechanical responses in the construction process of super-large cross-section tunnel: A case study of Gongbei tunnel. Tunnelling and Underground Space Technology, Vol. 115, 104044. https://doi.org/10.1016/j.tust.2021.104044

[22] Li, P.F., Zhao, Y., Zhou, X.J., 2016. Displacement characteristics of high-speed railway tunnel construction in loess ground by using multi-step excavation method. Tunnelling and Underground Space Technology, Vol. 51, 41-55. https://doi.org/10.1016/j.tust.2015.10.009

[23] Chen, Z.Y., Wang, Z.X., Su, G.S., et al, 2022. Construction technology of micro bench cut method for weak rock tunnel with high in-situ stress. Geotechnical and Geological Engineering, Vol. 40, 1407-1415. https://doi.org/10.1007/s10706-021-01971-0

[24] Shi, Y.Z., 2016. Evolution of ground settlement and support system behavior during benching excavation of a tunnel with super large cross section: A field monitoring case study. Electronic Journal of Geotechnical Engineering, Vol. 21, 4779-4798.

[25] Qiu, J.L., Fan, F.F., Zhang, C.P., et al, 2022. Response mechanism of metro tunnel structure under local collapse in loess strata. Environmental Earth Sciences, Vol. 81, 164. https://doi.org/10.1007/s12665-022-10256-5

[26] Zhang, H.J., Liu, G.N., Liu, W.X., et al, 2023. Analysis on the influence of dismantling temporary lining of closely-undercrossing subway. Geotechnical and Geological Engineering, Vol. 41, 3189-3202. https://doi.org/10.1007/s10706-023-02452-2

[27] Wu, B., Gao, B., Suo, X.M., et al, 2005. Mechanical simulation and analysis of construction behavior of urban metro tunnelling with small interval. China Journal of Highway and Transport, Vol. 18, 84-89. https://doi.org/10.19721/j.cnki.1001-7372.2005.03.019

[28] Yan, D.M., He, P., Chen, Z., et al, 2016. Research on excavation footage of tunnels in IV rock with two-bench construction method. Railway Standard Design, Vol. 60, 99-103. https://doi.org/10.13238/j.issn.1004-2954.2016.09.022

CIVIL ENGINEERING JOURNAL

Article no. 38

THE CIVIL ENGINEERING JOURNAL 4-2023

TESTING OF CLOSE-RANGE PHOTOGRAMMETRY AND LASER SCANNING FOR EASY DOCUMENTATION OF HISTORICAL OBJECTS AND BUILDINGS PARTS

Almedina Rapuca and Eva Matoušková

Czech Technical University in Prague, Faculty of Civil Engineering, Department of Geomatics, 16629 Prague 6, Thakurova 7, Czech Republic; almedinarapuca@gmail.com, eva.matouskova@fsv.cvut.cz

ABSTRACT

In contemporary times, technology has dramatically simplified the process of documenting cultural heritage objects. This paper aims to illustrate modern methodologies for documenting historical monuments by applying advanced technologies, as these case studies show. Two technologies were used: laser scanning and digital photogrammetry. The first subject of our study was a historically significant 16th-century building located in Jachymov, situated in the North-West region of the Czech Republic. The object was documented by laser scanning (BLK360) and using a standard digital camera Canon Powershot SX230 HS. The laser scanning data were post-processed using Cyclone Register 360 Plus, while photogrammetric point clouds were generated with Agisoft Metashape. The second object was building and sculpture in the historical UNESCO city of Telč. For this object laser scanning instruments, digital photogrammetry and a new low-cost ViDoc documentation system was used. Our study is focused on analyzing sets of point clouds obtained from the data processing, conducted using CloudCompare to draw insights and conclusions. It turns out that the rapid development of techniques and technology makes it possible to use low-cost devices for sufficiently accurate and fast documentation; however, the mentioned ViDOC device can only be used for very close and small objects up to about 5 meters. For the documentation of sculptures, classic close-range photogrammetry is especially appropriate; for the documentation of buildings, laser scanners are suitable; the problem lies in hidden spaces and it is often necessary to use either a platform or a combination with photogrammetry using a drone, especially for upper parts of the object.

KEYWORDS

Photogrammetry, Laser scanning, Cultural heritage, Object documentation, ViDOC

INTRODUCTION

Half a century ago, construction documentation relied mainly on geodetic methods, limited to the tape measure. Data collection was minimal, with most existing data presented in paper format. Nowadays, the concept of the digital twin has become a global phenomenon, marked by remarkable advances [1, 2].

Over the past decade, laser scanning, and photogrammetry have been the primary tool for 3D data collection of complex heritage objects. The need of documenting cultural heritage

objects is substantial and arises for various purposes. The need of accurate, fast and comprehensive documentation, especially of historic buildings, is demanded by today's world. Objects are often subject to destruction due to social neglect, wars, vandalism, natural phenomena, or rapid urban development. The documentation methods have evolved progressively through classical geodetic methods to today's laser scanning and automated methods of close-range photogrammetry in the form of structure from motion (SfM) and Multi View Stereo (MVS). Mobile laser scanning is developing very rapidly, especially in heritage care as mobile personal laser scanning [3-5].

The primary goal of these measurements is to accurately depict the object in a three-dimensional context. The resulting data performs several essential roles, initially focused on the object's representation, then expanding to encompass the assessment and detection of potential damage. Furthermore, those measurements prove valuable in the analysis and strategic planning of maintenance and preservation efforts for these culturally significant objects. In recent years, the use of mobile handheld laser scanners has become significant. Their advantage is fast and three-dimensional documentation of objects of interest. Similarly, drone imagery combined with terrestrial imagery has been used extensively in the last decade. Nowadays, the logical output of documentation of historic buildings is export to heritage building information modeling (HBIM), which enables a comprehensive description of the object and its management [6-9]. The following work aims to demonstrate the easy to use three-dimensional visualization of a historical cultural object through measurements from a laser scanner and a digital camera.

METHODS

Instruments

For measurements and point cloud generation, different instruments were chosen. In the first case study, a scanner Leica BLK360 and a common digital camera Canon PowerShot SX230HS were used [10, 11].

Fig. 1 – Laser scanner BLK360 (left) and Canon PowerShot SX230 HS (right)

The second case study used a BLK360 scanner, a Canon 450 camera and a new low-cost ViDoc device from Pix4D. The project was complemented by the analysis of older measurements of the same object with a Surphaser 25 HS laser scanner and a Pentax 645 camera.

Fig. 2 – ViDOC (left), Pentax 645 and laser scanner Surphaser 25 HS (right)

ViDoc is a simple device that includes ViDoc RTK rover device, phone case (for iPad Pro or iPhone 12 Pro and higher with lidar sensor) and GNSS antenna.

Leica BLK360 is a compact laser scanner. It is small and light (around 1kg) easy to transport and use only for one person in site. The scanner is equipped with a camera for point cloud coloring and a thermal sensor; it accomplishes a comprehensive 360-degree panoramic image capture and finishes a full-dome scan in less than 30 seconds (with smallest resolution without images) till 6 minutes (full resolution with HDR images), where the vertical field of view is 300˚ and the horizontal field of view is 360˚ [10]. Based on testing and technical parameters, the accuracy of a measured spatial point is 4mm on 10m distance. The BLK360 includes an app called BLK Live, allowing us to control the laser scanner's images and quickly assess the on-site data for feedback, quality assurance, and quality control using a tablet. After measurements, the Leica Cyclone REGISTER 360 software helps with quickly setting up and organizing the collected data in the field. Canon PowerShot SX230 HS is a common low-cost compact digital camera that was used to capture photos of the buildings inside. It is equipped with a 12.1-megapixel CMOS sensor, 14x optical zoom lens (from 5mm to 70mm), allowing you to capture distant subjects with remarkable clarity and precision. Additionally, it incorporates built-in GPS functionality, enabling geotagging and location tracking for photos [11]. An older Surphaser 25 HS laser scanner was used to document the sculptures in 2018. It is one of the most accurate scanners with an accuracy of 0.6 mm at 10 meters, which is exceptional and very suitable especially for sculptures [12]. The scanner does not have a camera, but the declared accuracy is excellent; other laser scanners are not very suitable for documenting sculptures, as they have worse accuracy and the sculptures do not have proper detail. This is already lost at an accuracy of a few millimetres. Therefore, nowadays it is better to use photogrammetry, which gives an accuracy of up to 0.1 millimetres without any problems if done correctly, and the camera is several orders of magnitude cheaper than a laser scanner. In 2018, a professional 51Mpix Pentax 645 camera was used to document the sculpture for comparison with the laser scanner (Figures 1 and 2), [13].

Case study

In terms of simple methods of documentation of historical elements and objects, two case studies were carried out. Both of them show the easy and quick possibilities of 3D documentation especially for endangered heritage objects.

Documentation of historical parts inside the object

The first case study is the documentation of building element in historic house where it was not clear if it would be saved for the future. This house and its parts is located in the town of Jáchymov, northwest part of the Czech Republic near the Germany border; the town was founded

in 1516 after the discovery of rich silver deposits. After silver and later tin were down mined in the area, the area rapidly declined, and the mines were no longer profitable. Marie-Curie Sklodowska discovered radium in the Jáchymov ore. This led to the reincarnation of the town with radon baths establishment. However, a major turning point came after the expulsion of the German population after 1945 following the end of World War II [14]. A population that had no relation to traditions and landscape slowly moved into the entire border area. Added to this was the decade-long exploitation of local uranium deposits by the former Soviet Union for strategic reasons and the labour camps for political prisoners following the communist takeover after 1948.

Fig.3 – Inside the house No.12, Jáchymov, year 2021. Gothic ribbed circular vault.

Many historic buildings have not been maintained for a long time. The landscape, population and employment opportunities have changed fundamentally, and these changes are still visible. The house no. 12 on the Republic Square in Jáchymov dates mostly from the turn of the Gothic and Renaissance periods. It was originally a noble house of a rich owner. The original parts of the structure from the time of the building's construction have been preserved (the cross vaults on the ground floor, the staircase to the first floor with a stone handrail and, in particular, the beautiful ribbed circular vault in the upper hall). Some details of the interior, the historic plasterwork on the first floor and the second-floor hall, and the exterior are also of considerable historical value. The entrance portal and the Renaissance lining of the window openings are original. The building was in a poor but habitable condition in the 1980s, but the rear wing and the support buildings behind the house were already in a state of desolation. Poorly executed anti-radon protection was also a factor, and the building degraded rapidly in the post-revolutionary period (after 1989). The great boom in property purchases during the Covid 19 pandemic caused a change of owner who decided to save the building. The pandemic and the high cost of construction work and materials in the post-Covid era delayed the work. Today, however, the building is in use again and has been well restored thanks to the efforts of the new owner (Figures 3 and 4).

Fig.4 – The house No. 12 in Jáchymov before (left) and after reconstruction (right) in 2023.

Documentation of a sculpture and facade of a historical building

The second part of the work was focused on the possibilities of low-cost documentation of monuments in the town of Telč. This historical town center has been a UNESCO World Heritage Site since 1992 [15]. The aim of the research was to compare data from the BLK360 laser scanner and the new low-cost ViDoc device. The first part was focused on the comparison of scanning time and accuracy in terms of the smaller historical house documentation on the square in Telč. The house No. 61 on Zachariáš of Hradec Square was selected; it is a single-story house with an archway. The originally late Gothic house was preserved during the Renaissance renovation. Further changes took place before the mid-16th century (under the ownership of the baker Michael). The reconstruction is dated on the sgraffito of the facade L.P. 1555. The imposing Renaissance façade with a Venetian-type gable with pilasters and cornices dominates the square. The façade is decorated with sgraffito with vegetative motifs[1].

Fig.5 – Two selected historical objects on Zachariáš of Hradec Square in Telč city

[1] https://pamatkovykatalog.cz/mestansky-dum-700198

Possibilities of sculpture documenting was also part of the research. There are several suitable objects in the Telč square, a fountain and the Baroque Marian Column, a plague column built in 1716-1720. In the past, we have already performed measurements (2015) with very high precision Surphaser 25HS scanner and photogrammetrically with a professional Pentax 645D 51MPix camera. The measurements are highly accurate but time consuming, including the data processing.

MEASUREMENTS AND PROCESSING

Gothic ribbed circular vault inside the house No.12, Jáchymov

The first measurements were done by laser scanner. 7 scans of the building interior buildings were done (Figure 6). After that, the measurement data can be transferred with Wi-Fi and open in software Leica Cyclone REGISTER 360.

The next step after data import was the registration. This step involves aligning and merging multiple scan positions to create a unified point cloud dataset. This can be done automatically, where the program will match points in different scans, where the user can edit one by one. Following this, quality control can be performed, checking for alignment errors, outliers, and other issues to ensure the data's accuracy. After removing any unnecessary parts from the point cloud, we can visualize the 3D scan using various software tools. Through these processing steps, we achieved a successful result: 16 lines with a 50% overlap and an overall Bundle Error of 0.004 meters. The measurement takes 40 minutes, the semi-automatic data processing takes 30 minutes on a common HP workstation (processor I-7, 32 GB RAM) to a colored joined point cloud. Together 30 million spatial object points were saved.

Fig. 6 – View of all merging scans in SiteMap

The second measurement was done by a digital camera Canon PowerShot SX230 HS. 238 images were taken with shortest focal length 5mm, Shuter 1/300, F-stop F/3.1 and resolution 4000x3000. Agisoft Metashape software was used based on Structure-from-Motion (SfM) and MVS (Muti View Stereo) technology. This software is used in many different fields of application [8-11]. The following processing images workflow was used (Figure 7):

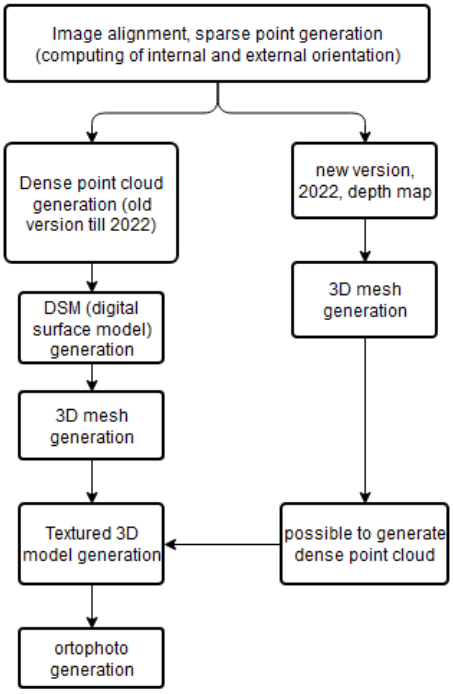

Fig. 7 – Agisoft Metashape flow-chart

The relative orientation was done by the “Align Photo” function in Agisoft Metashape software, where 283 from 238 images were co-registered. In this process, the program finds corresponding tie points between images. Using these points, it figures out how the images are positioned and rotated in relation to each other (internal and external parameters were calculated). The root-mean-square (RMS) reprojection error of relative orientation tie points was 1.37 pixels. Optimize Cameras function to refine relative orientation was used. After these steps, the software calculated the camera's internal settings through a self-calibration process. After that, the Dense Point Cloud was generated with High Quality parameter. After this, the triangle network known as the Mesh was calculated (Figure 8).

Fig. 8 – Point Cloud (left) and Mesh (Right)

At the end the Tiled Model or Textured 3D was generated with high quality. Build Texture allows adding the photos taken to the shape of the pre-created 3D Mesh object (Figure 9).

Fig. 9 – Textured 3D model of the object

Comparison of two-point clouds

The purpose of this step is to compare two measurement methods with different techniques. To do this, we took the point cloud data from Leica BLK360 as our reference point and compared it to the point cloud data derived from the digital camera. CloudCompare software was used to make this side-by-side comparison.

To initiate the process, we acquire two sets of point clouds, each originating from different data capture instruments. Following this data acquisition, the critical step of aligning these two-point clouds ensues. It's essential to note that the laser scanner data consistently serves as the reference dataset, while the data from the camera is adjusted to align with this reference. Once reference points in both datasets are identified, the orientation process can continue. Subsequently, a comprehensive analysis between these two datasets is undertaken, employing the "Cloud-to-Cloud" method. This method enables a detailed comparison of point clouds. As a result of this analysis, the outcome is comparison image generation, which provides insights and visual representation of the alignment and comparison between these two sets of data (Figure 10).

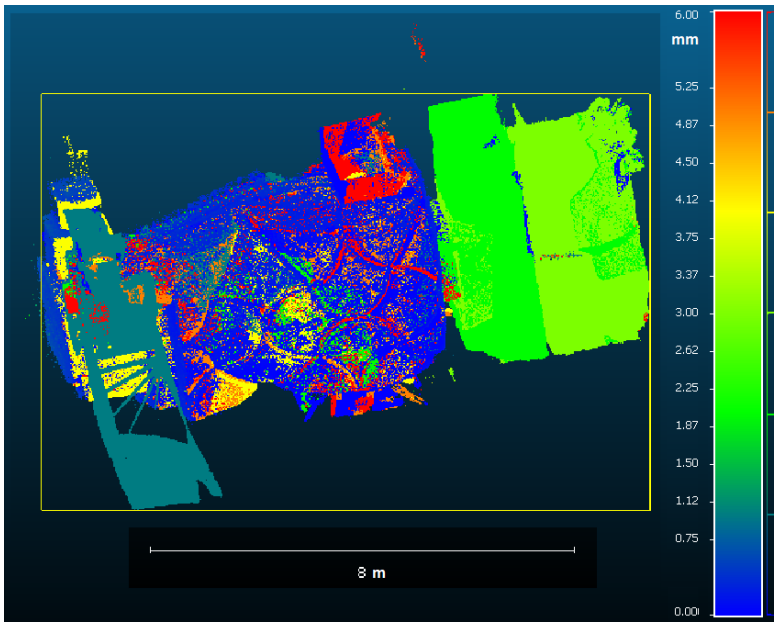

Fig. 10 – Comparison of point cloud from digital camera Canon PowerShot SX230 HS and Leica BLK360 laser scan

The default way to compute distances between two-point cloud is the 'nearest neighbor distance' for each point of the compared cloud, CloudCompare searches the nearest point in the reference cloud and computes their (Euclidean) distance. If the reference point cloud is dense enough, approximating the distance from the compared cloud to the underlying surface represented by the reference cloud is acceptable [16].

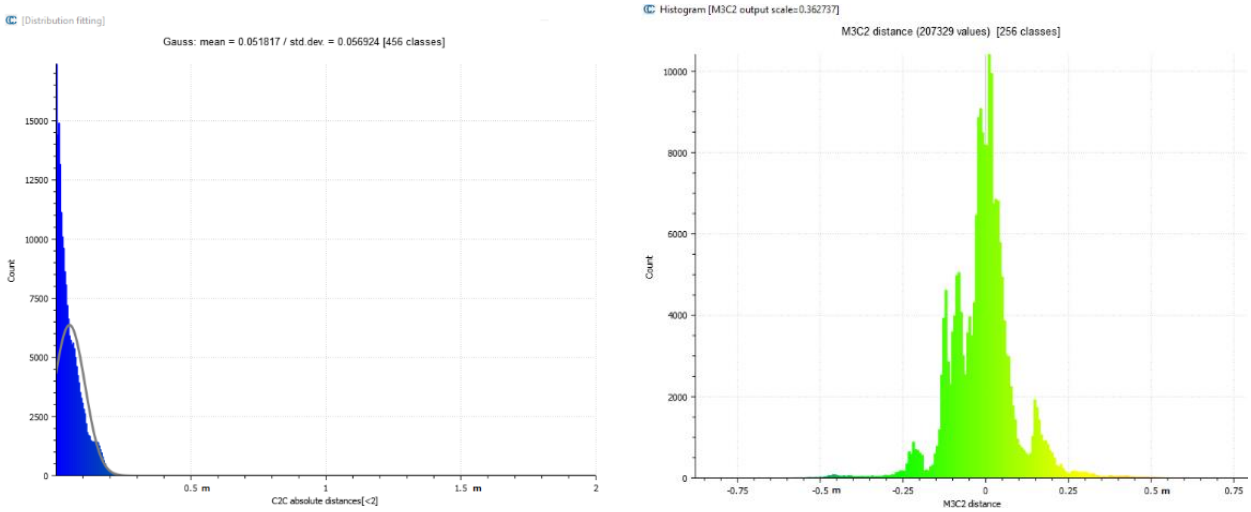

Fig. 11 – C2C absolute distance

To increase the accuracy of the product, it would be useful to have a control point and measurement with geodetic instruments. Unfortunately, this was not done in this project. For this

reason, we relied on CloudCompare for the comparative analysis of metrics between two sets of point clouds. It is essential to note that measurements obtained through the BLK360 laser scanner proved significantly more accurate compared to those obtained with the Canon digital camera, therefore we used like the reference the point cloud of the laser scanner (Figure 10-11).

Tab. 1 – Measurement analysis

Instrument	Measurement time (minutes, hours)	Processing time (hours)	Price (kEuro)	Precision (mm)	Range (m)
Canon PowerShot SX230 HS	30 minutes	1	0.5	3	10
BLK360	60 minutes	1	30	4	30

For smaller and indoor objects, the time and accuracy are comparable in terms of laser scanning or photogrammetry. From a photogrammetric point of view, the lighting plays a role and must be of good quality to obtain images; however, it is also possible to take pictures with a flash. In terms of price, a laser scanner is logically several orders of magnitude more expensive (Table 1).

Objects on the historical Telč square

Fig. 12 – The 3D model created from ViDOC (left) and using the BLK360 laser scanner (right)

The differences in documentation of historic house occured due to range of devices. The BLK360 laser scanner has a range of 30 meters, and the photogrammetric measurement has a practically similar range. The difference is mainly in the use of ViDOC equipment, which has a realistic range of just over 5 meters and is not well suited for buildings. However, low objects and sculptures can be documented very easily, quickly, and accurately with ViDOC (Figures 12 to 14).

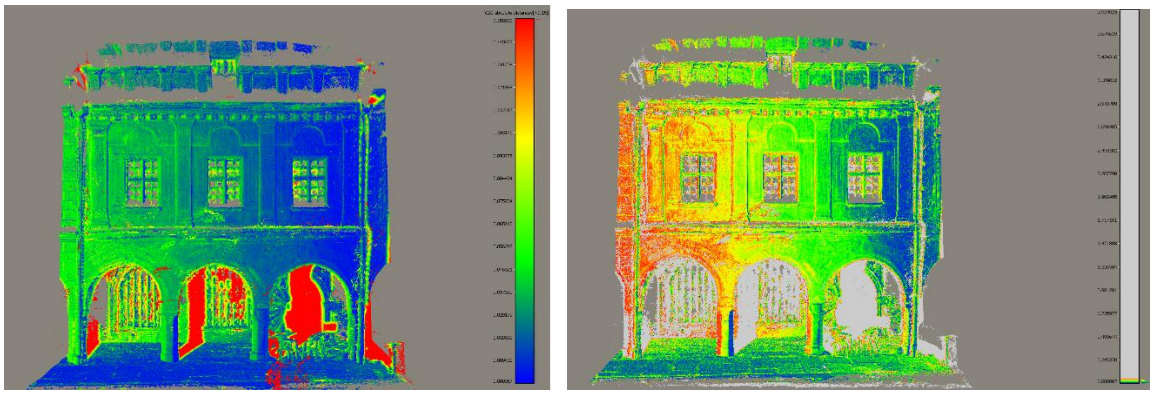

Fig.13 – The comparison of the BLK360 data with the ViDOC data. The BLK360 data was selected as a reference. In the picture differences especially in the hidden areas are shown (left, red color). The BLK360 scanner is static and measurements were taken from only one station, so there are several hidden areas. ViDOC is a mobile device and the model is more complex, it is possible to see a slight systematic deformation of the model, given by the oblique measurement with the BLK360 scanner, when its accuracy decreases with greater distance. On the left side a complex analysis is shown with hidden spaces, which were only on laser scanned data set (red color), better analysis is shown on the right figure; there are discrepancies no more than 5 centimetres.

Fig.14 – View of the object and position of the moving device, plan view and side view created by projection of the point cloud from the ViDOC device.

Fig.14 – View of the object and position of the moving device, plan view and side view created by projection of the point cloud from the ViDOC device.

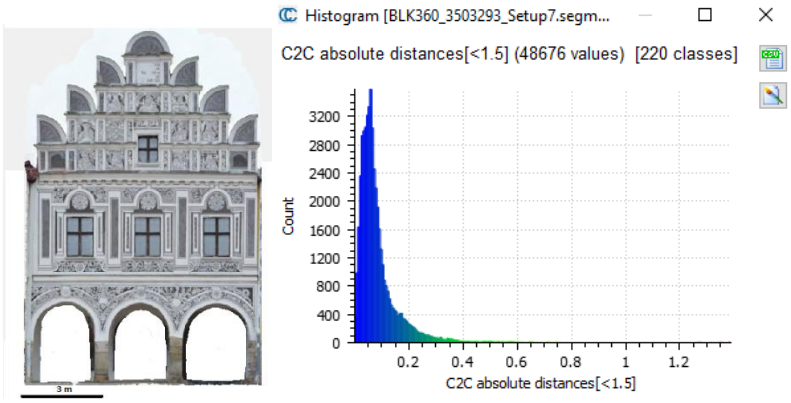

Fig.15 –Created orthophoto from Agisoft Metashape software (left) and comparison of BLK360 data with digital close-range photogrammetry (right); BLK360 data was used as reference data set. Most deviations are in the range of 1-2 centimeters, but at shorter distances up to 10 meters.

Using Agisoft Metashape software, a house 3D model, its orthophoto and a dense point cloud were created from the digital camera images (Figure 15). Twenty-two images and 3 geodeticaly measured control points with RMS of 4 mm were used, the calculated point cloud contains 4,798,102 points and the triangular mesh consists of 959,608 triangles. The generated point cloud was further compared with the output of the laser scanner BLK360 in CloudCompare software. After several adjustments iterations, a satisfactory result was obtained comparing the two point clouds. Most deviations between the point clouds are in the units of cm, however, especially in the window and ground floor area the inaccuracies are larger. The orthophoto was created with a pixel size of 3 mm.

Sculptures documentation

Sculpture documentation is problematic. It depends on its size and especially the spatial complexity of the sculptures, on the material, on the devices used and its accuracy, and mobility in terms of covered and small spaces. Various devices were used here, mobile ViDOC, an expensive and high-quality digital camera Pentax 645, a very accurate laser scanner Surphaser 25 HS, and data from the camera of the iPhone 11 smartphone (Figure 16 to 17).

Fig.16 – The textured 3D mesh from iPhone 11 (left) and a detail from this model (from about 3 meters). Right – 3D model from the ViDOC instrument. Based on the lidar sensor and RTK GNSS, the model is scaled, and it is possible to measure real distances on the model.

The difference in both models was mainly in the area of the head of the statue (it was not possible and allowed to scan) and reached a maximum of 2cm. Typically around 0.5-1 cm.

Tab. 2 – Measurements analysis (sculpture)

Instrument	Measurement time (minutes, hours)	Processing time (hours)	Price (kEuro)	Precision on ideal distance (mm)	Range (ideal, max) (m)	Georeference
iPhone	5 minutes	0.5	1	5	3 ; 20	Yes, low precision
Pentax 645D	30 minutes	2	10	0.1	3; 30	No, GCP´s necessary
ViDOC	10 minutes	0.5	6	5	3; 10	Yes, precise
Surphaser 25HS	1 hour	3	40	0.6	10; 40	No, GCP´s necessary

Sculpture documentation varies considerably in terms of time of data acquisition, processing, and cost of equipment. See Table 2.

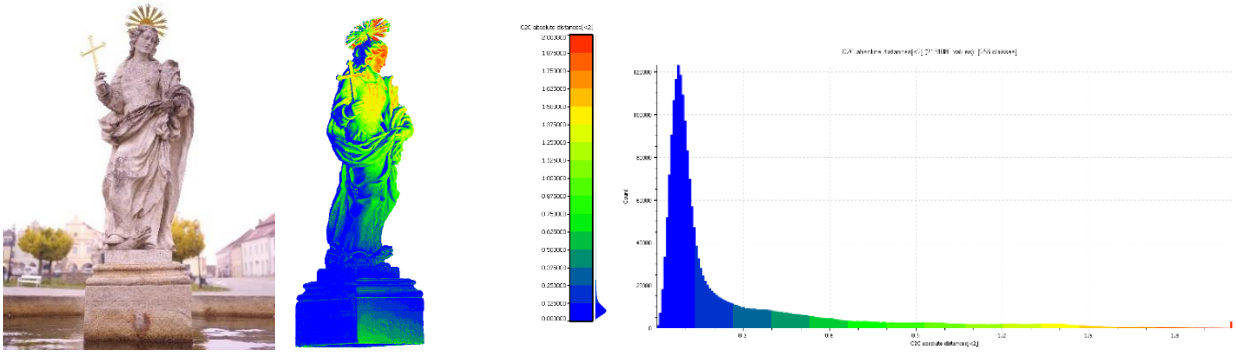

Fig.17 – Data processing (Surphaser 25HS and Pentax 645D), the between both models.

CONCLUSION

This paper describes the need of photogrammetry and laser scanner for the historical objects reconstruction. Instrument description used for the measurements was explained at the begining. Throughout this paper, we used two technologies for measurements: one involving a laser scanner and the other was photogrammetry. The first building was documented by laser scanner BLK360 and using a standard digital camera Canon Powershot SX230 HS. Other objects were a building and a sculpture in the city of Telč, for documentation here a BLK360 scanner, a Canon 450 camera, a new low-cost ViDoc device from Pix4D, an expensive and high-quality digital camera Pentax 645, Surphaser 25 HS laser scanner, and data from the camera of the iPhone 11 smartphone was used. This paper demonstrates how these measurements were done, processed and the accuracy achieved. Working with the laser scanner was relatively simple for creating a 3D model, and the processing was not overly complex. However, working with the digital camera and iPhone was slower due to manual photo-taking, and the overlapping in each photo varied. To execute the processing and analysis of our acquired data, various softwares were used. Following data processing, our study advances to the crucial phase of comparing the generated point clouds by CloudCompare software. For documenting sculptures, classic close-range photogrammetry works particularly well, while laser scanners work for documenting buildings. The challenge lies in hidden spaces or in upper parts of objects. Therefore, it may be necessary to incorporate two or more technologies in some cases.

ACKNOWLEDGEMENTS

This work was supported by the Czech Technical University in Prague, grant SGS23/052/OHK1/1T/11.

REFERENCES

[1] Pavelka, K., Raeva, P., Pavelka jr., K., Kýhos, M., and Veselý, Z. 2022. Analysis of Data Joining from Different Instruments for Object Modelling, Int. Arch. Photogramm. Remote Sens. Spatial Inf. Sci., XLIII-B2-2022, 853–860, https://doi.org/10.5194/isprs-archives-XLIII-B2-2022-853-2022

[2] Petrovič, D., Grigillo, D., Kosmatin Fras, M., Urbančič, T., Kozmus Trajkovski, K. 2021 Geodetic Methods for Documenting and Modelling Cultural Heritage Objects, International Journal of Architectural Heritage, 15:6, 885-896, https://doi.org/10.1080/15583058.2019.1683779

[3] Luhmann, T., Chizhova, M., Gorkovchuk, D., Hastedt, H., Chachava, N., Lekveishvili, N. 2019. Combination of Terrestrial Laserscanning, UAV and Close-Range Photogrammetry for 3D Reconstruction of Complex Churches in Georgia, Int. Arch. Photogramm. Remote Sens. Spatial Inf. Sci., XLII-2/W11, 753–761, https://doi.org/10.5194/isprs-archives-XLII-2-W11-753-2019

[4] Pavelka jr., K.. 2022. Photogrammetry, Laser Scanning and HBIM for Construction Diagnostic, Int. Arch. Photogramm. Remote Sens. Spatial Inf. Sci., XLVI-5/W1-2022, 171–176, https://doi.org/10.5194/isprs-archives-XLVI-5-W1-2022-171-2022

[5] Dlesk, A., Vach, K., Holubec, P. 2019. Analysis of Possibilities of Low-Cost Photogrammetry for Interior Mapping, Int. Arch. Photogramm. Remote Sens. Spatial Inf. Sci., XLII-5/W3, 27–31, https://doi.org/10.5194/isprs-archives-XLII-5-W3-27-2019

[6] Vileikis, O. 2023. A Strategy Using Heritage Documentation for Managing Change of the Historic Centre of Bukhara. ISPRS Annals of the Photogrammetry, Remote Sensing and Spatial Information Sciences, Volume X-M-1-2023, 29th CIPA Symposium “Documenting, Understanding, Preserving Cultural Heritage: Humanities and Digital Technologies for Shaping the Future”, Florence, Italy

[7] Tobiasz, A.; Markiewicz, J.; Łapiński, S.; Nikel, J.; Kot, P.; Muradov, M. 2019. Review of Methods for Documentation, Management, and Sustainability of Cultural Heritage. Case Study: Museum of King Jan III's Palace at Wilanów. Sustainability, 11, *7046*. https://doi.org/10.3390/su11247046

[8] Patias, P., Grussenmeyer, P., Hanke, K. 2008. Advances in Photogrammetry, Remote Sensing and Spatial Information Sciences: 2008 ISPRS Congress Book
Imprint CRC Press, pp. 22, ISBN 9780429207327

[9] Bouček, T.; Stará, L.; Pavelka, K.; Pavelka, K. 2023. Monitoring of the Rehabilitation of the Historic World War II US Air Force Base in Greenland Remote Sensing. 2023(15), ISSN 2072-4292. https://doi.org/10.3390/rs15174323

[10] Leica Geosystems. Leica BLK360 User Manual. Version 2.0 English. https://shop.leica-geosystems.com/leica_blk360_manual (accessed on 30 Sept. 2023).

[11] PowerShot SX230 HS Camera User Guide. https://pssx230hs (accessed on 30 Sept. 2023).

[12] Surphaser, laser scanner, https://surphaser.com/, (accessed on 30 Nov. 2023)

[13] Foto Škoda, https://www.fotoskoda.cz/pentax-645z-55-2-8-d-fa-sdm-aw/, (accessed on 30 Nov. 2023)

[14] Bohdalek, P., 2012. Jáchymov - famous mining town in Bohemian Erzgebirge, online https://doi.org/10.13140/RG.2.1.2735.5924

[15] Telč, https://whc.unesco.org/en/list/621/, (accessed on 30 Nov. 2023)

[16] CloudCompare. User Manual. Version 2.6.1. Available online: https://www.cloudcompare/manual.pdf (accessed on 30 Sept. 2023).

CIVIL ENGINEERING JOURNAL

Article no. 39

THE CIVIL ENGINEERING JOURNAL 4-2023

FINITE ELEMENT SIMULATION ANALYSIS OF STEEL TRUSS ARCH BRIDGE JACKING CONSTRUCTION

Xilong Zheng[1]and Wei Li[2]

1. *School of Civil and Architectural Engineering, Harbin University, No.109 Zhongxing Road, Harbin, Heilongjiang Province, China; sampson88@126.com*
2. *School of Civil and Architectural Engineering, Harbin University, No.109 Zhongxing Road, Harbin, Heilongjiang Province, China*

ABSTRACT

In this study, a spatial model of a steel truss arch bridge was established using the finite element software Midas/Civil to simulate and analyze the jacking construction process. The stress performance of the guide beam and main structure at each jacking stage was obtained. The results showed that in the first stage of jacking, the maximum stress and deflection values of the main girder were observed. The maximum stress on the upper edge of the main girder was 34.9 MPa, and on the lower edge, it was -60.4 MPa. The maximum deflection was -35.88 mm. The maximum stress in the guide beam occurred during the jacking process and was -53.2 MPa, corresponding to the cross-section at the root of the guide beam. The maximum deflection of the guide beam occurred in the maximum cantilever state and was -30.79 mm. During the arch rib jacking process, the maximum stress was -49.4 MPa. Both the maximum stress and deflection values were within the allowable range, indicating that the structure was in a safe state. This study provides a reference for similar bridge jacking construction projects.

KEYWORDS

Steel truss arch bridge, Jacking construction method, Simulation analysis, Simulation analysis, Construction phase

INTRODUCTION

Bridge construction methods can be divided into many types, including cantilever construction (basket construction method), support construction, hoisting construction, jacking construction method, rotation construction, etc [1-3]. Bridge construction methods are usually chosen based on factors such as local topography, bridge usage, and construction costs. In recent years, the jacking construction method has been widely used in bridge construction, especially in cases where the terrain is complex, there are navigation requirements under the bridge, and it is not suitable to install supports under the bridge [4-6].

In simple terms, the jacking construction method involves selecting a construction site on one side of the abutment, where the prefabrication (assembly) of the main girders, main arches, and other components takes place. After the prefabricated structure is completed, jacking equipment such as hydraulic jacks are used to push or pull the structure gradually towards the designated position [7]. Temporary facilities such as temporary piers, steel guide beams, jacking sliding tracks, and traction equipment are set up along the jacking direction. The method of pushing or pulling the

prefabricated structure to the specified position is known as the jacking construction method [8].

Among various types of bridges, steel truss arch bridges are widely used due to their high stiffness and aesthetic appearance [9-12]. However, research on the temporary facilities setting in integral jacking construction is mostly focused on girder bridges, with less attention paid to beam-arch composite structure bridges. For large-span beam-arch composite structures, there can be localized stress concentration due to their own weight [13-15]. Existing research lacks comprehensive understanding of the stress characteristics and deformation states and laws of temporary components and main structures during the jacking process. This study focuses on the simulation and analysis of the construction process of a steel truss arch bridge using the integral jacking construction method, aiming to investigate the stress performance of the guide beams and main structures at each jacking stage.

ENGINEERING BACKGROUND INTRODUCTION

This article takes a steel truss arch bridge as the engineering background. The main bridge structure adopts a lower deck steel truss arch beam structure with a main span of 106 m and a total width of 38 m. The roadway width is 24 m, accommodating six lanes in both directions. The main beam is a structure that bears the combined forces of the main longitudinal beam, steel cross beam, and secondary longitudinal beam. The bridge deck consists of orthotropic plates. The height of the beam at the bridge's centerline is 2.565 m, and the steel material used is Q345qC.

The arch ribs of the main bridge are in the form of steel trusses, with upper and lower layers of arch ribs. The upper and lower arch ribs are connected by vertical and diagonal struts to form a whole. Two trusses are arranged horizontally to enhance lateral stability. The upper arch rib has a span of approximately 142 m and a rise of 23.5 m. The lower arch rib has a span of approximately 103 m and a rise of 20 m. The net rise of the truss arch is 19.288 m, with a rise-span ratio of 1:5.5. There is a height difference of 3.5 m between the tops of the upper and lower arch ribs.

The bridge uses parallel wire suspension rods, with 30 suspension rods installed. The lower end of the suspension rods is anchored to the corresponding lug plate of the main longitudinal beam and cross beam. The upper end of the suspension rods is anchored to the lug plate on the transverse partition plate inside the arch rib's box structure. There are reinforcement ribs set on both sides of the lug plate, which serve as the main force transmission components. The weight of the bridge's dragging steel structure is 3816 t, the weight of the suspension rods is 10.7 t, the weight of the arch assembly support is 123.1 t, the weight of the guide beam is 83.8t, and the length of the guide beam is 25 m. The construction of this project adopts the continuous multi-point jacking method using dragging, as shown in Figure 1. The elevation and cross-section layouts of the bridge are shown in Figure 2 and Figure 3, respectively.

Fig.1 – Steel truss arch bridge completion effect picture

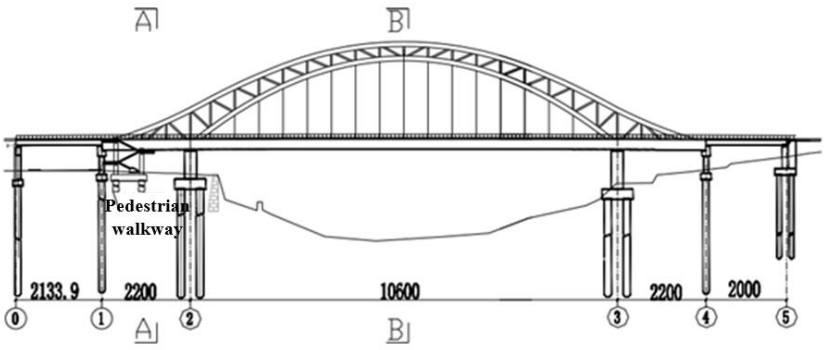

Fig.2 – Elevation layout diagram of the bridge

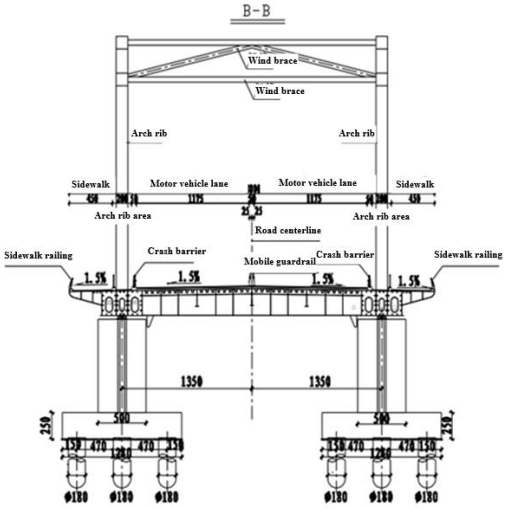

Fig.3 – Cross-sectional layout

INTRODUCTION OF INTEGRAL JACKING CONSTRUCTION PROCESS

Due to the requirement for navigable waterway underneath the bridge, it is not possible to install supports in the river. Therefore, the main bridge of this steel truss arch bridge adopts the integral jacking construction method. The main construction steps are as follows, as shown in Table 1 to Table 8.

Tab. 1 - Top-down construction process step one

Step one	Construction preparation
Construction schematic	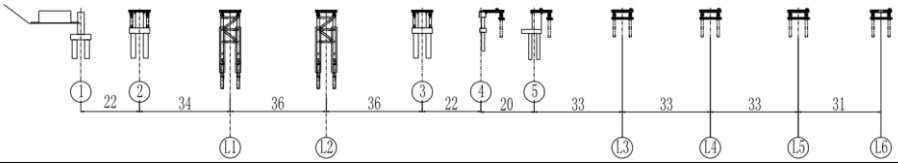
Content description	1. Set up two temporary support piers, L1 and L2, between piers 2 and 3. 2. Install sliding beam tracks on the temporary support piers and arrange the installation of horizontal and vertical jacks for adjustment purposes. Conduct testing and adjustment of the top pushing equipment.

Tab. 2 - Top-down construction process step two

Step two	Assembly of beam arch structure
Construction schematic	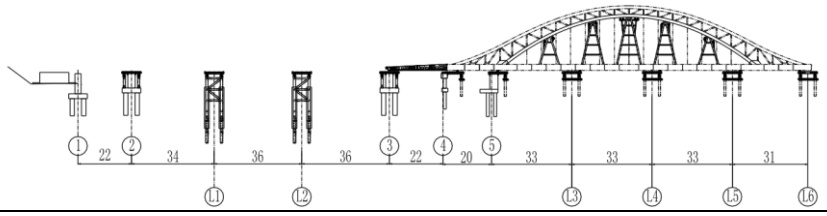
Content description	1. Assemble the steel box girder structure, arch ribs, suspension rods, and guide beams at the assembly site. 2. After installing the suspension rods, apply a certain amount of prestressing force as required. 3. Install the pier top pushing and alignment systems and adjust them accordingly. Once the top pushing system is ready, perform the necessary tests and adjustments.

Tab. 3 - Top-down construction process step three

Step three	The jacking operation is in progress
Construction schematic	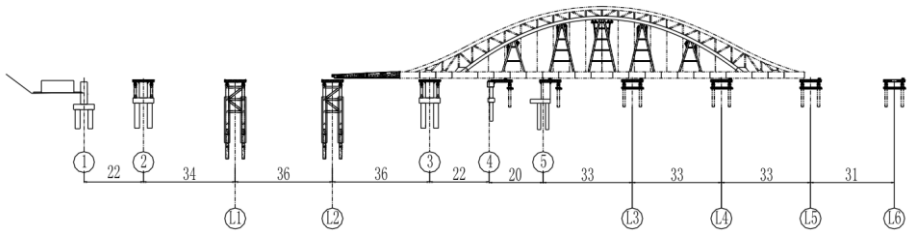
Content description	1. Start the pulling device and drag the steel beam forward by 33.75 m. 2. Activate the vertical jacks to detach the steel beam from the sliders. Move all the sliders back to the starting position of the pulling device. 3. The rear cantilever is 26.96 m.

Tab. 4 - Top-down construction process step four

Step four	The jacking operation is in progress
Construction schematic	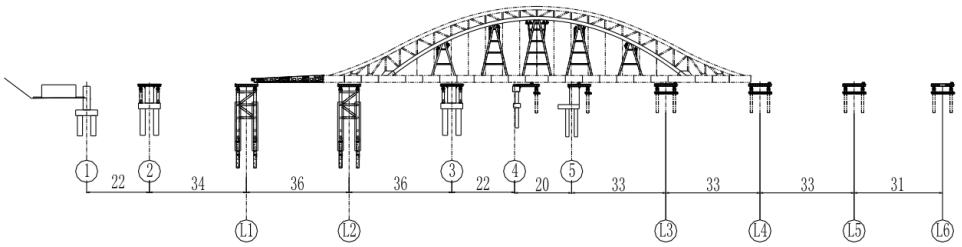
Content description	1. Start the pulling device and drag the steel beam forward for 33 m. 2. Activate the vertical jack to separate the steel beam from the sliders; move all the sliders back to the initial position of the pulling device. 3. The tail overhangs for 26.96 m.

Tab. 5 - Top-down construction process step five

Step five	The jacking operation is in progress
Construction schematic	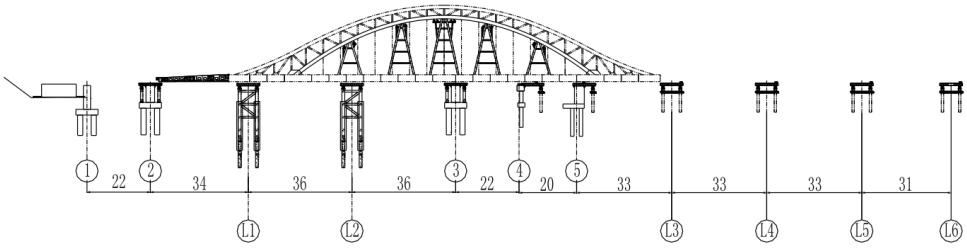
Content description	1. Start the pulling device and drag the steel beam forward for 33.75 m. 2. During the dragging process, dismantle the steel guide beams section by section. 3. Activate the vertical jack to separate the steel beam from the sliders; move all the sliders back to the initial position of the pulling device. 4. The tail overhangs for 26.96 m.

Tab. 6 - Top-down construction process step six

Step six	The jacking operation is in progress
Construction schematic	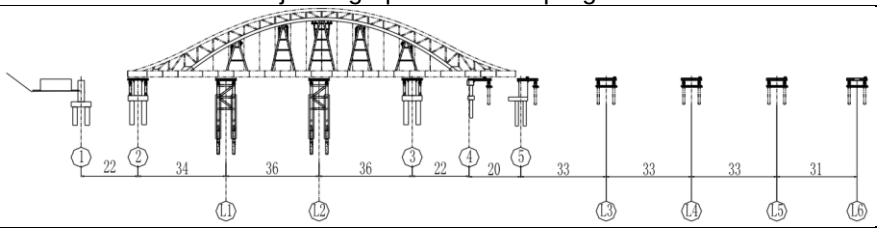
Content description	1. Start the pulling device and drag the steel beam forward for 33 m. 2. During the dragging process, dismantle the steel guide beams section by section. 3. Activate the vertical jack to separate the steel beam from the sliders; move all the sliders back to the initial position of the pulling device. 4. The tail overhangs for 10.5 m.

Tab. 7 - Top-down construction process step seven

Step seven	The jacking operation is in progress
Construction schematic	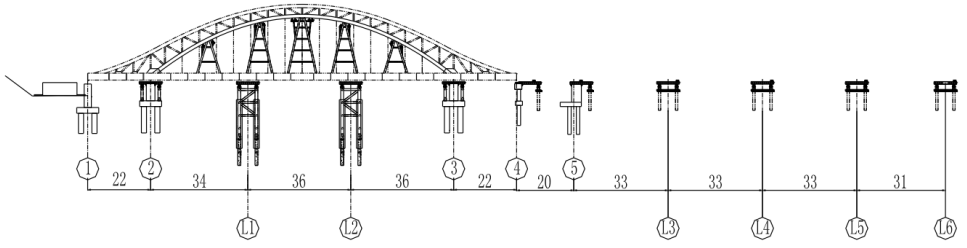
Content description	1. Start the pulling device and drag the steel beam forward for 17.25 m. 2. Drag the steel beam into its final position.

Tab. 8 - Top-down construction process step eight

Step eight	The jacking operation is in progress
Construction schematic	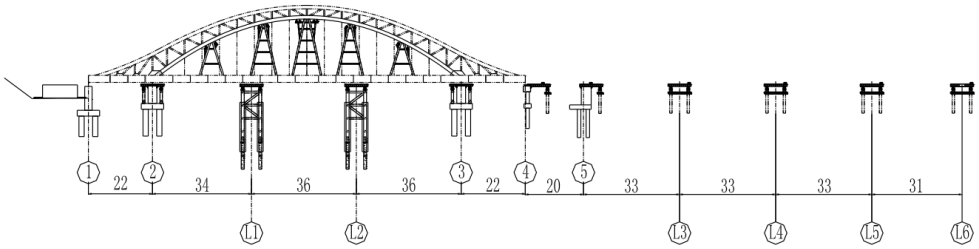
Content description	1. Activate the vertical jack to separate the steel beam from the sliders and use the three jacks to adjust the final position of the steel beam. 2. Dismantle the dragging sliders layer by layer to complete the overall placement of the beam.

FINITE ELEMENT MODULE METHOD

Model Overview

The model consists of 1389 nodes and 1728 elements of various types. The finite element model can be seen in Figure 4. The beam and the arch share a joint. The main beam and pier are connected by general support.

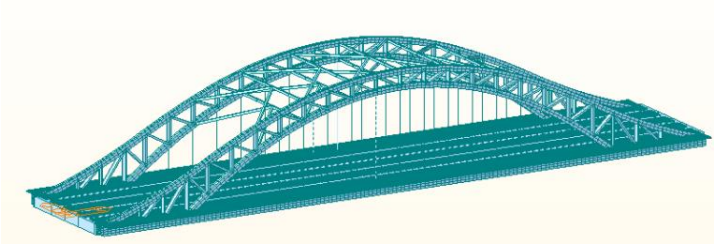

Fig.4 – Calculation model of a steel truss arch bridge

Division of construction conditions

According to the construction process, the analysis is divided into 34 construction stages, with each stage advancing the structure by 5 m. The main construction stages include the steel truss beam jacking stage and the maximum cantilever stage. Each construction stage activates the corresponding structural groups or boundary groups based on the actual conditions. The analysis simulates the stress and deformation of the main structure in each construction stage. Please refer to Table 9 for detailed description of each construction stage.

Tab. 9 - Calculation and analysis of load conditions explanation

Construction phase	Top push distance	Construction phase	Top push distance
1	Before top push	18	The top push distance is 80 m
2	Top push starts, with a push distance of 0 m	19	The top push distance is 85 m
3	The top push distance is 5 m	20	The top push distance is 90 m
4	The top push distance is 10 m	21	The top push distance is 95 m
5	The top push distance is 15 m	22	The top push distance is 100 m
6	The top push distance is 20 m	23	The top push distance is 105 m
7	The top push distance is 25 m	24	The top push distance is 110 m
8	The top push distance is 30 m	25	The top push distance is 115 m
9	The top push distance is 35 m	26	The top push distance is 120 m
10	The top push distance is 40 m	27	The top push distance is 125 m
11	The top push distance is 45 m	28	The top push distance is 130 m
12	The top push distance is 50 m	29	The top push distance is 135 m
13	The top push distance is 55 m	30	The top push distance is 140 m
14	The top push distance is 60 m	31	The top push distance is 145 m
15	The top push distance is 65 m	32	The top push distance is 150 m, and the top push is completed
16	The top push distance is 70 m	33	Remove the girder, temporary pier, and arch assembly bracket
17	The top push distance is 75 m	34	Completed Phase 2 pavement

ANALYSIS OF OVERALL JACKING CALCULATION RESULTS

Stress calculation result

The stress values during the jacking process are crucial for the safety of the structure, especially when using the integral jacking construction method, as the structure's self-weight can lead to stress concentration. The materials used in the bridge structure are all Q345 steel, so it is necessary to verify whether the stress in the structure is within the allowable range. Finite element software is used to perform simulation analysis on the structure and determine the construction stage and location with the highest stress.

(1) Main beam stress calculation results:

The upper and lower stress analyses of the main beam are performed separately for the maximum construction stages of the front and rear cantilevers. The stress envelop diagrams for the upper and lower edges of the main beam can be seen in Figure 5 to Figure 8. Detailed analysis results can be found in Figure 9 to Figure 10. The stress values are given in MPa, with "+" representing tension and "-" representing compression.

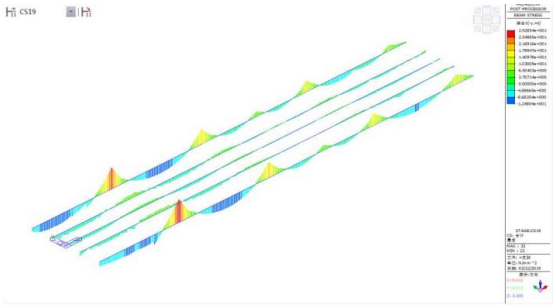

Fig. 5 – Maximum envelope stress diagram of the front cantilever of the main girder

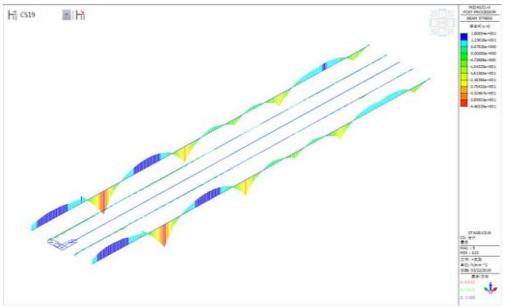

Fig. 6 – Maximum stress enveloping diagram of front cantilever main beam

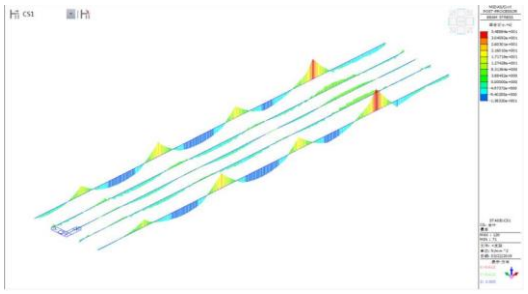

Fig.7 – Maximum stress enveloping diagram of rear cantilever main beam

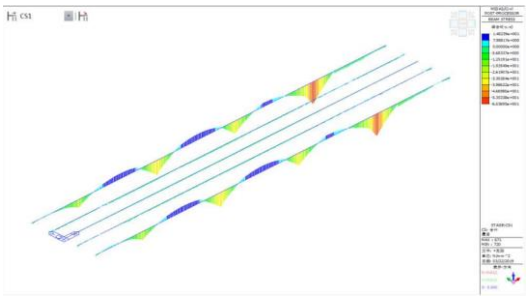

Fig.8 – Maximum stress enveloping diagram of the lower surface of the rear cantilever main beam

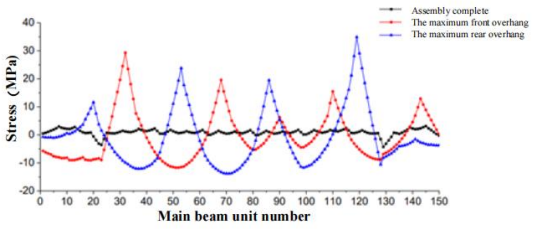

Fig.9 – Stress diagram of the upper surface of the main beam

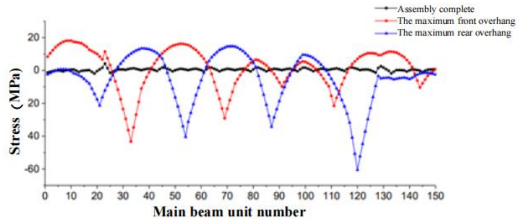

Fig.10 – Stress diagram of the lower surface of the main beam

From Figure 5 to Figure 8, it can be observed that the maximum stress in the rear cantilever of the main beam occurs in the first construction stage of the jacking process, when the rear cantilever has just left temporary support L6. Therefore, the maximum stress is generated at the end of the main beam. The maximum stress in the front cantilever of the main beam occurs in the 19th construction stage of the jacking process, when the main beam has been pushed out approximately 85 m and the front end is in a maximum cantilever state.

From Figure 9 to Figure 10, it can be seen that during the maximum construction stage of the front cantilever, the maximum stress on the upper edge of the main beam is 29.3 MPa, and the maximum stress on the lower edge is -44.7 MPa. During the maximum construction stage of the rear cantilever, the maximum stress on the upper edge is 34.9 MPa, and the maximum stress on the lower edge is 60.4 MPa.

The steel used in this structure is Q345 steel. It can be concluded that the overall stress of the structure during the jacking process is within the allowable range and the structure is safe and stable.

(2) Guideway stress calculation results:

The maximum stress in the guideway during jacking occurs in the 11th construction stage (with a cumulative jacking distance of approximately 45.75 m), and the maximum stress value is 53.2 MPa. The maximum stress stage and stress distribution in the guideway during the jacking process can be seen in Figure 11 to Figure 12.

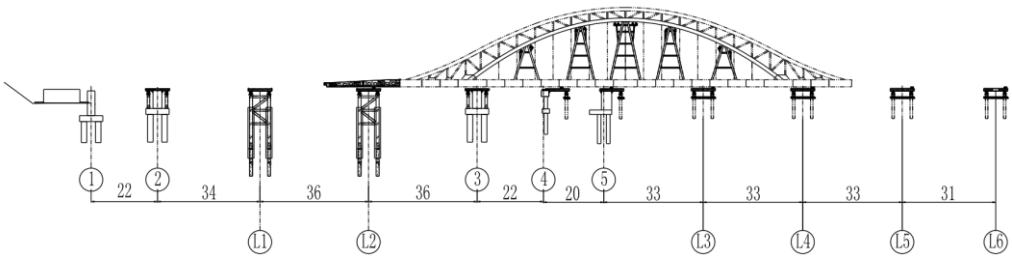

Fig.11 – Schematic diagram of the maximum stress stage of the guide beam

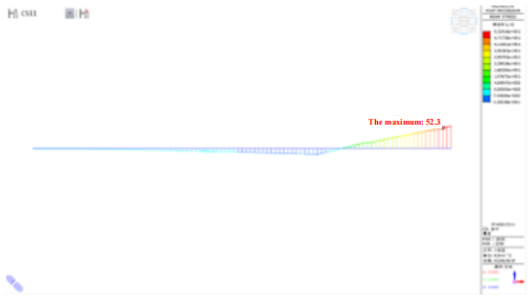

Fig.12 – Envelope diagram of maximum stress in the guide beam

From Figure 11 to Figure 12, it can be seen that during the overall jacking process, the maximum stress in the guideway occurs at the section where the guideway is connected to the main beam. This indicates that measures should be taken to strengthen the connection between the guideway and the main beam during the jacking process.

(3) Arch rib stress calculation results:

The maximum stress in the arch rib during jacking occurs in the 33rd construction stage. At this stage, the jacking is completed, the temporary piers are removed, and the arch rib assembly supports are dismantled. The maximum stress point is located at about 1/4 of the span from the lower arch ribs and at the arch foot, with a maximum stress value of -48.9 MPa.

The stage with the maximum stress and the stress distribution in the arch rib during the jacking process can be seen in Figure 13 to Figure 14.

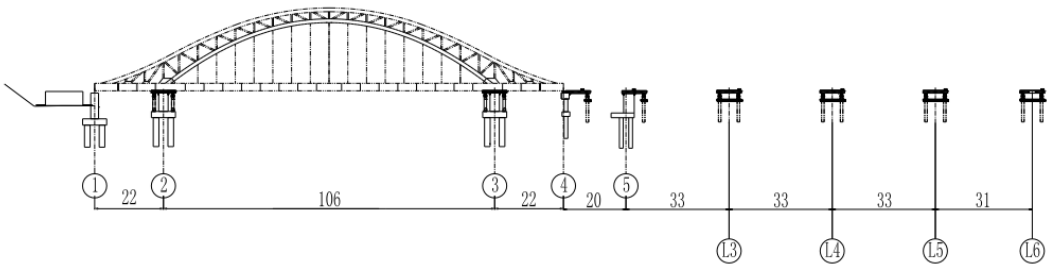

Fig.13 – Schematic diagram of the arch rib under maximum stress phase

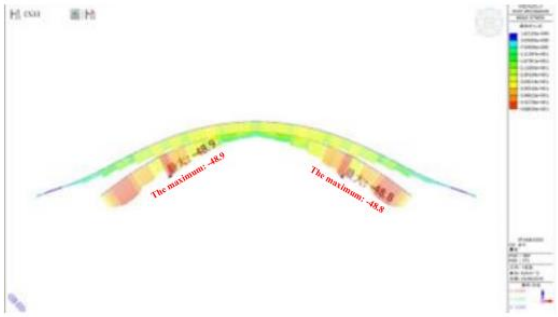

Fig.14 – Envelope diagram of maximum stress in the arch rib

Based on the above calculation results, it can be concluded that under the overall simulation analysis, the maximum stress in the arch rib during jacking is -48.9 MPa, which is within the allowable stress of the material. Therefore, the internal forces in the arch rib structure during the jacking process are well within the acceptable range.

Displacement calculation results

The displacement calculation in top-down construction is as important as stress calculation as it can also reflect the structural behavior. Through simulation analysis of a steel truss arch bridge during the top-down construction process, displacements at the front and rear ends of the guideway, as well as at the front and rear ends of the main beam, were calculated at each construction stage. The maximum displacement at the front end of the guideway is -30.79 mm, occurring in the 7th construction stage, while the maximum displacement at the rear end of the guideway is -8.14 mm, occurring in the 10th construction stage. As for the main beam, the maximum displacement at the front end is -13.14 mm, occurring in the 10th construction stage, and the maximum displacement at the rear end is -35.88 mm, occurring in the 1st construction stage. Please refer to Figure 15 to Figure 16 for more details.

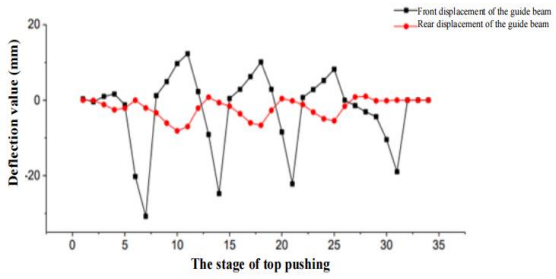

Fig.15 - The comparison of deflection between the front end and root of the guide beam

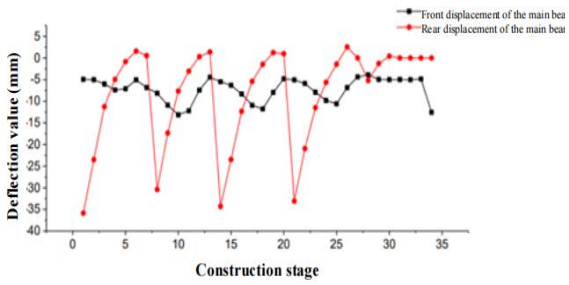

Fig.16 - The comparison of deflection between the front end and rear end of the main beam

From Figure 15, it can be observed that the front end of the guideway initially lifts during the 8th, 15th, and 22nd construction stages. After reaching a certain height, the upward trend gradually becomes gentler, and then it starts to descend, showing a noticeable regular pattern. The maximum deflection of the guideway occurs at the front end when it is in the maximum cantilever state, which happens during the 7th construction stage (with a cumulative jacking distance of 25 m), with a deflection value of -30.79 mm. The maximum deflection at the base of the guideway is -8.14 mm, occurring during the 10th construction stage. As for the main beam, the deformation at the front end is relatively stable, showing regular fluctuations. The maximum deflection occurs during the 10th construction stage (with a cumulative jacking distance of 40 m), with a deflection value of -13.14 mm.

The maximum deflection at the rear end of the main beam is -35.88 mm, occurring during the 1st construction stage. This is because, at the beginning of the jacking process, the rear end of the main beam loses temporary support, resulting in the maximum cantilever length and, consequently, the maximum deflection value.

Calculation results of reaction force at the top of temporary pier

During the top-down construction process of the bridge, a total of 6 temporary piers were installed, including 2 in the water (L1 and L2) and 4 on land (L3 to L6). The reaction forces at the top of these temporary piers are important data that reflect the bridge's structural behavior, and it is essential to calculate these forces.

(1) Maximum Reaction Force during Top-down Construction

According to the simulation calculation results, the maximum reaction force occurs during the 14th construction stage (with a cumulative jacking distance of approximately 62 m) at temporary pier L3# in the water. The magnitude of this reaction force is 6193.9 kN. The construction stage and the distribution of reaction forces are shown in Figure 17 to Figure 18.

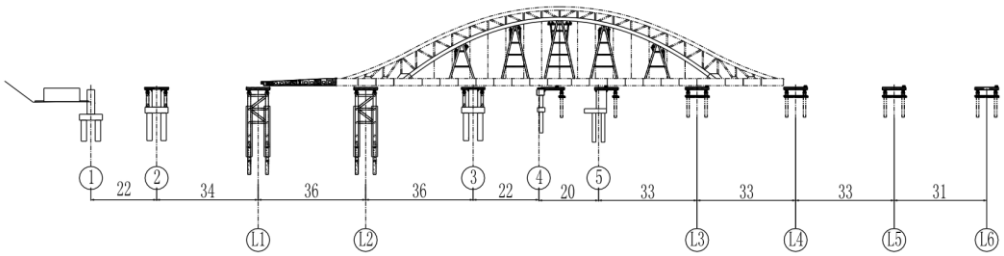

Fig.17 – The temporary pier reaction during the top-down construction phase

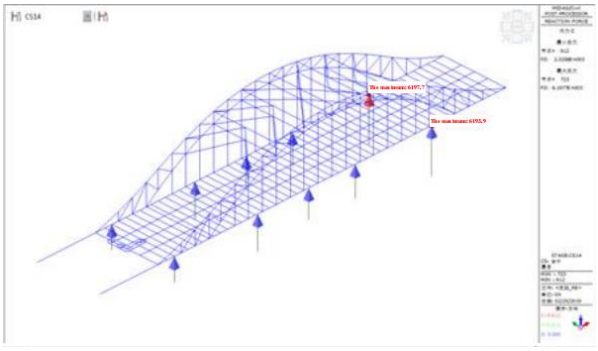

Fig.18 – The maximum reaction force result during the top-down construction process

(2) The reaction force at temporary pier L1# in the water

The maximum reaction force at temporary pier L1# occurs during the 25th construction stage (with a cumulative jacking distance of approximately 116 m). The magnitude of this reaction force is 5226.8 kN. The construction stage and the distribution of reaction forces are shown in Figure19 to Figure 20.

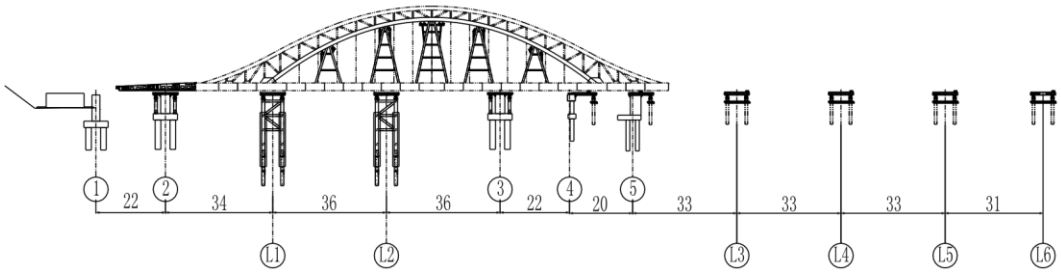

Fig.19 – L1# temporary pier's maximum reaction force occurs during the top-down construction phase of the launching process

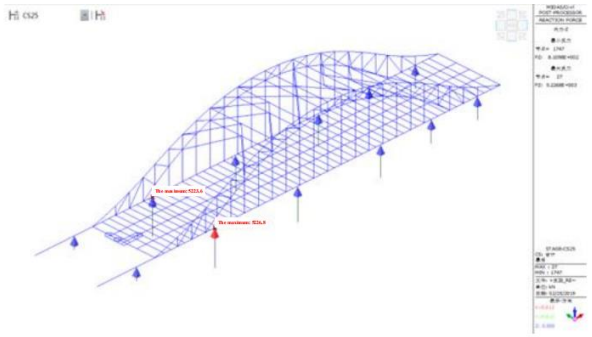

Fig.20 – The maximum reaction force of temporary pier L1# during the top-down construction process

(3) The reaction force at temporary pier L2# in the water

The maximum reaction force at temporary pier L2# occurs during the 17th construction stage (with a cumulative jacking distance of approximately 75 m). The magnitude of this reaction force is 5349.4 kN. The construction stage and the distribution of reaction forces are shown in Figure 21 to Figure 22.

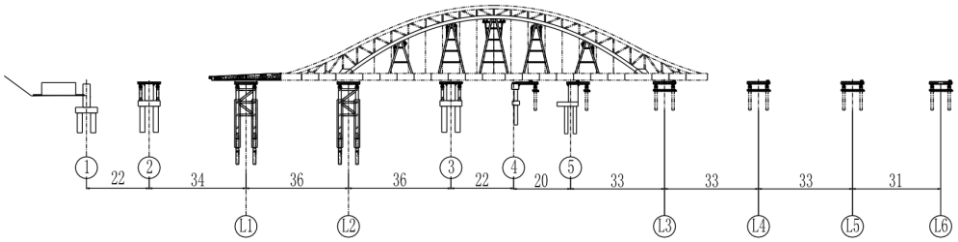

Fig.21 – The construction phase during which the maximum reaction force of temporary pier L2# occurs during the top-down construction process

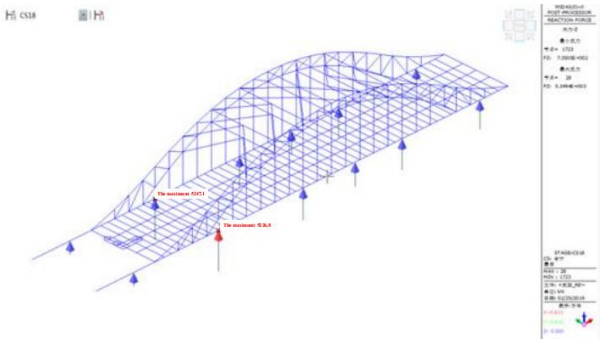

Fig.22 – The maximum reaction force of temporary pier L2# during the top-down construction process.

CONCLUSION

The study utilized the finite element software Midas/Civil to establish a spatial model and conduct a simulated analysis of the overall top-down construction process of a steel truss arch bridge. This analysis enabled the assessment of the structural performance and load distribution of the guide beam and main structure at each stage of the construction. The following conclusions were drawn:

(1) The maximum cantilever stage of the front end of the main beam occurs during the 19th stage of top-down construction (with a pushing distance of 85 m). The maximum stress on the upper flange is 29.3 MPa, while the maximum stress on the lower flange is -44.7 MPa. In the maximum cantilever stage of the rear end of the main beam, the maximum stress on the upper flange is 34.9 MPa, while the maximum stress on the lower flange is -60.4 MPa. At this stage, the rear cantilever has just left temporary support pier L6, resulting in the highest stress concentration due to the maximum cantilever length.

(2) The maximum stress on the guide beam during the top-down construction process occurs during the 11th construction stage (with a cumulative jacking distance of approximately 45.75 m). The maximum stress value is -53.2 MPa, and it corresponds to the cross-section at the base of the guide beam.

(3) The maximum deflection at the front end of the guide beam occurs during the maximum cantilever state, which is the 7th construction stage (with a cumulative jacking distance of 25 m). The maximum deflection value is -30.79 mm. The maximum deflection at the root of the guide beam is -8.14mm, occurring during the 10th construction stage.

(4) The maximum reaction force on the top of the pier during the top-down construction process occurs during the 14th construction stage (with a cumulative jacking distance of approximately 62 m), at temporary pier L3.

REFERENCE

[1] Li, F., Wu, P., and Yan, X. Analysis and monitoring on jacking construction of continuous box girder bridge[J]. Computers and Concrete, 2015, 16(1): 49-65.

[2] Hu, Da, et al. Analysis and prediction of pavement settlement caused by jacking construction of ultra-shallow rectangular shield frame bridge[J]. Mathematical Problems in Engineering, 2020: 1-14.

[3] Li, Jian, Zhigang Liu, and Peng Zhang. The hugest curved jacking pipe roof tunnel of Hong Kong-Zhuhai-Macao bridge[J]. ICPTT 2014: Creating Infrastructure for a Sustainable World, 2014: 422-431.

[4] Ma, Fengbo, et al. Safety Monitoring of Bearing Replacement for a Concrete High-Speed Railway Bridge Based on Acoustic Emission[J]. Journal of Performance of Constructed Facilities, 2022, 36 (3): 04022014.
[5] Zhang, Peng, et al. Key techniques for the largest curved pipe jacking roof to date: A case study of Gongbei tunne [J]. Tunnelling and Underground Space Technology, 2016, 59: 134-145.
[6] Lu W, Li W, Field monitoring of a tunnel bridge during jacking construction", 8th International Conference on Reliability, Maintainability and Safety. IEEE, 2009: 502-506.
[7] Shen J K. Based on the Different Specifications of Jacking Construction of Continuous Girder Bridge Reliability Analysis[J]. Applied Mechanics and Materials, 2014, 584: 2017-2022.
[8] Zhang H J, Peng Z Q, Li B L, et al. Control Technology on Jacking Closure Construction of Liangjiang Great Bridge[J]. Applied Mechanics and Materials, 2014, 587: 1430-1434,
[9] Li P, Liu X, Dai Z, et al. Stability analysis of braced structures under jacking construction of large span steel truss bridges[J]. IOP Conference Series: Earth and Environmental Science. IOP Publishing, 2021, 861(7): 072064.
[10] Xu L G, Wang Y L, Xu C J. Jacking technology for a simply supported girder bridge[J]. Applied mechanics and materials, 2014, 477: 675-680.
[11] Chen Z, Yan Q S, Jia B Y, et al. Large Span Continuous Girder Bridge Jacking Steel Hoop Stress Analysis[J]. Advanced Materials Research, 2013, 671: 991-995.
[12] He J, Gao X. Research of Synchronous Jacking up Construction Monitoring and Control Technologies of Bridge[J]. 2nd International Conference on Architectural, Civil and Hydraulics Engineering (ICACHE 2016). Atlantis Press, 2016: 39-44.
[13] Wang, Zhichao, et al. Settlement characteristics of jacked box tunneling underneath a highway embankment[J]. Journal of Performance of Constructed Facilities, 2019, 33(2): 04019005.
[14] Fan, Xin, et al. Construction Monitoring of Jacking Construction of Steel-Concrete Composite Beam in Self-Anchored Suspension Bridge[J]. Civil Engineering and Urban Planning 2012. 2012: 188-193.
[15] de Boer, Jan. The benefits of jacking and skidding for rapid installation of under-and overpasses[J]. Structural engineering international, 2011, 21(4): 419-425.

CIVIL ENGINEERING JOURNAL

Article no. 40

THE CIVIL ENGINEERING JOURNAL 4-2023

ANALYSIS AND OPTIMIZATION OF WIND RESISTANCE PARAMETERS FOR LATTICE-TYPE HIGH-MODULUS SUPPORTS BASED ON THE OPTIMAL CRITERIA METHOD

Qingyu Sui, Quansheng Sun, Jianxi Yang and Shijie Wang

School of Civil Engineering and Transportation, Northeast Forestry University, Harbin 150040, China; sunquansheng@nefu.edu.cn

ABSTRACT

Lattice high-molded support can generally be used for cast-in-place support for bridges, but for more than 50 meters of lattice high support, due to the wind, load and other factors, due to the support length and slenderness of the relatively large, relatively light and flexible structure and other characteristics of the role of the wind load is very sensitive. When the lattice high-molded stent construction is used in the typhoon area, it is easy to be damaged by the typhoon, and the structural design of the lattice high-molded stent and the construction of that technology are facing great challenges. In this paper, based on the new construction of a special bridge in Fujian, finite element analysis of four-legged and six-legged lattice bracing is carried out by ANSYS, and the effects of steel pipe diameter, number of columns, longitudinal and transversal spacing of bracing, and diagonal bracing structural parameters on structural performance are analyzed by using the coefficients of buckling stability and the coefficients of critical loading. The results of the study show that the main design variable for displacement sensitivity is the diameter of vertical rod; the main design variable for stress sensitivity is the diameter of diagonal rod; the main design variable for overall stability sensitivity is the diameter of diagonal rod; and the main design variable for overall stability sensitivity of total volume is the diameter of diagonal rod. And the optimal wind resistance parameters are: 4 lattice high-braced columns are selected, the section length should be controlled within 15m, and the total height should not be more than 70m, and the spacing of the columns is controlled between 7m and 8m. This study proposes a set of optimized design process method for wind-resistant lattice structure under the constraints of stiffness, strength and critical load factor, which improves the economy and ensures the reasonableness of the design, and can be used for the design of high-modular lattice bracket in typhoon area.

KEYWORDS

Lattice bracing, Wind effects, Optimality criterion method, Nonlinear analysis

INTRODUCTION

With the rapid development of China's economy and technology, coupled with the implementation of policies such as reform and opening up, and the Belt and Road Initiative, a large number of large bridges spanning rivers, seas, canyons, lakes, and existing roads have been successively completed. This has ushered in a golden period of vigorous development in the country's transportation infrastructure, with constantly refreshed lists of bridge spans. As bridges gradually move towards large spans, wind damage has also gradually come into view for engineers [1]. In recent years, with global climate warming and the frequent occurrence of extreme weather, the frequency of natural disasters has been increasing year by year. Due to geographical characteristics, coastal areas in China become the main targets of typhoons. Statistics show that Guangdong, Fujian, Zhejiang, and other regions are affected by typhoons about 7.2 times each year.

Currently, in China, large-span continuous concrete bridges are mainly constructed using the scaffolding method. Common types of scaffolding include fastener-type steel pipe scaffolding, bowl-type steel pipe scaffolding, portal scaffolding, among which the steel pipe truss modular support system has proven its practicality and effectiveness in practice, playing a crucial role in large-span bridge construction projects [2]~[6].

In recent years, the grid-type high-modulus support system has been widely used due to its convenient assembly and strong load-bearing capacity. Due to its towering, flexible structural form, as well as its light weight and low damping characteristics, the grid-type high-modulus support system has strong sensitivity to wind. Large-span bridges are usually located in areas with fast winds such as rivers, seas, and canyons, and the construction area occupied by scaffolding is usually extensive with high wind resistance. Therefore, it is necessary to carry out experimental research on the wind-resistant design optimization of scaffolding. During the construction of bridges, scaffolding not only serves to provide a working surface but also provides structural bearing capacity when the early concrete strength has not formed. The design and use of scaffolding determine the progress and safety of engineering projects. The wind stability of scaffolding has attracted the attention of many scholars at home and abroad.

During bridge construction, supports not only provide a working surface but also provide structural load-bearing capacity in the early stages before the concrete strength has fully developed. The design and use of supports determine the progress and safety of engineering projects. Support wind stability has attracted the attention of many domestic and foreign scholars [7]~[13]. In 2006, Xiu Lei [14] used simplified formulas and random vibration theory to simplify the wind-induced response of lattice-type tower structures into algebraic calculations. Using a first-order generalized load spectrum analytical model, they proposed a simplified calculation formula for the downwind wind-induced response of lattice-type tower structures. In 2022, Yang Wen [15] conducted nonlinear analysis research on the yielding mechanism of lattice-type steel-concrete tower structures based on static experiments of four ball-joint node models simulated using Abaqus finite element simulation software. The research results showed that node failure is mainly caused by strength failure and compressive member instability, and the difference in node plate thickness has a more significant impact on the bearing capacity of ball-joint nodes, while changes in the thickness ratio of the enclosure diameter have less impact on the bearing capacity of ball-joint nodes. In 2023, Jeddi Ashkan B [16] and others used the Kalman filter method to study the drag coefficient and gust response factor of double-loop lattice-type transmission towers, accurately estimating the impact of extreme wind-induced loads on lattice-type structures. Based on the aerodynamic characteristics and wind tunnel tests, an optimized Kalman filter model was proposed to integrate measurements from multiple sensors of the same and different types implemented in wind tunnel experiments. This approach, combined with optimization techniques, provided estimates of the wind load parameters of interest with high spatial resolution and accuracy in measuring response.

This study utilizes the ANSYS finite element simulation program to establish lattice-type high modulus supports under wind load, and, in combination with MATLAB programming software, for secondary development to improve structural optimization accuracy. The modified optimal criteria method is used to correct the stiffness, strength, and critical load factor constraint formulas, proposing a wind-resistant optimization design process for lattice-type high modulus supports based on the modified optimal rule."

CIVIL ENGINEERING JOURNAL

Article no. 40

THE CIVIL ENGINEERING JOURNAL 4-2023

ESTABLISHMENT OF FINITE ELEMENT ANALYSIS MODEL FOR LATTICE-TYPE HIGH MODULUS SUPPORT

Project overview

Tab. 1 - Support system material specifications（unit：mm）

Number	Foundation type	Column steel pipe	Flat-coupled steel pipe	Diagonal brace steel pipe	Steel
D0~9#	Reinforced concrete strip foundation	Φ720×14	Φ400×8	Φ400×8	Q345
D9~19#	Bored pile foundation	Φ1200×14	Φ720×14	Φ400×8	Q345

The bridge spans are configured as follows: 4 spans of 40 meters each, 4 spans of 40 meters each, 6 spans of 40 meters each, 5 spans of 40 meters each, and 4 spans of 32 meters each, with a total length of 888 meters. This study is based on a representative bridge, and the strait where the bridge is located can experience gusty winds exceeding 10 on the Beaufort scale in the absence of typhoon effects. Adequate clearance height is not guaranteed to ensure safe navigation. During the construction of the supports, the support height exceeds 15 meters, making it a high-modulus support construction.

Finite element model establishment

According to the design drawings, three-dimensional spatial computational models of four-legged lattice-type high modulus supports and six-legged lattice-type high modulus supports were established using finite element analysis software ANSYS for structural simulation analysis. The four-legged lattice-type high modulus support has a height of 41.7 meters and is divided into 722 nodes and 756 computational elements. The six-legged lattice-type high modulus support has a height of 52.4 meters and is divided into 1439 nodes and 524 elements. The finite element models are established as shown in Figure 1 and 2, with the X-direction representing the longitudinal bridge direction, and the Y-direction representing the transverse bridge direction.

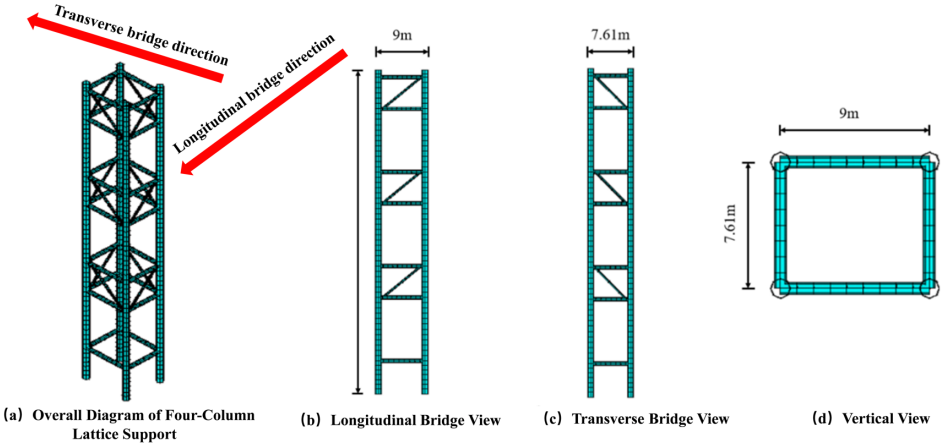

Fig. 1 - Four-Legged Lattice Support

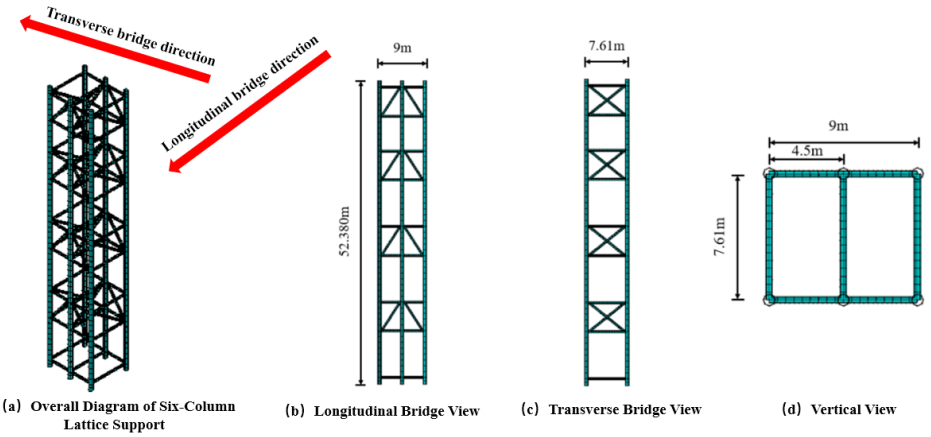

Fig. 2 - Six-Legged Lattice Support

Finite element model structural optimization

Node displacement optimization

In the process of structural optimization design for high-modulus supports under wind loads, displacement deformation is the primary manifestation of the structural stress state. Displacement constraint factors need to be considered in the structural optimization design. By controlling node movements, the deformation of the structure gradually decreases, ultimately meeting the constraints on structural stiffness.

In the structural shape optimization design of high-modulus supports under various load conditions, there are two control conditions: 1) the displacement of specified nodes must satisfy constraint conditions, and 2) the structural mass must be minimized. The mathematical model for the optimization problem is expressed as follows.

$$Findx = [x_1, x_2, \ldots, x_k]^T \tag{1}$$

$$minW = \sum_{e=1}^{n} L_e \rho_e A_e \tag{2}$$

$$u_{il} \leq u_i^*(i = 1,2,\ldots,m; l = 1,2,\ldots,p) \tag{3}$$

$$\underline{x}_j \leq x_j \leq \bar{x}_j(j = 1,2,\ldots,k) \tag{4}$$

Where: W is the mass of the structure; u_{ij} is the displacement of node i under the l-th loading condition; L_e、ρ_e, and A_e are the length, material density, and cross-sectional area of element e, respectively; n is the total number of bar elements in the structure; u_i^* is the upper limit on the displacement of node i under all conditions; m is the total number of constrained node displacements; p is the number of loading conditions; k is the number of design variables; $\bar{x}_j$ and $\underline{x}_j$ are the upper and lower limits of the design for the j-th node coordinate x_j, respectively.

Assuming that the support is subjected to a set of external forces P and is in equilibrium, the use of finite element analysis ensures the continuity of truss structure deformation. The structural equilibrium equations and the overall stiffness matrix, in terms of the change in quantity ΔK relative to node j and the displacement Δx_j, can be linearly expressed as:

$$Ku = P \tag{5}$$

$$\Delta K = \sum_{e=1}^{n_j} \Delta\, k_e \approx \left(\sum_{e=1}^{n_j} \frac{\partial k_e}{\partial x_j} \right) \cdot \Delta x_j \tag{6}$$

In the equation: K is the overall stiffness matrix; k_e is the element stiffness matrix; u is the column array of unknown node displacements; P is the column array of external loads. n_j is the number of elements connected to the movable node j, and $n_j \ll$ n; Δk_e is the change in the element stiffness matrix; Δx_j is the displacement step size of node j to node.

It can be derived that the first derivative of the total stiffness matrix with respect to x_j is equal to the sum of the first derivatives of the element stiffness matrices connected to node j. The formula is expressed as follows:

$$\frac{\partial K}{\partial x_j} = \lim_{\Delta x_j \to 0} \frac{\Delta K}{\Delta x_j} = \sum_{e=1}^{n_j} \frac{\partial k_e}{\partial x_j} \tag{7}$$

Taking the first derivative with respect to the design variable x_j on both sides, we obtain the first derivative of the column array of node displacements with respect to the coordinate x_j, $\frac{\partial u}{\partial x_j}$, and simultaneously left multiply it by a unit virtual load array F^{iT}. The term corresponding to the displacement-constrained node i is equal to unity, while all other terms are zero. The derivative of node i's displacement can be expressed as:

$$F^{iT} \cdot \frac{\partial u_i}{\partial x_j} = -F^{i^T} K^{-1} \frac{\partial K}{\partial x_j} u = -(u^i)^T \frac{\partial K}{\partial x_j} u \tag{8}$$

In the equation, u_i is the column array of node displacements caused by the unit virtual load F^i acting independently on the structure, and it satisfies:

$$K u^i = F^i \tag{9}$$

Substituting equation (7) into equation (9), we can calculate the sensitivity of node i's displacement relative to the movement of node j as:

$$\frac{\partial u_i}{\partial x_j} = -\sum_{e=1}^{n_j} (u_e^i)^T \frac{\partial k_e}{\partial x_j} u_e \tag{10}$$

In the equation, u_e^i and u_e are the column arrays of node displacements caused by the unit virtual load and external load, respectively.

When performing the calculation, it is only necessary to consider the elements in the support structure that are related to node j, and the elements not connected to node j can be omitted. The change Δu_{ij} in node i's displacement relative to the movement of node j can be approximated as:

$$\Delta u_{ij} \approx \frac{\partial u_i}{\partial x_j} \Delta x_j = -\left(\sum_{e=1}^{n_j} (u_e^i)^T \frac{\partial k_e}{\partial x_j} \right) \Delta x_j \tag{11}$$

The value of Δu_{ij} can be either positive or negative, depending on the direction of movement for node j. To reduce the displacement u_i of the specified node in the direction of its constrained value u_i^*, we have:

$$\Delta u_{ij} < 0 \ (j = 1,2, \dots k) \tag{12}$$

The direction of movement for node j is determined as follows:

$$sig(\Delta x_j) = sign\left(\sum_{\theta=1}^{n_j}(u_e^i)^T \frac{\partial k_e}{\partial x_j} u_e\right)(j = 1,2,\dots k) \tag{13}$$

The sig( ) in the equation represents the sign function. It can be seen that the direction of design variable search, i.e., the movement direction of node positions, is determined by sensitivity analysis.

Cross-section variation optimization

In the process of structural optimization design, it is necessary to calculate the response of the structure caused by external excitation. To assess the impact of design parameters on the structure's response, the problem involves solving the rate of change of structural response with respect to parameter variations. Taking the example of a plane bending beam element in the local coordinate system, the stiffness matrix is as follows:

$$k_e = \frac{El}{L^3}\begin{bmatrix} 12 & 6L & -12 & 6L \\ 6L & 4L^2 & -6L & 2L^2 \\ -12 & -6L & 12 & -6L \\ 6L & 2L^2 & -6L & 4L^2 \end{bmatrix} \tag{14}$$

In the calculation process, the plane beam element considers both axial deformation and bending deformation separately. The first-order derivative of the stiffness matrix for axial deformation is computed based on the stiffness matrix of the bar element, while the first-order derivative of the stiffness matrix for bending deformation is calculated using the minimum potential energy principle. From the stiffness matrix of the beam element, it is evident that the stiffness matrix of a pure bending beam element is proportional to the section's moment of inertia and does not include the cross-sectional area A. In most cases, the moment of inertia I of the beam section has a relationship with the cross-sectional area A and can be expressed using the following formula:

$$I = cx^s \tag{15}$$

Where c and s are constants determined by the section shape; x is the design variable.

In other words, when the cross-sectional area A is considered as the design variable, the first-order derivative of the stiffness matrix for the beam element with respect to A is：

$$\frac{\partial k_e}{\partial A} = \frac{\partial k_e^t}{\partial A} + \frac{\partial k_e^b}{\partial I}\cdot\frac{\partial I}{\partial A} = \frac{K_e^t}{A} + \frac{sK_e^b}{A} \tag{16}$$

In the equation, k_e^t represents the stiffness matrix for the bar element, and k_e^b represents the stiffness matrix for the bending element of the beam.

In the process of optimizing the lattice-type support structure, the cross-sectional area A can be decomposed into independent variables: diameter B and thickness T. The sensitivity of the diameter is the first-order derivative of the stiffness matrix for the beam element with respect to B, and the sensitivity of the thickness is the first-order derivative of the stiffness matrix for the beam element with respect to T. Diameter B and thickness T are not independent variables and can be converted to a general formula for differentiation with respect to the independent variable B or T.

In other words, when the beam cross-sectional diameter B is considered as the design variable, the first-order derivative of the stiffness matrix for the beam element with respect to B is:

$$\frac{\partial k_e}{\partial B} = \frac{\partial k_e^t}{\partial A}\cdot\frac{\partial A}{\partial B} + \frac{\partial k_e^b}{\partial B}\cdot\frac{\partial I}{\partial B} \tag{17}$$

The first-order derivative of the stiffness matrix of the beam element with respect to the thickness T of the beam section is given as follows:

$$\frac{\partial k_e}{\partial T} = \frac{\partial k_e^t}{\partial A}\cdot\frac{\partial A}{\partial T} + \frac{\partial k_e^b}{\partial T}\cdot\frac{\partial I}{\partial T} \tag{18}$$

RESEARCH ON WIND-RESISTANT OPTIMIZATION DESIGN BASED ON THE OPTIMAL CRITERIA METHOD

Parameter influence analysis

Analysis of the impact of lattice-type high-modulus support steel pipe diameter on the structure

In order to study the impact of lattice-type high-modulus support steel pipe diameter on the structure, it is assumed that the material of the lattice-type high-modulus support columns has a uniform cross-section and is homogeneous and elastic. Euler's critical load formula is used to calculate the critical load value.

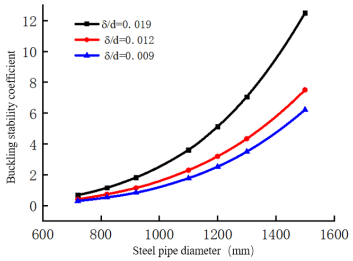

Fig. 3 - Trend of buckling stability factor variation for steel pipe piles with non-proportional diameters.

The ratio of steel pipe wall thickness δ to diameter d is an important control parameter for steel pipe manufacturing. Using this parameter, the critical buckling load factor for steel pipes of different diameters can be calculated. The relationship between the buckling stability factor and steel pipe diameter is shown in Figure 3-1.

From the analysis of the above figure, it can be inferred that when the ratio δ/d of steel pipes is the same, the critical buckling load factor of the structure is positively correlated with the steel pipe diameter, and the overall exponent continuously increases. When the steel pipe diameter remains unchanged and the wall thickness of the steel pipe is increased, the critical load factor of the structure increases with the increase of δ/d. This indicates that the cross-sectional dimensions of the support structure play a crucial role in its stability.

The influence analysis of the number of columns in the lattice-type high-modulus support structure

Reference to the Engineering Project, with Column Steel Pipe Diameters of Φ1200mm for Vertical Columns, Φ720mm for Horizontal Pipes, and Φ400mm for Diagonal Braces, for Further Investigation of the Relationship Between the Support Structure and the Number of Columns. By Establishing Finite Element Models for Single Columns, Double Columns, Four Columns, and Six Columns, the Critical Load Coefficient of the Support Structure is Calculated, as Detailed in Table 2 Below:

Tab. 2 - Statistical data of different column numbers and critical load coefficients of support structures

Column numbers	Critical load coefficients	Model diagram	Remarks
Single column	0.3009	（a）	Single column
Double column	0.3012	（b）	Lateral spacing 9.0m
Four column	10.830	（c）	Lateral 9.0m, Along-Bridge 7.61m
Six Column	10.890	（d）	2× Lateral 9.0m, Along-Bridge 7.61m

The results of different column numbers in Figure 4 show that when the number of columns in the lattice-type support increases in the horizontal plane, it has a limited effect on the structural stability. However, when the number of columns in the vertical plane increases, the critical load coefficient grows rapidly, indicating improved stability and enhanced resistance to external loads. When transitioning to a spatial lattice-type support and increasing the number of columns to 6, the critical load coefficient does not change significantly. Therefore, considering stability and economic factors, it is optimal to choose 4 columns for the steel pipe lattice columns.

Fig. 4 - Calculation results of models with different column numbers

Analysis of the impact of lattice-type high-modulus support spacing changes in the transverse and longitudinal directions

The longitudinal and transverse spacing of lattice-type support columns is an important parameter for evaluating the stability of the support structure. To investigate the relationship between longitudinal and transverse spacing and the stability of the support structure, considering a segment length of 12 meters and an assembly height of 60 meters, we have recorded the numerical variations in different longitudinal and transverse spacings and critical load values as follows.

Tab. 3 - Statistical table of different longitudinal and transverse spacing with critical load coefficients

Longitudinal and transverse arrangement	5.0×5.0m	6.0×6.0m	7.0×7.0m	8.0×8.0m	9.0×9.0m	10.0×10.0m
Critical load coefficient	5.61	6.15	6.36	6.34	6.21	6.03

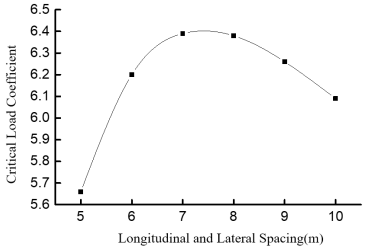

Fig. 5 - Graph of longitudinal and transverse spacing of braces and critical load factor variations.

The curve depicting the variation in longitudinal and transverse spacing and the critical load factor for grid-type braces exhibits a parabolic distribution. The spacing between braces falls within the range of 5-7m. The critical load factor increases with the widening of the brace spacing, reaching its peak at 7m. Between 7m and 10m, there is a decreasing trend in the critical load factor, indicating a decline in bracing stability. Notably, at a spacing of 8m, the critical load factor is slightly lower than at 7m, suggesting the possibility of the maximum critical load factor occurring within the range of 7m-8m. Therefore, for brace design, it is advisable to consider a spacing between 7m and 8m.

Impact analysis of diagonal bracing in grid-formwork high-shoring structures

The primary components of the grid-formwork high-scoring system include columns and horizontal struts. Diagonal bracing, serving as an auxiliary element, introduces certain effects.

Utilizing finite element analysis models for comparative analysis, the impact of diagonal bracing is assessed by contrasting the first three unstable modes.

For a grid-form column support system with diagonal bracing, the first-order critical load factor is 6.28, whereas without diagonal bracing, the factor reduces to 4.91. The second-order critical load factor is 6.46 with diagonal bracing and decreases to 5.18 without diagonal bracing. In the case of the third-order critical load factor, with diagonal bracing, it is 10.86, while without diagonal bracing, it reduces to 8.08. It is evident that the addition of diagonal bracing enhances the critical load factors of the support structure, resulting in an improvement ranging approximately between 25% and 35%. In structural design, diagonal bracing plays a crucial role.

Optimal criterion modification

Optimization is the process of simplifying a problem into a mathematical model that aligns with the practical loading conditions, and solving it through appropriate solution methods. Structural optimization requires determining three key aspects: 1) Independently varying optimization design variables; 2) An objective function concerning the design variables; 3) Constraint functions related to the feasible domain limits of the design variables.

$$\text{Design variables: } \{X\} = [X_1, X_2, \dots X_i, X_N]^T \tag{19}$$

$$\text{Objective function: } min\,imize\big(W(\{X\})\big) \tag{20}$$

$$\text{Constraint function: } \begin{matrix} f_k(\{X\}) = g_k(\{X\}) - g_k^U \le 0 (k = 1,2, \cdots m) \\ X_i^L \le X_i \le X_i^L \end{matrix} \tag{21}$$

In the equation: N is the total number of design variables X_i; m is the total number of constraint functions; $W(\{X\})$ is the expression of the objective function; g_k^U is the limit value; $\underline{X}_i^L$ and $\bar{X}_i^L$ are, respectively, the lower and upper limits of the design variable $\bar{X}_i^L$.

H.W. Kuhn and A.W. Tucker introduced the Kuhn-Tucker (K-T) conditions in 1951, which have become foundational in the field of nonlinear programming. The equation can be rewritten in the following form:

$$L(\{X\}, \lambda_k) = W(\{X\}) + \sum_{k=1}^{m} \lambda_k \left(g_k\{X\} - g_k^U\right) \tag{22}$$

Applying partial differentiation, the quadratic formula, and linear term simplification, we obtain:

$$X_i^{v+1} = X_i^v \left\{1 + \frac{1}{\eta}\left[\left(-\sum_{k=1}^{m} \lambda_k \frac{\delta g_k}{\delta X_i}\right) \Big/ \frac{\delta W}{\delta X_i} - 1\right]\right\}_v \tag{23}$$

In the equation, as the value of η increases, the differences in design variables decrease, controlled by dynamic changes to achieve convergence effects.Before obtaining the new design variables X_i^{v+1}, we first need to calculate the Lagrange multiplier λ_k. Considering the change in constraint functions $\left(g_k^{V+1} - g_k^v\right)$ due to variations in design variables $\left(X_i^{V+1} - X_i^v\right)$, this can be expressed as:

$$g_k^{V+1} - g_k^v = \sum_{i=1}^{N} \left(\frac{\delta g_k}{\delta X}_i\right)_v \left(X_i^{v+1} - X_i^v\right) \tag{24}$$

Considering that after the v+1 iteration, constraint k becomes an active constraint, i.e., we can derive a system of linear equations, expressed as follows:

$$\sum_{s=1}^{m}\lambda_s^v\sum_{i=1}^{N}\frac{\frac{\delta g_k}{\delta X_i}\frac{\delta g_s}{\delta X_i}}{\frac{\delta W}{\delta X_i}}X_i^v=-\sum_{i=1}^{N}\left(\frac{\delta g_k}{\delta X_i}\right)_v X_i^v-\eta(g_k^U-g_k^v) \tag{25}$$

When a value exceeds the predefined upper or lower limit for a variable, it is set equal to the upper or lower limit and remains unchanged within the current design cycle. At this point, the variable becomes inactive and remains unchanged in the next iteration when solving for λ_s^v

$$\sum_{s=1}^{m}\lambda_s^v\sum_{i=1}^{Na}\frac{\frac{\delta g_k}{\delta X_i}\frac{\delta g_s}{\delta X_i}}{\frac{\delta W}{\delta X_i}}X_i^v=-\sum_{i=1}^{Na}\left(\frac{\delta g_k}{\delta X_i}\right)_v X_i^v-\eta(g_k^U-g_k^v) \tag{26}$$

In the equation, Na is the number of active variables. After obtaining the Lagrange multiplier $\{\lambda\}_{m\times1}$ and substituting it into the solution to get X_i^{v+1}, if X_j^{v+1} exceeds the predefined limits of X_j^U or X_j^L, it is set as X_j^{v+1}=X_j^U or X_j^{v+1}=X_j^L, and the solution is carried out in the v+1 iteration.Therefore, when situation X_j^{v+1}>X_j^U (or X_j^{v+1}<X_j^L) occurs in the current iteration, it is possible to modify the equation in the next iteration as the sum of active and inactive variables.

$$\begin{cases} g_k^{v+1}-g_k^v=\sum_{i=1}^{Na}\left(\frac{\delta g_k}{\delta X_i}\right)_v\left(X_i^{v+1}-X_i^v\right)+\sum_{j=1}^{Np}\left(\frac{\delta g_k}{\delta X_j}\right)_v\left(X_j^U-X_j^v\right), X_j^{v+1}\rangle X_j^U \\ g_k^{v+1}-g_k^v=\sum_{i=1}^{Na}\left(\frac{\delta g_k}{\delta X_i}\right)_v\left(X_i^{v+1}-X_i^v\right)+\sum_{j=1}^{Np}\left(\frac{\delta g_k}{\delta X_j}\right)_v\left(X_j^L-X_j^v\right), X_j^{v+1}\langle X_j^L \end{cases} \tag{27}$$

In the equation, Np is the number of inactive variables in the current iteration. The stiffness matrix is modified as follows:

$$\begin{cases} \sum_{s=1}^{m}\lambda_s^v\sum_{i=1}^{Na}\frac{\frac{\delta g_k}{\delta X_i}\frac{\delta g_s}{\delta X_i}}{\frac{\delta W}{\delta X_i}}X_i^v=-\sum_{i=1}^{Na}\left(\frac{\delta g_k}{\delta X_i}\right)_v X_i^v-\eta(g_k^U-g_k^v)+\eta\sum_{i=j}^{Np}\left(\frac{\delta g_k}{\delta X_j}\right)_v\left(X_j^U-X_j^v\right), & X_j^{v+1}\rangle X_j^U \\ \sum_{s=1}^{m}\lambda_s^v\sum_{i=1}^{Na}\frac{\frac{\delta g_k}{\delta X_i}\frac{\delta g_s}{\delta X_i}}{\frac{\delta W}{\delta X_i}}X_i^v=-\sum_{i=1}^{Na}\left(\frac{\delta g_k}{\delta X_i}\right)_v X_i^v-\eta(g_k^U-g_k^v)+\eta\sum_{i=j}^{Np}\left(\frac{\delta g_k}{\delta X_j}\right)_v\left(X_j^L-X_j^v\right), & X_j^{v+1}\langle X_j^L \end{cases} \tag{28}$$

Therefore, when conducting the vv-th iteration of variable optimization using the optimal criterion method, if it is found that the results of the design variables in this iteration exceed the limit values, a new iteration is performed.

Optimization of grid-formwork high-shoring against wind based on geometric nonlinear analysis

Optimization of mathematical computational models

The objective of optimization is to minimize the weight of the grid-formwork high-shoring while meeting the requirements of various mechanical performances. Therefore, the mathematical model for the optimization of wind-resistant grid-formwork high-shoring structures based on geometric nonlinear analysis is as follows:

$$W=\sum_{i=1}^{N\theta}\gamma_i A_i l_i \tag{29}$$

Constraint conditions:

$$\begin{cases} \dfrac{u_{max}}{u^n} \\ \dfrac{\sigma_{max}}{\sigma^u} - 1 \le 0 \\ \dfrac{^c\lambda}{-5} \le -1 \end{cases} \quad (30)$$

In the equation, $^c\lambda$ is the critical load factor considering geometric nonlinear analysis, with a value of $^c\lambda$>5; displacement and stress constraints are set to the same limits as in linear analysis conditions.

Taking a four-legged grid-formwork high-shoring structure as a reference, the structural parameters are set as follows: the width of the shoring in the transverse bridge direction is determined to be 9m. The optimization variables include the thickness of the vertical strut T1, the thickness of the horizontal strut T2, the thickness of the diagonal strut T3, the width of the vertical strut in the along-bridge direction LL, and the diameters of the vertical B1, horizontal B2, and diagonal B3 struts—totaling 7 design variables. The initial design values are set as follows: T1=18 mm, T2=12 mm, T3= =10 mm, L=8000 mm, B1=1400 mm, B2=800 mm, B3=500 mm.

Displacement control follows the People's Republic of China's "Code for Design of Steel Structures" GB50017-2017 B.2, adopting the conservative value L/400. The safety factor for stress is set at 1.2, with a controlled stress of 179 MPa and a buckling coefficient control of 55. Using the ANSYS optimization calculation program with the OPT module, the structure is subjected to displacement, stress, structural stability, and volume sensitivity analyses. The main design variables influencing each control variable are determined, and significant adjustments are made to their design ranges. The sensitivity analysis is shown in Figure 6.

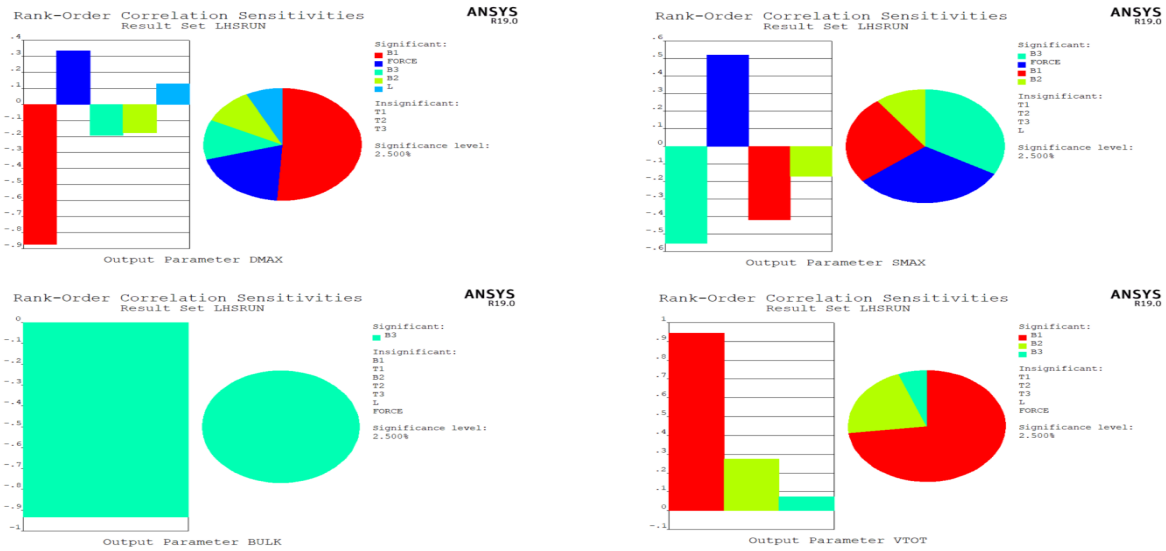

Fig. 6 - Sensitivity analysis of the shoring structure

Performing displacement, stress, structural stability, and volume sensitivity analyses on the model structure, as shown in Figure 5, reveals the following main design variables for each sensitivity: For displacement sensitivity, the primary design variable is the diameter of the vertical strut B1.For stress sensitivity, the primary design variable is the diameter of the diagonal strut B3.For overall stability sensitivity, the main design variable is the diameter of the diagonal strut B3.For overall volume stability sensitivity, the main design variable is the diameter of the diagonal strut B1.

Optimization objectives and constraint conditions must be defined numerically in the command flow so that they can be later read and called for algorithmic optimization. In APDL, extracting output results parameters (using the maximum displacement of the structure as an example) is done with the following command:

/POST1$DMAX=0$NSORT,U,Z$*GET,D_MAX,SORT,,MAX$*GET,D_MIN,SORT,,MAX$IF,ABS,(D_MAX),GT,ABS(D_MIN),THEN$DMAX=ABS(D_MAX)$ELSE$DMAX=ABS(D_MIN)$*ENDIF$PLNSOL,S,EQV,0$GET,EQVMAX,0,MAX

Based on the chosen constraint conditions, the wind-resistant optimization program calculations are conducted following the process outlined in Figure 6.

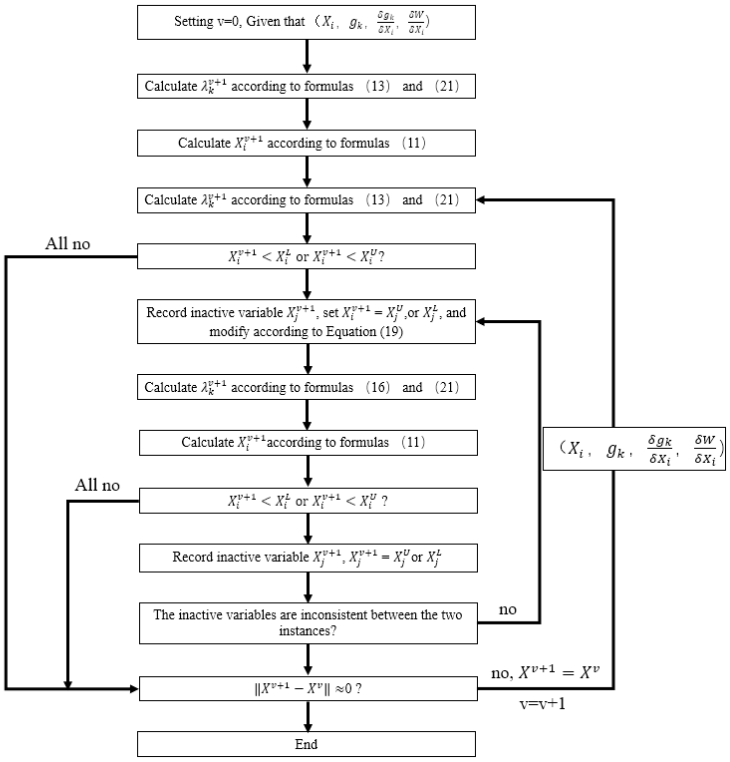

Fig. 7- Modified flow chart of optimal criterion method

Optimization of Mathematical Computational Models

(1) Iterative Results of Constraint Functions

Setting displacement and stress as constraint conditions, with a displacement constraint of 155mm and a stress constraint of 195MPa, plot the displacement response and the iterative representation of maximum equivalent stress as shown in Figures 8 and 9 after computational analysis.

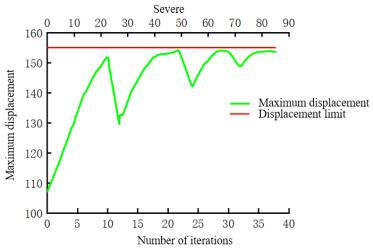

Fig. 8 - Iterative results of maximum displacement response of the structure

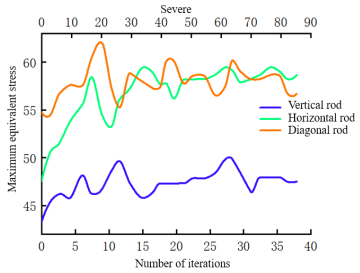

Fig. 9 - Iterative results of the maximum equivalent stress of the structure

(2) Iterative Results of Section Dimensions and Total Weight The iterative results of section dimensions and total weight are shown in Figures 10 and 11, respectively.

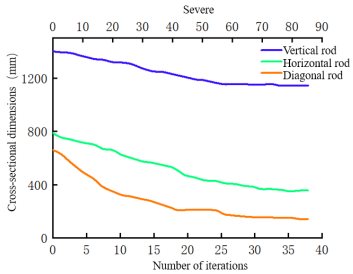

Fig. 10 - Iteration results of section width of member

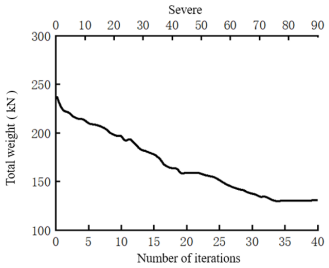

Fig. 11 - The total weight of the structure is iterated

Based on the analysis of the iterative curves above, the following conclusions can be drawn:

1) Geometric non-linear analysis is controlled by the top displacement constraint;
2) The maximum stress value occurs in the lower layer of the component's corner column;
3) The final section dimensions of the component decrease sequentially from the lower layer to the upper layer;
4) The curves exhibit good convergence;
5) Geometric non-linearity has an impact on the support structure.

Critical Load Factor Constraint

Setting the critical load factor as a constraint condition, with a constraint value of 5, perform computational analysis. Plot the iterative results of the structure's critical factor, section dimensions, and total weight, as shown in the respective figures.

(1) Iterative Results of Constraint Functions

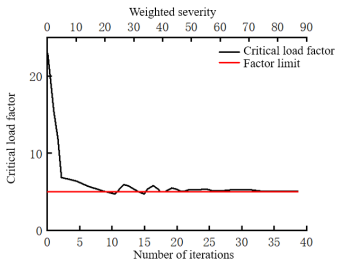

Fig. 12 - Iterative results of critical load factor of structure

(2) Iterative Results of Section Dimensions and Total Weight

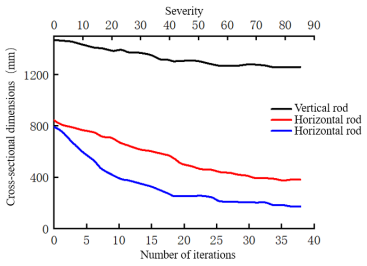

Fig. 13 - Iteration results of section width of member

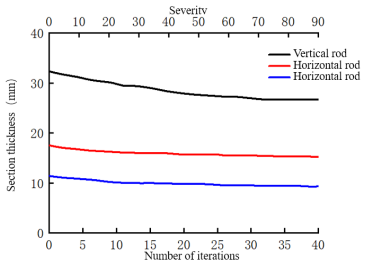

Fig. 14 - Iterative results of section thickness of members

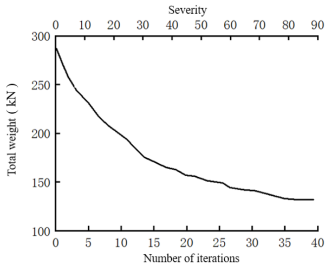

Fig. 15 - The total weight of the structure is iterated

From the analysis of the iterative curves above, the following results are obtained:

1. The critical load factor shows a good convergence in the inner loops, obtaining the corresponding limiting values.
2. The final section width of the components decreases sequentially from the bottom layer to the top layer.
3. All curves eventually converge.
4. The constraint conditions for the support structure are looser than those corresponding to the constraint conditions for the maximum structural displacement.

Displacement, stress, and critical load factor as constraint conditions

Setting displacement, stress, and critical load factor as constraint conditions with displacement constraint at 155mm, stress constraint at 195MPa, and critical load factor constraint at 5. After computational analysis, the iterative results of structural critical factor, maximum displacement response, section dimensions, and total weight are shown in Figures 16 to 21:

Iterative results of constraint functions.

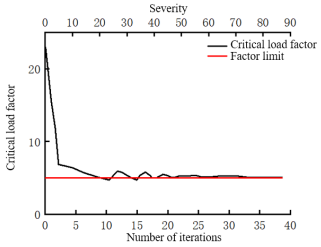

Fig. 16 - Iterative results of structural critical load factor

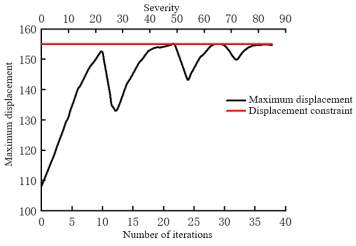

Fig. 17 - Iterative results of maximum displacement response in the structure

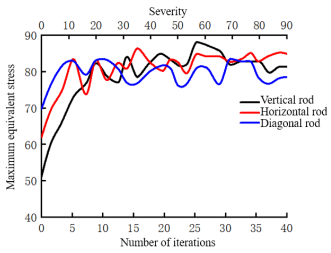

Fig. 18 - Iterative results of maximum equivalent stress in the structure

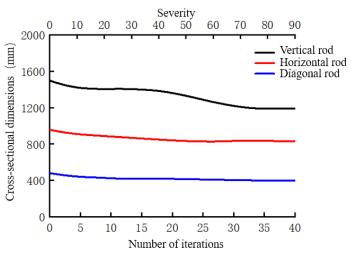

Fig. 19 - Iterative results of component section width

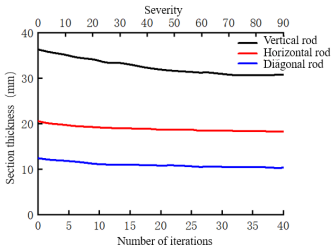

Fig. 20 - Iterative results of component section thickness

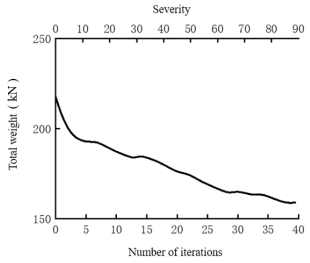

Fig. 21 - Iterative results of structural total weight

The results obtained from the above iterative curve analysis are as follows:

1) The support structure is controlled by the top displacement constraint;
2) The maximum stress value occurs in the lower layer of the component's corner column;
3) The final section dimensions of the component decrease sequentially from the lower layer to the upper layer;
4) All curves eventually converge.

CONCLUSIONS

Based on finite element analysis using ANSYS, a simultaneous optimization of finite element models is conducted for four-leg and six-leg lattice-type supports, considering displacement deformation constraints and stiffness constraints. The study employs buckling stability coefficients and critical load factors to analyze the influence of steel tube diameter, the number of columns, longitudinal and transverse spacing of the support, and diagonal brace structural parameters on the structural stress performance. The optimal design process utilizes a modified optimal criterion method with relevant formulas, and a design flowchart is proposed for the wind-resistant optimization of lattice-type structures satisfying constraints such as stiffness, strength, and critical load factors.

Results obtained are as follows:

1. The iterative curves of constraint functions, section dimensions, and total weight exhibit good convergence under various conditions, indicating the feasibility of the proposed method;

2. When the ratio δ/d of column steel tubes is the same, there is a positive correlation between the structural critical buckling load factor and the steel tube diameter. The section dimensions of the support structure play a crucial role in its stability. The optimal number of columns for spatial lattice-type supports is four. The variation curve of longitudinal and transverse spacing of the lattice-type support and the critical load factor shows a parabolic distribution. Increasing diagonal braces enhances the critical load factor of the support structure;

3. In the optimization process of the lattice-type support structure, the main design variable for displacement sensitivity is the vertical rod diameter (B1); for stress sensitivity, it is the diagonal rod diameter (B3); for overall stability sensitivity, it is the diagonal rod diameter (B3); and for overall volume stability sensitivity, it is the diagonal rod diameter (B1). The set top displacement limit serves a controlling role, and the maximum stress value occurs in the lower-layer corner column.

According to this optimized design process, the multi-leg lattice-type high support structure meets all control values within the national safety standards during construction. This implies an improvement in economic efficiency while ensuring the rationality of the design.

This study will provide a favorable basis for the design of the construction system for future sea-crossing bridges in China. However, there is still room for improvement in the simulation technology of the structure. Further research is needed for the refinement of node finite element simulation and the multi-scale modeling of the overall-local structure.

REFERENCES

[1] Wang Weixu, Wang Bin, Chen Cang, Yao Guanhua, & Huang Liang. 2022. Wind Resistance Analysis of Large Gantry Cranes for Bridge Construction. Highway (007), 067.
[2] Chen Zhaohui, Erik VanMarcke, Sun Yi, & Li Zhengliang. 2008. Review of Extreme Wind Speed Prediction Models for Conventional Wind and Hurricanes. Journal of Natural Disasters, 17(5), 6.
[3] Shen Ke liang. 2023. Analysis of the Construction Technology of Full-support Formwork in Bridge Engineering. Development Guidance of Building Materials (020), 021.
[4] Zhang Zhen. 2023. Application of Single-span Double-layer Bailey Beam Bracket in Cast-in-place Construction of High-pier Bridges. Anhui Architecture.
[5] Wang Shijie. 2021. Study on Wind-induced Response of Lattice-type High Pile in Typhoon-prone Area for Sea-crossing Bridges. (Doctoral dissertation, Northeast Forestry University).
[6] Zhang Yang, & Wang Xiaojing. 2018. Overall Stability Analysis and Design Suggestions for Lattice-type Support. Northern Traffic, (11), 4.
[7] Jiang Yue. 2020 Research on stability bearing capacity of steel column-beams supporting system. (Guilin university of technology).
[8] Law, S. S. , Bu, J. Q. , & Zhu, X. Q. . 2005. Time-varying wind load identification from structural responses. Engineering Structures, 27 (10), 1586-1598.
[9] Li Feng, Zou Lianghao, Liang Shuguo, Chen Yin. 2020. Spatial Correlation Study of Lateral Fluctuating Wind Loads on Grid Structure Tower. Journal of Vibration and Shock, 39(5), 7.
[10] Du Hang, Xu Haiwei, Zhang Yuelong, & Lou Wenjuan. 2022. Wind Pressure Characteristics and Wind-induced Vibration Response of Large-span Flexible Photovoltaic Support Structure. Journal of Harbin Institute of Technology (010), 054.
[11] Guan Xian, & Tang Guohua. 2022. Study on the Mechanical Behavior of Suspended Scaffold Method in the Construction of Reinforced Concrete Composite Beams. Highway Traffic Science and Technology, 39(10), 84-90.
[12] Hwang, J. S. , Kareem, A. , & Kim, H. .2011. Wind load identification using wind tunnel test data by inverse analysis. Journal of Wind Engineering & Industrial Aerodynamics, 99(1), 18-26.
[13] Tan Wenshu. 2017. Research on Wind-resistant Optimization Method of Lattice Tall Structure Based on Genetic Algorithm and Critical Load Factor. (Doctoral dissertation, Guangzhou University).
[14] Yu Xiulei, Liang Shuguo, & Zou Lianghao. 2006. Simplified Calculation of Downwind Wind-induced Vibration Response of Lattice Tower. Journal of Huazhong University of Science and Technology: Urban Science Edition (z2), 3.
[15] Wen Yang, Yu Jiao, & Meng Chunnan. 2022. Study on the Yield Mechanism of the Encased Spherical Plate Branch Node in the Lattice Steel-Concrete Wind Power Generation Tower. Journal of Chongqing University (005), 045.
[16] B. A J ,Ziad A & Abdollah S , et al. 2023 Revisit of underestimated wind drag coefficients and gust response factors of lattice transmission towers based on aeroelastic wind tunnel testing and multi-sensor data fusion. Engineering Structures,278.
[17] Fan Xinliang, & Wang Tong. 2021. Implementation of Finite Element Model Modification Software Based on ANSYS. Mechanical Manufacturing and Automation, 50(1), 4.
[18] Zhou Peng. 2023. Euler Formula Analysis of Critical Force for Local Reinforcement of Tower Components. China Building Metal Structure, 22(3), 86-88.

CIVIL ENGINEERING JOURNAL

Article no. 41

THE CIVIL ENGINEERING JOURNAL 4-2023

A STYLE GUIDE FOR THE CIVIL ENGINEERING JOURNAL USING OF MODERN TECHNOLOGIES FOR VISUALIZATION OF CULTURAL HERITAGE

Karel Pavelka jr. and Jan Pacina

Czech Technical University in Prague, Faculty of Civil Engineering, Thakurova 7, Prague 6, 16629, Czech Republic; karel.pavelka@cvut.cz, jan.pacina@fsv.cvut.cz

ABSTRACT

This paper explores the historical evolution and contemporary applications of photogrammetry and laser scanning in cultural heritage preservation, focusing on the restoration of the Shush synagogue in Iraqi Kurdistan. It traces the development of documentation techniques, highlighting photogrammetry's pivotal role and the impact of the digital revolution. The case study of Project Shush illustrates the practical use of geomatics techniques, advanced 3D modelling, and collaboration with NGOs and authorities. The methodology outlines the use of technologies like terrestrial laser scanners (BLK360, Zeb-Revo) and UAVs, emphasizing their mobility and accuracy. Results detail the project stages, showcasing the creation of a detailed 3D model and the use of Unreal Engine for visualization. The conclusion emphasizes the importance of 3D documentation in cultural heritage and celebrates the success of the Shush synagogue restoration as a testament to technological advancements in preservation. Our research has shown that the joining of different 3D object documentation technologies significantly improves the quality and speeds up the workflow. Comparison of partial point clouds in software CloudCompare on a case study of a smaller historic building showed differences in the internal structure in centimetres, while for the external parts that were covered with vegetation the differences reached up to decimetres.

KEYWORDS

Photogrammetry, Laser scanning, TLS, PLS, Cultural heritage, UAV, Shush, Iraqi Kurdistan

INTRODUCTION

The history of documentation in cultural heritage dates back centuries, with early civilizations employing various methods to record and preserve their cultural artefacts. The Renaissance marked a significant period in the history of documentation, as scholars and artists began to catalogize and document cultural artefacts systematically, manuscripts, and artworks, laying the foundation for modern archival practices. The 19th century saw the establishment of museums and libraries, where systematic documentation became an integral part of preserving and showcasing cultural heritage collections. With the emergence of photography in the 19th century, documentation expanded to include visual records, offering a more accurate and detailed representation of cultural artefacts. At the end of the 19th century, photography began to be used as a source of measurement information and photogrammetry was developed [1]. The early 20th century witnessed the refinement of photogrammetry techniques, especially during World War I and II, when aerial reconnaissance photography played a crucial role in mapping and intelligence gathering. Post-World War II, advancements in photogrammetry accelerated, with the development of analytical plotting instruments and stereo plotters that allowed for more precise measurements and detailed mapping of terrain. The latter half of the 20th century saw the integration of computers into photogrammetric

processes, enabling the automation of measurements and calculations, significantly enhancing the efficiency and accuracy of documentation. Aerial photogrammetry continued to evolve, with the introduction of satellite imagery in the 1970s providing a new dimension to large-scale mapping and environmental monitoring [2,3]. The late 20th century and early 21st century brought about a digital revolution in photogrammetry, with the shift from analogue film to digital sensors, and the development of sophisticated software for image processing and 3D modelling [4, 5, 6]. Unmanned Aerial Vehicles (UAVs) or drones became popular tools for photogrammetric documentation in the 21st century, offering a cost-effective and flexible means to capture high-resolution images for mapping and 3D reconstruction [7,8]. Advances in computer vision, artificial intelligence, and machine learning have further streamlined photogrammetric processes, allowing for faster and more automated extraction of spatial data from images. Photogrammetry serves as a foundational 3D documentation method, utilizing overlapping photographs to reconstruct three-dimensional models. Today, photogrammetrical documentation continues to play a vital role in the interdisciplinary field of cultural heritage, bridging the gap between technology and preservation, and providing valuable insights into our shared past. High-resolution imagery obtained through photogrammetry allows for the detailed documentation of intricate features on artefacts, architectural elements, or artworks, facilitating scholarly analysis and research. Photogrammetry has become an integral part of interdisciplinary collaborations in cultural heritage, fostering connections between archaeologists, historians, conservators, and technologists for comprehensive documentation and analysis [3,4]. Laser scanning has become an important technology in the documentation of cultural heritage. Emitting laser beams to measure distances, LiDAR (Light Detection and Ranging) instrument joined with scanning device generates precise point clouds that faithfully represent the surfaces of objects and environments. This method excels in capturing fine details, making it indispensable for the documentation of complex sculptures, reliefs, and historical landscapes. Introduced in the late 20th century, laser scanning quickly gained prominence in cultural heritage due to its ability to capture precise spatial data by emitting laser beams and measuring their reflections. Today, the laser scanning involves more technologies, especially time-of-flight or structured light scanning. Each technology has its own specifics, and its application depends on the type of object and the required accuracy. Cultural heritage sites, such as archaeological ruins or historical buildings, benefit from laser scanning's ability to create detailed point clouds, offering a comprehensive digital record of the site's topography and architectural features [10]. Laser scanning excels in capturing fine details, making it an invaluable tool for documenting intricate sculptures, reliefs, and other delicate elements of cultural artefacts with minimal physical contact. Mobile laser scanning systems mounted on vehicles or drones enable the efficient documentation of large-scale cultural heritage landscapes, offering a dynamic perspective for research and management purposes. The development of hand-held mobile scanning devices has made the most progress in the last decade. These are commonly called personal laser scanners (PLS), equipped with an inertial measurement unit (IMU), a laser scanning head and often other equipment such as a camera for point cloud colouring or GNSS/RTK (Global Navigation Satellite System Real Time Kinematic) equipment [9, 11, 12, ,13]. Their accuracy is lower compared to static laser scanners (terrestrial laser scanning - TLS), but the advantages are speed of measurement, ease of operation and mobility. Advances in laser scanning technology, including multi-sensor integration and improved data processing algorithms, have enhanced the speed and accuracy of data acquisition, making it a powerful tool for cultural heritage professionals. The integration of 3D documentation methods in cultural heritage preservation has ushered in a new era of exploration, conservation, and understanding. As technology continues to advance, these methods will play an increasingly vital role in safeguarding and promoting the appreciation of our diverse cultural legacy for future generations. Today, the field of documentation in cultural heritage continues to evolve, with advancements in technology, including 3D scanning, virtual reality, and artificial intelligence, offering new tools for more comprehensive and immersive preservation of our shared cultural legacy. The integration of 3D documentation with VR (virtual reality) and AR (augmented reality) technologies allows for immersive experiences in cultural heritage. Researchers,

educators, and the public can virtually explore historical sites, interact with artefacts, and engage in educational experiences that bridge the gap between the past and the present.

Case project Shush

The project's objective involved conducting historical documentation of the sanctuary through contemporary geomatics techniques and generating a digital 3D model of the structure. Following this, it became imperative to create a 3D model depicting the proposed reconstruction solution based on the acquired 3D model. The ultimate deliverable includes an all-encompassing visualization of the building post-reconstruction, incorporating alterations to the surroundings. This visualization serves as a crucial output for the reconstruction investors.

In 2020, the partnership between NGO ARCH[1] and GEMA ART International[2] broadened its scope to include the rescue mission of a shrine located in the Northern Iraqi village of Shush near Akre (Province Duhok, Figure1). Regrettably, the project, backed by US government funding, encountered setbacks during its preparatory phase due to disruptions caused by the Covid-19 pandemic. For centuries, minority religious communities in the mountainous regions of present-day Iraq have thrived, sheltered by the natural landscape. The Shush synagogue, dedicated to the prophet Ezekiel, served its purpose until 1950, when the Jewish population relocated to Israel. Subsequently, neglect and severe climatic conditions led to rapid deterioration of the monument, resulting in the collapse of sections of its exterior masonry. The interior became a refuge for local herds as the surrounding area transformed into pastureland [3], [4].

An extensive survey conducted in 2021, inclusive of detailed photogrammetric 3D documentation, provided crucial data essential for planning the restoration project. Initial groundwork began in September 2022. However, an archaeological survey in the vicinity caused a delay in commencing the actual restoration work until late February 2023, following the winter season. Restoration efforts involved various tasks such as cleaning the masonry, reinforcing perimeter stonework, grouting cracks, reconstructing the roof, conserving historic plaster, restoring the interior floor, rebuilding shrine-retaining walls, and installing an access staircase. The collaboration with the Kurdistan Region Antiquities Authority played a pivotal role in ensuring the project's success. Daily oversight by an archaeologist ensured the proper management of the site. GEMA ART made significant contributions by documenting archaeological discoveries, utilizing advanced 3D modelling techniques, and implementing historical construction methods revealed during the restoration process. Notably, ancient construction techniques inspired the integration of large ceramic vessels into the reconstructed roof, maintaining fidelity to the original methods (Figures 2-3).

The aim of the project was the complete restoration of the historical monument. The first step was to create a complex model using laser scanning and photogrammetry. The precise and detailed documentation became the basis for the reconstruction. The model created by combining geodetic technologies was analysed and completed for the needs of the investor and once approved, the completed model served as the basis for the restoration work.

[1] https://www.archfoundation.in/

[2] https://www.gemaart.com/en/restoration-of-the-shrine-in-shush/

[3] https://www.rudaw.net/english/culture/19102022

[4] https://database.ours.foundation/79E81Y8/

Fig. 1 – Iraq and location of the Shush village (www.mapy.cz)

(a) (b)

Fig.2 –Original status in 2019

Fig.3 – Measurement with laser scanner BLK360

MATERIALS AND METHODS

Transporting large laser scanners and related equipment to remote destinations, in this case Iraqi Kurdistan, poses significant challenges, primarily due to distance, cost of transport and security, which could lead to potential damage during check-in processes and controls. However, recent technological advances in laser scanners have solved these problems. In particular, the emergence of smaller, portable laser scanners has made it easier to work in remote locations, such as the use of the TLS BLK 360 or PLS ZEB REVO in this case study. UAV / DJI Mavic Pro drone was used for photogrammetric work. The images were used to create a photogrammetric textured model not only of the building itself, but also of the wider surroundings. The BLK360 is a miniaturized laser scanner (TLS), easy to transport and easy to use. It has only one button and it can be operated using a tablet or a smartphone. This instrument takes standard panoramic scans in 6 minutes with capturing of HDR (High Dynamic Range) images; the accuracy is 4 millimetres on 10 metres, which is sufficient for most historical structural objects. A standard individual scan from the BLK360 device typically generates a data size of 600 MB. Another innovation on the market is the introduction of handheld mobile laser scanners (PLS). These scanners offer a remarkable advantage in terms of mobility as they allow scanning on the move. This contrasts with traditional land-based scanners that require a stationary position for scanning, which significantly speeds up the process of scanning objects. Initially, the accuracy of these mobile scanners was significantly lower compared to conventional terrestrial scanners. However, continuous technological advances have led to new models being released every year, which have continuously improved their accuracy. For example, FARO's latest product, known as Orbis, represents a breakthrough capability that allows operators to scan on the move as well as static scanning, marking a significant advance in the laser scanner market. Similar new models have been introduced by Trimble (Hoovermap), Leica (BLKGO), GreenValley (LiGrip) and a number of others. The new models are rapidly reducing the accuracy gap between PLS and conventional ground-based scanners (TLS), making their accuracy more comparable. The mobile laser scanner ZEB-REVO Go was used for this study. This PLS, manufactured by GeoSLAM, is a mobile handheld scanner using SLAM (Simultaneous Localization and Mapping) and IMU technology [14]. This technology seamlessly integrates newly scanned sections with the existing dataset and IMU data, reducing the need for extensive post-processing to merge individual scans, unlike ground-based scanners. This PLS operates independently of the GNSS signal, allowing mapping of large areas without signal dependency, for example in mines or building interiors. Older types had relatively low accuracy and measurement data density, but this has improved significantly recently with the advent of new laser heads and improved SLAM technology. The ZEB REVO Go used scans at a rate of 40,000 points per second and the accuracy of the scanned points is 1-3 cm

per 10 meters depending on the type of object. But this is sufficient for many objects. Especially for underground historical objects or ruins it is an excellent tool. A definite drawback is that this type does not have a camera to colour the point cloud. After 32 minutes' walk the instrument generates approximately 200 MB.

Methodology

Based on all the captured data presented in the previous chapter, it was possible to create an accurate and complete 3D model of the object including its cascading surroundings by combining them. The mapping of the surroundings was an essential part of the assignment, as the terrain is very complex, made up of cascades and platforms that need to be considered when planning the reconstruction and creating a new path to the object. Basically, each technology was used to make the most of their efficiency, i.e. laser scanning with a BLK 360 terrestrial scanner was done on the inside of the building and the outside of the garden with emphasis on the transition - outside / inside where the most problems could arise and at the same time there was a need to have these things documented most accurately, because of the thickness of the walls, the interior condition and the position of the interior in relation to the exterior. 8 terrestrial scans were performed. The SLAM technology for the ZEB-REVO mobile laser scanner was beneficial in its fast-scanning process time compared to terrestrial position scanning, so it was possible to scan the object itself including the surroundings to obtain a measurable quality model. A DJI Mavic Pro drone was used to obtain detailed texture and overall view of the area of interest, with a total of 158 images taken from different angles and directions.

Unreal Engine

Unreal Engine (UE) is a game engine created by Epic Games. The game engine includes a set of tools and resources that make it possible to create realistic 3D visualizations, standalone virtual reality applications, and weather simulations, realistic object shading, and more. It is thus a comprehensive software that has almost unlimited visualization possibilities. All final visualization outputs have been processed in this software.

RESULTS

The creation of digital documentation, documents and final design were divided into 3 stages. The first stage consisted of an initial detailed model of the building and a drawing of the required output, i.e. the modifications that needed to be made. Initially in the digital model, and later the basis of this output, the reconstruction of the object. This phase was also based on a thorough consultation with the restoration company, where a consensus had to be found between the possible scope of work and the financial plans for the reconstruction. Several proposals were therefore made, as shown in Figures 4-7.

The main pillar of the first stage was the creation of a detailed and accurate complex 3D model of the object. Here, it was necessary to correctly follow the thickness of the walls and to correctly intersect the windows of the tomb, which were not visible from the outside because they were overgrown with weeds and thorns. However, the partial outlines made it at least clear where they were located. Thanks to the laser scan from the inside of the tomb, where the windows were uncovered, and thanks to the preserved panes, it was clear what the scale of the windows was, then the process of blending with the outside was accurate.

(a)

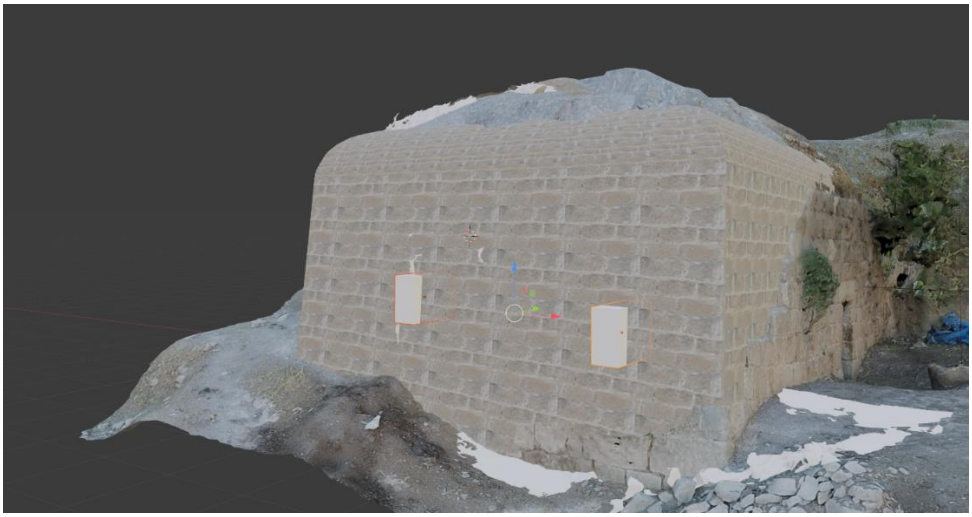

(b)

Fig.4 – Modelling of the object and filling missing parts

In Figures 4 a and b it is possible to see which technology was used to create the windows. The models were superimposed on each other, making it clear from the visible walls on the outside of the tomb where the walls originally ran. Thus, blocks were created from the inner part of the tomb to follow the outline of the window openings. These blocks were interlocked and stretched to go through the whole building, then made transparent to the rest of the model structure, giving us the exact location of the two window openings from the outside.

Now a comprehensive 3D model of the building has been obtained, including all important peripheries such as window openings, existing preserved walls, etc. Now we need to start creating options for the future state, or the final state after the future reconstruction, based on historical photographs and suggestions from structural engineers and architects. The solution was limited by the historic appearance, so the goal is to get as close to the historic condition as possible after reconstruction but strengthening the important sections that caused the couple. The cause of the destruction of the building was of course also the time itself and the lack of interest in the management of the building.

Fig. 5 – Preliminary 3D model

In second stage, the garden space was reduced to approximately half the planned extent in phase 1. The basic initial visualisation was therefore redesigned to meet the new requirements. In addition, a pathway for incoming visitors and caretakers was required at this stage, as currently there was only an inaccessible pathway leading to the building along a cascading slope and this was not a comfortable access.

The final design was therefore a staircase made of boulders available on the slope that did not copy the shortest route but the best one, i.e. cascading up the platforms that the slope contains. It is thus also much more efficient in terms of construction than building a straight staircase and a completely new path. The development of Stage 2 can be seen in Figures5-6.

In this phase, we started to work with the prepared model in Unreal Engine, which is an ideal environment for detailed visualizations including materials, shadows and more. The Unreal Engine gave the project a whole new dimension, including making the tomb and its possible state after reconstruction available in virtual reality [15, 16].

Fig.6 – Preliminary model with a modelled staircase that was finally created as a more natural.

The third and final stage was the final visualisation, which was done exclusively in Unreal Engine. Here, it was necessary to fine-tune the material used for the staircase and the tomb itself to make the visualization of the planned state of the building after reconstruction as realistic as possible.

Fig.7 – Final model with natural staircase

Data processing

The captured data needed to be processed and cleaned of outliers. The data cleaning was largely done in Geomagic Wrap software, which is an ideal tool for minor cleaning of point clouds. By taking dates from different devices, the data could be combined freely to create a detailed model of the synagogue and the surrounding area. As part of the study, a detailed comparison of the output from the instruments used was also carried out. The comparison of the outputs (point clouds) was done in CloudCompare software (Figure 8).

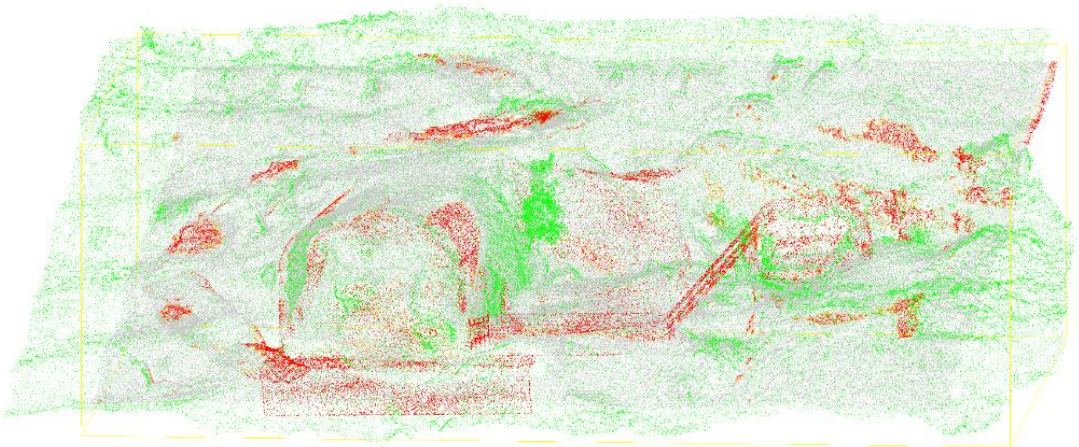

Fig.8 – Representation of the areas that have been added and processed in the final visualisation and VR (red colour shows the added areas - comparison of the UE model and the point cloud from the geodetic survey); however, the UE model is not in point form and therefore the differences are mainly in the parts that have been added to the model.

In general, based on known facts and parameters, the most accurate data should be from the BLK360 terrestrial laser scanner. In the normal case, very close-range photogrammetry would be more accurate, but the photogrammetric model was only processed from drone photos and our equipment did not include a total station or GNSS/RTK to make the photogrammetric model more

accurate due to its size based on control points. Therefore, for our purposes, the laser scanner and the model created from its data replaces the total station and the control points, which is a certain trend in geodesy nowadays. But here we only mention absolute accuracy, the photogrammetric model is essential for this project, as it is the only instrument used that can produce a good quality textured polygon model. The laser scanner measurements here were mainly used for accurate dimensions, model checking and modelling of the interior of the synagogue. The inner part of the synagogue is almost devoid of light, so the use of laser scanners was a logical choice here.

However, it is important to note that there are other parameters besides accuracy and texture generation that need to be considered when comparing the use of equipment and technologies. One of the important factors for this project was device compactness and measurement time (Tab 1).

Tab. 1 - Comparison of technologies used.

	Measurement time	accuracy	output
DJI Mavic pro	20 minutes outside	1 cm	Images only, 1.5 GB
BLK360	1 hour (inside / outside)	4 mm	images and scans, 3.6 GB
ZEB-REVO	10 minutes (inside / outside)	2-3 cm	Scans only, 80 MB, 4,687,083 points

To make an adequate comparison, a more accurate scale had to be given to the photogrammetric model. The scale was calculated from the drone sensor only, which uses the World Geodetic System (WGS84). The unit in the drone without the use of the RTK module is not accurate and thus there are deviations when comparing the model with the laser scanner data. In addition, it was necessary to remove WGS84 system from the model data and use only the local coordinate system of Agisoft Metashape software, which was used to process the photogrammetric data and calculate the texture. Data with WGS84 coordinates cannot be opened in Geomagic Wrap and CloudCompare software, only a straight line is usually shown instead of the model.

On the other hand, laser scanning has a precise scaled model (BLK360 and ZEB-REVO data used here) but no orientation in space. The orientation was done in Geomagic Wrap software, as was the registration (first manual and then global), which merged the models. Scale adjustment of the photogrammetric model was also performed in the same software. Subsequently, all three models were uploaded to CloudCompare, where the actual analysis of each model was performed. First, only the exterior parts were compared, and in the case of the data from both laser scanners, the interior of the synagogue was also compared.

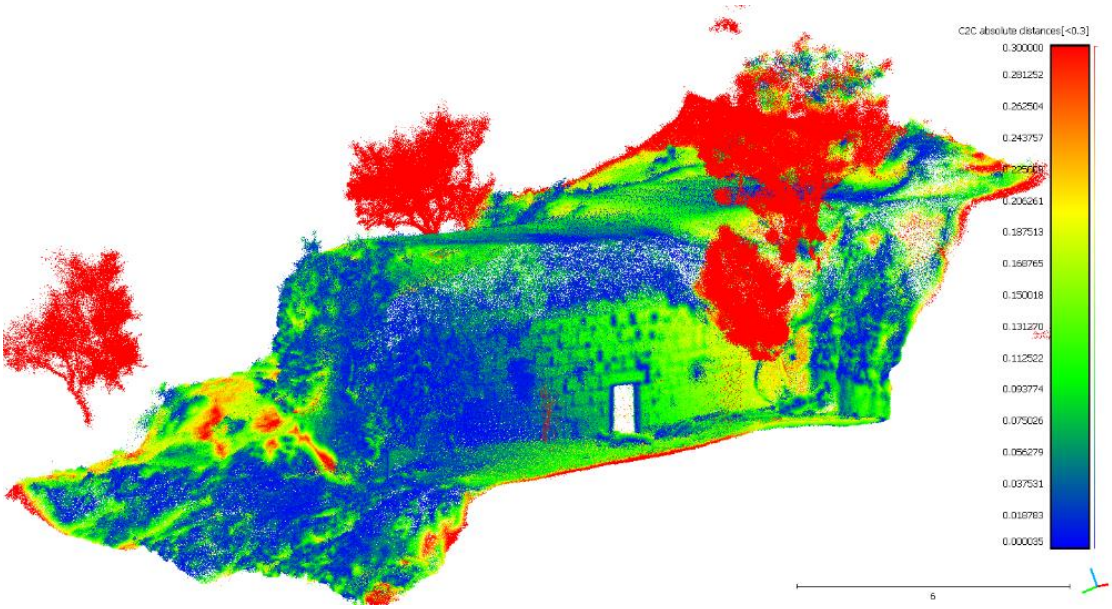

Fig.9 – Comparing of BLK360 and ZEB-REVO data (BLK360 as a reference model)

In Figure 9 it can be observed the difference between the data from the PLS Zeb-Revo and TLS BLK360. The model from BLK360 was always used as reference data. Errors up to 15 cm in position are marked in different colour, larger errors are marked in red. On the structure itself, in the parts that are not covered with vegetation, the error ranges from 2 to 8 cm. In the parts where there is vegetation, including the surroundings with a moraine of fallen masonry and stones, the deviations sometimes exceed 20 cm, which is due to the hidden parts and the density of the points, which is an order of magnitude lower for ZEB-REVO.

Another model compared is the photogrammetric model (Figures 10,11). Since the surveying was done only from drone images, it can be assumed that the model will not be as accurate in space, especially in the parts around vegetation. This assumption was confirmed by comparison. Especially the frontal part that was covered by shrubs was inaccurate compared to the laser scan from BLK360. In Figure 10, points with deviations up to 15 cm are shown in colour (Figure 10), points with larger deviations are shown in red (Figure 11). The areas without points that were created around the model are due to trees that were mostly in that area, shading the terrain. Thus, classically, a digital surface model (DSM) can mainly be generated from aerial photographs.

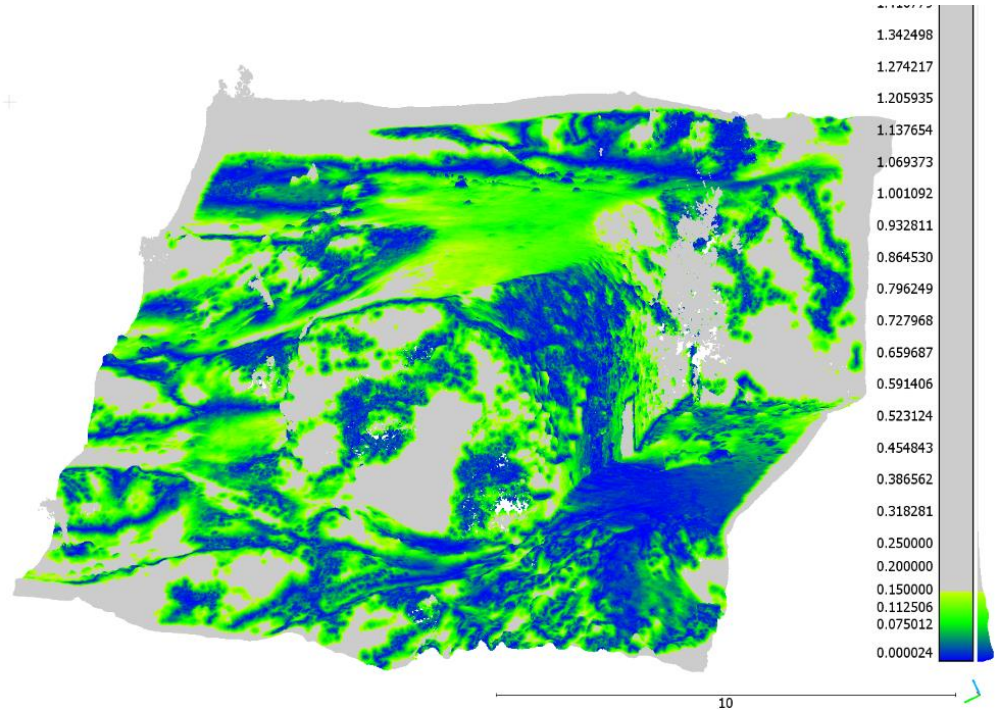

Fig.10 – Comparing of BLK360 and drone photogrammetry (BLK360 as a reference model, points with deviations up to 15 cm)

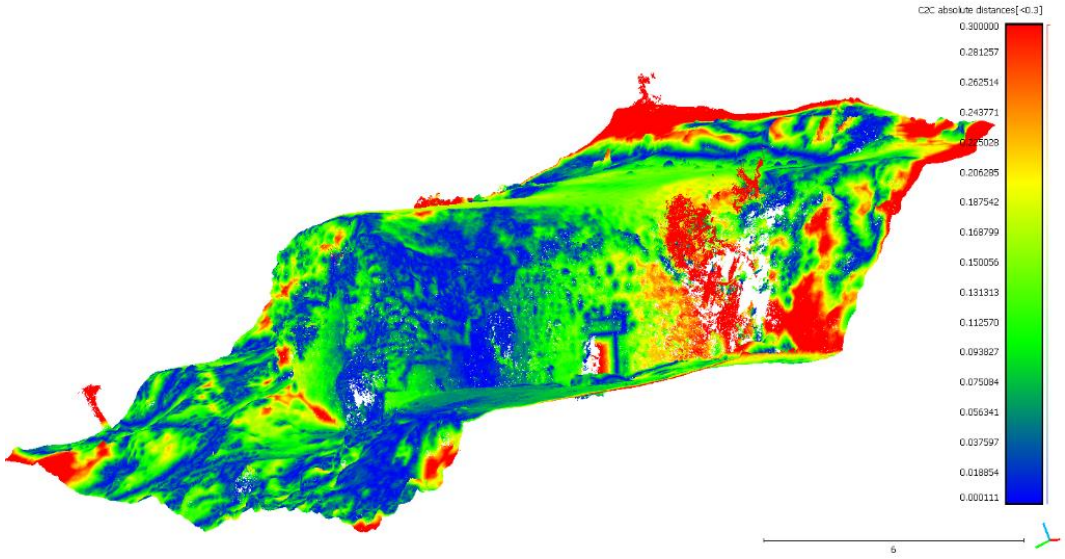

Fig.11 – Comparing of BLK360 and drone photogrammetry (BLK360 as a reference model)

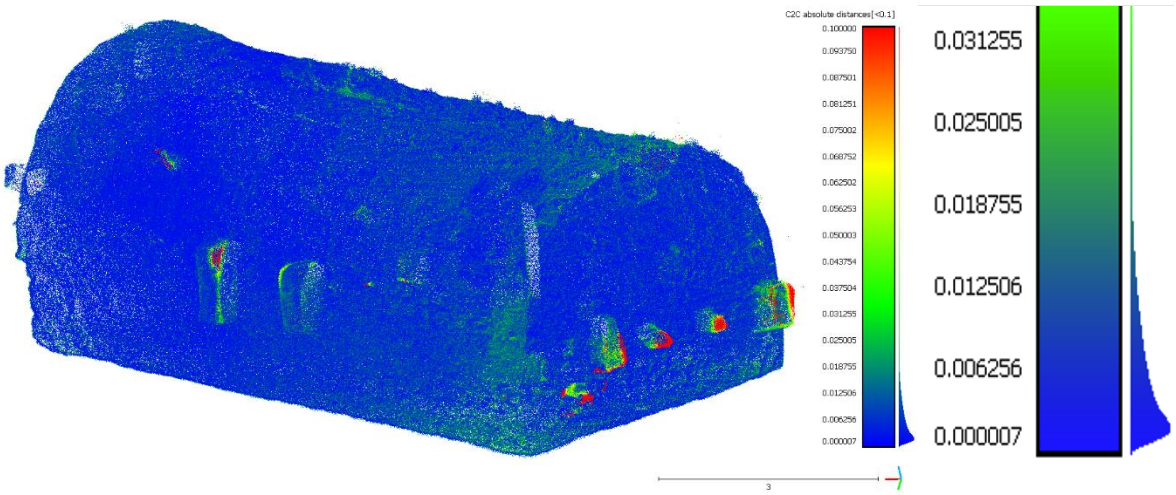

Fig.12 – Inside parts were documented very precise.

When comparing the interior of the synagogue, it was found that for the interior spaces the variations are significantly smaller, which is also due to the basic use of both scanners. Here most of the points were almost identical, with maximum deviations found in the hard-to-reach window areas, which were overgrown with vegetation; however, this can in no way be considered a measurement error. Most of the points were within 1 to 2 cm of the maximum deviation (Fig ure12).

(a) *(b)*

Fig. 13 – Reality and visualization (a,b)

The final visualisation is shown in Figure 13 in comparison with the actual state after the reconstruction, completed in 2023 based on the metric documentation (Figure 14) described in this article.

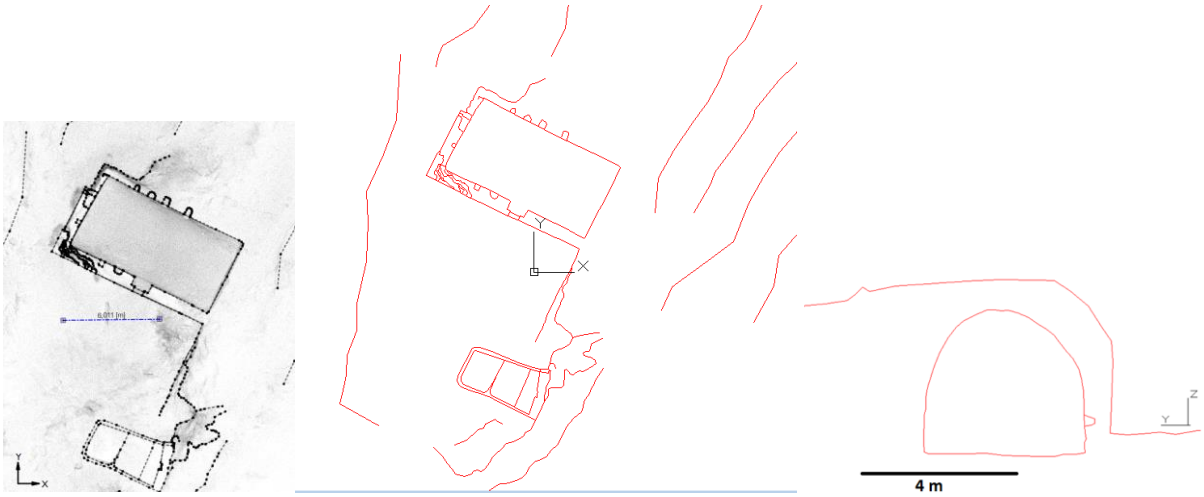

Fig. 14 – Output prom PLS ZEB-REVO - vectorisation of the point cloud (left) and cross-section are very easily done in several minutes (middle and right transfer to ACAD).

CONCLUSION

Within the project, data was acquired by two laser scanners (TLS and PLS) and drone images were taken for photogrammetric processing. The result of the measurements was a visualization created in the UE game engine, which served as a basis for the restorers to plan the work, also point clouds were taken and calculated, which served as a basis for measurements in 3D space and for cross-checking the data. As part of the study, a comparison of the models and technologies used was also carried out. As expected, the most accurate model was the one from BLK360. The main output was to be the previously mentioned visualization and plans, photogrammetric processing was also needed, which resulted in a model including high quality texture. The inaccuracies in the surrounding area were not entirely significant, the result was a model of the surroundings with sufficient resolution for the restorers, plans and sections for the construction activity. The virtually completed model was pre-approved by the investor, so here visualization and virtual reality helped significantly, which is now becoming a desirable tool and output for planning and visualization.

ACKNOWLEDGEMENTS

This work was supported by the Czech Technical University in Prague grant SGS23/052/OHK1/1T/11.

REFERENCES

[1] Albertz, J., Wiedemann, Al. 1998. From Analogue to Digital Close-Range Photogrammetry. Online https://www.researchgate.net/publication/2332200_From_Analogue_To_Digital_Close-Range_Photogrammetry

[2] Kovacs, F. 2015. Documentation of cultural heritage; techniques, potentials, and constraints. ISPRS - International Archives of the Photogrammetry, Remote Sensing and Spatial Information Sciences. XL-5/W7. 207-214. 10.5194/isprsarchives-XL-5-W7-207-2015.

[3] Sužiedelytė-Visockienė J, Bagdžiūnaitė R, Malys N, Maliene V. 2015. "Close-range photogrammetry enables documentation of environment-induced deformation of architectural heritage". Environmental Engineering and Management Journal. 14 (6): 1371–1381.

[4] Marčiš, M., Barták, P., Valaška, D., Fraštia, M., Trhan, O. 2016. USE OF IMAGE BASED MODELLING FOR DOCUMENTATION OF INTRICATELY SHAPED OBJECTS. ISPRS - International

Archives of the Photogrammetry, Remote Sensing and Spatial Information Sciences. XLI-B5. 327-334. 10.5194/isprs-archives-XLI-B5-327-2016.
[5] Li, Y., Du, Y., Yang, M. et al. A review of the tools and techniques used in the digital preservation of architectural heritage within disaster cycles. Herit Sci 11, 199 (2023). https://doi.org/10.1186/s40494-023-01035-x
[6] Shults, R.; Levin, E.; Aukazhiyeva, Z.; Pavelka, K.; Kulichenko, N.; Kalabaev, N.; Sagyndyk, M.; Akhmetova, 2023. N. A Study of the Accuracy of a 3D Indoor Camera for Industrial Archaeology Applications. Heritage, 6, 6240-6267. https://doi.org/10.3390/heritage6090327
[7] Šedina, J.; Housarová, E.; Raeva, P. 2019. Using RPAS for the detection of archaeological objects using multispectral and thermal imaging European Journal of Remote Sensing., 52(sup1), 182-191. ISSN 2279-7254.
[8] Bouček, T.; Stará, L.; Pavelka, K.; Pavelka, K., Jr. 2023. Monitoring of the Rehabilitation of the Historic World War II US Air Force Base in Greenland. Remote Sens., 15, 4323. https://doi.org/10.3390/rs15174323
[9] Pavelka, K.; Matoušková, E.; Pavelka, K., Jr. 2023. Remarks on Geomatics Measurement Methods Focused on Forestry Inventory. Sensors, 23, 7376. https://doi.org/10.3390/s23177376
[10] Grussenmeyer, P.,Alby, E., Assali, P.,Poitevin, V., Hullo, J.-F., Smigiel, E. 2011. Accurate Documentation in Cultural Heritage by merging TLS and high-resolution photogrammetric data. Proceedings of SPIE - The International Society for Optical Engineering. 8085. 10.1117/12.890087.
[11] Rodríguez-Gonzálvez, P., Jiménez Fernández-Palacios, B., Muñoz-Nieto, Á., Arias, P., González-Aguilera, D. 2017. Mobile LiDAR System: New Possibilities for the Documentation and Dissemination of Large Cultural Heritage Sites. Remote Sensing. 9. 189. 10.3390/rs9030189.
[12] Di Stefano, F., Chiappini,S., Gorreja,A., Balestra, M., Pierdicca, R. 2021.Mobile 3D scan LiDAR: a literature review, Geomatics, Natural Hazards and Risk, 12:1, 2387-2429, DOI: 10.1080/19475705.2021.1964617
[13] Kukko, A., Kaartinen, H., Hyyppä, J., Chen, Y.W. 2012. Multiplatform Mobile Laser Scanning: Usability and Performance. SENSORS, 12, p. 11712-11733 DOI:10.3390/s120911712
[14] Malinverni, E. S., Pierdicca, R., Bozzi, C.A., Bartolucci,D. "Evaluating a Slam-Based Mobile Mapping System: a Methodological Comparison for 3D Heritage Scene Real-Time Reconstruction" . 2018. Metrology for Archaeology and Cultural Heritage (MetroArchaeo), Cassino, Italy, 2018, pp. 265-270, doi: 10.1109/MetroArchaeo43810.2018.13684.
[15] Gaafar, H. 2015. Virtual Reality: A Technological Tool for Preserving Built Heritage. Journal of Association of Arab Universities for Tourism and Hospitality. 12. 121-134. 10.21608/jaauth.2015.67444.
[16] Pavelka, K.jr.; Raeva, P. 2019. Virtual museums - the future of historical monuments documentation and visualization In: Int. Arch. Photogramm. Remote Sens. Spatial Inf. Sci. International Society of Photogrammetry and Remote Sensing, p. 903-908. XLII-2-W15. ISSN 2194-9034.

CIVIL ENGINEERING JOURNAL

Article no. 42

THE CIVIL ENGINEERING JOURNAL 4-2023

FLAT ROOF CLASSIFICATION AND LEAKS DETECTIONS BY DEEP LEARNING

David Zahradník, Filip Roučka and Linda Karlovská

Czech Technical University in Prague, Faculty of Civil Engineering, Department of Geomatics, Thákurova 7, Praha 6, Czech Republic; david.zahradnik@fsv.cvut.cz

ABSTRACT

This paper presents an efficient and accurate method for detecting flat roof leaks using a combination of unmanned aerial vehicles (UAVs) and deep learning. The proposed method utilizes a DJI M300 drone equipped with RGB and thermal cameras to capture high-resolution images of the roof. These images are then processed to create orthomosaics and digital elevation models (DEMs). A deep learning model based on the U-NET architecture is then used to segment the roof into different classes, such as PVC foil, windows, and sidewalks. Finally, the damaged insulation is identified by analyzing the temperature distribution within the PVC foil segments. The proposed method has several advantages over traditional inspection methods. It is much faster and efficient. An UAV can collect images of a large roof in a matter of minutes, while traditional methods can take several days or weeks. The orthomosaics and temperature maps generated by the UAV are much more detailed than the images that can be collected by a human inspector. Third, the UAV-based system is safer. The UAV can collect images of the roof without the need for a human inspector to climb onto the roof, which can be dangerous. The results of this study show that the proposed method is an effective and accurate way to detect flat roof leaks. The deep learning model was able to achieve an overall accuracy of 95% in segmenting the roof into different classes. The method was also able to identify damaged insulation with a high degree of accuracy.

KEYWORDS

Thermography, Remote sensing, CNN, U-NET, Flat roof leak detection, Deep learning

INTRODUCTION

Flat roofs in large industrial halls are the weakest link in the whole building. A flat roof is characterized by its low pitch, which gives the advantage of covering a large area at a lower cost than pitched roofs. The flat roof has one major drawback in the form of slow rainwater drainage. Flat roofs can have a slope almost to the horizon, i.e. in the range of 0-1 degrees, which is often used on modern buildings or to create a roof terrace. Low pitch, which ranges between 1-5 degrees, is a common choice for commercial buildings and allows for a variety of uses such as solar panels or roof gardens. Roofs with a moderate pitch (5-10 degrees) are suitable for residential and commercial buildings and allow for relatively easy maintenance and efficient drainage. Due to the slow rate of rainwater runoff, great emphasis is placed on the design of flat roofs and their subsequent control according to the composition.

There are several compositions of flat roofs, and each plays a key role in providing stability, insulation and weather protection to this modern roof structure. We start with the roofing material, which is the first layer that forms the outer surface of the roof. This covering can be made from a variety of materials such as asphalt board, PVC sheeting, EPDM (ethylene propylene diene monomer rubber) rubber membranes, TPO (thermoplastic olefin) sheeting or concrete tiles, and is designed to resist weathering and provide an aesthetically pleasing appearance like on Figure 1.

This is followed by a waterproofing layer, which is key to keeping the roof dry. This layer prevents water from penetrating the structure and can be made of different waterproofing materials such as bitumen sheeting or liquid waterproofing. This is followed by insulation, which serves to maintain the interior temperature and ensure the energy efficiency of the building. Insulation materials include foam, mineral wool, expanded polystyrene (EPS) or extruded polystyrene (XPS). The drainage system, comprising the roof pitch and drainage elements such as gutters, downspouts and roof mats, is another important element. Its purpose is to quickly drain rainwater and prevent water from standing on the roof, which could cause failures. Security against wind and weather can be achieved by using a wind barrier.

Fig. 1 – Example of typical flat roof

Flat roofs covered with PVC membranes or even other membranes are susceptible to cracks, holes and other wear and tear caused by careless handling during construction, degradation from UV rays or others. Rainwater subsequently runs off through the hole into other layers of the roof composition. The water can remain in the waterproofing layer where it causes a reduction in the functionality of the thermal insulation in which the insulation becomes a conductor of heat. Water can seep through to the inside of the building and damage the interior and equipment of the building. An example of a flat roof leak is visible in Figure 2.

Regular inspection of flat roofs is key to addressing leaks effectively. Various methods exist for detecting holes in PVC foil roofing, including visual inspection, electropulse testing, needle testing, and smoke testing. These non-destructive techniques enable precise localization of holes in small areas, typically within a radius of about 0.5 meters. However, for larger roofs exceeding 10,000 square meters, employing these methods can become costly. An alternative solution for such extensive roofs involves thermography conducted by unmanned aerial vehicles (UAVs), offering efficient detection and assessment of leaks.

Thermography offers a non-invasive glimpse into the building's health, but accurate interpretation hinges on meticulous data acquisition. Surface emissivity, the culprit of varied thermal signatures even in identical materials, can be tamed through combined thermal camera and contact thermometer measurements. Reflected apparent temperature, another influential factor, is addressed by incorporating a reference object for subsequent corrections. Atmospheric attenuation, caused by air temperature and humidity, is easily mitigated by post-processing corrections based on weather station data. Finally, the camera-object distance, automatically embedded in modern thermograms, eliminates distance-related biases. By diligently accounting for these factors, thermography empowers researchers and professionals with reliable data to pinpoint heat loss,

thermal anomalies, and potential damage, paving the way for optimal building health and energy efficiency.

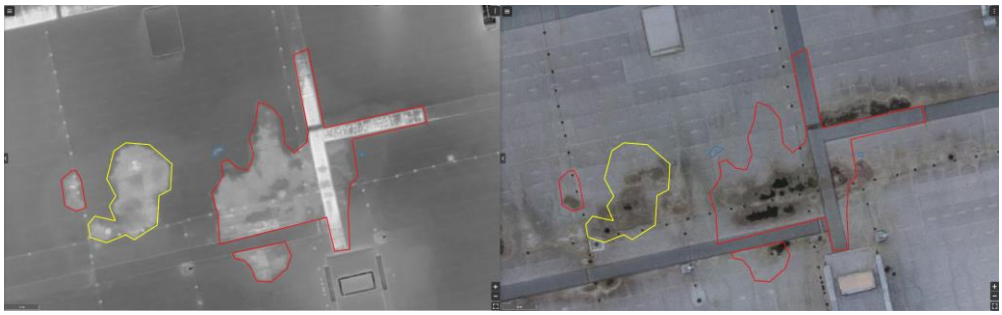

Fig. 2 – Flat roof leak sample

Thermal images captured by terrestrial thermal cameras require adjustments for perspective correction [1] and compensation for reflected longwave radiation from the Sun [2]. Despite their low resolution, thermal images can be processed using SfM (Structure from Motion) techniques [3]. Combining RGB images with thermal images enhances model detail [4], and aerial thermal imaging complements terrestrial coverage [5].

Detecting defects becomes challenging due to shadows, addressed either by capturing images under cloudy conditions or by segmenting thermal images for analysis [6]. Aerial thermal imaging, utilizing uncooled thermal cameras, suffers from vignetting nonuniformity, necessitating temperature calibration for accuracy [7]. Moreover, aerial thermography aids in calibrating building envelope models to meet energy efficiency standards [8-9].

The use of thermal cameras on drones has only recently begun. Lightweight thermal cameras had very low resolution and it was practically difficult to process the data by SfM. It was only about five years ago that improvements were made, the resolution of thermal cameras was increased and the software was adapted [10].

Thermography is an important tool in modern engineering and construction, allowing non-invasive detection and evaluation of defects in structures without compromising their integrity. To find a flat roof leaks, the total area of the roof must be recorded. It is therefore easier to use UAVs for data collection and subsequent processing of thermograms into orthomosaics than single thermograms. Thermograms that capture thermal distributions can be processed similarly to standard RGB images, except that they have a lower resolution. Professional thermal imaging cameras often offer a resolution of 640x512 px, which is significantly lower than standard RGB images. This limitation must be considered when photogrammetrically processing thermographic data [11-15].

Convolutional Neural Networks (CNNs) represent a class of deep learning architectures adept at tasks like image recognition and processing. Inspired by the human visual cortex, CNNs comprise layers designed to process input data hierarchically. At the outset, CNNs usually feature a convolutional layer tasked with feature extraction from the input image. This layer employs filters, small weight matrices, applied across different regions of the input, resulting in feature maps that encode detected features. Following the convolutional layer, a pooling layer is typically employed to downsample the feature maps, reducing their size while retaining essential information. The common max pooling operation selects the maximum value within specified regions of the feature map. This sequence of convolutional and pooling layers iterates through the network, progressively extracting more intricate features. Finally, a fully connected layer often concludes the CNN, responsible for classifying the input into predefined categories. [16] CNNs find wide-ranging applications, including land cover classification [17], tree species detection [18], and damage assessment following earthquakes [19].

U-Net stands out among convolutional neural network (CNN) architectures due to its specialization in pixel-level segmentation tasks, scheme of the network is in Figure 3. While traditional CNNs typically classify entire images, U-Net excels at identifying individual pixels belonging to specific classes within an image. This capability makes it particularly well-suited for tasks such as object detection, semantic segmentation, and instance segmentation. In drone orthophotos, U-Net can be trained to distinguish various elements such as buildings, roads, vegetation, water bodies, or even specific objects based on the application [21]. Through segmentation, this process effectively isolates these elements from the background, enabling detailed analysis and quantification. For instance, U-Net has been applied to scenarios such as detecting fallen trees after hurricanes or other disasters [22] and windthrow events [23]. Deep learning detection isn't limited to RGB or satellite data inputs. While RGB images are commonly used as the primary dataset, and most backbone models require RGB images, digital elevation models (DEMs) can also be utilized. Multi Directional Hillshade based on DEM data with three bands with 8 bits similar to RGB are suitable for Deep learning [24]. Another option is to leverage elevation data directly from the DEM, along with derived features such as slope (ranging from 0° to 90°) and terrain curvature [25]. These alternative data sources provide additional information that can enhance the capabilities of models like U-Net in various applications.

Deep Learning is also usable for Thermal abnormality detection. RGB images are used for the segmentation of visible buildings into walls, windows and doors and abnormality is localized by the temperature threshold of the anomaly area determined from the multimodal temperature distribution of the target domain [26].

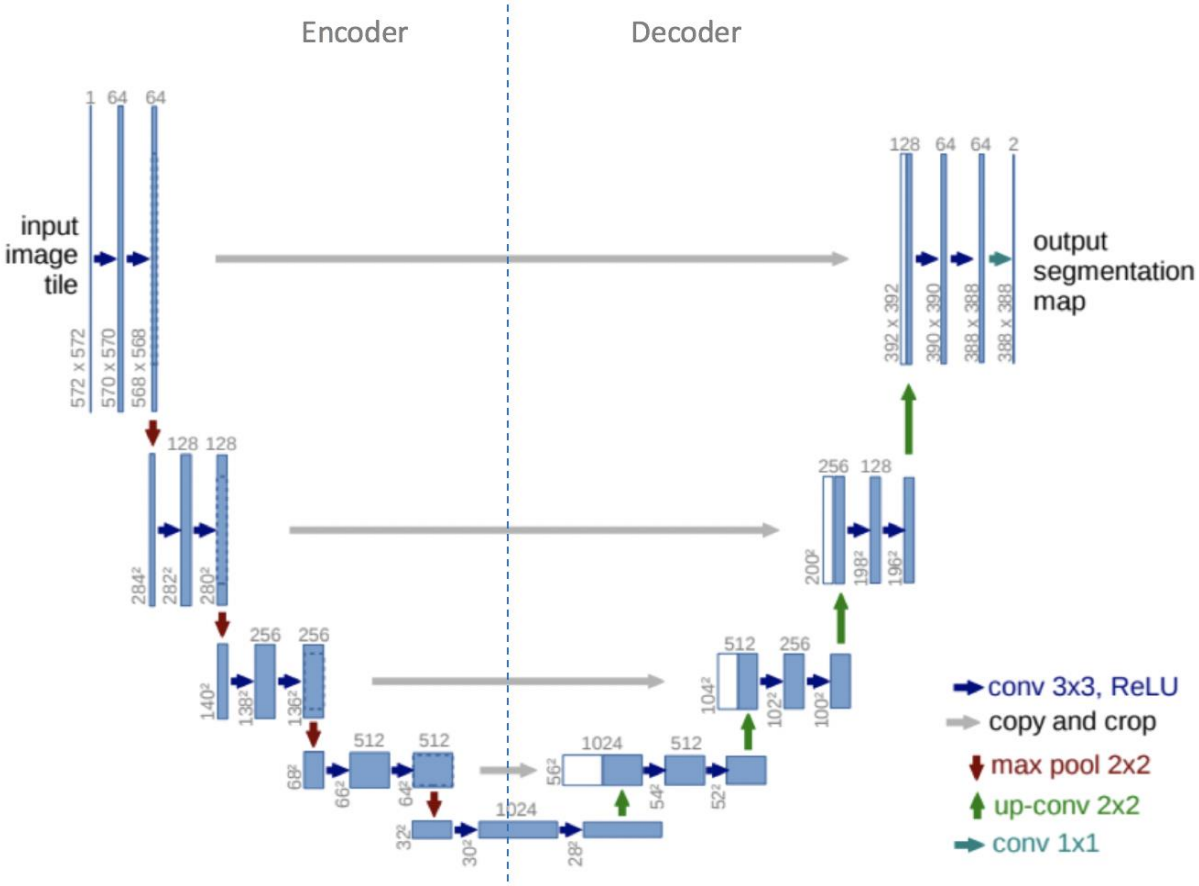

Fig. 3 – U-NET scheme [20]

METHODS

Testing data

Dozens of flat roofs were used for testing, flown from 2021 to 2024. The total area exceeds over 825,000 m2 of flat roof area. Data collection was carried out on selected halls across the Czech Republic with implementation by NDN Tech company. The roofing on all flat roofs was made of PVC foil, on which flat roof leaks were searched. Roofs contain other categories like windows, walking paths, lightning rods and components, the percentage is in Figure 4.

Data for roof leak detection was collected using a DJI M300 drone equipped with a DJI P1 RGB camera and a DJI H20T thermal camera. RGB images were collected during the day to ensure good lighting conditions for the creation of a digital elevation model (DEM) and an RGB orthomosaic. Thermal images were collected after sunset to take advantage of the thermal contrast between the insulation and the surrounding environment.

High thermal contrast is essential for accurate leak detection. This contrast is most pronounced during the cooling and heating phases of the day when the insulation and the surrounding environment are at different temperatures.

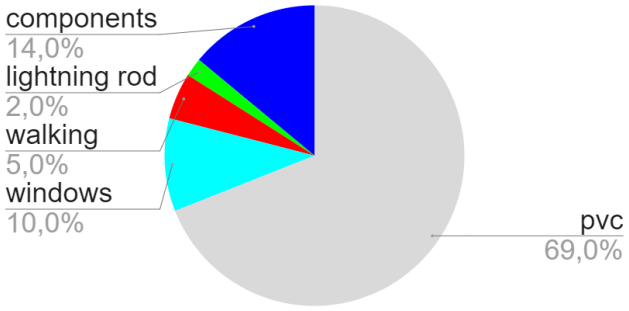

Fig. 4 – Diagram of the percentile of class on the roof

Workflow of automatic flat roof leak detection

The full workflow consists of several steps based on image collection, preprocessing raw images, processing Ortomosaic and DEM in Agisoft Metashape, preprocessing raster data, training and applying the CNN model, raster segmentation and classification of a flat roof leak. The Workflow scheme is visible in Figure 5.

Data is collected by DJI M300 with DJI P1 and DJI H20T camera with automatic planning mission over a flat roof. All images have coordinates from the RTK module connected to the nearest GNSS permanent station. RGB images were captured during the day with good light conditions. TIR images were captured after sunset to eliminate reflected radiation and spot radiation emission with high contrast between damaged insulation and fine. Image specifications are in Table 1 below.

TIR images captured on UAV contain relative temperature and raw data. For absolute material temperature, TIR images must be calibrated by material emissivity, reflected radiation, atmospheric radiation, air temperature, humidity and distance from the object. Most elements are known from auxiliary measurements except material emissivity. Material emissivity is known from laboratory tests, but in real conditions, emissivity is far from the laboratory value. During the data acquisition method of determination, material emissivity and absolute material temperature were found as calibration of the thermograms. Calibration of the thermograms is performed using temperature calibration points. At the calibration points the absolute temperature is measured with a contact thermometer. For thermograms with a captured calibration point, the emissivity of the

material is determined retrospectively and applied to the rest of the thermograms in the TIR dataset. Thermal calibration points are selected on the PVC foil of the flat roof. The temperature of these points is measured before the UAV flies and after to control temperature drop. Points are signalized by an aluminium target to be visible on TIR images.

RGB images are processed in Adobe Lightroom from raw to jpg to correct exposure, fix highlights and pull shadows. The images are then processed in Agisoft Metashape to create DEM and RGB orthomosaics. Image coordinates sometimes contain the wrong position due to a lack of mobile signal when using GNSS correction. To avoid this problem, it is better to align the photo relative and after alignment apply georeferencing by image coordinates. Images with wrong coordinates contain higher position errors and fine georeferencing is prevented.

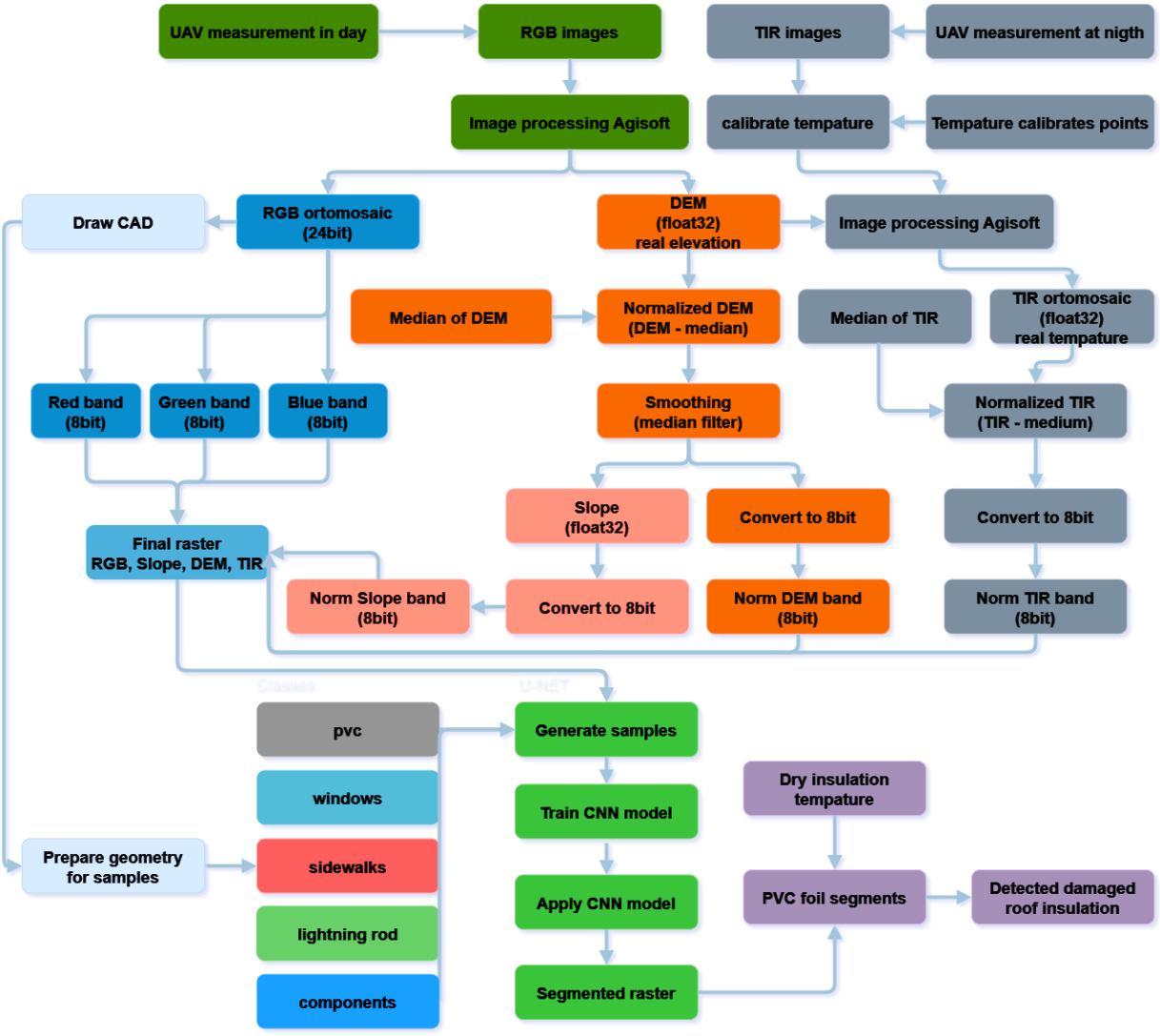

Fig. 5 – Process scheme

Processing of TIR images in Agisoft Metashape is done as RGB images except for DEM computation. Due to the low resolution of TIR images, it is better to use DEM from RGB images. Georeferencing with RTK coordinates allows the blending of RGB and TIR datasets without common control points. Ortho Mosaicing of the TIR dataset is based on DEM from the RGB

dataset. Results from image processing in Agisoft Metashape are RGB orthomosaic (24bit), DEM (32bit float), and TIR orthomosaic (32bit float).

Tab. 1 - Methods of processing time

	RGB images	TIR images
cameras	DJI P1	DJI H20T
resolution [px]	8192x5460	640x512
lens [mm] / Equival.	35	58
FOV [°]	63.5	40.6
time	day	sunset
above ground level (AGL) [m]	80	50
ground sample distance (GSD) [cm]	1	4.4
Overlap	80%, 60%	90%, 80%

Before training CNN (Convolutional Neural Network) model, rasters must be united into the same data type. Different data types are not allowed by the CNN model like 8bit vs. 32bit float. Most CNN models work with RGB data due to the most common sensor. Thermal data for the detection of flat roof leaks are also valuable information for classification by the CNN model. Objects on flat roofs are made from different materials with different emissivity and temperatures shown on thermograms in Figure 6. For example, the ventilation temperature on flat roofs is temperature-dependent on the cooling or heating process. The colour may be the same as PVC foil but the temperature is diametral different, this will help the CNN model to differentiate objects. Problems appear when each flat roof is inspected at a different time and season, and air condition and building operating temperatures are different. For purposes of the CNN model, data must be normalized by the median of TIR orthomosaic, which is the average temperature of PVC foil. Normalization excluded different temperatures across flat roof datasets.

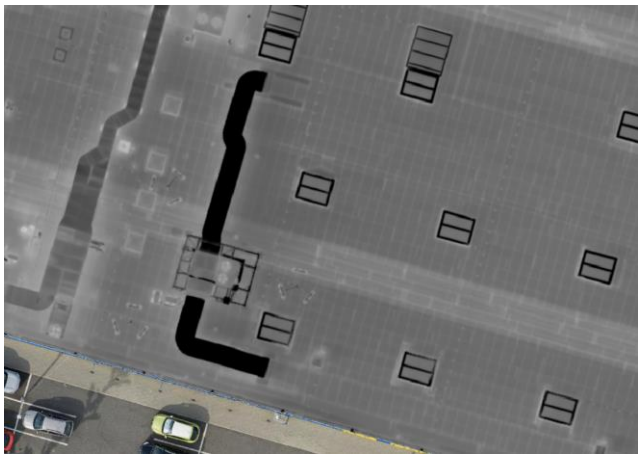

Fig. 6 – Example of TIR orthomosaic

During the photogrammetry process in Agisoft MetaShape to achieve RGB and TIR orthomosaic DEM is created. DEM can extract useful information for the CNN model like altitude and slope. Altitude has the same problem as temperature, it is unique on each flat roof. Each building is built in a different area with some altitude. The usage of raw height from DEM for the CNN model will be not sufficient. Dem must be normalized by the median of DEM values, which is the height of a flat roof. The flat roof value on normalized DEM will be 0; other components will have different values. Some flat roofs have different levels, each level can be inspected for flat roof leaks. A flat roof level has a value other than 0 on normalized DEM and the CNN model can misclassify the level. The solution is to calculate slope based on DEM, but DEM by photogrammetry process may contain noise on PVC foils because of low contrast on RGB images and GSD. Due to the issue, DEM must be filtered to achieve smooth values Figure 7. For smoothing DEM used a median filter with a 3x3 kernel. After the smoothing slope can be calculated and the wrong values on PVC foil disappear, the comparison is visible in Figure 6.

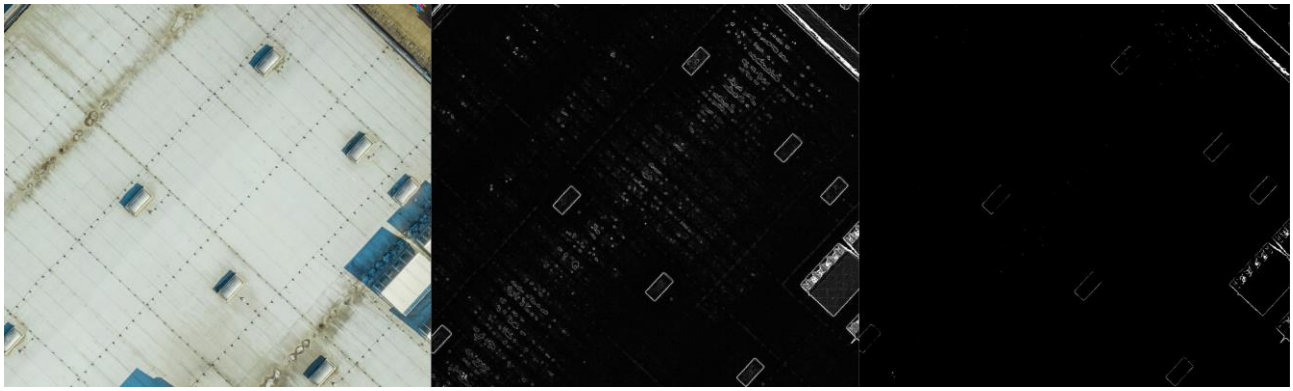

Fig. 7 – RGB orthomosaic (left), Slope before DEM filtering (middle), Slope after DEM filtering (right)

The RGBDTS raster used for creating samples for the U-NET model is composed of bands Red, Green, Blue, nDEM (normalized Digital Elevation Model), nTIR (normalized Thermal infrared) and Slope. All bands have the same 8-bit type for usage in the CNN model. For sample creation, CAD drawings are used for the first classification of flat roofs. CAD drawings were created as part of a job of flat roof inspection by company NDN tech. Computer aided design CAD drawings were converted into polygons representing each class of flat roof: PVC foil, windows, sidewalks, lightning rods and components.

Trimble eCognition - CNN approach

Using the Vector-based segmentation in Trimble eCognition was then from the polygons created image objects. These image objects were then classified responding to the number and type of input classes. From these classified image objects were then created samples for the CNN. The type of samples was used in RAW format, sample count was 50 000 and the sample patch size was 32 pixels. Samples were made for each layer of RGB texture. The Convolutional Neural Network contained 2 hidden layers. The kernel of the first layer was set at 7 and the number of distinct feature maps was 12. The kernel of the second layer was set to 5. The CNN was trained with a 0.0006 learning rate, with 5000 training steps and 50 samples were used in each training step. After applying the CNN, heat maps of each class were created. The Values of heat maps represent probabilities of occurrence of each class.

The RGBDTS raster is used with OBIA segmentation to achieve segments most similar to real objects of flat roofs. Object-Based Image Analysis (OBIA) is a technique that moves beyond the traditional pixel-based analysis commonly used in remote sensing. Instead of treating individual

pixels as the smallest unit of analysis, OBIA groups pixels into meaningful objects or segments based on their spectral, spatial, and contextual characteristics (shape and compactness). This approach allows for a more accurate and context-aware interpretation of the data. Segments are classified into PVC foil, windows, sidewalks and other classes by heatmap from the CNN model. With classified PVC foil, it is possible to divide segments into damaged and fine insulation. Damaged insulation has a higher temperature compared to fine insulation. PVC foil segments are classified by the rule: IF temperature PVC foil exceeds 0 from nTIR class as a flat roof leak.

ArcGIS - U-NET approach

The U-NET model's training chips were generated using 256x256 pixel tiles extracted from the RGBDTS raster data. Each tile contained polygons defining the different classes present in the scene. Training chips were in the "Classified Tiles" format.

The U-NET model underwent training with data augmentation techniques specified in Table 2. The training was conducted in batches of 8 samples for 20 epochs, with 10% of the data designated for validation purposes. A ResNet34 architecture served as the backbone for the deep learning model.

Tab. 2 - Methods of processing time

	Min	Max	Step
Rotate	0	360	10
Brightness	0.4	0.6	1
Contrast	0.7	1.5	1
Zoom	0.7	1.3	1

Flat roof leaks were extracted on segmented PVC foil at a higher temperature than the rest PVC foil.

RESULTS

Trimble eCognition - CNN - heatmaps

The application of a Convolutional Neural Network (CNN) within the eCognition software yielded unsatisfactory results. This can be attributed to several limitations. Each image chip could only receive a single class label, leading to misclassification when containing multiple classes within its boundaries. Smaller chip sizes might not capture sufficient textural information crucial for the accurate classification of flat roof elements. Introducing more than three distinct classes resulted in insufficient heatmap resolution for effective classification Figure 8.

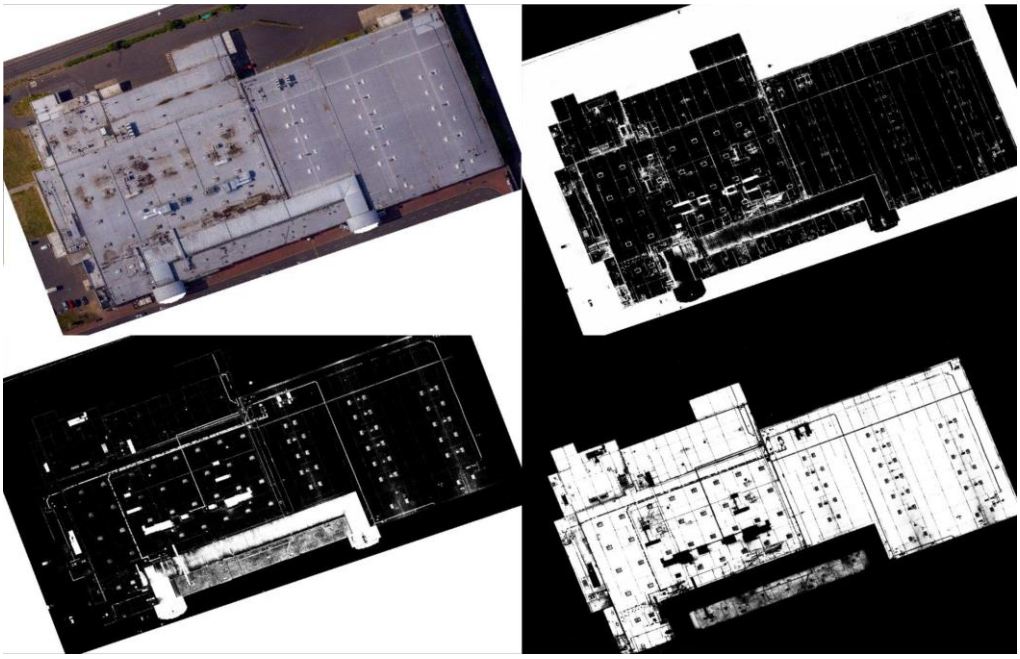

Fig. 8 – Results from eCognition

ArcGIS - U-NET pixels segmentation

Leveraging U-NET within ArcGIS effectively segmented flat roof classes. Employing larger image chips successfully preserved textural information crucial for accurate classification. Notably, the Classified Tiles format proved advantageous by enabling the representation of multiple classes within a single chip, thereby mitigating mislabelling issues.

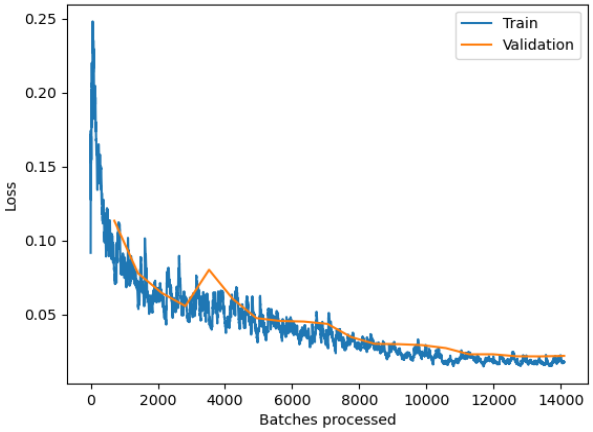

Fig. 9 – Training loss

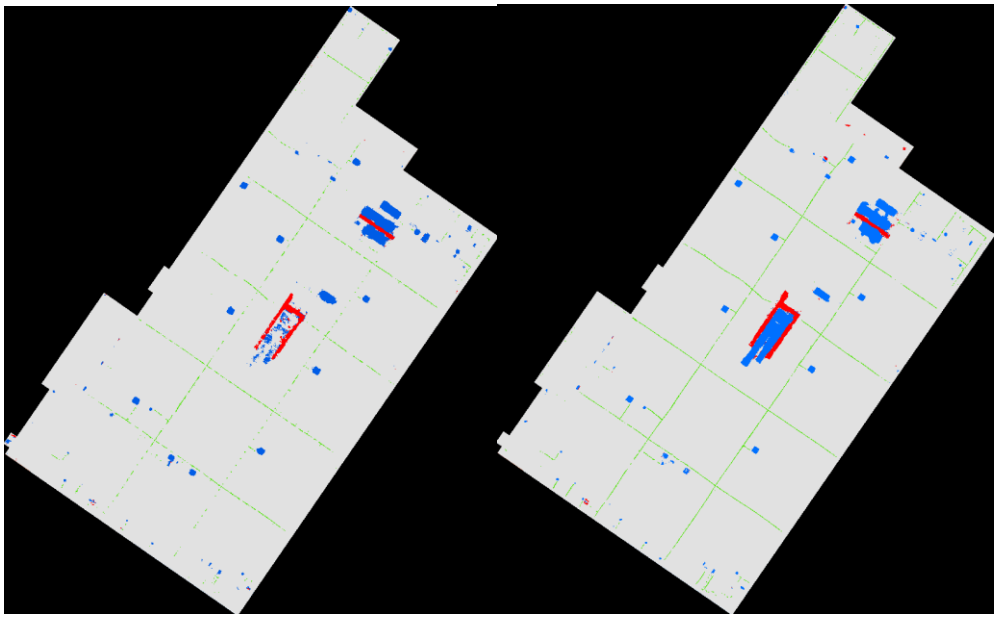

Fig. 10 – Results from ArcGIS

The efficacy of utilizing RGBDTS raster data was assessed against RGB raster data in terms of segmentation performance. Specifically, this evaluation focused on a flat roof scenario, employing identical network architectures, backbones, and other relevant parameters for both datasets. The results indicated superior segmentation outcomes when employing the RGBDTS raster compared to the RGB raster. Notably, there was no discernible difference in testing times between the two raster types, with both requiring equivalent time for one training epoch. Figure 10 visually represents the enhanced segmentation achieved across all three classes. This underscores the limitation of relying solely on colour information, particularly when distinguishing between classes with similar greyish hues. The resulting training results based on the RGBDTS raster are visible in Table 3 according to the evaluation equations (1-3) for deep learning.

$$Precision = \frac{TP}{TP+FP} \quad (1)$$

$$Recall = \frac{TP}{TP+FN} \quad (2)$$

$$F1\ score = \frac{TP}{TP+\frac{1}{2}(FP+FN)} \quad (3)$$

Tab. 3 - Methods processing time

	PVC	windows	lightning rod	components	walking
precision	0.994304	0.989148	0.926059	0.815632	0.980574
recall	0.995657	0.990409	0.937605	0.807025	0.952942
f1	0.994980	0.989778	0.931796	0.811306	0.966561

CONCLUSION

This study successfully demonstrated a streamlined and precise approach to flat roof leak detection, merging the power of remote sensing data and deep learning. By leveraging a DJI M300 drone equipped with RGB and thermal cameras, we captured comprehensive roof data and processed it into orthomosaics and DEMs. The U-NET deep learning model excelled at segmenting the roof into distinct classes (PVC foil, windows, sidewalks), paving the way for leak identification. Damaged insulation was pinpointed by analyzing temperature variations within PVC foil segments, effectively revealing leaks.

This novel method surpasses traditional inspection methods in several key aspects. Firstly, it boasts remarkable speed and efficiency, allowing UAVs to capture large roof areas in minutes, compared to days or weeks required by conventional methods. Secondly, the UAV-based system delivers superior accuracy, generating highly detailed orthomosaics and temperature maps that far exceed the capabilities of human inspectors. Most importantly, it prioritizes safety by eliminating the need for inspectors to physically climb roofs, thereby mitigating potential dangers.

The achieved results are highly promising, showcasing an overall segmentation accuracy of 95% for the deep learning model and a high degree of success in pinpointing damaged insulation. This innovative approach holds immense potential to revolutionize flat roof inspections, offering significant advantages:

Inspections can be completed much faster, reducing time and resource expenditure. Detailed data acquisition and analysis lead to more precise leak detection and damage assessment. Eliminating the need for manual roof access minimizes risks for inspectors. Detailed roof condition information facilitates informed maintenance and repair decisions.

By integrating additional classes (attics, ventilation systems, drainage elements) and refining the deep learning model with more data, the system's capabilities can be further expanded. This paves the way for a future where UAV-based inspections become the norm, ensuring safer, more efficient, and cost-effective flat roof management.

ACKNOWLEDGEMENTS

This work was supported by the Grant Agency of the Czech Technical University in Prague, grants SGS23/052/OHK1/1T/11.

REFERENCES

[1] Antón García, D., & Amaro Mellado, J. L. 2021. Engineering graphics for thermal assessment: 3D thermal data visualisation based on infrared thermography, GIS and 3D point cloud processing software. Symmetry, 13(2(335)), https://doi.org/10.3390/sym13020335

[2] Acuña Paz y Miño, J., Duport, N., & Beckers, B. 2021. Pixel-by-pixel rectification of urban perspective thermography. Remote Sensing of Environment, 266, 112689, https://doi.org/10.1016/j.rse.2021.112689

[3] Dlesk, A., Vach, K., and Holubec, P., 2018. Usage of Photogrammetric Processing of Thermal Images for Civil Engineers. (2018). Int. Arch. Photogramm. Remote Sens. Spatial Inf. Sci., XLII-5, 99–103, https://doi.org/10.5194/isprs-archives-XLII-5-99-2018

[4] Adamopoulos, E., Volinia, M., Girotto, M., & Rinaudo, F. 2020. Three-Dimensional Thermal Mapping from IRT Images for Rapid Architectural Heritage NDT. Buildings, 10(10):187, https://doi.org/10.3390/buildings10100187

[5] Daffara C, Muradore R, Piccinelli N, Gaburro N, de Rubeis T, Ambrosini D. 2020. A Cost-Effective System for Aerial 3D Thermography of Buildings. Journal of Imaging. 6(8):76. https://doi.org/10.3390/jimaging6080076

[6] Huang, Y., Shih, P., Hsu, K. T., & Chiang, C. 2020. To identify the defects illustrated on building facades by employing infrared thermography under shadow. NDT & E International. https://doi.org/10.1016/j.ndteint.2020.102240

[7] Yuan, W., & Hua, W. 2022. A Case Study of Vignetting Nonuniformity in UAV-Based Uncooled Thermal Cameras. Drones, 6(12), 394.
[8] Bayomi, N., Nagpal, S., Rakha, T.,, Fernandez,J.E. 2021. Building envelope modeling calibration using aerial thermography, Energy and Buildings, Volume 233, 110648, ISSN 0378-7788, https://doi.org/10.1016/j.enbuild.2020.110648.
[9] Rakha, T., El Masri,Y., Chen, K., Panagoulia, E., De Wilde, P. 2021. Building envelope anomaly characterization and simulation using drone time-lapse thermography, Energy and Buildings, 111754, ISSN 0378-7788, https://doi.org/10.1016/j.enbuild.2021.111754
[10] Straková, H.; Šedina, J.; Bila, Z. Monitoring of Heaps Using Various Technologies. 2015. Civil Engineering Journal. 2015/ 2 ISSN 1805-2576. https://doi.org/10.14311/CEJ.2015.02.0011
[11] Dlesk, A., Vach, K., & Pavelka, K. 2022. Photogrammetric Co-Processing of Thermal Infrared Images and RGB Images. Sensors. https://doi.org/10.3390/s22041655
[12] Dlesk A, Vach K, Pavelka K. 2021. Transformations in the Photogrammetric Co-Processing of Thermal Infrared Images and RGB Images, Sensors. 2021; 21(15):5061. https://doi.org/10.3390/s21155061
[13] Motayyeb, S., Samadzedegan, F., Javan, F. D., & Hosseinpour, H. 2023. Fusion of UAV-based infrared and visible images for thermal leakage map generation of building facades. Heliyon, 9(3)
[14] Stokowiec, K., & Sobura, S. 2022. Hand-held and UAV camera comparison in building thermal inspection process. In Journal of Physics: Conference Series (Vol. 2339, No. 1, p. 012017). IOP Publishing.
[15] Kuo, C. F. J., Chen, S. H., & Huang, C. Y. 2023. Automatic detection, classification and localization of defects in large photovoltaic plants using unmanned aerial vehicles (UAV) based infrared (IR) and RGB imaging. Energy Conversion and Management, 276, 116495.
[16] Osco, L. P., Marcato, J., Ramos, A. P. M., De Castro Jorge, L. A., Fatholahi, S. N., De Andrade Silva, J., Matsubara, E. T., Pistori, H., Gonçalves, W. N., & Li, J. 2021. *A review on deep learning in UAV remote sensing*. International Journal of Applied Earth Observation and Geoinformation. https://doi.org/10.1016/j.jag.2021.102456
[17] Naushad, R., Kaur, T., & Ghaderpour, E. 2021. Deep Transfer Learning for Land Use and Land Cover Classification: A Comparative Study. Sensors. https://doi.org/10.3390/s21238083
[18] Natesan, S., Armenakis, C., & Vepakomma, U. 2019. *Resnet-Based Tree Species Classification Using UAV Images*. (2019). The International Archives of the Photogrammetry, Remote Sensing and Spatial Information Sciences. https://doi.org/10.5194/isprs-archives-xlii-2-w13-475-2019
[19] Yi-Jun, L., Mohammadi, M. E., & Wood, R. L. 2020. Deep Learning Classification of 2D Orthomosaic Images and 3D Point Clouds for Post-Event Structural Damage Assessment. Drones. https://doi.org/10.3390/drones4020024
[20] How U-net works? | ArcGIS API for Python. 2024. https://developers.arcgis.com/python/guide/how-unet-works/
[21] Reachsumit (2024). GitHub - reachsumit/deep-unet-for-satellite-image-segmentation: Satellite Imagery Feature Detection with SpaceNet dataset using deep UNet. GitHub. https://github.com/reachsumit/deep-unet-for-satellite-image-segmentation
[22] Reder, S., Mund, J., Albert, N. G., Waßermann, L., & Miranda, L. 2021. Detection of Windthrown Tree Stems on UAV-Orthomosaics Using U-Net Convolutional Networks. Remote Sensing. https://doi.org/10.3390/rs14010075
[23] Kislov, D. E., & Korznikov, K. A.2020. Automatic Windthrow Detection Using Very-High-Resolution Satellite Imagery and Deep Learning. Remote Sensing. https://doi.org/10.3390/rs12071145
[24] Satari, R., Kazimi, B., & Sester, M. 2021. Extraction of linear structures from digital terrain models using deep learning. AGILE: GIScience Series. https://doi.org/10.5194/agile-giss-2-11-2021
[25] A Deep Learning Model for Identifying Mountain Summits in Digital Elevation Model Data. 2018. IEEE Conference Publication | IEEE Xplore. https://ieeexplore.ieee.org/stamp/stamp.jsp?tp=&arnumber=8527481
[26] Park, G., Lee, M., Jang, H. I., & Kim, C. 2021. Thermal anomaly detection in walls via CNN-based segmentation. Automation in Construction. https://doi.org/10.1016/j.autcon.2021.103627